INFORMATION TO USERS

This manuscript has been reproduced from the microfilm master. UMI films the text directly from the original or copy submitted. Thus, some thesis and dissertation copies are in typewriter face, while others may be from any type of computer printer.

The quality of this reproduction is dependent upon the quality of the copy submitted. Broken or indistinct print, colored or poor quality illustrations and photographs, print bleedthrough, substandard margins, and improper alignment can adversely affect reproduction.

In the unlikely event that the author did not send UMI a complete manuscript and there are missing pages, these will be noted. Also, if unauthorized copyright material had to be removed, a note will indicate the deletion.

Oversize materials (e.g., maps, drawings, charts) are reproduced by sectioning the original, beginning at the upper left-hand corner and continuing from left to right in equal sections with small overlaps.

Photographs included in the original manuscript have been reproduced xerographically in this copy. Higher quality 6" x 9" black and white photographic prints are available for any photographs or illustrations appearing in this copy for an additional charge. Contact UMI directly to order.

Bell & Howell Information and Learning
300 North Zeeb Road, Ann Arbor, MI 48106-1346 USA
800-521-0600

UMI®

MMW SCATTERING BY TREE TRUNKS AND SURROUNDING ENVIRONMENT MODELING & ANALYSIS

by

Alaa E. El-Rouby

A dissertation submitted in partial fulfillment
of the requirements for the degree of
Doctor of Philosophy
(Electrical Engineering)
in The University of Michigan
2000

Doctoral Committee:
Professor Fawwaz T. Ulaby, Co-Chair
Assistant Research Scientist Adib Y. Nashashibi, Co-Chair
Professor Anthony W. England
Associate Professor Kamal Sarabandi
Professor Andrew E. Yagle

UMI Number: 9990886

Bell & Howell Information and Learning Company
300 North Zeeb Road
P.O. Box 1346
Ann Arbor, MI 48106-1346

ACKNOWLEDGEMENTS

All gratitude is due to Allah.

I would like to express my sincere gratitude to Prof. Fawwaz T. Ulaby for his continuous financial support and academic guidance throughout the course of this work, and to express my heartfelt gratitude to Dr. Adib Y. Nashashibi for his invaluable friendship, and long hours of help and advice that helped me to complete my work. I also like to express my appreciation and thanks to my doctoral committee members for their comments and remarks that helped me to finalize this thesis.

Special acknowledgments and thanks are due to the members of the Muslim Community Association of Ann Arbor, for their spiritual support throughout the course of this work and a lot of thanks are due to the following friends and colleagues for their help and enlightening conversations during my graduate studies: Dr. Roger De Roo, Dr. Liland Pierce, Patti Wolfe, Eray Yasan, and Mohamed Abdel Moneum.

Last but not least, my gratitude to my wife, parents, and family always remains. Their loving support and prayers are what i need most.

TABLE OF CONTENTS

LIST OF FIGURES

CHAPTER 1

INTRODUCTION

The need for compact and affordable sensors capable of detecting and tracking man-made targets in the presence of clutter has attained significant prominence over the past decade. Millimeter wave sensors have been proposed for these applications because of their compact size, high resolution, and their ability to work in, almost, all weather conditions. Recent developments in millimeter-wave (MMW) technology have made MMW radars a viable approach for these applications.

Scattering by man-made targets in the presence of clutter is a very complex problem that involves a large number of parameters. These include the system parameters (incidence angle, system bandwidth, footprint area, etc.), parameters associated with man-made target (strength of the radar backscatter from the man-made target, frequency response, etc.), and clutter parameters (homogeneity of the clutter, physical parameters, water content, etc.). The high degree of complexity of the scattering problem along with the large number of parameters involved make the detection and

tracking problems very convoluted. Hence, an accurate characterization of MMW polarimetric radar backscatter from clutter (the background) is an essential component in designing the optimal sensor and in developing detection algorithms. Of special importance is the characterization of the radar backscatter from tree trunks since they represent a major class of targets that may be confused with man-made targets by a MMW radar. This confusion is expected in power-based detection algorithms due to the anticipated high radar cross section (RCS) of tree trunks compared to other types of clutter. The high RCS of tree trunks is expected because of their vertical physical extents, as well as the bistatic nature of the scattering process. This expectation was confirmed by an observation reported by researchers at the Army Research Laboratory (ARL) [54]. It was observed that in forested areas synthetic aperture radar (SAR) images at near grazing angles had several bright pixels with RCS levels on the order of magnitude of those associated with man-made targets (vehicles). These bright pixels were found to correspond to tree trunks.

In addition, because of the large variation in shape, size, and material of man-made targets, the backscatter from a man-made target is difficult to specify, particularly at MMW frequencies where the wavelength is much smaller than the dimensions of the man-made target. This behavior of the backscatter from man-made targets adds more complexity to the scattering problem and makes it more difficult to develop an efficient detection algorithm that is capable of detecting man-made targets in the presence of clutter. One of the basic ideas to enhance the capabilities of detection algorithms is to increase their input information. Along this line, many approaches have

been introduced and applied to enhance the detection capabilities of remote sensing systems. These approaches can be divided into two main categories as follows:

I- Performing more radar measurements

An examples of this approach involves the introduction of polarimetric measurements instead of power-only measurements. Another example involves the data fusion of multiple sensors output [51].

II- Exploiting more features from the available radar measurements

Examples of this approach are the E-pulse technique [11, 10], and the use of information from both time and frequency domains, combined together, to make a detection decision [38].

Comparing these two approaches, the first one is expected to lead to better results, but it also implies larger sensor size and greater cost.

For a number of proposed applications, such as vehicle collision-avoidance systems and low-altitude military target detection sensors, the configuration is such that a MMW radar will be operated at near grazing incidence. Although, numerous investigations and extensive measurements of the radar backscatter from terrain have been conducted over the past three decades at centimeter wavelengths, far fewer observations have been made at millimeter wavelengths, particularly at near grazing angles (high incidence angles). Therefore, this thesis is intended to fill the gap of available information at MMW frequencies with a focus on near-grazing incidence as a step towards the development of optimal remote sensing systems that have the ability to

detect and track man-made targets in the presence of clutter.

1.1 Motivation

Electromagnetic (EM) wave scattering by terrain is a stochastic process, as opposed to a deterministic process. Many models had been proposed, at lower frequencies, to characterize the statistics of EM scattering by natural terrain. Among those models are (a) the popular model of Rayleigh fading [16], (b) several non-Rayleigh fading models including, among others, the log-normal distribution, and the Rician distribution, [16, 36, 47], and (c) the K-distribution, which have been used in many observational studies [9, 31, 46]. While model (a) was mostly applied on cases of statistically homogeneous terrain, the models in (*b*) and (*c*) were in general reported for heterogeneous terrain. Moreover, these models were based on data at lower frequencies, hence, not necessarily applicable at MMW frequencies. The differences among these models may be attributed to the differences in the degree of homogeneity of the terrain under consideration, but this explanation needs to be examined more rigorously, which in turn requires the availability of a reliable data set of MMW scattering for various types of terrain at angles near grazing incidence.

In addition to the need to examine the statistical and angular variability of MMW scattering by terrain at near grazing angles, scattering by tree trunks is a component of particular importance that also needs to be considered. Many studies have been

performed, such as those reported in [33, 17], to analyze and model electromagnetic scattering by tree canopies. Other studies focused on the scattering by the trunk segment of forested areas [35, 50]. In any study that deals with electromagnetic interaction among tree trunks or between tree trunks and the ground plane underneath, a model for the scattering by tree trunks must be involved. In some studies such as [35, 48], the tree trunk is approximated as a smooth dielectric cylinder of finite length. This approximation is valid only at low frequencies where the roughness component of the trunk surface is much smaller than the wavelength. In other studies [32, 33, 49], the rough layer (the bark layer) of the tree trunk is approximated by an equivalent periodically corrugated dielectric layer of dielectric constant different from that of the internal layers of the trunk. This second approach is also not valid at MMW frequencies because of the following reasons: (a) the electromagnetic wave is attenuated by the bark layer and the wave that penetrates the air-trunk boundary into the trunk interior is highly attenuated, (b) the rough layer for many tree species is inappropriate to be considered as a periodic series of grooves, and (c) due to the short wavelength at MMW frequencies ($\lambda \simeq 3\ mm$ at 95 GHz), any irregularity in the assumed periodicity of the grooves on the order of $\lambda/10$ ($\simeq$ 0.3 mm at 95 GHz) results in a violation of the basic assumption of this second approach.

The lack of reliability and experimental verification of the current models at MMW frequencies raises the need for the development of an accurate model for MMW scattering by tree trunks that is capable of handling trunks with arbitrary roughness parameters. Hence, the candidate approach for modeling the scattering by a tree

trunk at MMW frequencies is to treat it as a rough, dielectric cylinder. For a cylinder with a slightly rough surface, the small perturbation method is applicable, as reported in [8, 27], but for very rough surfaces, corresponding to MMW frequencies, no studies have thus far (to our knowledge) been reported on scattering by rough cylinders. This need for an accurate and a general model for scattering by rough, lossy, dielectric cylinder and its application to tree trunks at MMW frequencies (high frequencies in general) represents a main motivation for carrying out this part of the research. Such a model is also needed in order to study the phenomenon of occurrence of high RCS values by tree trunks and to calculate the associated probability.

The modeling and characterization of the scattering by terrain and tree trunks were originally aimed to contribute to enhance the performance of detection algorithms. Other factors that deepened our interest in studying the detection problem and narrowed our focus to resolving the possible confusion between man-made targets and tree trunks were: (a) the challenging complexity of the problem of detecting man-made targets in the presence of clutter along with the concurrent need of a number of remote sensing applications, such as vehicle collision-avoidance systems and low-altitude military target detection systems, for this detection ability, and (b) the confusion between tree trunks and man-made targets reported by researchers at ARL [54].

1.2 Outline

In this thesis we study and analyze MMW scattering by natural terrain, at near grazing angles, in general and by tree trunks in particular. In addition, we deploy the characterization of the scattering from terrain and tree trunks at MMW frequencies and at low grazing angle to study the problem of detecting man-made targets in the presence of clutter.

The study of MMW scattering by natural terrain, Chapter 2, includes: (a) modeling the characteristics of the statistical variability of the radar backscatter from natural terrain, and (b) studying the angular variability and the dynamic range of the backscattering coefficient of various types of terrain at near grazing angles.

Scattering by tree trunks ended up being a major focus of this study. Radar scattering by a rough, lossy, dielectric cylinder is examined as a model for characterizing the scattering by tree trunks. In Chapter 3, we present analytical models for the coherent and incoherent components of the scattering by a rough, lossy, dielectric cylinder. Also, we verified the validity of these models and examined their accuracy experimentally. In Chapter 4 we present the details and results of a series of experiments that were conducted to: (a) measure the dielectric constant of the wooden material of the tree trunk, (b) verify the assumption that the bark layer is lossy enough to hide, from a radar standpoint, the interior dielectric structure of the trunk, (c) incorporate the radar system impulse response into the theoretical model

predictions, (d) measure the coherent and incoherent angular backscatter responses of a rough, conducting cylinder and a section of tree trunk to compare them to the theoretical model predictions, and (e) measure the roughness parameters of the rough cylinder and the section of the tree trunk . These experimental measurements along with the incoherent model were deployed, in Chapter 5, to study the possibility of occurrence of high RCS value from tree trunks. In addition, in Chapter 5, we introduce a methodology to calculate the probability of occurrence of high RCS values from a tree trunk above a ground plane.

Another topic that we considered in this thesis is a way to resolve the possible confusion (which occurs with power-based detection algorithms) between tree trunks and man-made targets. Two general approaches to resolve such a confusion were identified through a search of the literature. These approaches are: (a) performing more radar measurements, and (b) exploiting more features from the available radar measurements. To that end, we adopted approach (b). Towards that, in Chapter 6, we present an analytical study of the characteristics of the frequency correlation function (FCF) from the detection standpoint and relate these characteristics to the time-domain scattered signal. In Chapter 7, we report on an outdoor measurement campaign that was designed and conducted to investigate the use of an FCF-based features in detection. The results of this campaign led to the introduction of the FCF bandwidth (FCFBW) as a detection feature. In addition, in Chapter 7 we developed an FCFBW-based detection algorithm and evaluated its performance. A more rigorous study of the characteristics of the FCF and its relation to the type of

targets (terrain versus single scatterer) and relevant system parameters is performed using numerical simulation. The details of the numerical simulation are presented in Chapter 8. Also in this Chapter, we introduce three more FCF-based detection features (in addition to FCFBW) and use them to develop an enhanced detection algorithm.

CHAPTER 2

MMW SCATTERING BY TERRAIN AT NEAR GRAZING ANGLES

2.1 Introduction

When we characterize the radar backscatter behavior of a target, be that a point target —such as a truck, a fence, or an urban feature— or a distributed target — such as a field of corn or a forest canopy— we usually do so in terms of two sets of parameters: the target parameters and the sensor parameters. The target parameters include shape factors and dielectric attributes, and the sensor parameters include the wave frequency f, the incidence angle θ, the receive-transmit polarization configuration (such as HV for a horizontally polarized receiver and a vertically polarized transmitter), and (possibly) the dimensions of the cell illuminated by the radar antenna. In the microwave region, numerous investigations and extensive measurements of the backscatter from terrain have been made over the past three decades at centimeter wavelengths, but much fewer observations have been made at millime-

ter wavelengths, particularly at high incidence angles (low grazing angles). In this chapter we will study the MMW backscatter from natural terrain at near grazing angles with focus on 95 GHz. The study in this chapter were performed to answer the following questions:

1. What is the statistical model of the backscatter from homogeneous/heterogeneous terrain at MMW frequencies and at near grazing angles?, is there a universal statistical model for the backscatter from terrain?, and if not, what are the reasons behind differences among statistical models proposed in the literature for the backscatter from terrain?.

2. What is the dynamic range of the backscatter from homogeneous terrain at MMW frequencies and at near grazing angles?, and how does the backscattered signal (in volt amplitude or power amplitude) depend on the angle of incidence?.

By way of introducing some of the terms we intend to use in this chapter, let us consider the hypothetical scene depicted in Fig. 2.1. The scene consists of several fields of vegetation (grass, for example) at various stages of growth. Each field is *statistically homogeneous*, meaning that it exhibits the same local statistics (in terms of plant height, density, water content, etc.) for any location within that field. The scene is imaged by a distant radar with resolution-cell area A at the range corresponding to the scene under consideration. The dimensions of A are such that: on one hand, each cell contains many randomly distributed scatterers, thereby satisfying one of the assumptions of the Rayleigh fading statistics [16], while on the other hand A is much

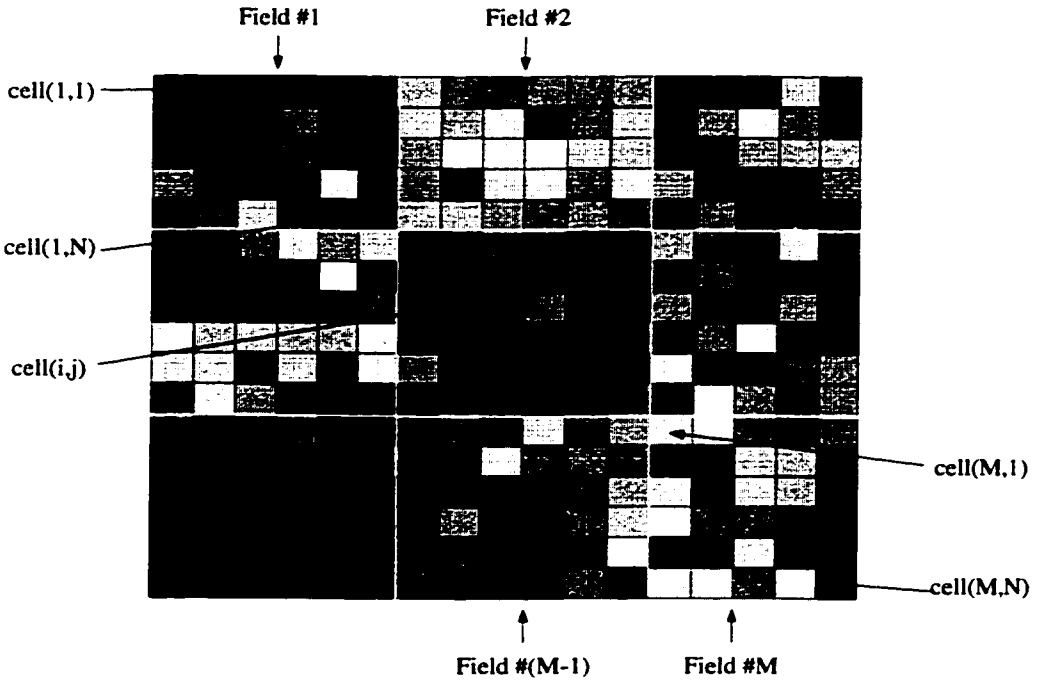

Figure 2.1: Illustration of a radar image of a scene consisting of M fields of vegetation, with each field occupied by N illuminated cells.

smaller than the overall field dimensions. Because of this latter feature, the number of cells N contained in each field is sufficiently large as to allow us to examine the statistical properties of the radar backscatter variation across a given field. Each cell in the scene is denoted by a combination of two indices, i and j, defined as follows:

- i = field index, with $i = 1, 2, \cdots, M$ fields,
- j = cell index within a field, with $j = 1, 2, \cdots, N$ cells.

The radar response can be characterized by the following quantities:

- $\sigma_A(i,j) = \sigma(i,j)/A$ = radar cross section per unit area of cell (i,j),
- $\sigma_i^0 = <\sigma_A(i,j)>_j = \frac{1}{N}\sum_{j=1}^{N}\sigma_A(i,j)$ = scattering coefficient of field i,
- $p_i(\sigma_A)$ = probability density function (*pdf*) of σ_A for all cells of field i, and
- $p(\sigma_A)$ = *pdf* of σ_A for all cells of all fields within the scene.

In terms of the scene depicted in Fig. 2.1, $p_i(\sigma_A)$ might be the *pdf* of one of the fields of vegetation, whereas $p(\sigma_A)$ would be the *pdf* for the entire class of vegetation (all fields) present in the scene. We make this distinction for an important reason. Many papers appear in the literature in which the authors have fitted radar backscatter data from terrain, often referred to as radar clutter, to the K-distribution [9, 31, 46], implying that the Rayleigh fading model [16] is inapplicable. As we stated before, in this chapter, we aim to characterize the statistics of the radar backscatter from homogeneous terrain, like field i in the hypothetical scene of Fig. 2.1, and from heterogeneous terrain, like the whole scene of Fig. 2.1. In addition, we will investigate and search the reasons behind differences among statistical models proposed in the literature for the backscatter from terrain.

The Rayleigh model is based on three main assumptions:

(a) each cell should contain large number of scatterers to satisfy the central limit theory upon which the Rayleigh statistical model is based,

(b) the scatterers should be randomly distributed in location within the radar-illuminated cell so as to satisfy the assumption that the returns are characterized by a uniform phase distribution, and

(c) the strengths of the returns from the scatterers are comparable in magnitude, or, equivalently, that no individual (or few) scatterer(s) should dominate over the others.

These conditions are usually satisfied for any terrain target with statistically homogeneous properties, so long as the cell dimensions are much larger than the dimensions of individual scatterers.

According to the Rayleigh statistical model, the total backscattered signal from terrain is a complex random quantity, its phase is a uniform $(0, 2\pi)$ random variable, and its real and imaginary parts are uncorrelated, zero-mean Gaussian random variables. In other words, if we presented the backscattered signal in the scattering matrix format, any element of the scattering matrix (denoted by S) would be presented as:

$$S = S_o\, e^{j\phi} = S' + jS'', \tag{2.1}$$

where S' and S'' are the real and imaginary parts of S, respectively. Hence, S' and S'' are uncorrelated, zero-mean Gaussian random variables, and we can express the *pdf* of ϕ, S', and S'' as:

$$\begin{aligned} pdf(\phi) &= \frac{1}{2\,\pi}, \\ pdf(x) &= \frac{1}{\sqrt{2\pi\sigma^2}}\, e^{-(\frac{x^2}{2\,\sigma^2})}\Big|_{x=S' \text{ or } S''} \quad , \end{aligned} \tag{2.2}$$

where $\sigma = \sqrt{\overline{S'^2}} = \sqrt{\overline{S''^2}}$, with the bar over the variable refers to its statistical average. Based on these *pdf's* of S', S'', and ϕ we can derive the *pdf* of the amplitude and of the power of the backscattered signal which are found to be of Rayleigh and exponential distribution as follows:

$$pdf(S_o) = \frac{S_o}{2\,\sigma^2}\, e^{-(\frac{S_o^2}{2\,\sigma^2})}. \tag{2.3}$$

$$pdf(S_o^2) = pdf(P) = \frac{1}{\overline{P}}\, e^{-(P/\overline{P})}. \tag{2.4}$$

In what follows, we will describe the sources of the data used in this study as well as the setup used in data acquisition, data processing steps, and the terrain classification procedure, Sections 2.2 - 2.3. In Section 2.4, we will study and model the statistics of the radar backscatter from both homogeneous and heterogeneous terrain. In that section, we will consider the statistics of the real and imaginary parts, the voltage amplitude, and the power of the backscattered signal for both the cross and copolarizations. The statistical analysis will be followed, in Section 2.5, by a study of the angular variability of the signal backscattered from various types of terrain at near grazing angles.

2.2 Data Sources

This study is based on an extensive data set acquired at 95 GHz. This data set was acquired by a polarimetric scatterometer system belonging to the Army Research Laboratory, ARL. The ARL system is a pulse radar that operates in a frequency stepped mode between 95 and 95.64 GHz [40]. It is configured to transmit 100-ns

long pulses (with an equivalent range resolution of 15 m) at 45 W peak power and a pulse repetition frequency of 10 KHz. Using a 6-inch diameter horn antenna operated in a monostatic mode, the effective two-way antenna beamwidth is 1°. The radar operates in a fully coherent mode and can measure the scattering matrix of a target in either the linear, V/H, polarization coordinate system or the circular, LHC/RHC, polarization system. A total of five different calibration targets are employed in the calibration procedure. When deployed in the field for measuring the backscatter from terrain, the radar is mounted on an elevation-over-azimuth computer-controlled pedestal at a height of about 10 m above ground level. At a grazing angle of 3.4°, the dimensions of the ground cell measured by the radar are 2.9 m in azimuth and about 15 m in range. For the purpose of random noise reduction, the measurements of each cell were repeated at least 8 times (ramps) at all of the 64 frequency steps, so those measurements were averaged coherently while recalibrating the data. This system operates in an imaging mode where it scans a certain area of terrain. The backscattered signal from the terrain is then stored on a computer disk while, in the same time, the optical image of the cells being measured are stored on video tapes. The video tape real-time optical images has, on top of the optical image, the cell coordinates and the measurement time stamp printed as a legend at the bottom of the screen. The radar image data was obtained over periods of 6-7 weeks at Yuma, AZ in 1992 and at Grayling, MI in 1992 and 1994. During each campaign of measurements the same area of terrain was observed repeatedly at random times within this 6-7 week periods. Each of these observations is called a mission.

Each cell (a pixel in the radar image) of the scanned terrain were observed at each of the 64 equally spaced (by 10 MHz) frequencies extending between 95 and 95.64 GHz. For this radar system, which has a range resolution $\Delta R = 15$ m, the decorrelation bandwidth Δf is given by [16, p. 72]:

$$\Delta f \simeq \frac{150}{\Delta R} \text{ MHz} = 10 \text{ MHz}. \tag{2.5}$$

Hence, the multi-frequency radar observations are statistically independent, which means that the total number of statistically independent samples of any type available from a given mission (one-time observation of a scene) is $64N_c$, where N_c is the number of terrain cells of this specific type.

2.3 Data Extraction and Processing

The optical real-time video images of the missions of terrain scanning were browsed and 7 different types of homogeneous terrain were identified. Those types are: deciduous tree canopy, coniferous tree canopy, bare soil, short grass, bushes, wet snow cover, and fresh snow cover. The radar linear polarization (H/V polarization system) backscatter data of more than 2000 cells of those types of terrain were extracted.

The acquired data were calibrated by the ARL as follows:

1. A-to-D offsets are subtracted.

2. I/Q receiver amplitude and minor phase distortions are removed.

3. Radar-dependent polarimetric distortions are removed using Barnes' matrix

technique (this removes cross-polarization leakage and frequency-dependent amplitude and phase errors). The result is radar-cross-section in units of squared meters and phase in radians.

4. A range correction is applied. Amplitude units are converted to dBm^2.

But, since the ARL calibration procedure does not consider the effect of the antenna pattern on the acquired data, we wrote a code to correct the data for the antenna effect or the illuminated area effect.

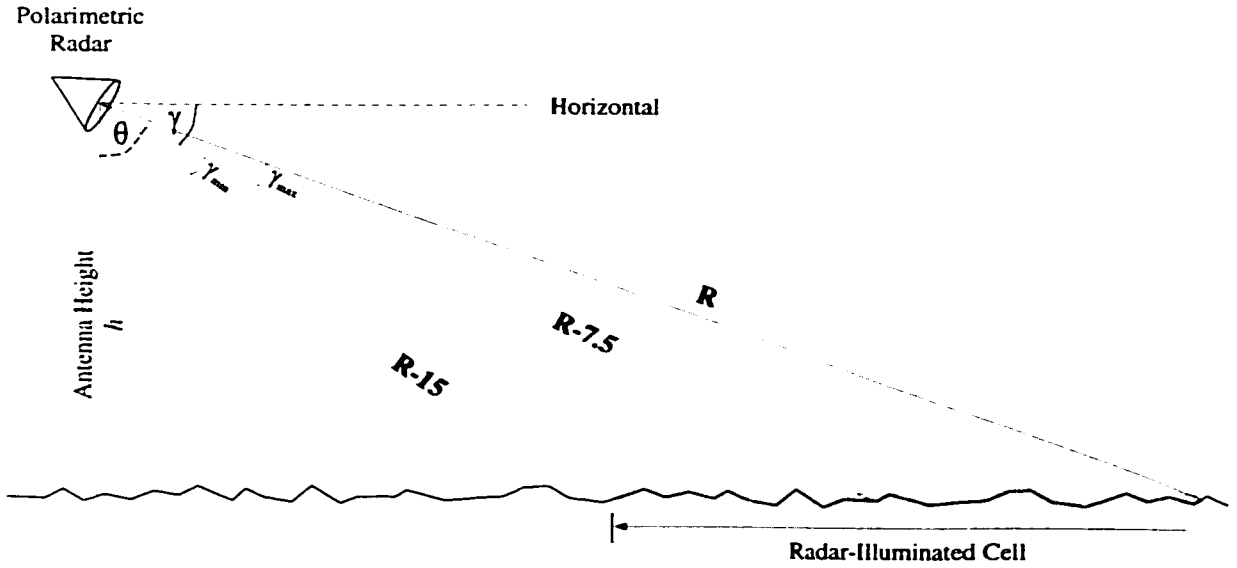

Figure 2.2: ARL measurement setup.

Because the measurements were done in a real environment and the measured pixels are not all at the same relative height with respect to the radar, we found that considering an absolute height of the antenna over all of the measured cells could

result in inaccurate results. Therefore, we designed our recalibration code to calculate the relative height between the antenna and the measured pixel for every pixel based on the power level from the pixel at different ranges. Where, in this procedure, we average the received power over all the frequency steps for each of the measured ranges individually, then we pick the range that gives the highest received power to be the base for our setup parameters calculations.

Our date extraction and recalibration procedure can be summarized as follows:

1. Extract the scattering matrices of the pixel over all the frequency steps and over all ramps (by ramp we mean one scan over the whole frequency steps), then average the scattering matrices coherently over the whole ramps. In other words, for every frequency step the data of all the ramps are averaged coherently to reduce the effect of noise on the measurements.

2. For every range, average the sum of the co-polarized (VV and HH) backscattered power over the whole frequency steps. Then, make the setup parameters calculations based on the range corresponding to the maximum backscattered sum of the two co-polarized powers. This was done in order to overcome the lack of a surveyed height profile of the terrain associated with radar data.

3. From the geometry shown in Fig. 2.2, calculate the relative height of the antenna over the measured pixel as follows:

$$h = (R - 7.5) * cos\,(90 - \gamma)\,, \tag{2.6}$$

where R is the range corresponding to the maximum backscattered power.

4. Using both the chosen range and range resolution (15 meters), calculate the minimum and maximum angles from the center of the beam to both edges of the measured cell as follows:

$$\begin{aligned} \gamma_{max} &= \gamma - sin^{-1}\left(\frac{h}{R-15}\right) \\ \gamma_{min} &= sin^{-1}\left(\frac{h}{R}\right) - \gamma \quad . \end{aligned} \tag{2.7}$$

5. Calculate the, single measurements, pseudo-Mueller matrix of all the frequency steps.

6. undo the range calibration performed by ARL and apply the antenna pattern calibration, which involves dividing the backscattered response by the illumination integral IA as follows:

$$IA = R_o^4 * \int_{illuminated\ area} \frac{G_r G_t}{R^4}\, da \ ,$$

where, R_o is the range to the center of the cell (which was used by ARL), and G_r, G_t are the receiver and transmitter gain respectively. In discrete form, IA can be expressed as:

$$IA = R_o^4 * \sum_{all\ i's} \frac{G_{ri} G_{ti}}{R_i^4}\, da_i \tag{2.8}$$

and

$$M = \frac{M'}{IA} \tag{2.9}$$

Where:

- M' is the pseudo-Mueller matrix before removing the range calibration done by ARL,
- R_i is the distance from the radar to the cell number i of the illuminated area, and
- The subscript i refers to the cell number i of the illuminated area.

Since the antenna pattern was measured at 0.1^o angular steps, the illuminated area was discretized based on 0.1^o angular steps, in both the azimuth and elevation directions, too.

2.4 Radar Backscattering Statistics

The validity of the Rayleigh statistical model was examined for each of the 7-types of statistically homogeneous terrain identified from the video tapes (deciduous tree canopy, coniferous tree canopy, bare soil, short grass, bushes, wet snow cover, and fresh snow cover). The examinations were performed over several near grazing incidence angles around 85^o for each of the principle polarization configurations: VV, HV, and HH. In each individual case, the measured histogram of the backscatter from terrain were examined against the pdf's of the Rayleigh statistical model. We started by the Rayleigh statistics because it is supported by a rigorous theoretical derivations and it was reported for the statistics of the backscatter from statistically homogeneous terrain in many studies at lower frequencies [16].

In more details, histograms of the real and imaginary parts of the measured scattering matrix elements S'_{vv}, S''_{vv}, S'_{hh}, S''_{hh}, S'_{hv}, and S''_{hv}, of terrain were generated and compared to the zero-mean Gaussian pdf. In addition, we performed comparisons between the measured histograms of $|S_{vv}|$, $|S_{hh}|$, and $|S_{hv}|$ and the Rayleigh pdf and between the measured histograms of $|S_{vv}|^2$, $|S_{hh}|^2$, and $|S_{hv}|^2$ (which are proportional to σ^o_{vv}, σ^o_{hh}, and σ^o_{hv}) and the exponential pdf. The cumulative distribution function, $P(X \leq X_o)$, were also used to examine the accuracy of the Rayleigh statistical model in describing the statistics of the radar backscatter from statistically homogeneous terrain, where,

$$P(X \leq X_o) = \int_0^{X_o} p(X)\ df. \tag{2.10}$$

The comparisons between the pdf's of the Rayleigh statistical model and the histograms of the measured quantities (real and imaginary parts, amplitude, and power of the backscattered field) were performed based on two different bases: (a) the absolute quantities, which show some statistical variability in the mean and/or standard deviation values from mission to mission or from cell to cell due to the variation of the physical parameters of the cell either spatially or over time, and (b) the normalized (to the mean or the standard deviation of the measurements of each cell) value, which is done to leave the measurements with the effects of the scattering process alone as a source of randomness and remove the randomness caused by the physical conditions variabilities. Similar tests for the validity of the Rayleigh statistical model were performed on the absolute and normalized data of all the cells, aggregated together in one data set, of the 7-different homogeneous types. This later test is used to examine

the statistics of the backscatter from statistically heterogeneous terrain.

Examples of the results of the comparison between the measured histogram of terrain (short grass) and the exponential *pdf* (based on both the absolute and normalized values) are shown in figures 2.3 and 2.4. The exponential pdf is the pdf of the Rayleigh statistical model for the backscattered power. In this example 14,976 spatial and frequency statistically independent data points are available at 86.6°. Figure 2.3 compares the histogram of the measured σ_A to the exponential pdf and the measured cumulative distribution to the exponential corresponding one for both VV and HV-polarizations. The same data was normalized (denoted here by $F = \frac{\sigma_A}{\sigma_i^o}$) to σ_i^o which is the average over the 64 frequency statistically independent samples of each cell individually. Then compared to the exponential pdf again as shown in Fig. 2.4. As expected, due to physical parameters variability from cell to cell or from mission to mission, Fig. 2.3 shows more deviations from the theoretical model than the deviations shown in Fig. 2.4. However, Fig.2.3 shows some deviations from the theoretical models, these deviations are small. This small deviation can be attributed to the high degree of statistical homogeneity of the physical parameters (density, height, water contents, etc.) of the short grass-covered terrain. An important point to note here is that, although the short grass data shows a high degree of statistical homogeneity, and hence a good agreement with the Rayleigh statistical model, the normalized data (Fig. 2.4) shows a higher level of agreements between the statistics of the measured data and the Rayleigh statistical model. This is because of the removal of the physical parameters variability (by normalization) and leaving the data with the randomness

associated with the scattering process, alone, which is well (analytically and experimentally) described by the Rayleigh model.

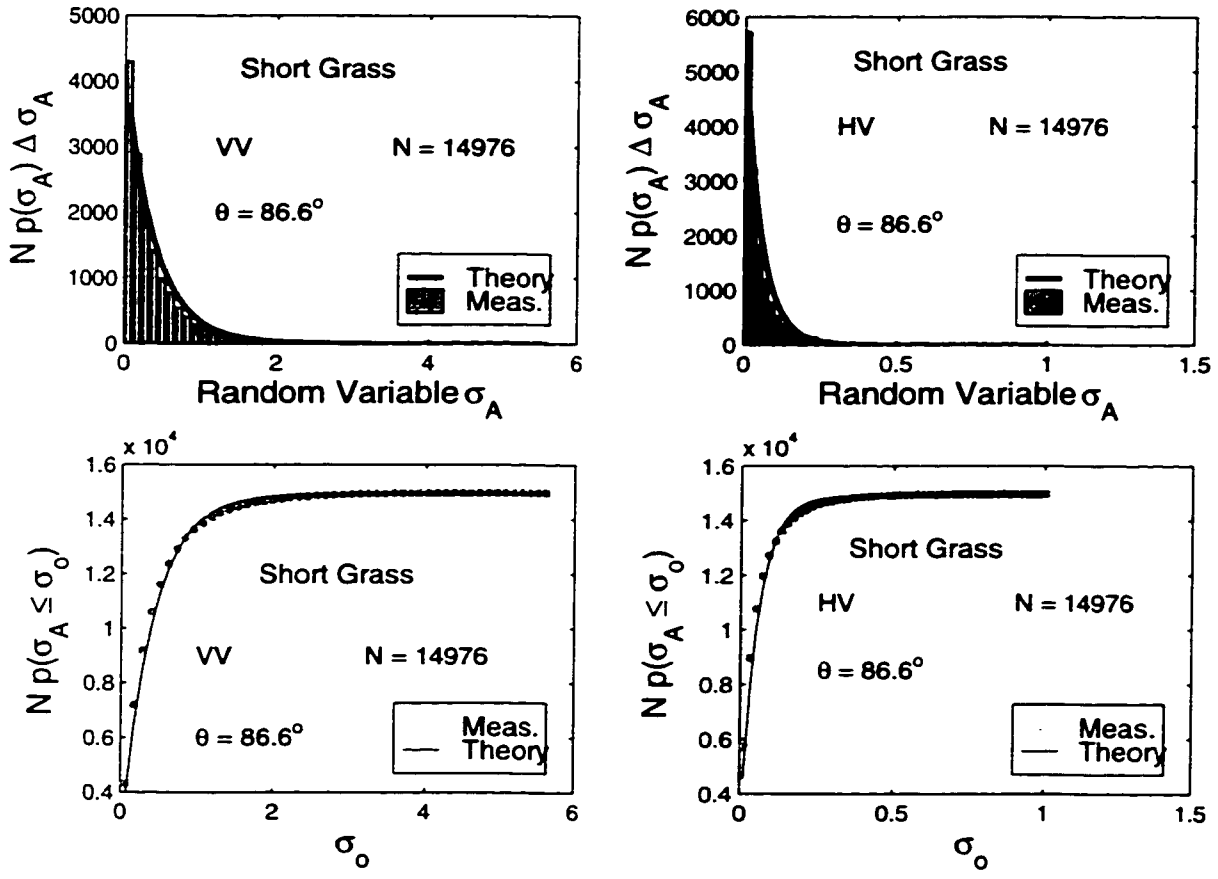

Figure 2.3: Comparison between the short grass measured histogram of σ_A and its cumulative distribution function, $P(\sigma_A \leq \sigma_o)$, and the theoretical expectations based on the exponential pdf.

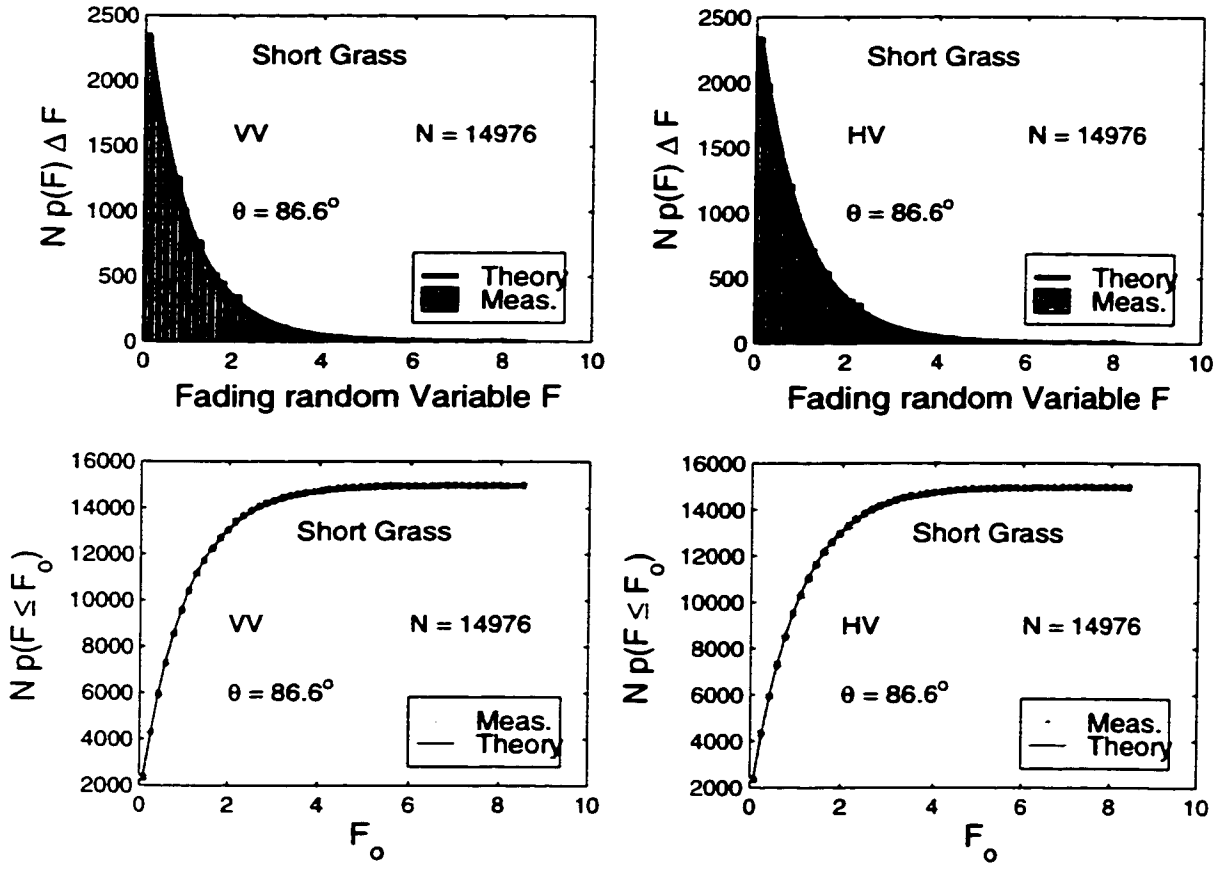

Figure 2.4: Comparison between the short grass measured histogram of the random variable F and its cumulative distribution function, $P(F \leq F_o)$, and the theoretical expectations based on the exponential pdf.

Another example is the case of coniferous tree canopy which are shown in figures 2.5 and 2.6. It is important to note that the data for tree does not include mixed categories; a cell observed by the radar is defined to belong to the terrain type called trees only if the cell contains trees and no other categories. Thus, a cell that was partially a ground surface and partially a tree was excluded from consideration. However this being the case, the data of the coniferous tree, Fig. 2.5, shows a much larger deviations from the theoretical model when compared to the case of short grass, Fig. 2.3. This comparison (between Fig. 2.3 and Fig. 2.5) indicates that the coniferous trees have less physical parameters statistical homogeneity (leaf density, air gap distribution, water of contents, etc.) than the case of short grass. In other words, the coniferous tree canopy is less homogeneous, from the radar backscatter perspective, than the short grass. Removing the physical parameters variabilities from the data, by normalization, results in very good agreements between the statistics of the normalized measurements and the theoretical model, as illustrated in Fig. 2.6.

These examples depicted in figures 2.3 - 2.6 represent the typical behavior, with some variations depending on the level of physical parameters homogeneity of the type of terrain, for all the combinations of terrain types, incidence angles, and polarizations examined in this study.

These results and observations can explain the reasons behind the differences between the statistical models, proposed in the literature, for the backscatter from terrain. That is, in the literature many models are proposed based on fitting the

histogram of the measurements to a probability distribution function, pdf, without considering the degree of homogeneity of the terrain. In other words, the randomness, and hence the statistical properties, of the scattering by terrain can be attributed, mainly, to two sources: (a) the phase interference of the field backscattered from all the scatterers in the illuminated cell, and (b) the variations of the physical parameters of the terrain from a statistically-independent cell to another. The Rayleigh statistical model explains the behavior of the first component, while the second component is too general to have a unique statistical model. Hence, trying to model the characteristics of the two components together would lead to a variety of statistical models based on the behavior of the second component of physical parameters variability.

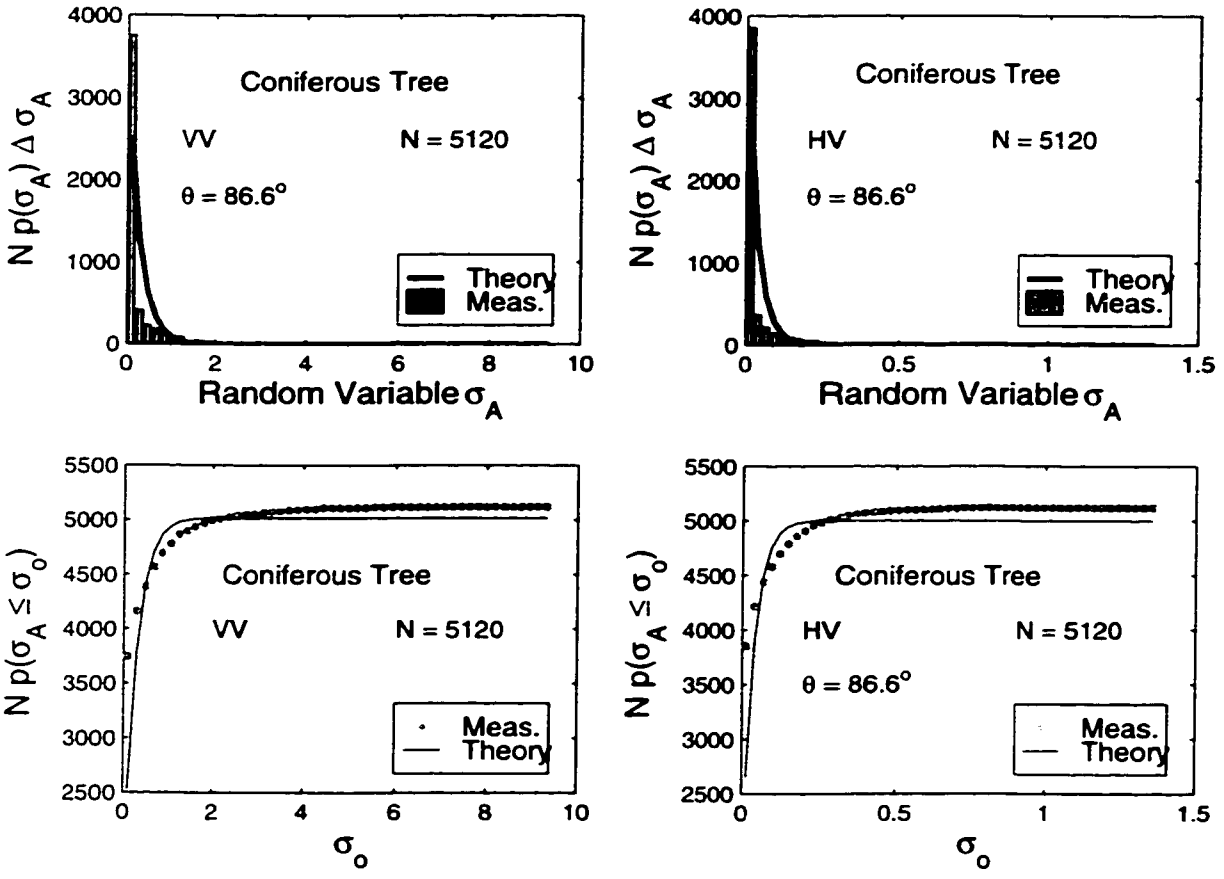

Figure 2.5: Comparison between the coniferous tree measured histogram of σ_A and its cumulative distribution function, $P(\sigma_A \leq \sigma_o)$, and the theoretical expectations based on the exponential pdf.

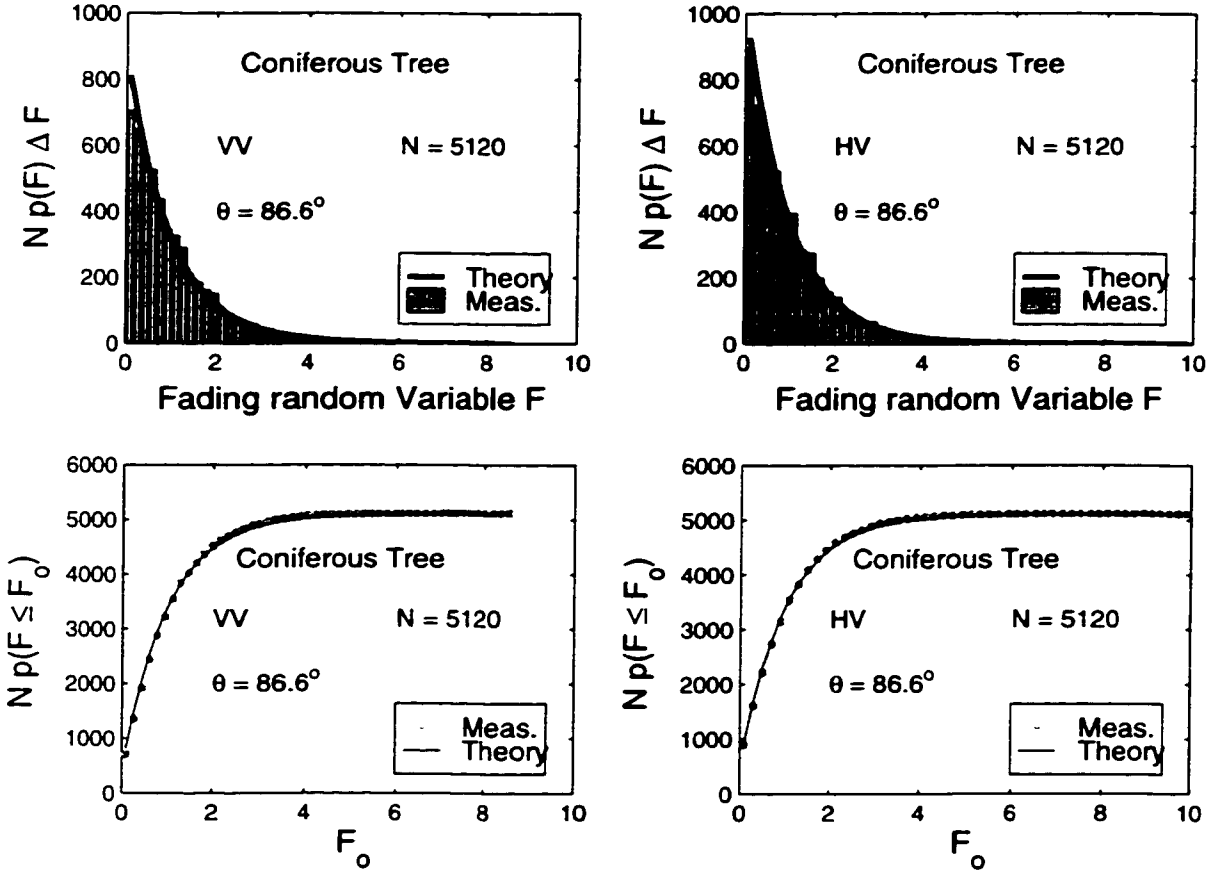

Figure 2.6: Comparison between the coniferous tree measured histogram of the random variable F and its cumulative distribution function, $P(F \leq F_o)$, and the theoretical expectations based on the exponential pdf.

Previous examples showed that the higher the degree of statistical homogeneity of terrain, the closer its statistics to the Rayleigh statistical model. This observation is examined further by considering the case of extreme heterogeneous terrain where the data of all the 7 different terrain types is combined together to form one set.

Figures 2.7 and 2.9 show comparisons between the measured histograms of the absolute backscattered amplitude and backscattered power with the Rayleigh and exponential pdf's, respectively. As expected, due to the low degree of statistical homogeneity, the comparisons show large deviations from the Rayleigh statistical model (which does not account for physical parameters variation statistics). While in the case of normalized quantities, figures 2.8 and 2.10, the comparisons show very good agreements to the pdf's of the Rayleigh statistical model.

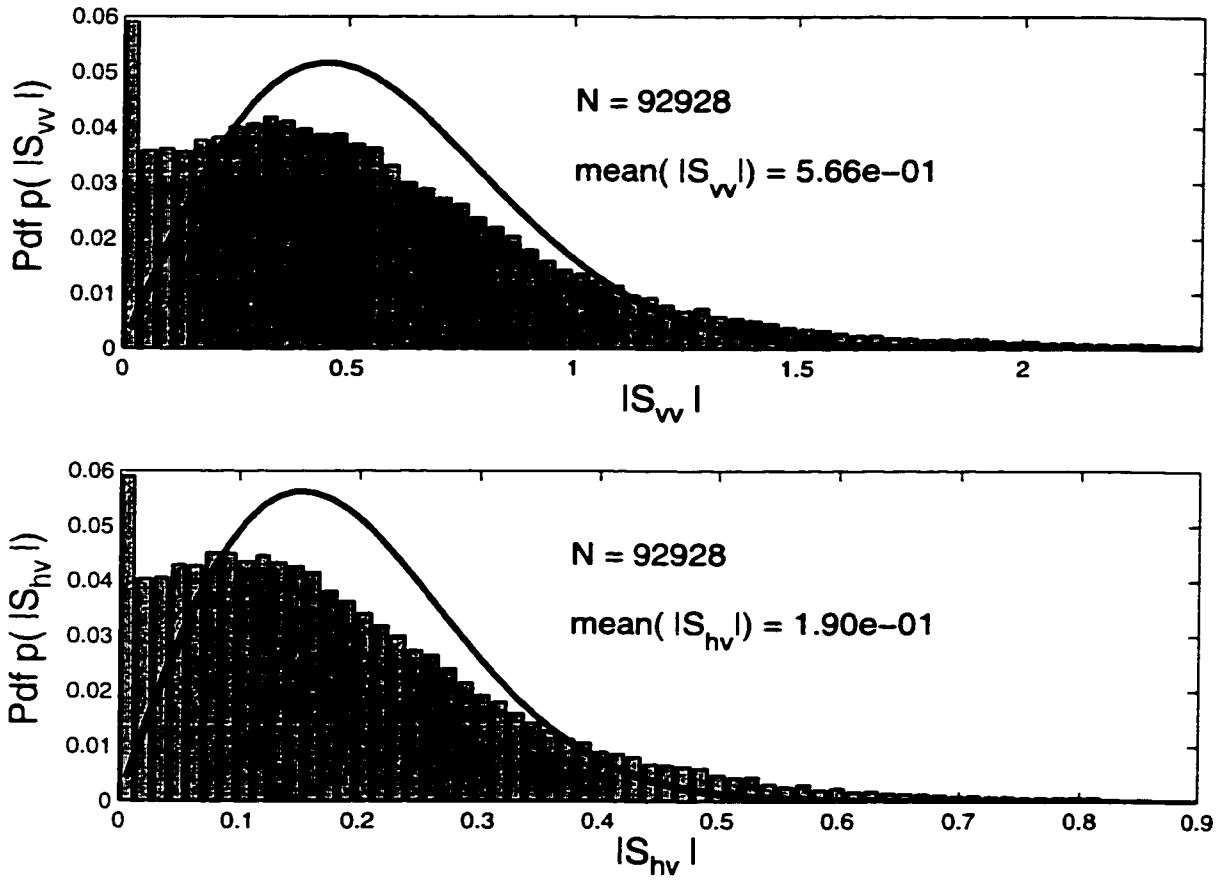

Figure 2.7: Comparison between the measured histogram of the amplitude (absolute value) of the backscattered E-field from heterogeneous terrain and the theoretical expectations based on the Rayleigh pdf for VV and HV-polarizations.

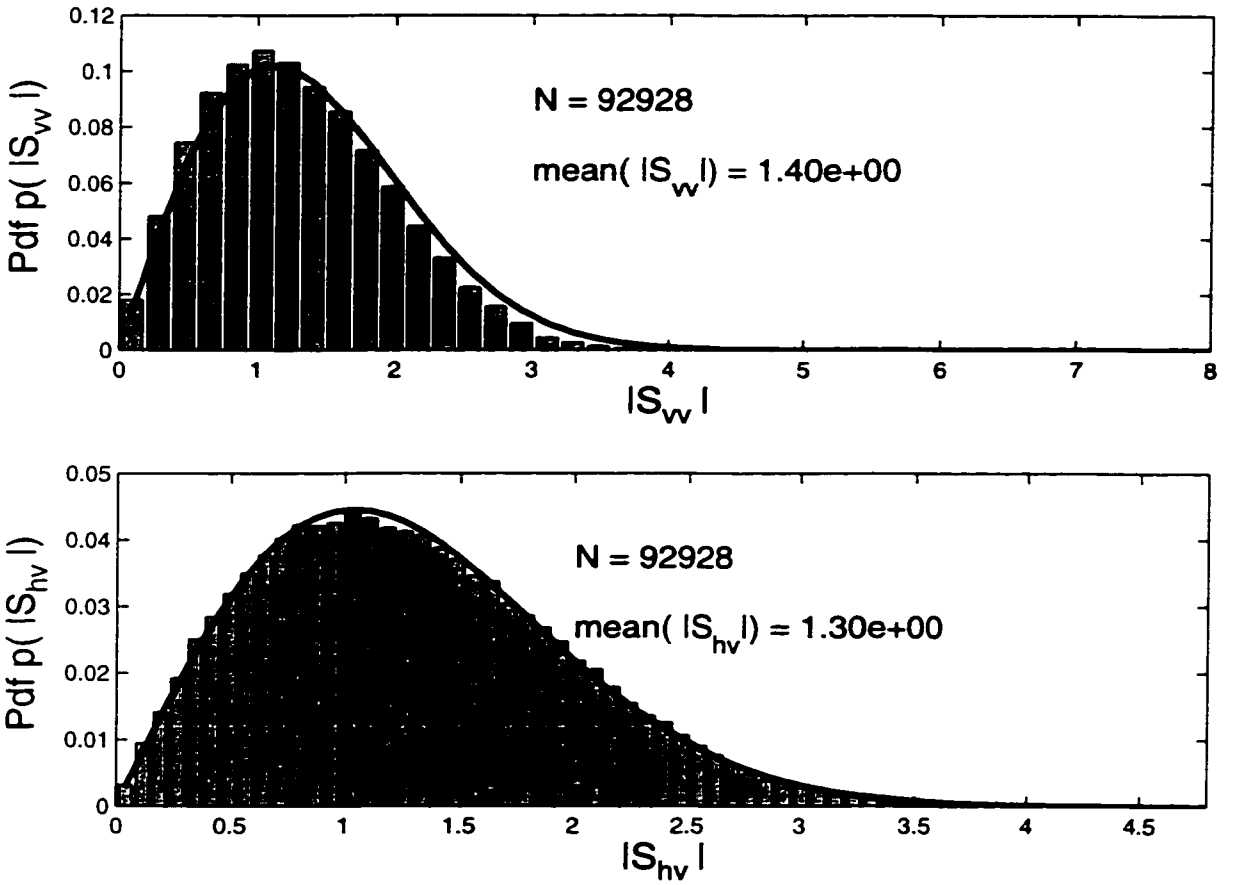

Figure 2.8: Comparison between the measured histogram of the amplitude (normalized value) of the backscattered E-field from heterogeneous terrain and the theoretical expectations based on the Rayleigh pdf for VV and HV-polarizations.

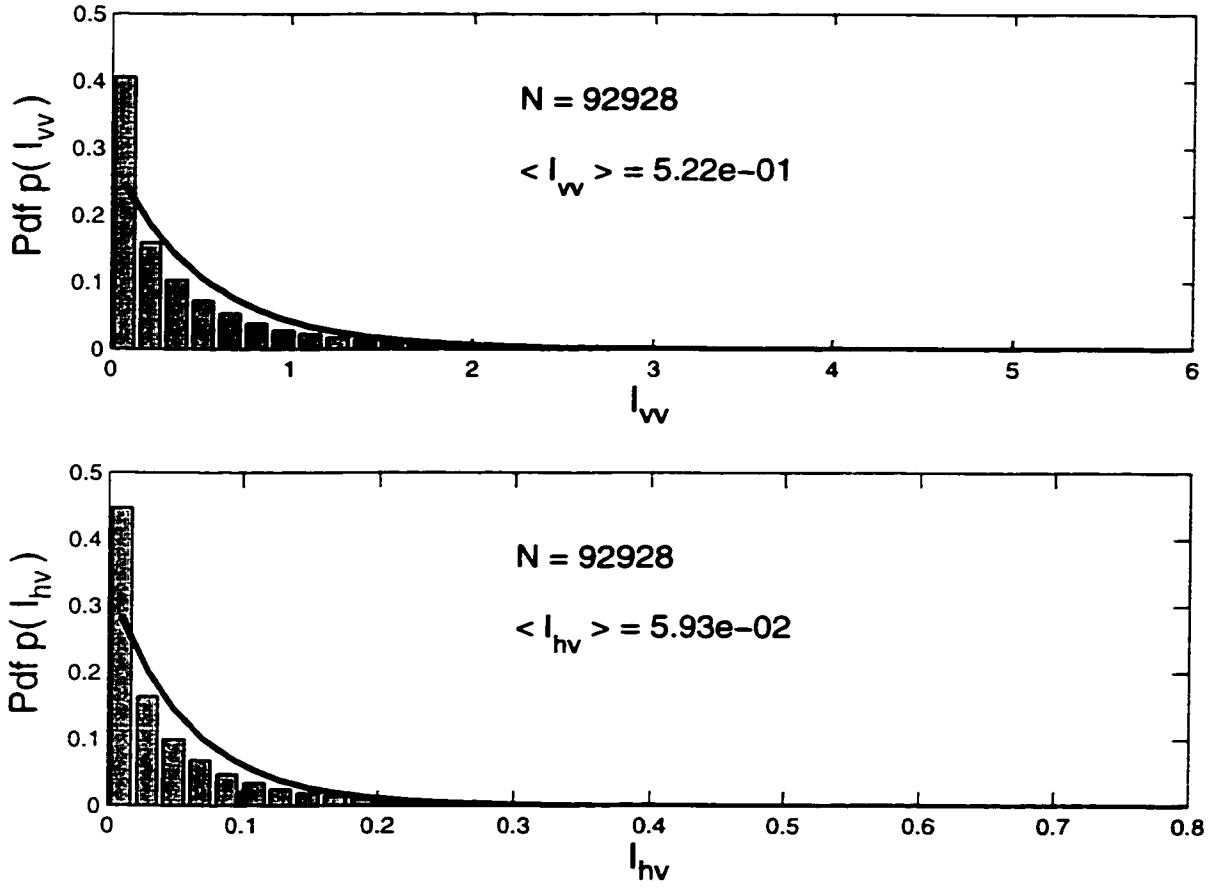

Figure 2.9: Comparison between the measured histogram of the power (absolute value) backscattered from heterogeneous terrain and the theoretical expectations based on the exponential pdf for VV and HV-polarizations.

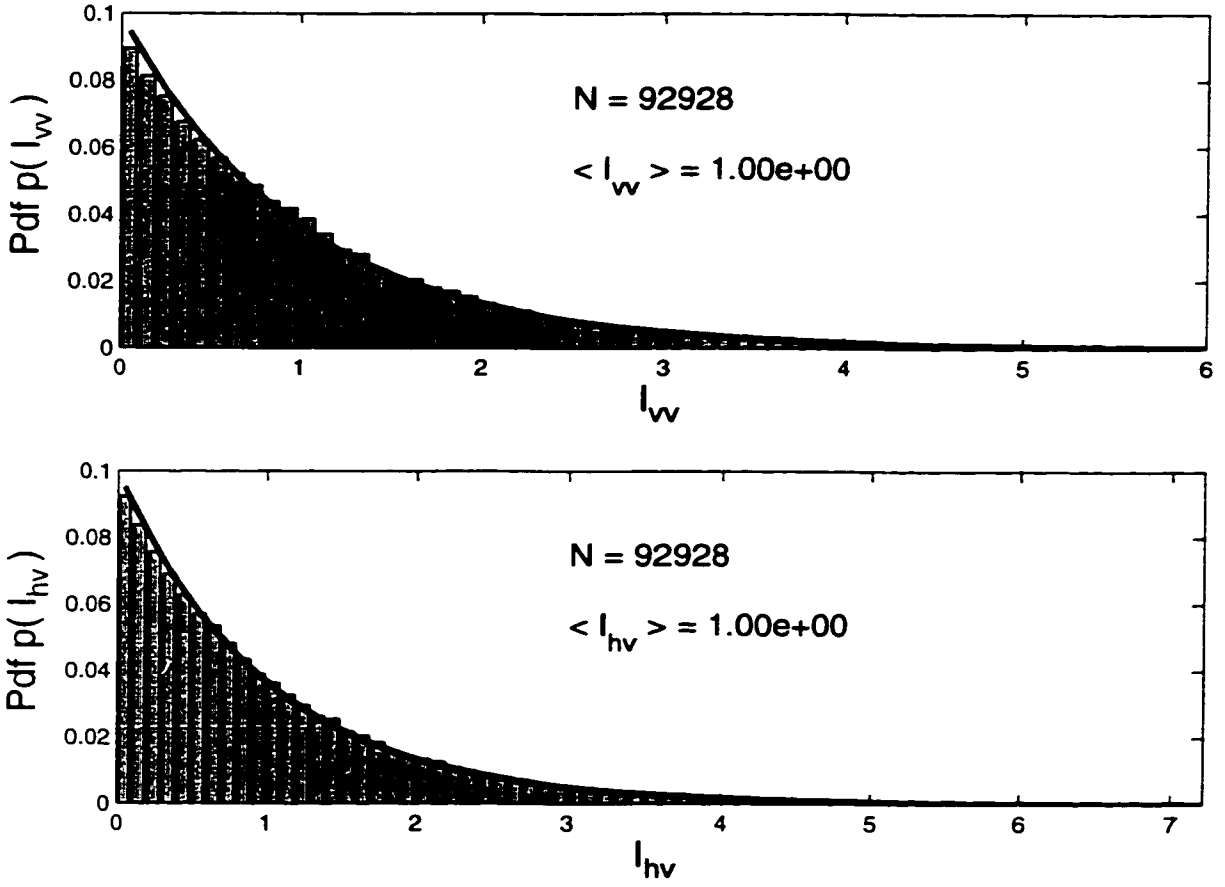

Figure 2.10: Comparison between the measured histogram of the power (normalized value) backscattered from heterogeneous terrain and the theoretical expectations based on the exponential pdf for VV and HV-polarizations.

2.5 Angular Response of σ^0

Another important part of this study is to characterize the relationship between the incidence angle and the MMW backscattered from terrain at near grazing angles. As mentioned in the preceding section, within the narrow range of incidence angles between $84^o - 89^o$ of the data set at hand, the statistical characters of the backscattered signal do not show any noticeable dependence on the incidence angles. In this section we will focus on the dynamic range of the backscattering coefficient of the four linear polarizations (VV, HH, VH, HV) and the dependency of the average scattering coefficient σ^o on the incidence angles. Figures 2.11-2.17 show the dynamic ranges of the backscattering coefficient, for the four linear polarizations, for each of the 7 types of homogeneous terrain extracted from the ARL data set along with their σ^o as functions of the incidence angle. Based on the results shown in figures 2.11-2.17, we have the following observations:

(a) The vegetation classes (grasses and trees) exhibit σ^o-variations due to the variations of density, height, shape of the vegetation, and moisture content, in the case of surfaces, the variation is, mainly, a result of roughness and moisture content variations, and the backscatter from snow is governed by crystal size, liquid water content, snow depth and snow density [22, 20, 52],

(b) The 95-GHz data set of radar backscatter from terrain at hand shows that the VV-polarization and the HH-polarization levels of the backscattering coefficient are always within 2 dB of one another regardless of the incidence angle and in most of the cases the difference is close to zero.

(c) The dynamic ranges of the four linearly polarized backscattering coefficients of surface terrain types (in which the backscattering is more due to surface scattering, like bare soil, snow-covered surfaces) tend to widen with the increase of the incidence angle, which, in part, can be attributed to the decrease of the backscattered power level which cause the data to be more susceptible to noise. In contrary, for the volumetric terrain types (in which the backscattering is more due to volume scattering, like trees and bushes) the dynamic range seems to be independent of the incidence angle.

Similar observations on a much larger data set, [23, 24], exhibit similar dependency of the backscattering coefficient on the incidence angles.

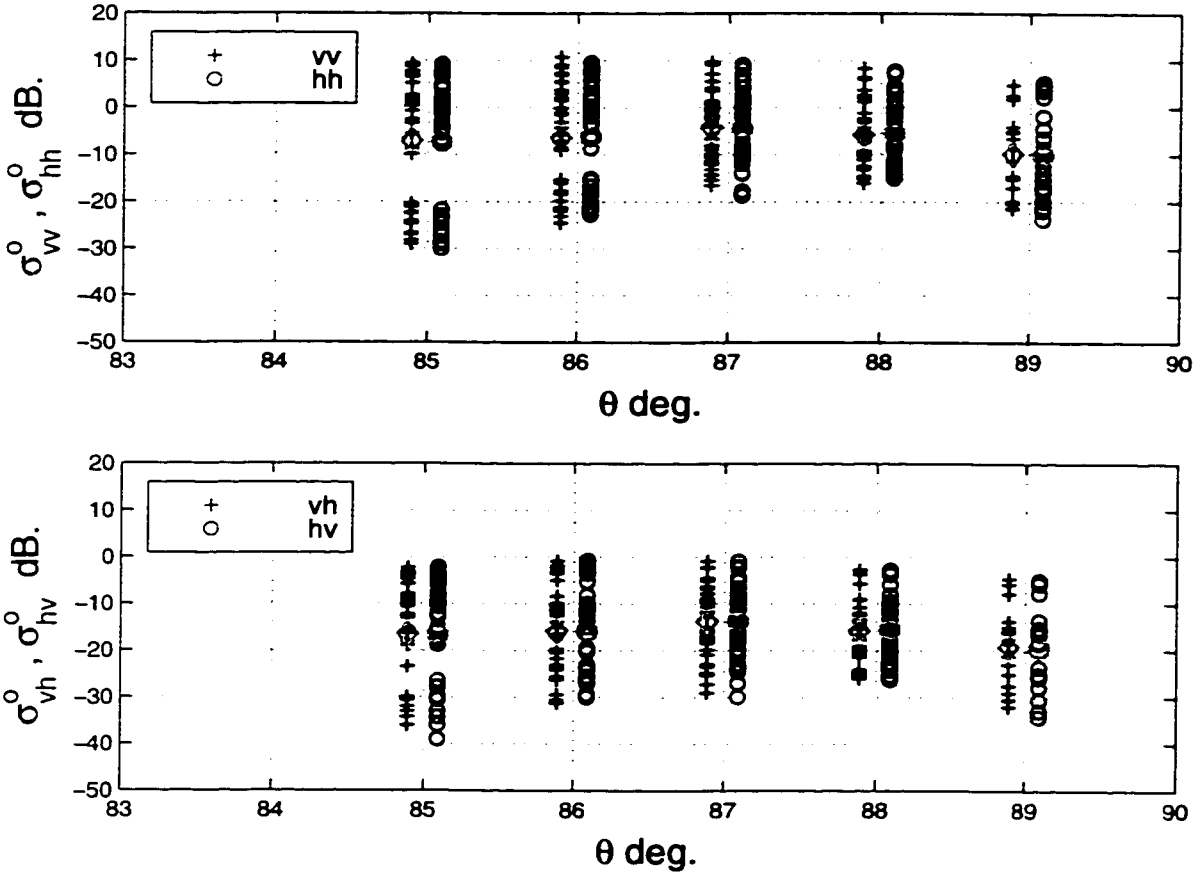

Figure 2.11: The dynamic range, and the average value (plotted in gray color) of the backscattering coefficients σ^o_{vv}, σ^o_{hh}, σ^o_{vh}, and σ^o_{hv} for deciduous tree canopy as functions of incidence angle.

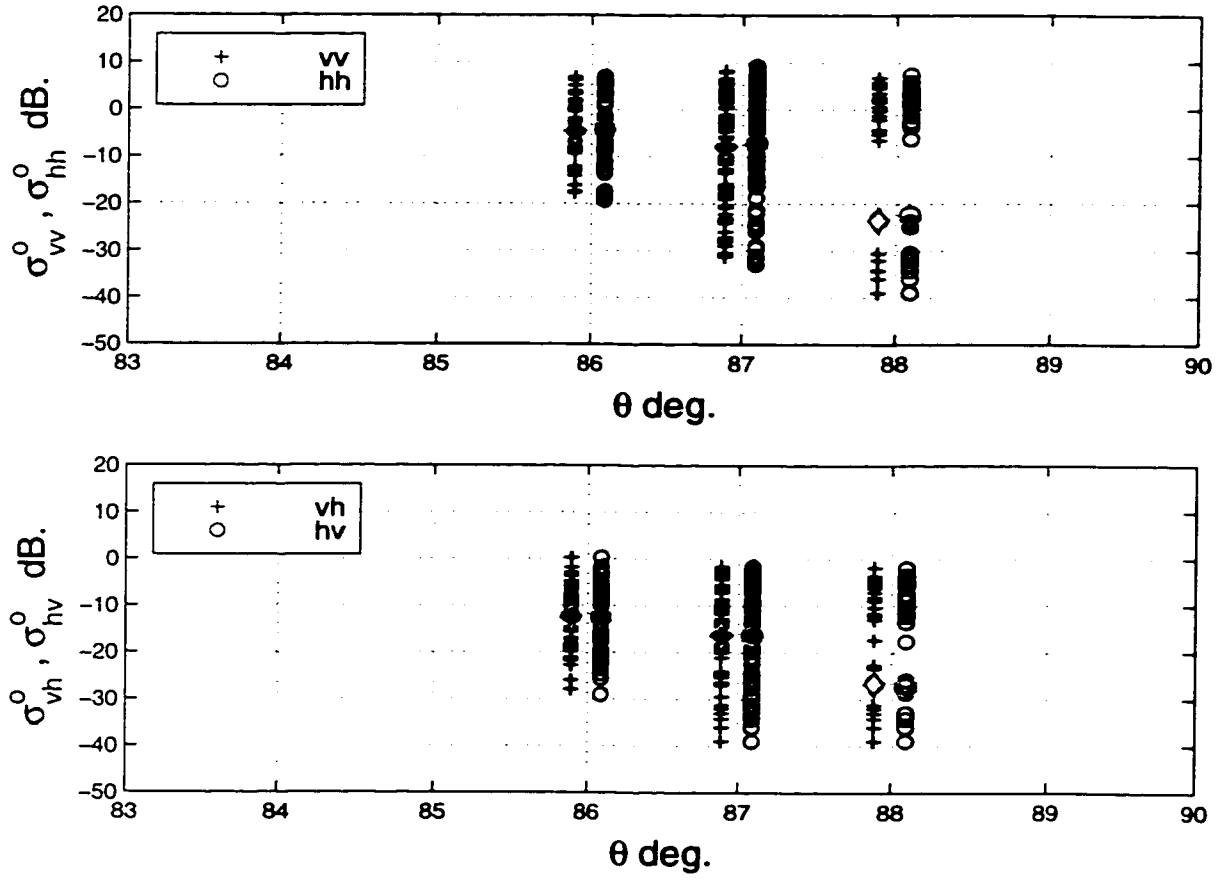

Figure 2.12: The dynamic range, and the average value (plotted in gray color) of the backscattering coefficients σ^o_{vv}, σ^o_{hh}, σ^o_{vh}, and σ^o_{hv} for coniferous tree canopy as a functions of incidence angle.

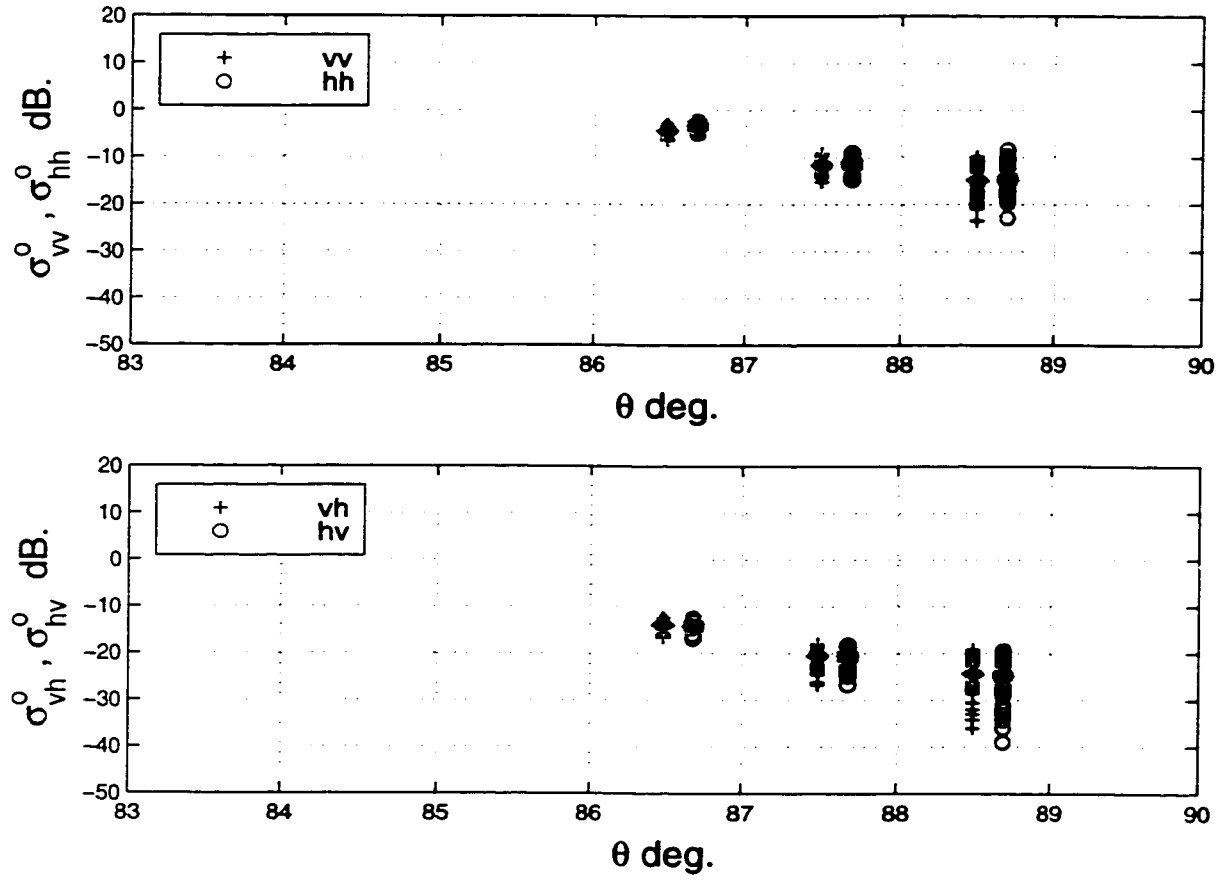

Figure 2.13: The dynamic range, and the average value (plotted in gray color) of the backscattering coefficients σ^o_{vv}, σ^o_{hh}, σ^o_{vh}, and σ^o_{hv} for bare soil as functions of incidence angle.

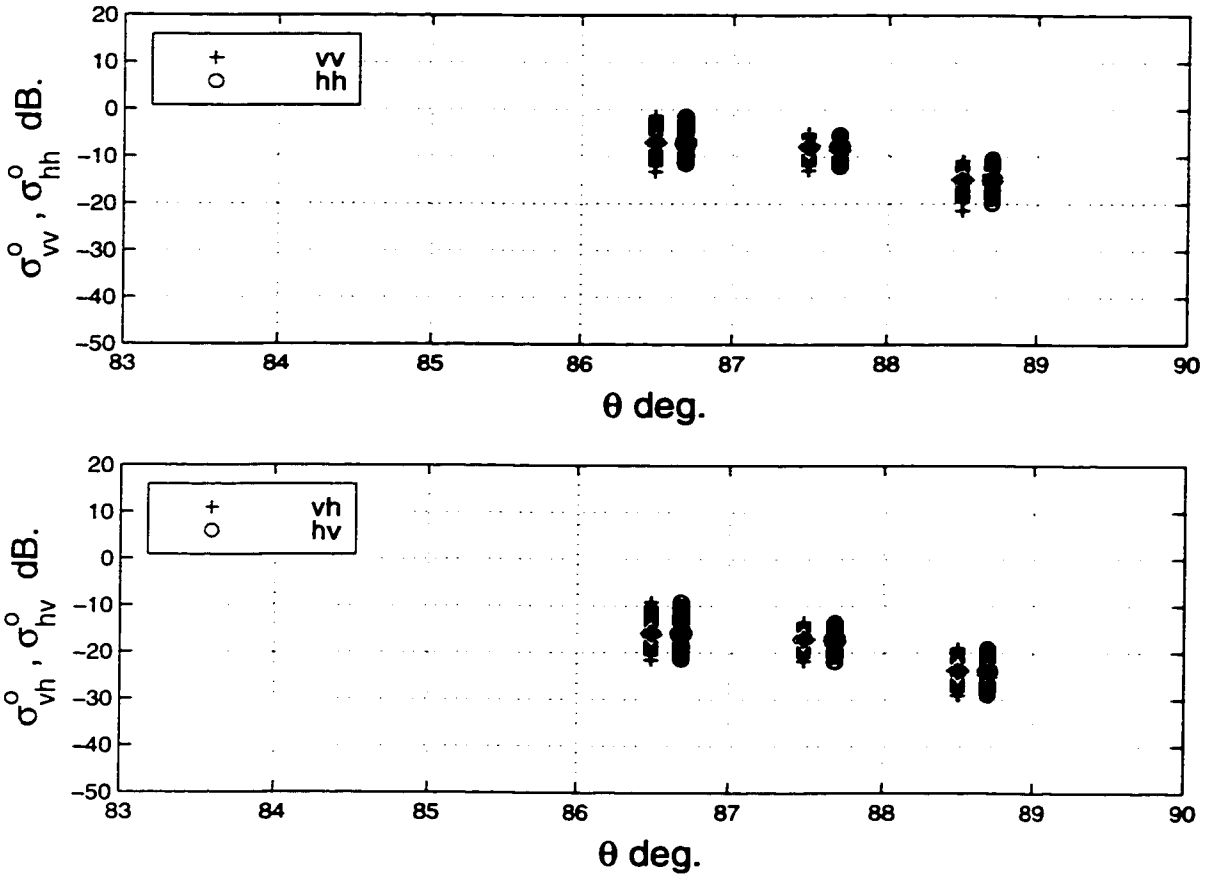

Figure 2.14: The dynamic range, and the average value (plotted in gray color) of the backscattering coefficients σ^o_{vv}, σ^o_{hh}, σ^o_{vh}, and σ^o_{hv} for short grass as functions of incidence angle.

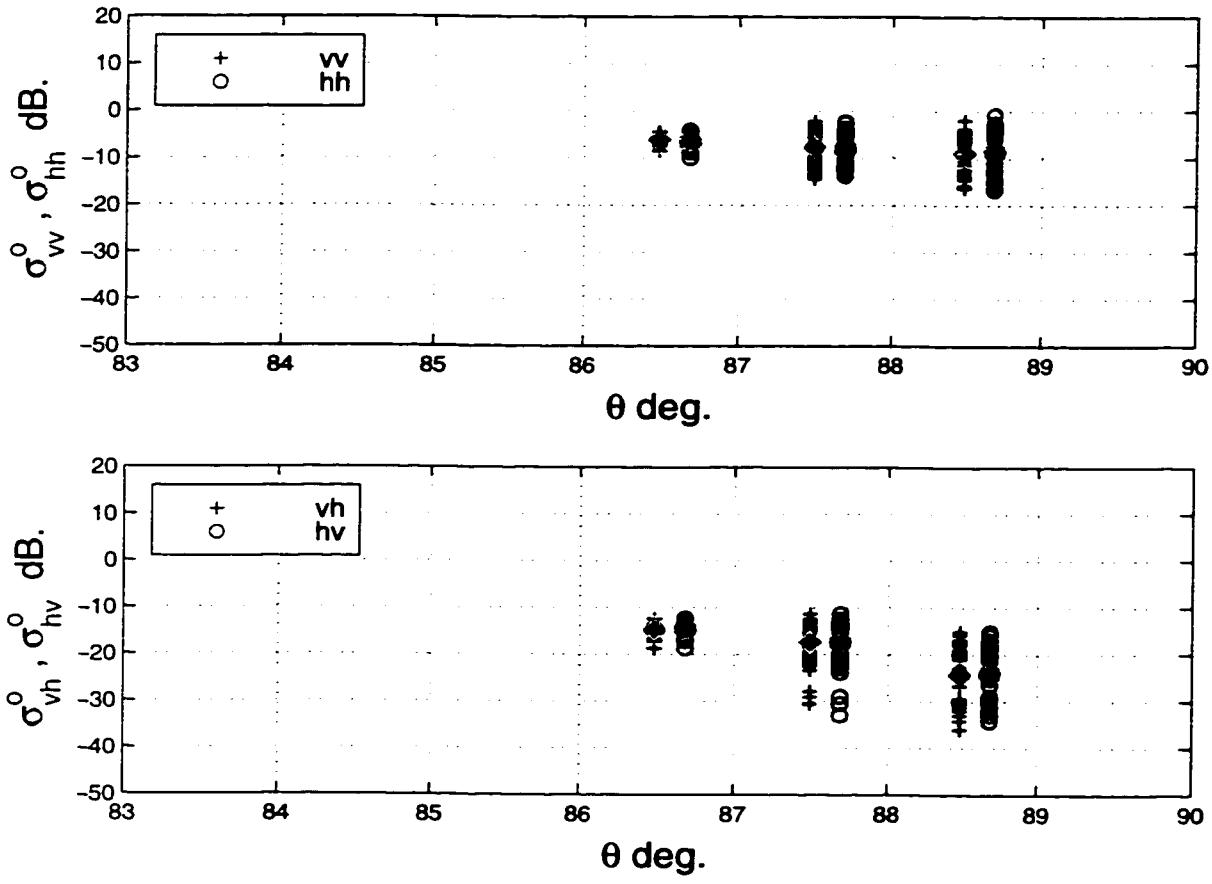

Figure 2.15: The dynamic range, and the average value (plotted in gray color) of the backscattering coefficients σ^o_{vv}, σ^o_{hh}, σ^o_{vh}, and σ^o_{hv} for bushes as functions of incidence angle.

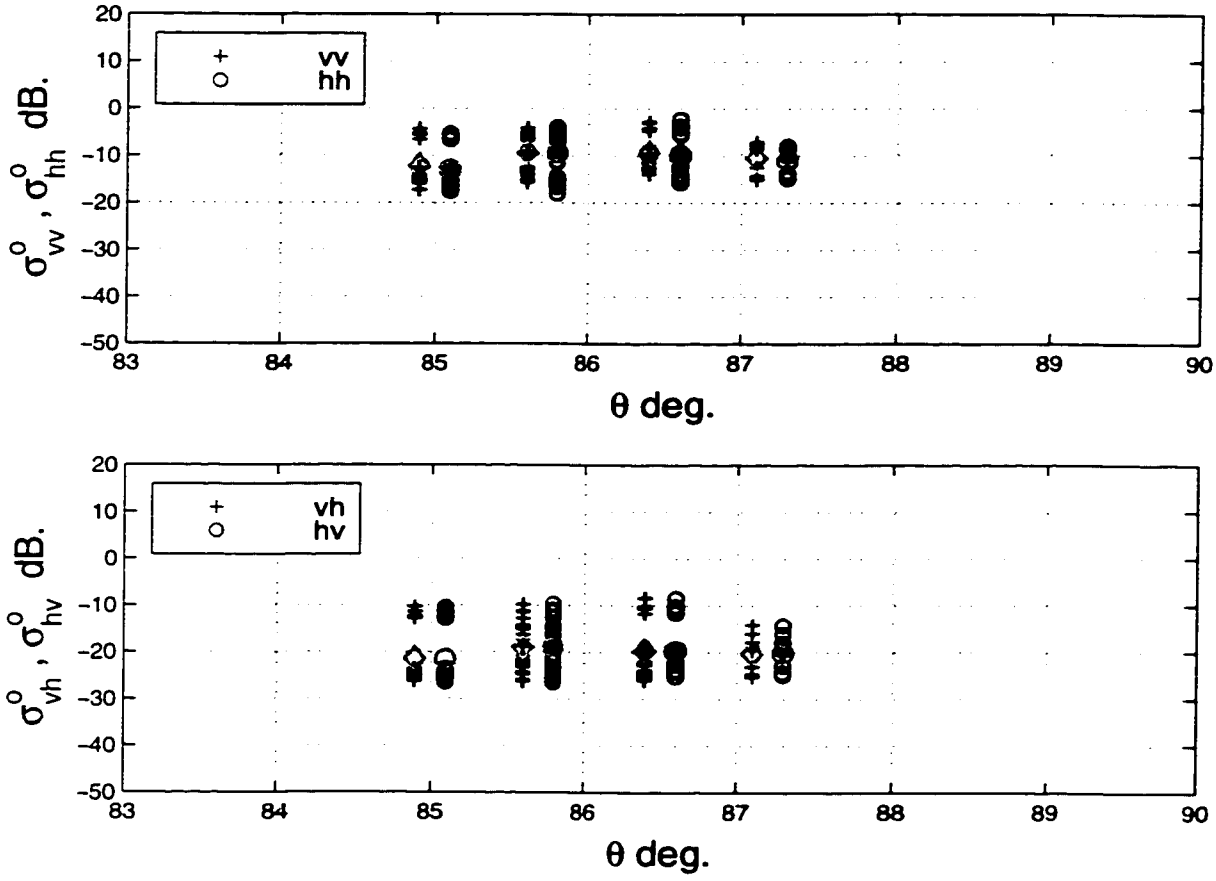

Figure 2.16: The dynamic range, and the average value (plotted in gray color) of the backscattering coefficients σ^o_{vv}, σ^o_{hh}, σ^o_{vh}, and σ^o_{hv} for wet snow covered terrain as functions of incidence angle.

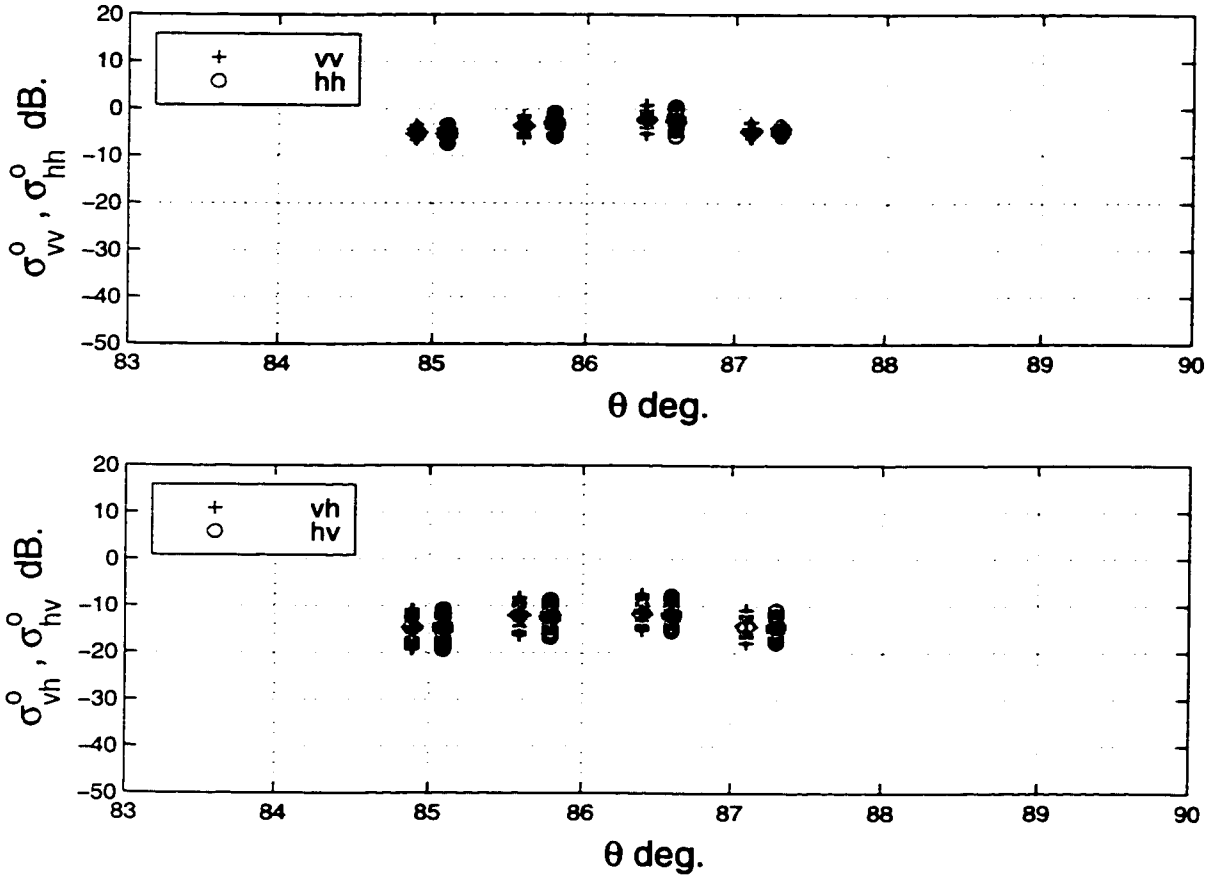

Figure 2.17: The dynamic range, and the average value (plotted in gray color) of the backscattering coefficients σ^o_{vv}, σ^o_{hh}, σ^o_{vh}, and σ^o_{hv} for fresh snow covered terrain as functions of incidence angle.

2.6 Conclusions

This study reaffirms that the Rayleigh fading model is applicable for characterizing the statistical behavior of the radar backscatter from statistically homogeneous distributed targets, such as terrain surfaces, at near grazing angles so long as the illuminated cell is large enough to contain many scatterers, and, additionally, no single (or few) scatterer(s) dominate over all others. In addition, this study showed that, the radar backscatter from heterogeneous terrain obeys conditional Rayleigh distribution. In other words, knowing the pdf of the local mean scattering level of heterogeneous terrain, $p(\sigma_i^o)$, can be used along with the Rayleigh model to derive its statistical properties. Further study of this latter point led to the application of the Bayes formula to derive the pdf of the scattering from heterogeneous terrain as follows, [42, 43]:

$$p(\sigma_A) = \int_0^\infty p_i(\sigma_A \mid \sigma_i^o)\, p(\sigma_i^o) d\sigma_i^o, \tag{2.11}$$

or in the discrete format

$$p(\sigma_A) = \sum_{all\ local\ fields} p_i(\sigma_A \mid \sigma_i^o)\, P(\sigma_i^o). \tag{2.12}$$

In a number of studies reported in the literature [31, 46], it was stated that the *pdf* of the backscattering cross section per unit area, $p(\sigma_A)$, exhibited a long tail, requiring the use of the K-distribution to fit the data. This type of behavior was not observed in the present study. The above Bayes formula is a good explanation for

the difference. Another possible explanation for this difference between this study and the other studies is that, the data in the other studies, which is based on high-resolution SAR images of terrain, may have included non-terrain targets or that some of the pixels contained only 1 or 2 dominant scatterers, thereby violating one of the tenets of the Rayleigh model. Such a situation can easily arise if the pixel of a high resolution radar image contains a single trunk of a tree.

Another contribution of this study is the documentation of the dynamic ranges exhibited by σ^0 for various terrain types at near grazing angles for all linear polarization combinations at 95 GHz [25, 44, 45].

CHAPTER 3

MMW SCATTERING MODEL FOR ROUGH, LOSSY, DIELECTRIC CYLINDERS

3.1 Introduction

Accurate characterization of radar backscatter from tree trunks is a significant component for a number of remote sensing applications that are probable to work near forested areas. One of these applications is detection and tracking of man-made targets in the presence of clutter, especially near forested areas. Other applications are, vehicle collision-avoidance systems, and remote characterization and extraction of physical parameters of forested areas. Many studies have been performed to analyze and model electromagnetic scattering by tree canopies at different frequency ranges, such as [33, 17]. Other studies, such as those reported in [35, 50], focused on the scattering by the layer of tree trunks in forested areas . In any study dealing with the electromagnetic interaction among tree trunks or between tree trunks and the ground plane underneath them, a model for scattering by tree trunks must be

involved. In some studies, such as [35, 48], a tree trunk is approximated as a smooth, dielectric cylinder of finite length. This approximation is valid only at low frequencies where the roughness of the bark layer is much smaller than the wavelength and, therefore, can be ignored. In other studies [32, 33, 49] the rough layer (the bark layer) of tree trunks is approximated by an equivalent periodically corrugated dielectric layer around an inner dielectric cylinder. This second approach is, also, not valid at MMW frequencies because of the following reasons: (a) the electromagnetic wave is highly attenuated by the bark layer, and therefore, the effect of the inner dielectric layers can be ignored, (b) the bark layer for many tree species is inappropriate to be considered as a periodic series of grooves, and (c) due to the small wavelength at MMW frequencies ($\lambda \simeq 3\ mm$ at 95 GHz), any irregularity in the assumed periodicity of the grooves on the order of $\lambda/10$ ($\simeq$ 0.3 mm at 95 GHz) violates of the basic assumption of this second approach.

The lack of reliability and experimental verification of the current models at MMW frequencies raise the need for an accurate model for MMW scattering by tree trunks. Hence, a candidate approach for modeling the scattering by a tree trunk at MMW frequencies is to treat it as a rough, lossy, dielectric cylinder. For a cylinder with a slightly rough surface, the small perturbation method is applicable, as reported in [8, 27], but its reliability is limited to conducting, circular cylinders. For a very rough surfaces, corresponding to MMW frequencies, no studies have thus far (to our knowledge) been reported on the scattering by rough cylinders. This need for an accurate model for the MMW scattering by rough, lossy, dielectric cylinder and its application

to tree trunks represents a main motivation for carrying out this research work.

In this chapter, we will study, theoretically, the MMW polarimetric scattering by rough, lossy, dielectric cylinders as a model for the scattering by tree trunks. As shown in Fig. 3.1, the backscattering by a tree trunk above a ground plane is composed of four main scattering components which can be divided into three categories:

1. direct backscattering by the tree trunk,

2. direct backscattering by the ground plane, and

3. three components of interaction between the trunk and the ground plane (trunk-ground-receiver, ground-trunk-receiver, and higher order interaction components, e.g. trunk-ground-trunk-receiver, which can be neglected because of their small contributions to the total scattered field).

In the rest of this chapter, analytical model derivations for the coherent (Section 3.2.2) and incoherent (Section 3.2.3) components of the scattering by rough, lossy, dielectric cylinders are presented.

3.2 Theoretical Analysis

To the first order, a tree trunk can be modeled as a lossy, dielectric cylinder with a random rough surface (the bark layer). However, the problem of the radar scattering by rough, lossy, dielectric cylinder is more complicated than the old problem of scattering by smooth, lossy, dielectric cylinder, it is useful to shed some light on the

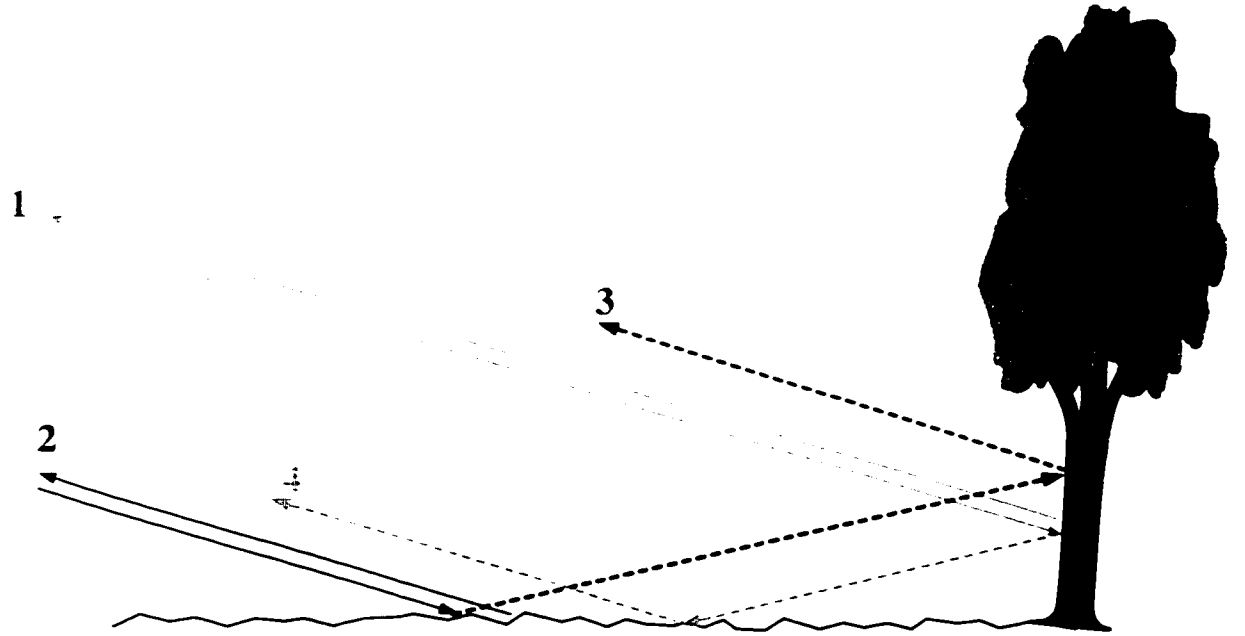

Figure 3.1: The four main components of the radar backscattered from a tree trunk above a ground plane.

case of smooth cylinder as it represents a fairly important background to the case of interest. According to [33, 49], at MMW frequencies, the diameter of a typical trunk is much larger than the radar signal wavelength ($\lambda \approx$ 1 *cm* at 35 GHz and $\approx$ 3 *mm* at 95 GHz). Hence, the semi-exact solution of the bistatic scattering by a smooth dielectric/conducting cylinders [26], becomes computationally inefficient. Moreover, the solution fails when the cylinder's cross section is not circular. These deficiencies can be overcome at high frequencies by applying the geometric optics approximation (GO). Lin and Sarabandi [49], used the GO approximation to derive a solution for the scattering by a lossy, dielectric cylinder with a large radius of curvature compared to the wavelength.

In the remainder of this section, the GO solution for the case of a smooth, lossy, dielectric cylinder, [49], is reproduced for completeness, followed by the derivations for the coherent and incoherent components of the scattering response of a rough, lossy, dielectric cylinder.

3.2.1 Geometric Optics Approximate Solution for the Scattering by Smooth Cylinders

This derivation assumes that the cylinder's permittivity has a large imaginary part, so that creeping waves and effects of glory rays could be neglected. According to the GO model and under these assumptions, the cylinder is replaced with fictitious electric and magnetic currents, and these currents are approximated by the currents of the local tangential plane. To simplify the derivation two local coordinate systems $(\hat{x}', \hat{y}', \hat{z}')$ and $(\hat{n}, \hat{t}, \hat{l})$ are established with respect to the position of the cylinder and at any point on the surface, respectively. For convenience, a global coordinate system $(\hat{x}, \hat{y}, \hat{z})$ is used to express the unit vectors of the local coordinate systems. These different coordinate systems are shown in Fig. 3.2, where their unit vectors are defined as:

$$\hat{\mathbf{t}} = \frac{\hat{\mathbf{n}} \times \hat{\mathbf{k}}_\mathbf{i}}{|\hat{\mathbf{n}} \times \hat{\mathbf{k}}_\mathbf{i}|}, \qquad \hat{\mathbf{l}} = \hat{\mathbf{n}} \times \hat{\mathbf{t}}, \tag{3.1}$$

where $\hat{\mathbf{n}}$ is a unit vector normal to the cylindrical surface at any point.

$$\hat{\mathbf{y}}' = \frac{\hat{\mathbf{z}}' \times \hat{\mathbf{k}}_\mathbf{i}}{|\hat{\mathbf{z}}' \times \hat{\mathbf{k}}_\mathbf{i}|}, \qquad \hat{\mathbf{x}}' = \hat{\mathbf{y}}' \times \hat{\mathbf{z}}'. \tag{3.2}$$

The unit vector $\hat{x}'$ is chosen to be in the plane defined by the vector of the incident wave and the axis of the cylinder, $\hat{k}_i$ and $\hat{Z}'$, such that the lit surface is described by $\frac{-\pi}{2} < \phi' < \frac{\pi}{2}$.

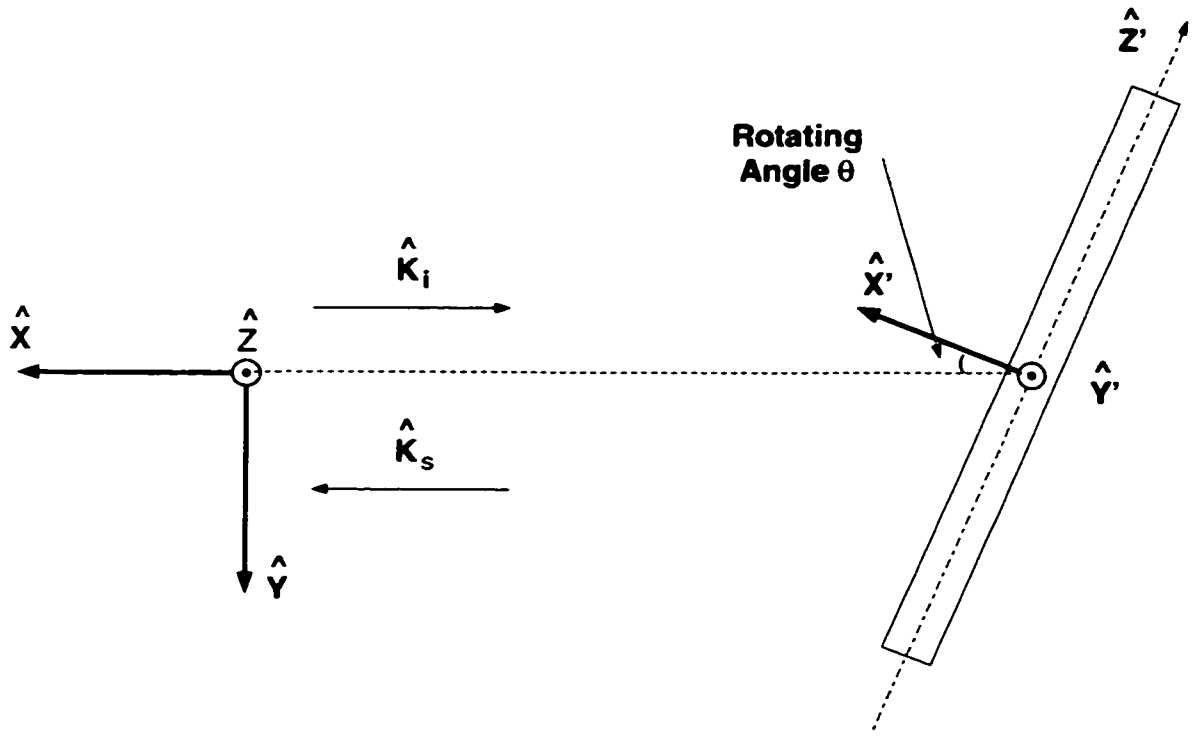

Figure 3.2: Sketch illustrating local and global coordinate systems.

The fields of the local tangential plane, used in the GO approximation, are the total tangential fields resulting from combining the incident and reflected fields at every point on the surface of the cylinder. These total fields, ($E = E^r + E^i$) and ($H = H^r + H^i$), are expressed as:

$$\begin{pmatrix} E_l \\ E_t \end{pmatrix} = \begin{pmatrix} 1 - R_{vv} & 0 \\ 0 & 1 + R_{hh} \end{pmatrix} \begin{pmatrix} E_l^i \\ E_t^i \end{pmatrix},$$

$$\begin{pmatrix} H_l \\ H_t \end{pmatrix} = \begin{pmatrix} 1 - R_{hh} & 0 \\ 0 & 1 + R_{vv} \end{pmatrix} \begin{pmatrix} H_l^i \\ H_t^i \end{pmatrix}. \tag{3.3}$$

Where R_{vv} and R_{hh} are the Fresnel reflection coefficients of the surface of the cylinder at the local angle at any point on the surface. The electric and magnetic currents J and M are defined by:

$$J = \hat{\mathbf{n}} \times H_\perp, \qquad M = -\hat{\mathbf{n}} \times E_\perp \tag{3.4}$$

Assuming the radius of the cylinder is a and its length is b, the electric and magnetic Hertz vector potentials can be expressed as follows:

$$\Pi_e(\bar{r}) = \frac{iZ_0}{4\pi k_0} \frac{e^{ik_0 r}}{r} \int_{-b/2}^{b/2} \int_{-\pi/2}^{\pi/2} J(z', \phi')\, e^{-ik_0 \hat{\mathbf{k}}_s \cdot \bar{r}'}\, a \;\; d\phi' dz', \tag{3.5}$$

$$\Pi_m(\bar{r}) = \frac{iY_0}{4\pi k_0} \frac{e^{ik_0 r}}{r} \int_{-b/2}^{b/2} \int_{-\pi/2}^{\pi/2} M(z', \phi')\, e^{-ik_0 \hat{\mathbf{k}}_s \cdot \bar{r}'}\, a \;\; d\phi' dz'. \tag{3.6}$$

For a uniform plane incident wave, both J and M have the location dependent factor $e^{ik_0 \hat{\mathbf{k}}_i \cdot \bar{r}}$. Thereby, we can factor it out and define $J = \bar{J} e^{ik_0 \hat{\mathbf{k}}_i \cdot \bar{r}}$ and $M = \bar{M} e^{ik_0 \hat{\mathbf{k}}_i \cdot \bar{r}}$. Where $\bar{J}$ and $\bar{M}$ are vector functions of (R_{vv}, R_{hh}), and R_{vv} and R_{hh} depend on the angle between $\hat{\mathbf{k}}_i$ and $\hat{\mathbf{n}}$ at each point on the surface. Assuming that we are in the far field of the cylinder, the scattered electric field can be expressed in terms of the Hertz vector potential as follows:

$$\begin{aligned} \bar{E}_s(\bar{r}) &= \nabla \times \nabla \times \Pi_e(\bar{r}) + ik_o Z_o \nabla \times \Pi_m(\bar{r}) \\ &= -k_o^2 \left(\hat{\mathbf{k}}_s \times \hat{\mathbf{k}}_s \times \Pi_e(\bar{r}) + \hat{\mathbf{k}}_s \times Z_o \Pi_m(\bar{r}) \right). \end{aligned} \tag{3.7}$$

Where in equation(3.7) the far field approximation of the Curl operator ($\nabla \times \frac{e^{ik_0 r}}{r}\hat{f} \approx ik_0 \frac{e^{ik_0 r}}{r}\hat{r} \times \hat{f}$) was used. Knowing the surface height profile and the dielectric constant of the cylinder, enables us to evaluate R_{vv} and R_{hh} at every point on the surface of the cylinder, consequently $\bar{E}_s(\bar{r})$ can be evaluated using the following expression:

$$\bar{E}_s(\bar{r}) = \frac{e^{ik_0 r}}{r} \left(\hat{\mathbf{k}}_s \times \hat{\mathbf{k}}_s(Z_0\ I(\bar{J})\ ) + \hat{\mathbf{k}}_s \times I(\bar{M})\ \right), \tag{3.8}$$

where

$$I(C) = \frac{ik_0}{4\pi} \int_{-b/2}^{b/2} \int_{-\pi/2}^{\pi/2} C\ \ e^{ik_0(\hat{\mathbf{k}}_i - \hat{\mathbf{k}}_s).\bar{r}'}\ a\ d\phi' dz', \tag{3.9}$$

and C can be either a scalar or a vector.

Starting from the scattering matrix, which relates the scattered and incident electric fields as shown below,

$$\begin{pmatrix} E_v^s \\ E_h^s \end{pmatrix} = \frac{e^{ik_0 r}}{r} \begin{pmatrix} S_{vv} & S_{vh} \\ S_{hv} & S_{hh} \end{pmatrix} \begin{pmatrix} E_{v'}^i \\ E_{h'}^i \end{pmatrix}, \tag{3.10}$$

and with some algebraic manipulations involving the following inner products:

$$\begin{aligned}
\hat{\mathbf{v}}_s \cdot \hat{\mathbf{k}}_s \times (\hat{\mathbf{k}}_s \times Z_0 I(\bar{J})) &= -I(Z_0 \bar{J} \cdot \hat{\mathbf{v}}_s), \\
\hat{\mathbf{h}}_s \cdot \hat{\mathbf{k}}_s \times (\hat{\mathbf{k}}_s \times Z_0 I(\bar{J})) &= -I(Z_0 \bar{J} \cdot \hat{\mathbf{h}}_s), \\
\hat{\mathbf{v}}_s \cdot (\hat{\mathbf{k}}_s \times I(\bar{M})) &= -I(\bar{M} \cdot \hat{\mathbf{h}}_s), \\
\hat{\mathbf{h}}_s \cdot (\hat{\mathbf{k}}_s \times I(\bar{M})) &= I(\bar{M} \cdot \hat{\mathbf{v}}_s),
\end{aligned}$$

the diagonal elements of the scattering matrix can be expressed as:

$$S_{vv} = I(C_{vv}) = I\Big((\hat{\mathbf{l}} \cdot \hat{\mathbf{v}}_\mathbf{s}) Z_0 J_{lv} + (\hat{\mathbf{t}} \cdot \hat{\mathbf{v}}_\mathbf{s}) Z_0 J_{tv} + (\hat{\mathbf{l}} \cdot \hat{\mathbf{h}}_\mathbf{s}) M_{lv} + (\hat{\mathbf{t}} \cdot \hat{\mathbf{h}}_\mathbf{s}) M_{tv}\Big)$$

$$S_{hh} = I(C_{hh}) = I\Big((\hat{\mathbf{l}} \cdot \hat{\mathbf{h}}_\mathbf{s}) Z_0 J_{lh} + (\hat{\mathbf{t}} \cdot \hat{\mathbf{h}}_\mathbf{s}) Z_0 J_{th} - (\hat{\mathbf{l}} \cdot \hat{\mathbf{v}}_\mathbf{s}) M_{lh} - (\hat{\mathbf{t}} \cdot \hat{\mathbf{v}}_\mathbf{s}) M_{th}\Big) \quad (3.11)$$

where:

- J_{pq} and M_{pq} are the electric and magnetic currents along $\hat{p}$ direction induced by a $\hat{q}$-polarized incident wave (p can be t or l and q can be v or h),
- $\hat{h}_j = \hat{Z} \times \hat{k}_j / |\hat{Z} \times \hat{k}_j|$ $\quad \hat{v}_j = \hat{h}_j \times \hat{k}_j$ (and j can be i or s),
- equation (3.11) is valid to evaluate the radar backscatter from any cylindrical surface, rough or smooth, with circular or of arbitrary cross section as long as the integration $\boldsymbol{I(.)}$ is performed over the lit surface and the assumptions of high imaginary dielectric constant and large surface's radius of curvature with respect to wavelength are satisfied, and
- the GO is a first-order approximation model which is not capable of evaluating the cross-polarized elements of the scattering matrix, S_{vh} and S_{hv}.

In case of a smooth, conducting, circular cylinder of radius a and length b, the expression in equation (3.9) reduces to:

$$
\begin{aligned}
I(C) &= \frac{ik_0}{4\pi}\int_{-b/2}^{b/2}\int_{-\pi/2}^{\pi/2} C\ e^{-ik_0 aB\cos(\phi'-\tilde{\phi})} e^{ik_0(\hat{k}_i-\hat{k}_s).\hat{z}z'} a\ d\phi' dz' \\
&= \frac{ib}{2\pi}\frac{sinV}{V} e^{-ik_0 Ba}\sqrt{\frac{k_0 a}{2B}}\cdot\left\{F[\sqrt{\frac{k_0 Ba}{2}}(\frac{\pi}{2}+\tilde{\phi})] + F[\sqrt{\frac{k_0 Ba}{2}}(\frac{\pi}{2}-\tilde{\phi})]\right\}\ C_s
\end{aligned}
\tag{3.12}
$$

where;

- $B = \sqrt{((\hat{k}_i-\hat{k}_s)\cdot\hat{x}')^2 + ((\hat{k}_i-\hat{k}_s)\cdot\hat{y}')^2}$,
- $\tilde{\phi} = tan^{-1}\left(\frac{-(\hat{k}_i-\hat{k}_s)\cdot\hat{y}'}{-(\hat{k}_i-\hat{k}_s)\cdot\hat{x}'}\right)$,
- $V = \frac{k_0 b}{2}(\hat{k}_i-\hat{k}_s).\hat{z}'$,
- C_s is the non-exponential term of equation (3.9) evaluated at the stationary phase point, and
- $F(.)$ is the Fresnel integral, which is valid provided that $k_0 Ba \gg 1$ and $\tilde{\phi}$ are away from the shadow boundary [33].

Upon substituting (3.12) into equation (3.11), analytical expressions for the diagonal elements of the scattering matrix of a smooth, lossy, dielectric (or conducting,) circular cylinder is obtained. The angular dependence of $|S_{vv}|$ of a smooth, conducting cylinder, with radius of 3.75 cm and length of 150 cm, calculated using the above GO model at 95 GHz, is illustrated in Fig. 3.3.

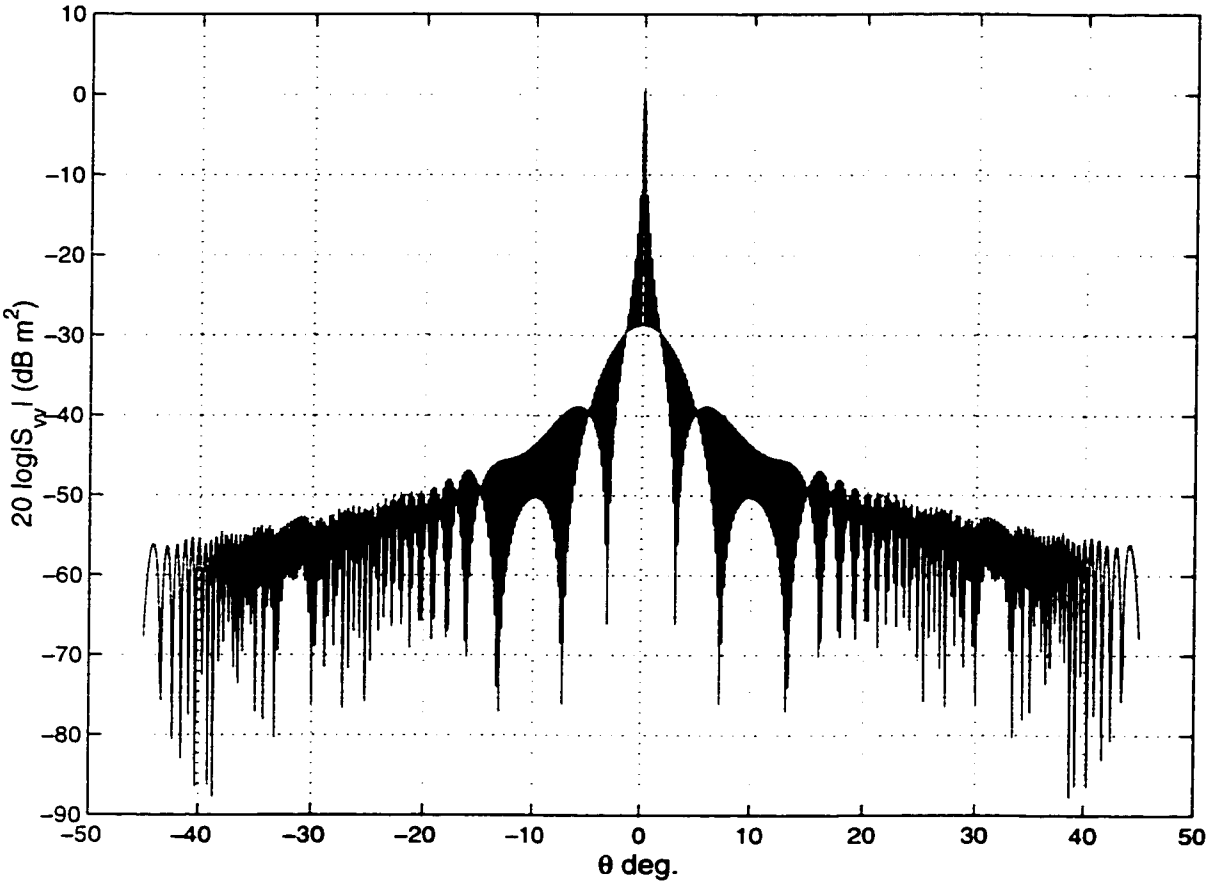

Figure 3.3: The backscattered radar cross section of a smooth, conducting cylinder with radius of 3.75 cm and length of 150 cm as a function of the incidence angle θ at 95 GHz, where normal incidence is at $\theta = 0°$.

3.2.2 Coherent Scattering by Rough, Lossy, Dielectric Cylinder

In general, the backscattered field is composed of two components, coherent and incoherent. In case of a rough cylinder, the coherent component can be attributed to a smooth cylinder of a diameter equal to the mean diameter of the rough cylinder, while the incoherent component can be attributed to the randomness of the rough surface. The coherent component is obtained from equation (3.11) by computing the ensemble average ($< . >$) of S_{vv} and S_{hh}, which reduces to the evaluation of $< I(C) >$. In other words, the copolarized coherent elements of the scattering matrix are expressed mathematically as:

$$< S_{vv} > \;=\; < I(C_{vv}) >, \qquad < S_{hh} > \;=\; < I(C_{hh}) > . \tag{3.13}$$

For a lossy, dielectric cylinder with rough surface whose radius of curvature is large with respect to the wavelength, the expression of $I(C)$, equation (3.9), can be written in the following form:

$$I(C) \;=\; \frac{ik_o}{4\pi} \int\int_{s'} C\; e^{ik_o(\hat{k}_i - \hat{k}_s).\bar{r}'}\; ds' \;=\; \frac{ik_o}{4\pi} \int\int_{s'} C\; e^{iQ}\; ds' \tag{3.14}$$

Where,

- $k_o(\hat{k}_i - \hat{k}_s) = q_{x'}\hat{x}' + q_{y'}\hat{y}' + q_{z'}\hat{z}'$
- $\bar{r}' = h(y', z')\hat{x}' + y'\hat{y}' + z'\hat{z}'$
- $h(y', z') = \sqrt{a^2 - y'^2} + f(y', z')$, a is the mean radius of the rough cylinder,

- $f(y', z')$ is a random function describing the surface roughness,

- $Q = k_o(\hat{k_i} - \hat{k_s}).\bar{r'} = q_{x'}h(y', z') + q_{y'}y' + q_{z'}z'$,

- $ds' = dy'dz'.\sqrt{1 + h_{y'}^2 + h_{z'}^2}$, and

- $h_{y'} = \frac{\delta h}{\delta y'}$, and $h_{z'} = \frac{\delta h}{\delta z'}$.

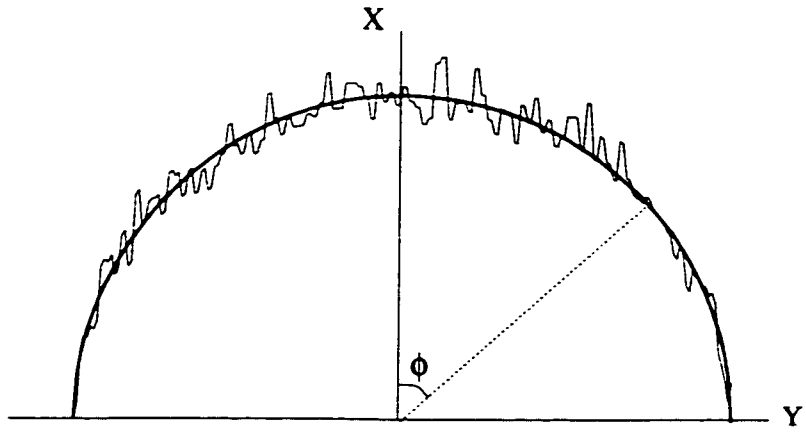

Figure 3.4: Illustration of the proposed mathematical function to describe the surface roughness of a circular cylinder.

An example of the roughness component along with the mean circular cylindrical surface are depicted in Fig. 3.4. A note worth mentioning here is that this mathematical description of the roughness is not accurate to a high degree at angles $|\phi| > \pi/4$. However, this mathematical description of the roughness is still very useful in this model which uses the stationary phase (SP) approximation. Under SP approximation the main contribution to the integration over the lit surface comes from the strips around the strip of stationary phase, which is at $\phi = 0$ for the backscattering case.

Therefore, for bistatic configurations that result in SP at angles $|\phi| < \pi/4$, this way of describing roughness is expected to lead to accurate results. That is, this roughness function approximation represents a compromise between the range of validity of the models at hand and the simplicity of derivation. In other words, by this approximation we narrowed the range of validity of our models, but we introduced an accurate solutions for the backscatter setup and for a wide range of bistatic setup of interest to many applications.

Substituting Q and ds' into equation (3.14), $I(C)$ can be expressed as:

$$I(C) = \frac{ik_o}{4\pi} \int\int_s C \; e^{i(q_{y'}y' + q_{z'}z')} e^{i(q_{x'}h(y',z'))} \sqrt{1 + h_{y'}^2 + h_{z'}^2} \; dy'dz' \qquad (3.15)$$

At MMW frequencies, $Q \gg 1$, hence, the SP approximation can be applied (at the SP point $\frac{\delta Q}{\delta y'} = 0$ and $\frac{\delta Q}{\delta z'} = 0$). The application of the SP approximation leads to $h_{y',s} = \frac{-q_{y'}}{q_{x'}}$ and $h_{z',s} = \frac{-q_{z'}}{q_{x'}}$, and reduces equation (3.15) to:

$$I(C_s) = \frac{ik_o}{4\pi} \sqrt{1 + \frac{q_{y'}^2 + q_{z'}^2}{q_{x'}^2}} \, C_s \int\int_{s'} e^{i(q_{y'}y' + q_{z'}z')} \; e^{i(q_{x'}h(y',z'))} \; dy'dz'$$

$$= \frac{ik_o}{4\pi} \frac{q}{q_{x'}} \, C_s \int\int_{s'} e^{i(q_{y'}y' + q_{z'}z')} \; e^{i(q_{x'}\sqrt{a^2 - y'^2})} \; e^{i(q_{x'}f(y',z'))} \; dy'dz', \quad (3.16)$$

where the subscript s indicates that the term is evaluated at the SP point. The ensemble average of $I(C_s)$ is expressed as:

$$< I(C_s) >= \frac{ik_o}{4\pi} \frac{q}{q_{x'}} \, C_s \int\int_{s'} e^{i(q_{y'}y' + q_{z'}z')} \; e^{i(q_{x'}\sqrt{a^2 - y'^2})} < e^{i(q_{x'}f(y',z'))} > dy'dz', \quad (3.17)$$

which is applicable to any rough surface that satisfies the SP condition ($Q \gg 1$). In general, this integration can be evaluated numerically (but, it is, computationally, highly demanding). However, for the common case of a rough surface with Gaussian distribution roughness function we reduced this integration to an analytical closed form solution.

Special Case:

A rough surface with Gaussian distribution roughness function:

For a surface roughness function, $f(y', z')$, which is Gaussian with zero-mean and σ-standard deviation, $< e^{i(q_{x'} f(y', z'))} >$ becomes the characteristic function of the Gaussian random function which is equal to $e^{-\frac{\sigma^2}{2} q_{x'}^2}$. Substituting the characteristic function in equation (3.17), we can rewrite $< I(C_s) >$ as:

$$< I(C_s) >= \frac{ik_o}{4\pi} \frac{q}{q_{x'}} e^{-\frac{\sigma^2}{2} q_{x'}^2} C_s \int \int_{s'} e^{i(q_{y'} y' + q_{z'} z')} e^{i(q_{x'} \sqrt{a^2 - y'^2})} \, dy' dz' \qquad (3.18)$$

Performing the integration with respect to z' results in:

$$< I(C_s) >= \frac{ik_o}{4\pi} \frac{q}{q_{x'}} \, e^{-\frac{\sigma^2}{2} q_{x'}^2} \, \frac{b \, sin(q_{z'} b/2)}{q_{z'} b/2} \, C_s \int_{-a}^{a} e^{i(q_{y'} y')} \, e^{i(q_{x'} \sqrt{a^2 - y'^2})} \, dy' \qquad (3.19)$$

Substituting $y' = a \, sin\phi'$, $dy' = a \, cos\phi' \, d\phi'$, $T = \sqrt{q_{x'}^2 + q_{y'}^2}$, and $\tilde{\phi} = tan^{-1}(\frac{-q_{y'}}{-q_{x'}})$ (hence, $q_{x'} = -T \, cos\tilde{\phi}$, and $q_{y'} = -T \, sin\tilde{\phi}$), the previous equation can be rewritten

as:

$$< I(C_s) > = \frac{ik_o}{4\pi}\frac{q}{q_{x'}} e^{-\frac{\sigma^2}{2}q_{x'}^2} \frac{b\, sin(q_{z'}b/2)}{q_{z'}b/2} \cdot \cdot C_s \int_{-\pi/2}^{\pi/2} e^{-iTa(sin\tilde{\phi}\ sin\phi' + cos\tilde{\phi}\ cos\phi')}\ a\ cos\phi'\ d\phi' \qquad (3.20)$$

Since $(sin\tilde{\phi}\ sin\phi' + cos\tilde{\phi}\ cos\phi') = cos(\phi' - \tilde{\phi})$ and $Ta \gg 1$ at MMW frequencies, the SP approximation can be applied as follows:

$$< I(C_s) > = \frac{ik_o}{4\pi}\frac{q}{q_{x'}} e^{-\frac{\sigma^2}{2}q_{x'}^2}\ b\ sinc(\frac{q_{z'}b}{2\pi})\ e^{-iTa}\ cos\tilde{\phi}\ C_s \int_{-\pi/2}^{\pi/2} e^{iTa\frac{(\phi'-\tilde{\phi})^2}{2}} a\ cos\phi' d\phi'$$

$$< I(C_s) > = \frac{ik_o}{4\pi}\frac{a}{}\frac{q}{q_{x'}} e^{-\frac{\sigma^2}{2}q_{x'}^2}\ b\ sinc(\frac{q_{z'}b}{2\pi})\ e^{-iTa}\ cos\tilde{\phi}\ \sqrt{\frac{2}{Ta}} \cdot \cdot \left\{ F(\sqrt{\frac{Ta}{2}}(\pi/2 - \tilde{\phi})) - F(\sqrt{\frac{Ta}{2}}(-\pi/2 - \tilde{\phi})) \right\} C_s \qquad (3.21)$$

Which is similar to the expression of the scattering from smooth cylinder, equation (3.12), multiplied by $\frac{q}{q_{x'}} e^{-\frac{\sigma^2}{2}q_{x'}^2}\ cos\tilde{\phi}$. This expression states that, the coherent response of a rough cylinder decreases in amplitude, while maintaining a pattern similar to that of a smooth cylinder, with the increase of the roughness standard deviation in case of Gaussian roughness function.

3.2.3 Incoherent Scattering by Rough, Lossy, Dielectric Cylinder

The starting point for deriving the model of the incoherent component is the expression of $I(C_s)$ given in equation (3.16), namely,

$$I(C_s) = \frac{ik_o}{4\pi}\frac{q}{q_{x'}} C_s \int\int_{s'} e^{i(q_{y'}y' + q_{z'}z')}\ e^{i(q_{x'}\sqrt{a^2 - y'^2})}\ e^{i(q_{x'}f(y',z'))}\ dy'dz'.$$

Based on the above equation, the ensemble average of the total scattered power from a rough cylinder is given by

$$\begin{aligned} < I(C_s)I^*(C_s) > &= < |I(C_s)|^2 > \\ &= \frac{k_o^2 q^2}{(4\pi q_{x'})^2} |C_s|^2 \int\int_{s_1'} \int\int_{s_2'} e^{i(q_{y'}(y_1'-y_2')+q_{z'}(z_1'-z_2'))} \cdot \\ &\cdot \; e^{iq_{x'}(\sqrt{a^2-(y_1')^2}-\sqrt{a^2-(y_2')^2})} < e^{iq_{x'}(f(y_1',z_1')-f(y_2',z_2'))} > \; dy_1' dy_2' dz_1' dz_2' \end{aligned} \tag{3.22}$$

And the power of the coherent component scattered from a rough cylinder (based on equation (3.18)) is given by:

$$\begin{aligned} | < I(C_s) > |^2 &= \frac{k_o^2 q^2}{(4\pi q_{x'})^2} e^{-\sigma^2 q_{x'}^2} |C_s|^2 \int\int_{s_1'} \int\int_{s_2'} e^{i(q_{y'}(y_1'-y_2')+q_{z'}(z_1'-z_2'))} \cdot \\ &\cdot \; e^{iq_{x'}(\sqrt{a^2-(y_1')^2}-\sqrt{a^2-(y_2')^2})} \; dy_1' dy_2' dz_1' dz_2' \end{aligned} \tag{3.23}$$

The incoherent power is the difference between the average total power and the coherent power. Mathematically

$$|I_{inc}|^2 = < |I(C_s)|^2 > - | < I(C_s) > |^2. \tag{3.24}$$

In general these two integrals can be evaluated numerically for rough surfaces with arbitrary statistical properties (but, it is, computationally, highly demanding). However, for the common case of a rough surface with exponential characteristic function we reduced the expression of $|I_{inc}|^2$ to a closed form solution, as shown below.

Special Case:

A rough surface with exponential characteristic function:

For cylinders with rough surfaces with exponential characteristic functions of the form:

$$< e^{i[q_{x'}(f(y_1,z_1)-f(y_2,z_2))]} > = e^{-q_{x'}\tau\sqrt{(y_1-y_2)^2+(z_1-z_2)^2}}. \quad (3.25)$$

the average total scattered power equals:

$$< |I(C_s)|^2 > = \frac{k_o^2 q^2}{(4\pi q_{x'})^2} |C_s|^2 \int\int_{s_1'} \int\int_{s_2'} e^{i(q_{y'}(y_1'-y_2')+q_{z'}(z_1'-z_2'))} \cdot$$
$$\cdot \; e^{iq_{x'}(\sqrt{a^2-(y_1')^2}-\sqrt{a^2-(y_2')^2})} < e^{iq_{x'}(f(y_1',z_1')-f(y_2',z_2'))} > dy_1'dy_2'dz_1'dz_2'$$

$$< |I(C_s)|^2 > = \frac{k_o^2 q^2}{(4\pi q_{x'})^2} |C_s|^2 \int\int_{s_1'} \int\int_{s_2'} e^{i(q_{y'}(y_1'-y_2')+q_{z'}(z_1'-z_2'))} \cdot$$
$$\cdot \; e^{iq_{x'}(\sqrt{a^2-(y_1')^2}-\sqrt{a^2-(y_2')^2})} \, e^{-q_{x'}\tau\sqrt{(y_1-y_2)^2+(z_1-z_2)^2}} \, dy_1'dy_2'dz_1'dz_2' \quad (3.26)$$

At MMW frequencies and for incidence angles not very far from the direction normal to the axis of the rough cylinder, $q_{x'} >> 1$. Consequently, the coherent power (equation (3.23)) can be neglected due to its very small amplitude, resulted from the decaying exponential $e^{-\sigma^2 q_{x'}^2}$ term, with respect to the average total power (equation (3.22)). Hence, $|I_{inc}|^2 \approx < |I(C_s)|^2 >$.

We can perform the double integral on y_1 and y_2 using the stationary phase approximation if $e^{-q_x\tau\sqrt{(y_1-y_2)^2+(z_1-z_2)^2}}$ is slowly varying ($\tau \leq 0.1$) with respect to $e^{i\,q_{y'}(y_1'-y_2')} \, e^{iq_{x'}\,(\sqrt{a^2-(y_1')^2}\,-\,\sqrt{a^2-(y_2')^2})}$.

The SP point is at $y_1 = y_2$ and by performing the following substitutions;

- $y'_1 = a\ sin\phi'_1, \qquad dy'_1 = a\ cos\phi'_1\ d\phi'_1,$

- $y'_2 = a\ sin\phi'_2, \qquad dy'_2 = a\ cos\phi'_2\ d\phi'_2,$

- $T = \sqrt{q_{x'}^2 + q_{y'}^2}$, and

- $\tilde{\phi} = tan^{-1}(\frac{-q_{y'}}{-q_{x'}})$, hence, $q_{x'} = -T\ cos\tilde{\phi}$, and $q_{y'} = -T\ sin\tilde{\phi}$,

and similar to the derivation of equation (3.21), the expression of I_{inc} can be rewritten as:

$$\begin{aligned} I_{inc}(C) &= \frac{k_o^2 q^2}{(4\pi q_{x'})^2}\ I_z\ \left| a\ cos\tilde{\phi}\ e^{-iTa} \int_{v=\sqrt{\frac{Ta}{2}}(-\frac{\pi}{2}-\tilde{\phi})}^{\sqrt{\frac{Ta}{2}}(\frac{\pi}{2}-\tilde{\phi})} e^{iv^2} \sqrt{\frac{2}{Ta}} dv \right|^2 \\ &= \frac{k_o^2 q^2}{(4\pi q_{x'})^2}\ I_z\ |C_s|^2\ a^2\ cos^2\tilde{\phi}\ \frac{2}{Ta} \Big(F(\sqrt{\frac{Ta}{2}}(\frac{\pi}{2} - \tilde{\phi})) - F(\sqrt{\frac{Ta}{2}}(-\frac{\pi}{2} - \tilde{\phi})) \Big)^2 \end{aligned} \tag{3.27}$$

where,

$$I_z = \int_{-b/2}^{b/2} \int_{-b/2}^{b/2} e^{iq_{z'}(z_1 - z_2)} e^{-q_{x'}\tau(z_1 - z_2)}\ dz_1\ dz_2. \tag{3.28}$$

With the change of variable $V = z_1 - z_2$, $U = z_2$, shown in Fig. 3.5, the two folded integration can be done by performing the integration first along V. For constant V the integral function is constant and is proportional to the length of the line confined to the original region of integration, hence I_z equals:

$$I_z\ =\ 2 \int_0^b (b - V)\ cos(q_{z'}\ V)\ e^{-q_{x'}\tau V}\ dV \tag{3.29}$$

At MMW frequencies $q_{x'}\tau\ >>\ 1$, hence, due to the decaying exponential term $e^{-q_{x'}\tau V}$, the integration limit can be extended from b to ∞ without affecting the ac-

curacy of the result.

Using the two following identities (which are reported in [28] pp. 490 , 477 respectively),

$$\int_o^\infty x^{\mu-1}\, e^{-\tau\, x}\, cos(\delta\, x)\, dx \;=\; \frac{\Gamma(2)\; cos(\mu\; tanh^{-1}(j\delta/\tau)\; /j)}{\delta^2+\tau^2} \tag{3.30}$$

$$\int_o^\infty e^{-\tau\, x}\, cos(\delta\, x+\lambda)\, dx \;=\; \frac{\tau\; cos(\lambda)\; -\; \delta\; sin(\lambda)}{\delta^2+\tau^2} \tag{3.31}$$

where $\Gamma(x)$ is the Gamma function of x, I_z can be expressed as

$$I_z \;=\; 2b\,\frac{q_{x'}\tau}{(q_{x'}\tau)^2+q_{z'}^2} \;-\; \frac{2\;\Gamma(2)\; cos(2\; tanh^{-1}(jq_{z'}/(q_{x'}\tau))\; /j)}{(q_{x'}\tau)^2+q_{z'}^2} \tag{3.32}$$

Which when substituted in equation (3.27) gives the closed form solution for the incoherent scattering component from a rough, lossy, dielectric cylinder of surface roughness with exponential characteristic function.

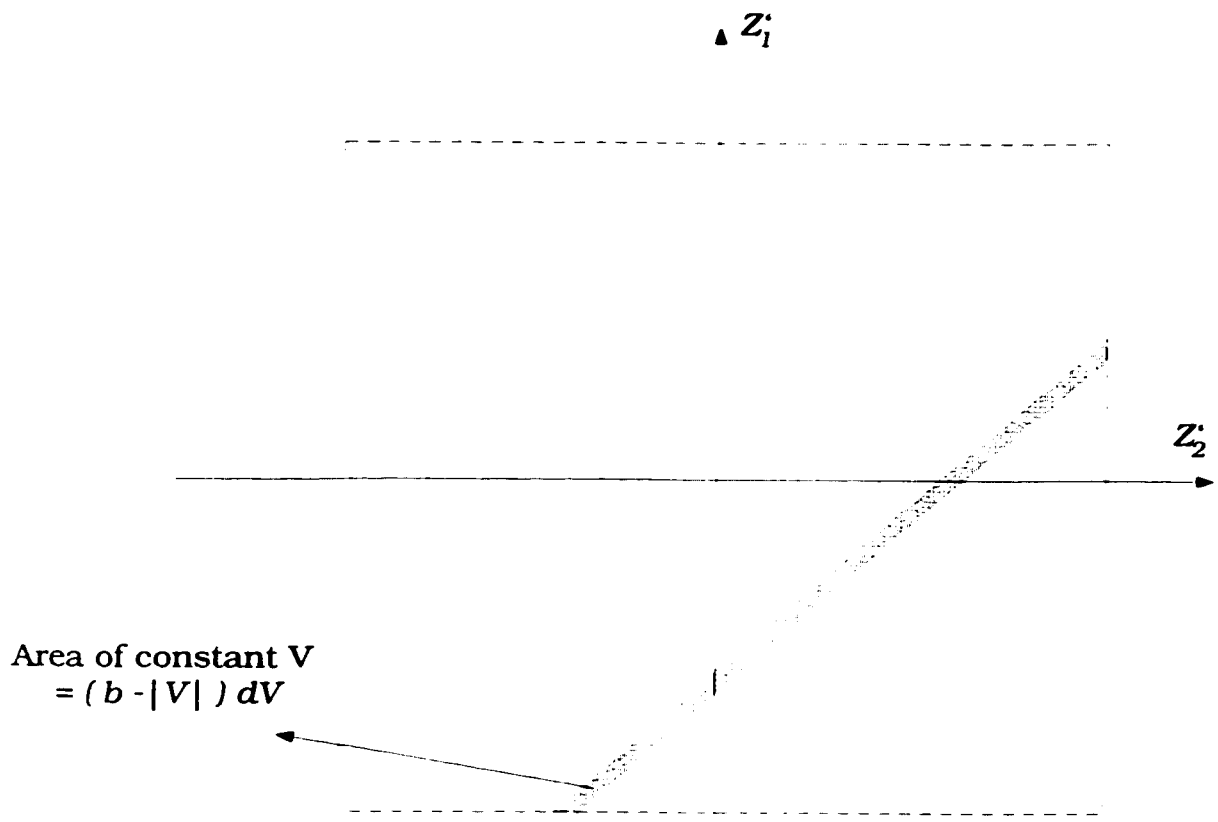

Figure 3.5: Sketch illustrating the method used to conduct the integration I_z.

3.3 Conclusions

Based on the Kirchoff's approximation, the problem of MMW scattering by rough, lossy, dielectric cylinder was formulated. Then, following the geometric optic (GO) approximation, general solutions for both the coherent and incoherent components of MMW scattering by rough, lossy, dielectric cylinder were developed. These general coherent and incoherent solutions are in the forms of two and four folded integrals, respectively. For the common case of rough cylinder having a Gaussian distributed roughness, we reduced the coherent solution to a closed form expression. Also, for the common case of cylinder having a surface roughness with exponential characteristic function, we reduced the solution to a closed form expression. The models for both the coherent and the incoherent components are valid for the backscattering and a wide range of bistatic configurations.

CHAPTER 4

EXPERIMENTAL VERIFICATION OF THE MMW SCATTERING MODEL FOR ROUGH, LOSSY, DIELECTRIC CYLINDERS AND ITS APPLICATION TO TREE TRUNKS

4.1 Introduction

One of the main deficiencies of the models available in the literature for the scattering by rough cylinder is the lack of experimental verification. To avoid this deficiency a set of experiments aimed at measuring the MMW scattering response of a rough conducting cylinder and a section of a tree trunk were performed. The purpose of this measurements is to, experimentally, examine the validity of the analytical models developed in Chapter 3. This goal (model verification) required the performance of another set of experiments and measurements to: (a) measure the dielectric constant of a tree trunk, Section 4.3, (b) incorporate the radar system impulse response into

the model prediction, Section 4.4, and (c) measure the roughness parameters of both the rough conducting cylinder and the section of the tree trunk, Section 4.6. These measured parameters were then applied to the analytical models to evaluate their predictions which were compared to the measurements to examine the accuracy of these models.

However, the analytical models are valid for both the backscatter and a wide rang of bistatic configurations, the experimental work of this chapter is focused on the backscattering configuration to avoid the complexity of the bistatic configuration.

4.2 Radar System Description

The University of Michigan 95-GHz polarimetric scatterometer was used in this experimental study conducted to verify the analytical models. The U-M system is a truck-mounted, network analyzer-based polarimetric radar system that operates over a bandwidth of up to 2 GHz centered at 95-GHz. Using a coherent-on-receive measurement technique, the system is capable of measuring the Mueller matrix of a target by sequentially transmitting six different polarizations (vertical(V), horizontal (H)), 45° linear, 135° linear, LHC, and RHC) and receiving simultaneously the V and H-polarized components of the backscattered field for each transmitted polarization [7, 18, 19]. The transmitted power level is 3 dBm and calibration is accomplished by employing a technique that uses a metallic sphere and any depolarizing target

(whose scattering matrix need not be known) [6]. This calibration procedure provides measurements with an accuracy of $\pm$ 1 dB in magnitude and $\pm 5°$ in phase. The radar uses a 3-inch diameter horn antenna for transmission and a 6-inch diameter horn antenna for reception arranged in a pseudo-monostatic mode. This configuration produces a two-way beamwidth of 1.4°. For measurements at incidence angles up to 70° from nadir, the system is mounted a top a truck-mounted boom, and for measurements at angles near grazing, the radar is mounted on a computer-controlled gimbal housed inside of a van. The gimbal is used to control the radar look direction in both azimuth and elevation.

4.3 Dielectric Constant Measurement

In the models for the coherent and incoherent scattering response of rough cylinders developed in Chapter 3 we assumed that the cylinder is made of a lossy dielectric material. To examine the validity of this assumption for the case of tree trunks, an experiment was conducted to measure the dielectric constant of the wooden material of tree trunks.

The experiment was designed to measure the backscatter from a circular disk positioned along the radar's bore-sight with its circular base facing the radar as shown in Fig. 4.1. In this experiment a thick (enough, with respect to the wavelength, to be considered infinitely deep) wooden disk (cut from a tree trunk), was used. Since the disk fills a small portion of the radar beam centered around the bore-sight, the incident field can be considered as a plane wave. At MMW frequencies, GO approximation

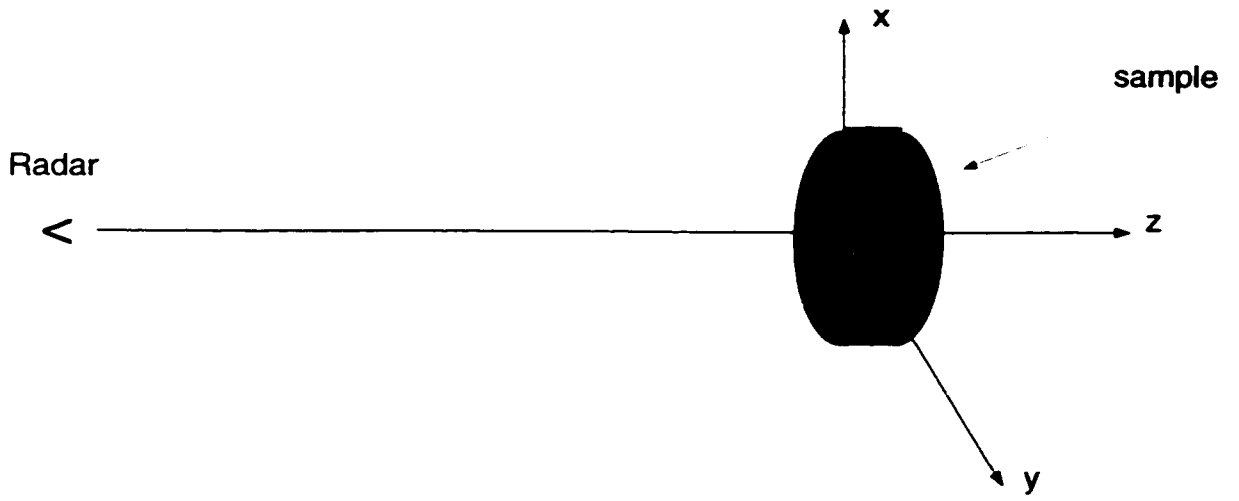

Figure 4.1: The setup used for dielectric constant measurement of a disk cut from a tree trunk.

can be used to evaluate the field scattered by the circular disk. Applying the GO approximation to the circular surface of the disk of radius a, the backscattered field from a V-polarized incident field can be expressed as:

$$E_s(\bar{r}) = \hat{x}\frac{-2i\ k_o\ e^{2ik_o\ r}}{4\pi r^2}\ E_o\ \pi\ a^2\ \Gamma, \tag{4.1}$$

where, E_o is the amplitude of the incident field , Γ is the complex Fresnel reflection coefficient of the half space of the wooden disk, and r is the distance from the radar to the disc. Without loss of generality, the zero-reference plane was taken to be at the radar system. The complex reflection coefficient of the material of the tree trunk can be determined by calibrating it against a material with known reflection coefficient

(conducting material in our case). As follows:

$$\frac{E_s}{E_o}\Big|_{wood} = \hat{x}\frac{-2i\ k_o\ e^{2ik_o\ r}}{4\pi r^2}\ E_o\ \pi\ a^2\ *\Gamma_{wood} * G_s$$

$$\frac{E_s}{E_o}\Big|_{metal} = \hat{x}\frac{-2i\ k_o\ e^{2ik_o\ r}}{4\pi r^2}\ E_o\ \pi\ a^2\ *\Gamma_{metal} * G_s$$

where G_s is a coefficient that depends on the radar system parameters. Assuming that it is possible to position the two samples at the same position accurately enough to ignore the phase difference in the $e^{2ik_o\ r}$ term, we can write

$$\frac{\frac{E_s}{E_o}\Big|_{wood}}{\frac{E_s}{E_o}\Big|_{metal}} = \frac{\Gamma_{wood}}{\Gamma_{metal}} \tag{4.2}$$

and from that expression the complex reflection coefficient can be evaluated, and consequently the complex dielectric constant of the sample. However, it is a straight forward, theoretically speaking, procedure to determine the complex reflection coefficient of the sample, practically it is a difficult task. This difficulty arises from the fact that the two samples (wooden and metallic) must be positioned in the same place with an accuracy of at least $\lambda/10$ which is about 0.3 mm at 95 GHz. Since the positioning accuracy requirement is very tough to achieve manually, the experiment was repeated many times with different samples and only the measurements that resulted in a dielectric constant that is independent of the frequency —over the operating bandwidth of 1 GHz— were considered. The dielectric constant independence of frequency was considered as an indicator of accurate positioning of the two samples at the same position. Figure 4.2 shows an example of one of these measurements. Four measurements, out of many others, achieved this frequency-independence criteria and

resulted in an average trunk dielectric constant of $\epsilon_{trunk} \simeq 2 + j0.7$. The water contents of these samples were 30% on the average.

Another accurate method was reported by Li [12] in his thesis, but it requires the preparation of a thin sample of the material under consideration. According to that method, the sample should be thin enough to allow electromagnetic field to propagate through it a round trip without major decrease in its amplitude due to dielectric losses. This criteria forces the thickness of the sample to be on the order of 2–3 mm, which is difficult to achieve for the trunk material (which is a wet wood cut across or parallel to the tree fiber). The thiner the disc cut from the trunk, the faster the evaporation of its water content (and hence its dielectric constant variation), the higher the probability of developing cracks while cutting, and the faster the shape of the disk to vary to either a concave or a convex shape. This shape variation is a natural process associated with the evaporation of the water content of wood , specially if it is cut across the trunk fiber.

Since one of the main objectives of this experiment is to check the validity of assuming the bark layer to be lossy dielectric material to the extent that causes the wave penetrating it to the internal layers of the trunk to be highly attenuated. And since the above methodology of measuring the dielectric constant has a tough accuracy (in positioning) requirement, another experiment was performed to check the validity of this assumption. Towards that, the following procedures were followed:

1. Cut the bark layer of a cylindrical disk from the tree trunk, and back the bark layer (which is in a cylindrical shell shape) with a metal sheet.

2. Measure the backscattering from the above setup (bark layer shell backed with metal sheet).

3. Remove the metal backing and record the difference in the backscattered field, $|S_{vv}|$.

4. Repeat the same procedure after repositioning the bark layer to different positions and calculate the average variation in $|S_{vv}|$.

5. Measure the water content of the bark layer.

Performing this experiment over a large number of samples which were rough and their thicknesses (including the thickness of the rough layer) were between $0.2''$ and $0.4''$, we obtained the following results:

Wet sample weight (gm.)	Dry sample weight (gm.)	Water content (%)	Average variation of $20log\|S_{vv}\|$
63.9	54.3	15%	$< 0.5\ dB$
69.4	58.3	16%	$< 0.5\ dB$
52.4	48.2	8%	$1 - 3\ dB$
47.7	43.3	9%	$1 - 3\ dB$
54.3	54.3	0%	$> 6\ dB$
58.3	58.3	0%	$> 6\ dB$

From the above results we concluded that the bark layer of a tree trunk is lossy —when wet and thick enough— enough to hide, from radar point of view, the internal dielectric structure of the trunk at MMW frequency. Hence, the analytical derivations of the scattering by rough, lossy, dielectric cylinders are applicable to the case of tree trunk for many species.

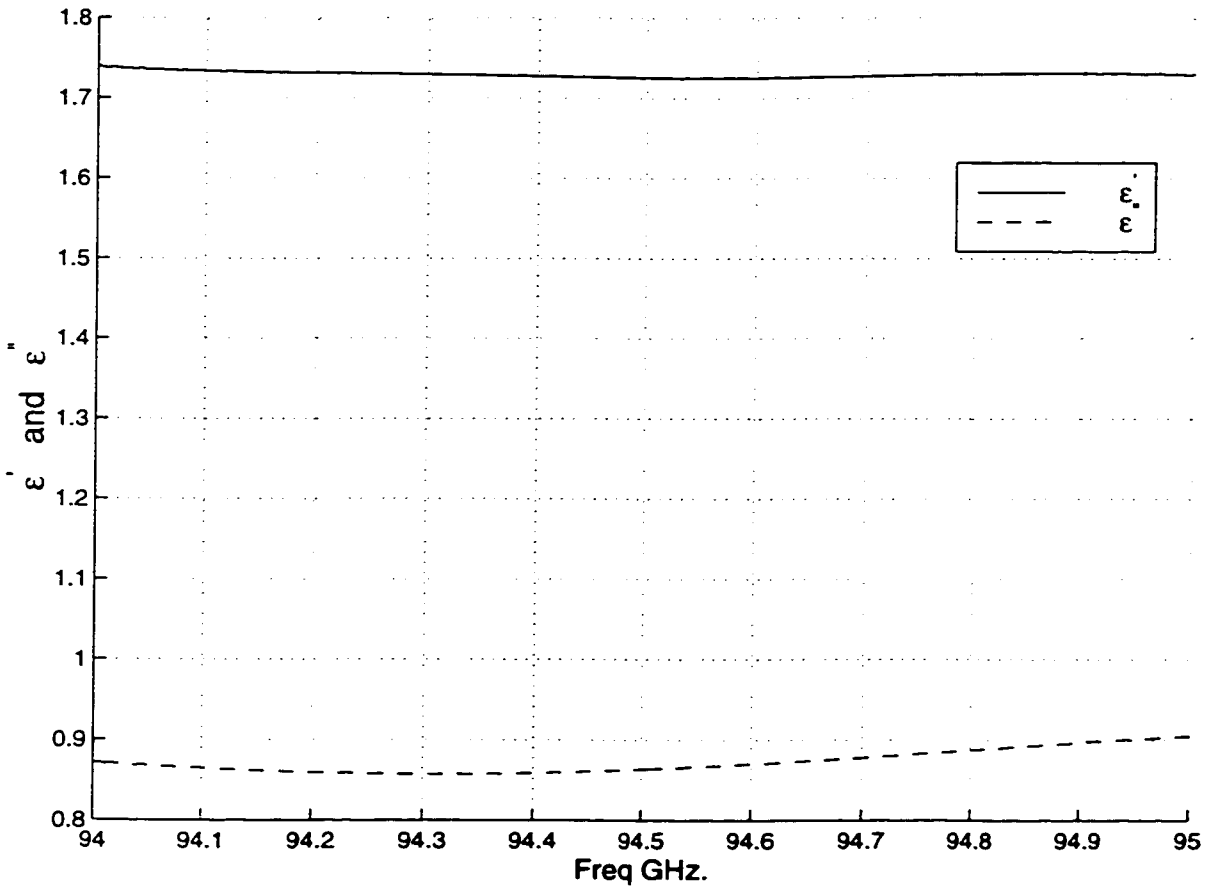

Figure 4.2: Example of the frequency-independent dielectric constant measurement which is adopted as an indicator of accurate positioning of the used samples.

4.4 Radar System Impulse Response

In the models proposed in the Chapter 3, both plane wave incidence and an isotropic antenna pattern for the receiver were implicitly assumed. These assumptions hold well when the cylinder under consideration subtends over a small portion of radar beamwidth (i.e. acting as a point target). However, in a confined indoor measurement setup, where the cylinder fills the radar beam in at least one dimension (along the cylinder's axis), the assumption of point target measurements is no longer valid. Instead, a spherical wave confined within the radar beamwidth and incident on the cylinder, must be considered. In this case, the measured backscattered response is the product of convolving the actual response of the cylinder with the radar's antenna pattern. In principle, removal of the antenna pattern contribution *via* deconvolution is needed, in order to validate the model predictions against measured data. Yet, in practice, it is difficult to conduct this deconvolution efficiently and successfully. An alternative approach would be to convolve the theoretical model predictions with the actual radar system pattern, then compare the resulting theoretical response to the measured one.

In this study, the U-M 95 GHz dual antenna radar system was used and operated over 1 GHz bandwidth (15 cm range resolution). In addition, the 3-dB beamwidth of the transmit and receive antennas of this system are 2.8° and 1.4°, respectively. As a first order approximation, the pattern of the transmit antenna was assumed isotropic. This approximation is justified by the fact that the beamwidth of the transmit an-

tenna is twice as wide as that of the receive antenna . Under this approximation, the receive antenna pattern represents, in effect, the impulse response of the radar system.

To convolve the theoretical response prediction with the impulse response of the radar system, the standard technique outlined in [14] was used. To test the validity of this technique, a set of backscattering measurements of a smooth, conducting cylinder with a radius of 3.75 cm and a length 0f 150 cm were conducted as a function of incidence angle. Then, the theoretical response based on the GO approximation, shown in Fig. 3.3 (which had a narrow backscattered pattern of 0.2° centered around the normal incidence), was convolved with the impulse response of the radar system using the standard technique in [14] . The normalized backscattered patterns of both, the measured and the simulated (after convolving it with the radar system impulse response), responses are plotted in Fig. 4.3 as a function of the radar incidence angle, with respect to the normal to the axis of the cylinder. A very good agreement was observed between the normalized patterns. However, the two responses exhibit a difference, on the absolute basis, as opposed to the normalized basis, in peak values of about 15 dB as depicted in Fig. 4.4.

From figures. 4.3 and 4.4, we concluded that the technique proposed in [14] provides a good approximate approach for incorporating the system response into the theoretical model to predict the shape of the scattering pattern, but it is not capable of predicting the correct magnitude of the scattering pattern. To improve on the accuracy of this method, the antenna pattern of the transmitter antenna was incorporated

too. Hence, the system impulse response becomes the product of the antenna gain patterns of both the receive and transmit antennas. Applying this modification to the system's impulse response, the good agreement between the shapes of the measured and theoretical backscattered patterns was maintained and the difference between their respective peaks was reduced from 15 dB to about 9 dB.

To further improve on the accuracy of incorporating of the radar system effect into the theoretical model predictions, we propose an alternative approach. The proposed approach utilizes the radar equation for one-dimensional distributed target. This new technique takes into account the amplitude and phase variations (instead of the amplitude variation only as in [14]) of the incident wave over the illuminated target. The following section discusses this technique in details.

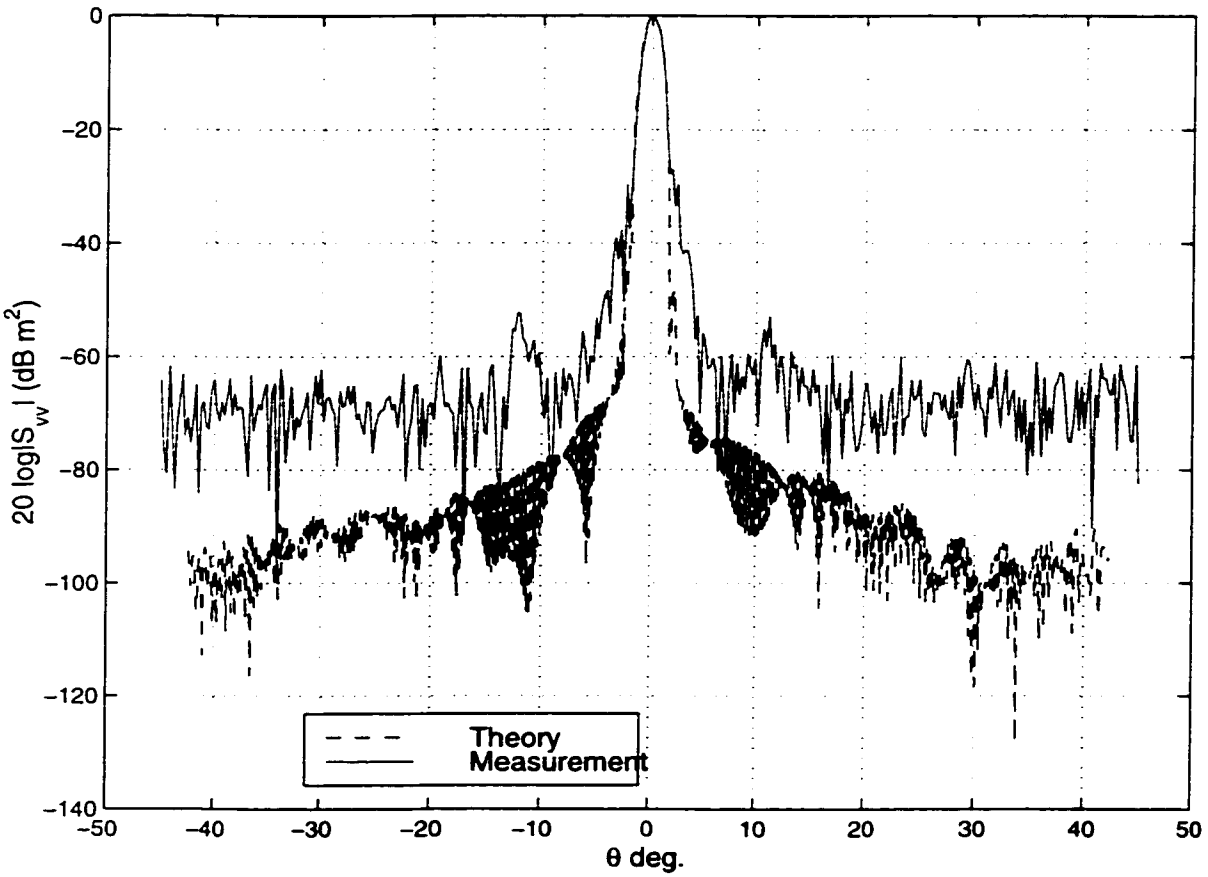

Figure 4.3: Comparison between theory and measurements of the radar backscattered from a smooth conducting cylinder (normalized patterns). The system response was incorporated following the technique outlined in [14] (note: the radar system's noise floor was about -70 dBm^2).

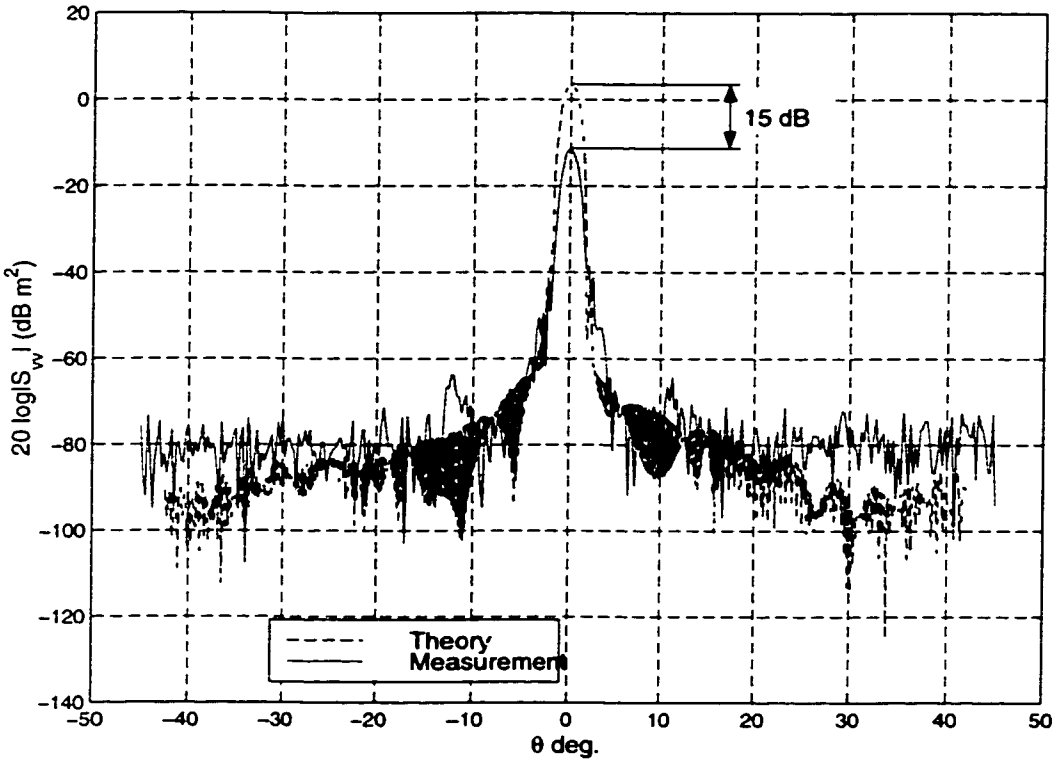

Figure 4.4: Comparison between theory and measurements of the radar backscattered from a smooth conducting cylinder (absolute values). The system response was incorporated in the theoretical prediction following the technique outlined in [14] (note: the radar system's noise floor was about -70 dBm^2).

4.4.1 One-dimensional Radar Equation Method

To accurately account for the radar system impulse response, the cylinder was divided into N short segments each of length dl, as shown in Fig. 4.5. The cylinder's scattering matrix element S_{vv} —and similarly the S_{hh}— can be expressed as:

$$S_{vv}(\theta) = \sum_{i} \Delta\ S_{vv,i}(\theta)\ g_{r,v}(\theta_i)\ g_{t,v}(\theta_i)\ e^{jk_o(R_i - R_o)}\ \times\ \frac{R_o}{R_i} \tag{4.3}$$

where:

- $g_{r,v}(\theta_i)$, $g_{t,v}(\theta_i)$ are, respectively, the receiver and transmitter antenna gain associated with segment i of the cylinder which makes an angle θ_i with the radar's bore-sight.

- $e^{jk_o(R_i - R_o)} * \frac{R_o}{R_i}$ is a propagation factor (referenced to bore-sight), in both phase and amplitude, at the location of the ith segment of the cylinder,

- $\Delta S_{vv,i}$ is the differential scattering matrix, vv-element, of the i_{th} segment of the cylinder.

In equation (4.3), $\frac{\lambda}{\sqrt{4\pi}}$ was dropped from the radar equation since it was compensated for when the calibration technique, outlined in [6], was applied to the measured response. Using this approach to incorporate the system effect into the theoretical model predictions results in an excellent agreement, as shown in Fig. 4.6, between the measured and theoretically computed backscattered pattern of the smooth conducting cylinder. The agreement extends to both the peak value and the shape of the backscatter pattern. A difference of about 1 dB in peak values was observed which is on the order of the measurement error.

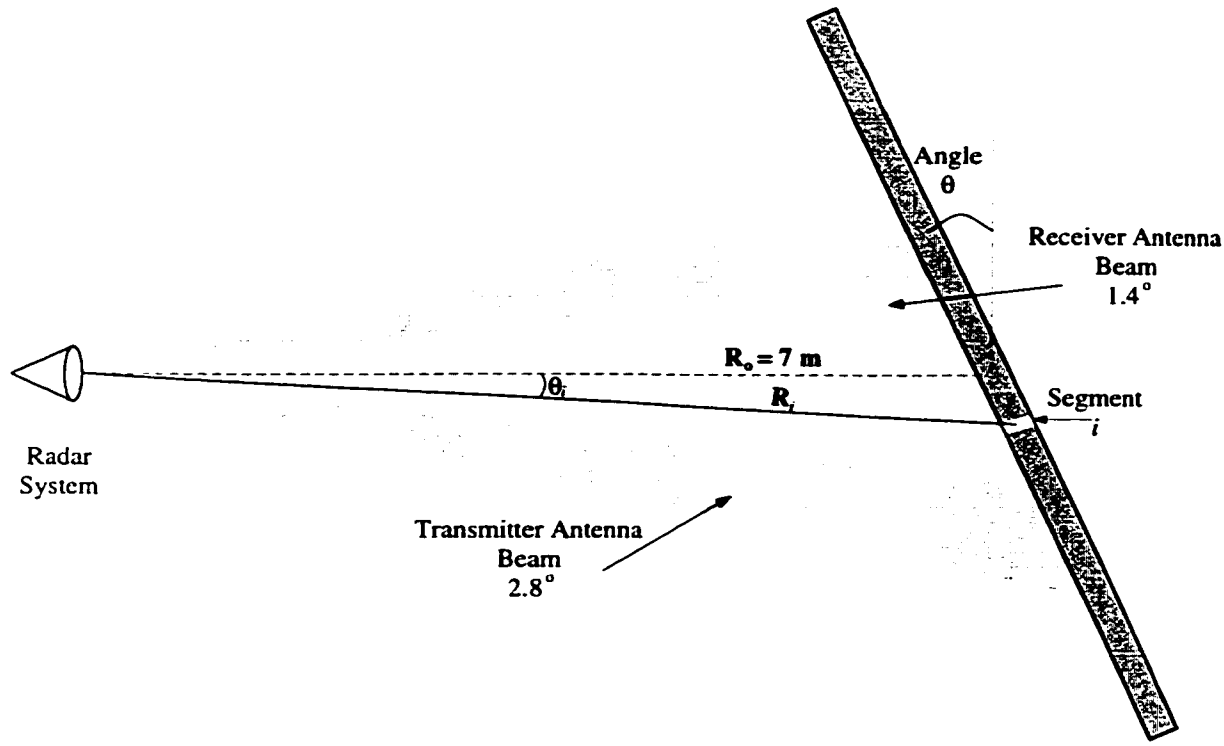

Figure 4.5: Sketch illustrating the details of the setup used to measure the radar backscattered from cylinders and the parameters of the one-dimensional radar equation method.

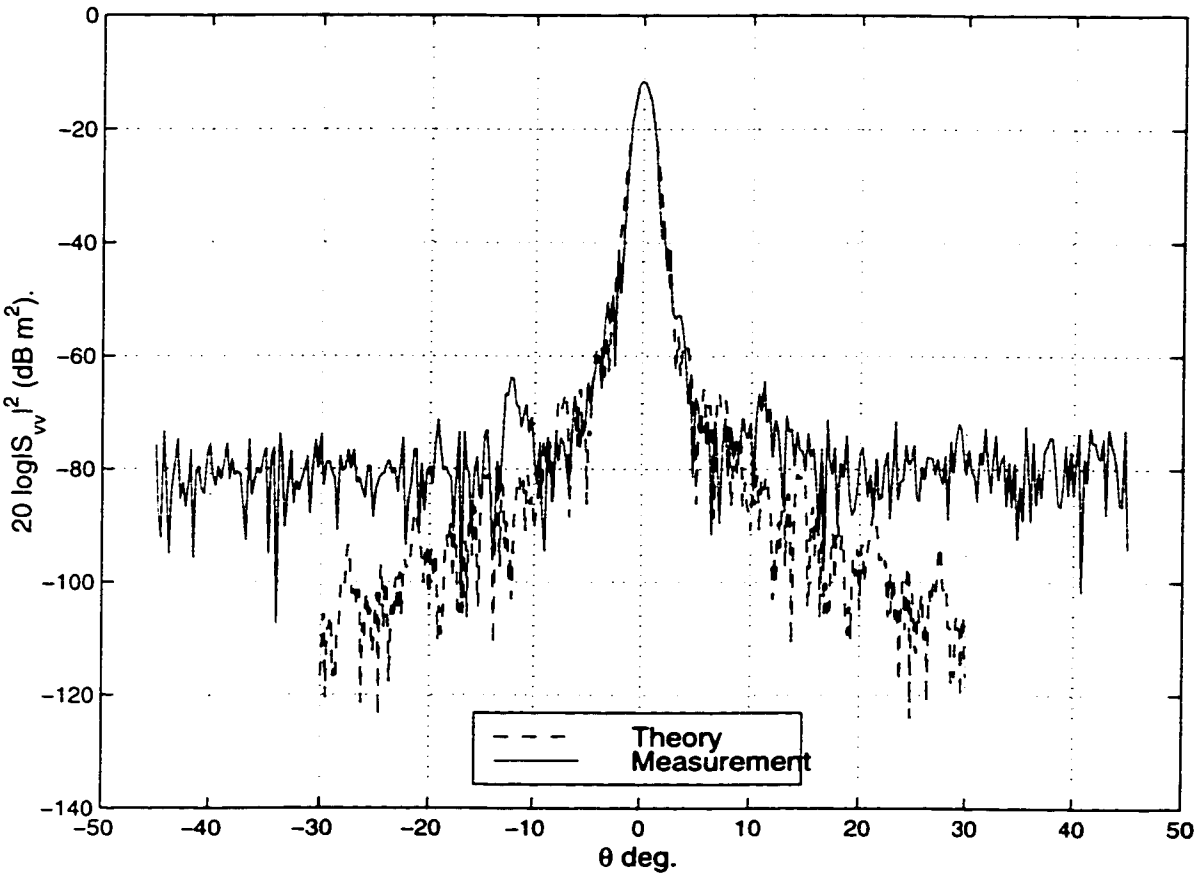

Figure 4.6: Comparison between theory and measurements of the radar backscattered from a smooth conducting cylinder. The system response was incorporated using the new proposed technique of equation(4.3).

4.5 Measurements of the Radar Backscattered from Rough Cylinders

A series of indoor measurements were conducted to examine the theoretical predictions against measurements. The measurements were conducted on a rough, conducting cylinder, and a section of a real trunk. Figures 4.7 and 4.8 show the experimental setup used to measure the backscatter response of the rough conducting cylinder and the tree trunk section, respectively. The mean diameter of the conducting cylinder is 11.4 cm, while the mean diameter of the trunk is 8.9 cm. Both targets, were positioned horizontally over a Styrofoam pedestal on top of a rotating (turn) table. The turn table along with the timing and recording of the measurements of the elements of the scattering matrix are computer controlled. Measurements were conducted over incidence angles between $-30^{o} \leq \theta \leq 30^{o}$ (normal incidence to the axis of the cylindrical target is at $\theta = 0^{o}$) at 1^{o} angular increments. Since, these measurements are statistical, as opposed to deterministic as in the case of the smooth cylinder, 20 statistically independent measurements were conducted at every incidence angle. The statistically independent samples were generated by rotating the cylinder and the trunk around their longitudinal axes. The statistically independent samples were doubled by making use of the fact that the two angles $+\theta_i$ and $-\theta_i$ are statistically independent samples, and the scattering angular response of the cylinder/trunk can be seen as a function of $|\theta_i|$. That is, we take advantage of the angular symmetry about the line perpendicular to the longitudinal axis of the cylinder/trunk.

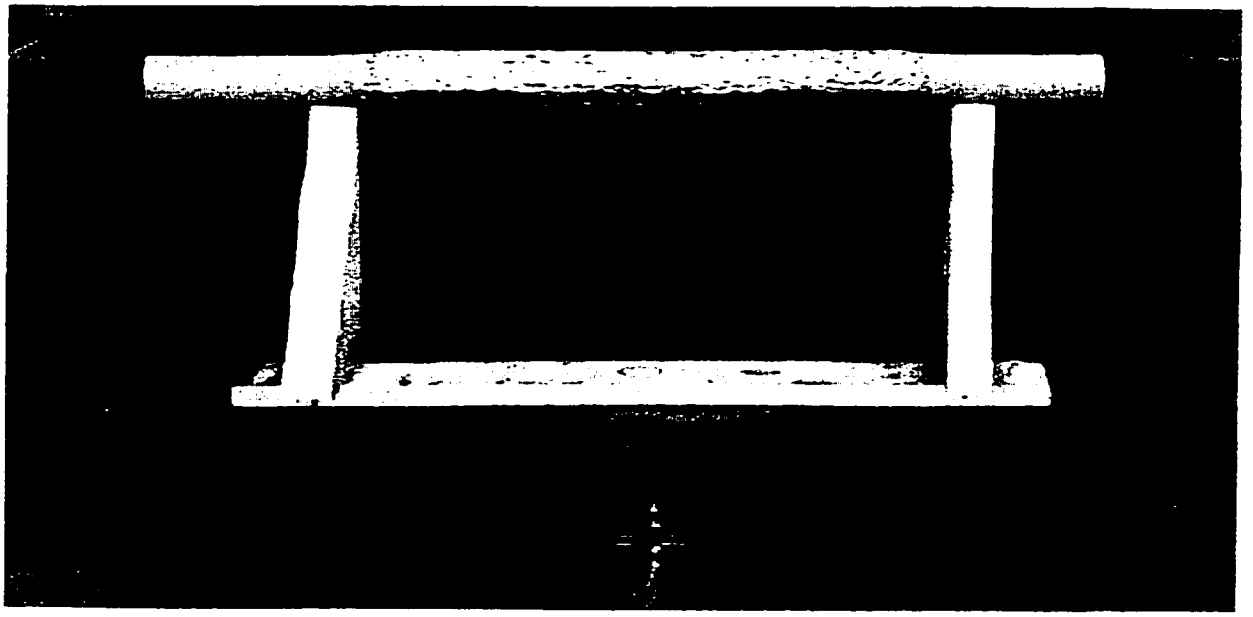

Figure 4.7: The indoor setup used to measure the backscattered RCS pattern of the rough conducting cylinder.

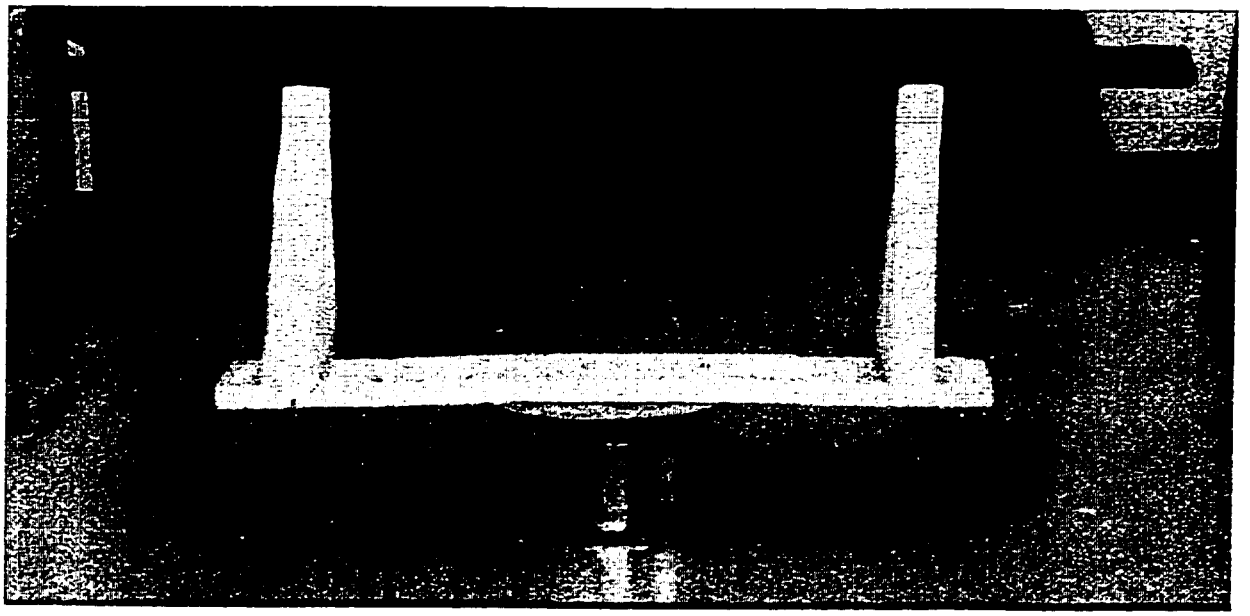

Figure 4.8: The indoor setup used to measure the backscattered RCS pattern of the tree trunk section.

In figures 4.9 and 4.10, the measured coherent and incoherent components of the backscatter RCS of the rough, conducting, cylinder are plotted as a function of the incidence angle θ, with respect to the normal to the axis of the cylinder. It is important to note that the reported coherent component does not represent the exact coherent backscatter response of the rough, conducting cylinder. This is attributed to the difficulty of rotating the cylinder around its axes without physically displacing it towards or away from the radar (at 95 GHz, a displacement of the order of 1 mm produces a substantial phase error of 120°), beside the low level of the coherent signal which is comparable to the noise level. Similarly, the measured coherent and incoherent components of the backscatter RCS of the section of the tree trunk are plotted as a function of incidence angle θ in figures 4.11 and 4.12. The coherent component of Fig. 4.11, also, does not represent the exact coherent backscatter response of the section of the tree trunk. That is attributed to the difficulty of rotating the trunk around its axis without physically displacing it towards or away from the radar, in addition to the nature of the axis (not straight) of the tree trunk section and the low level of the coherent signal which is comparable to the noise level.

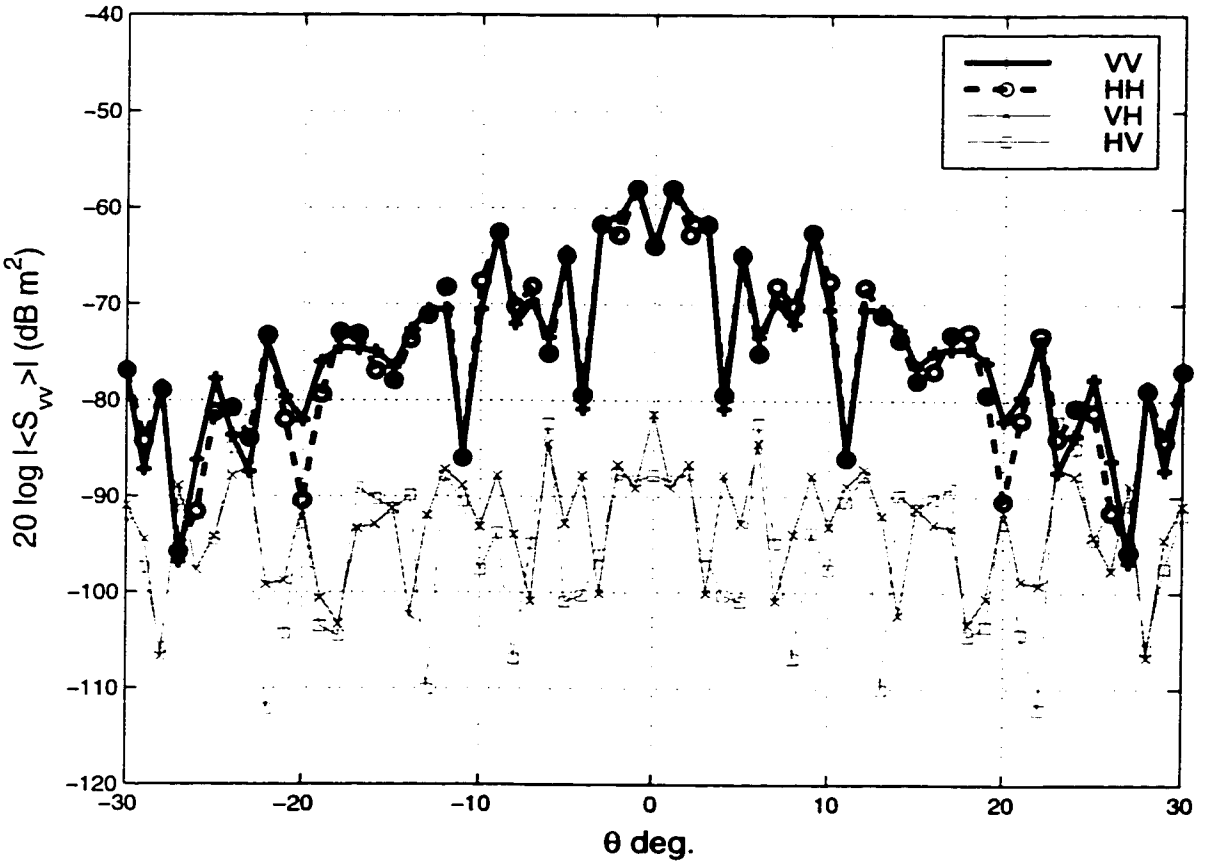

Figure 4.9: The cross and co-polarizations of the coherent backscattered RCS of the rough conducting cylinder.

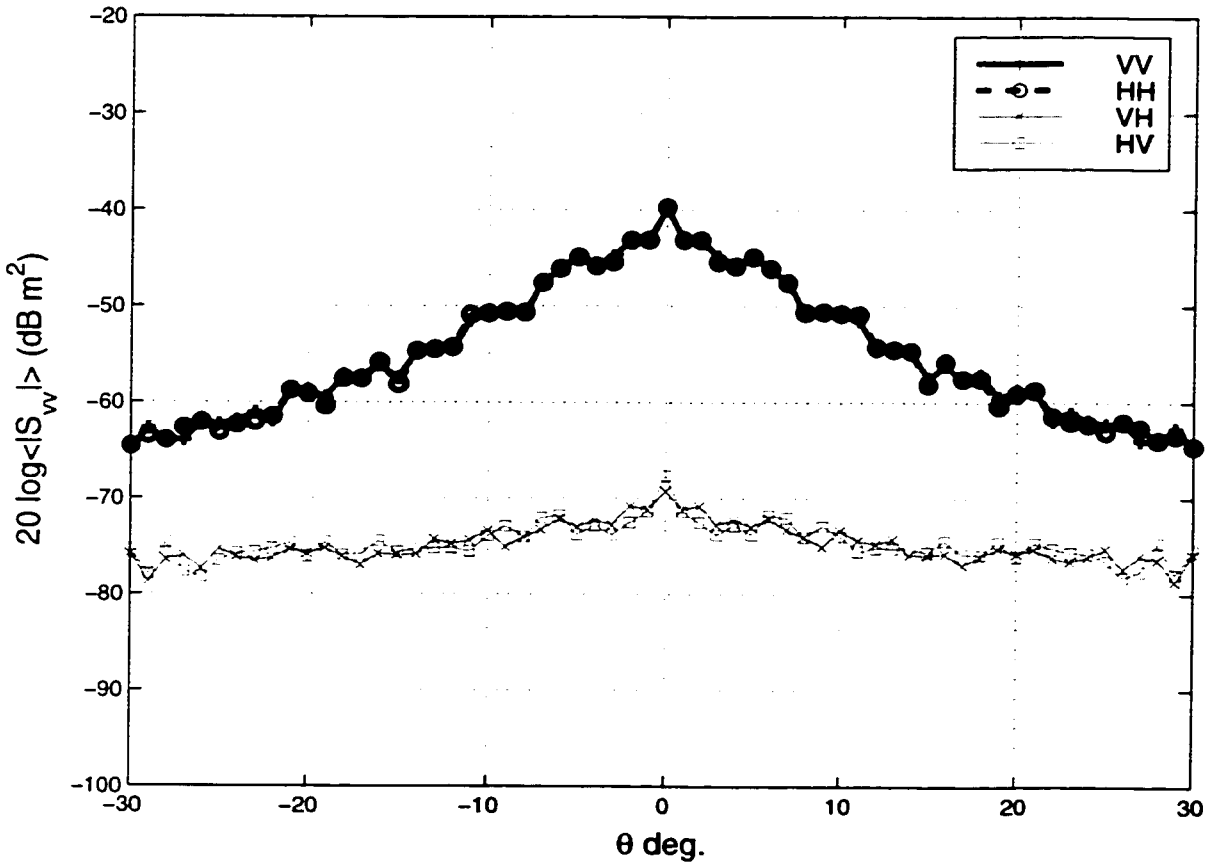

Figure 4.10: The cross and co-polarizations of the incoherent backscattered RCS of the rough conducting cylinder.

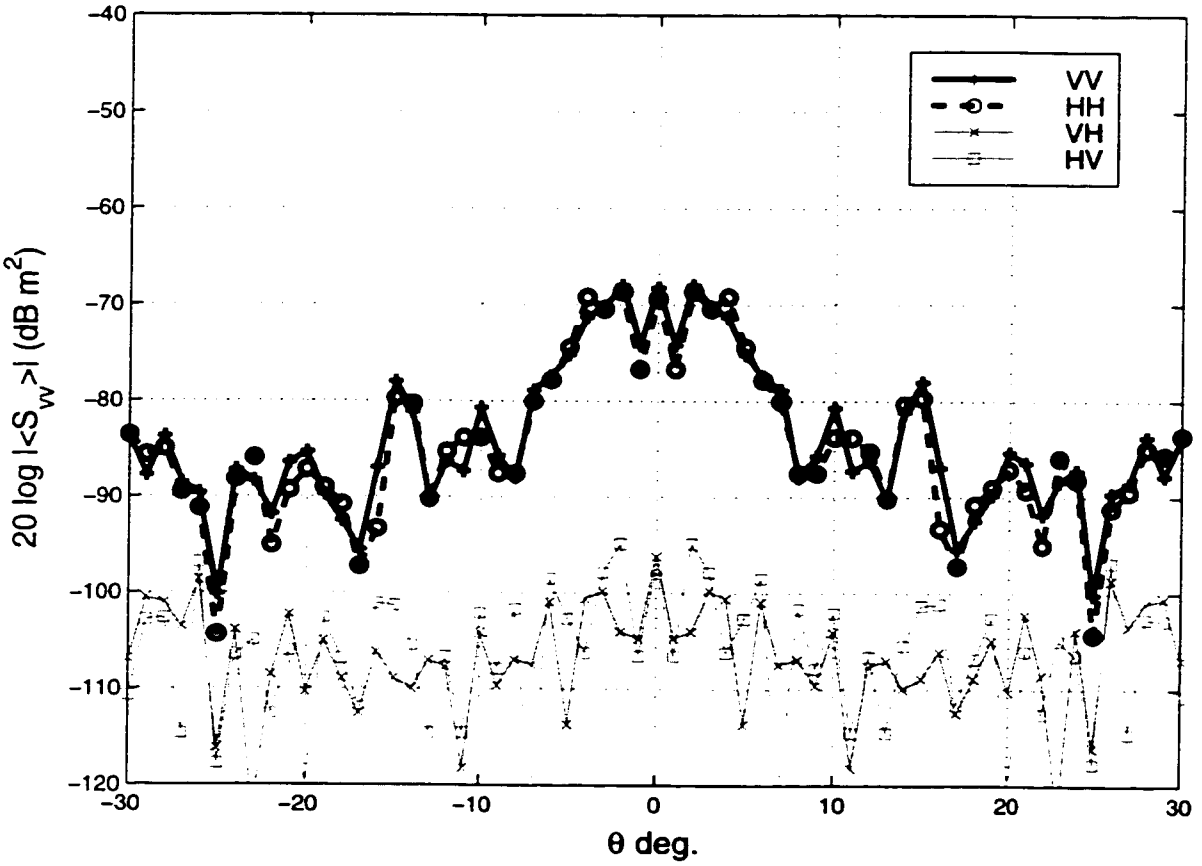

Figure 4.11: The cross and co-polarizations of the coherent backscattered RCS of the section of the tree trunk.

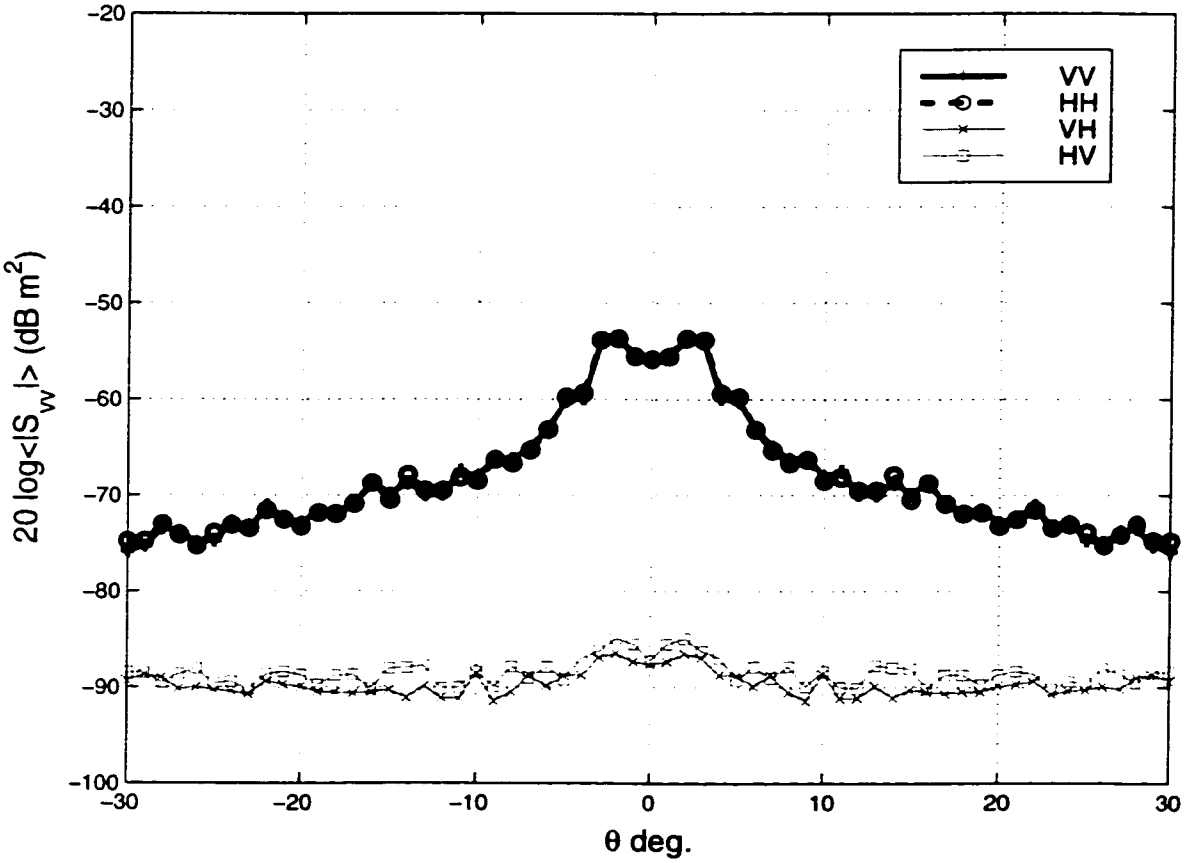

Figure 4.12: The cross and co-polarizations of the incoherent backscattered RCS of the section of the tree trunk.

4.6 Laser Profiler System

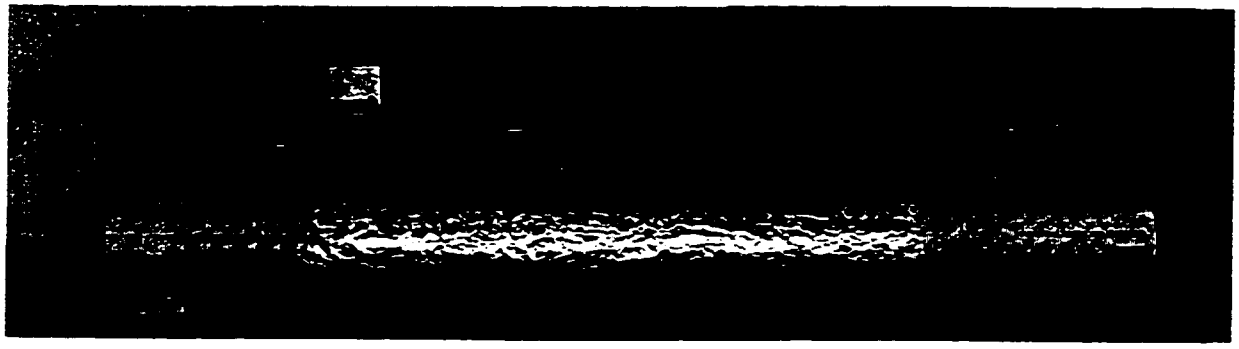

Figure 4.13: The laser profiler system.

The laser profiler system shown in Fig. 4.13 uses a computer controlled mobile (along one axis) laser head, which is capable of measuring its height above a target with the accuracy of ± 0.3 mm. The position of the laser head along the axis of motion and the timing of registering the measured height are controlled *via* a personal computer software. The horizontal (along the axis of motion) resolution of the laser profiler system is on the order of 0.5 mm. This laser profiler system was used to measure the surface height profiles of both the rough conducting cylinder and the tree trunk section along 8 different axial traces which are statistically independent to estimate the statistical roughness parameters of their surfaces. The statistically independent traces were generated by rotating the cylinder and the trunk around their longitudinal axes to 8 different positions and record the associated height profiles. Figures 4.14 and 4.15 show the 8 traces of the rough, conducting cylinder and the tree trunk section, respectively. It is noticeable that the rough conducting cylinder trace profiles include some spikes. These spikes are error values. This error is caused

by the nature of the laser head which works with non-shining surfaces and gives better results with surfaces of colors close to white. To improve the performance of the laser profiler system, these height profile measurements were performed after covering the surface with a very thin layer of flour (because it is white). The shining nature of the metallic rough surface prevents further improvement of the measurements of the metallic cylinder. However, because these spikes represents a very high frequency component of the surface roughness, they were removed by proper low-pass filtering.

The height profile traces, figures 4.14 and 4.15, were used to extract the statistical properties of the two surfaces, the rough conducting cylinder and the section of the tree trunk. The histograms of the measured height profiles of the two surfaces, shown in figures 4.16 and 4.17, were found to be close to the Gaussian pdf's with zero-mean. The standard deviations, based on averaging over the 8 profile traces, of the height profiles of the rough, conducting cylinder and the tree trunk section were found to be 1.1 and 0.914 mm, respectively. Figures 4.18 and 4.19 show the measured ensemble average of the correlation function, $< e^{iq_{x'}(f(z_1)-f(z_2))} >$, as a function of the distance $|z_1 - z_2|$ along with the continuous function that best fit it. The ensemble average of the correlation function of the rough, conducting cylinder was best fitted with $e^{(-0.055\ q_{x'}|z_1-z_2|)}$ and that of the tree trunk section was best fitted with $e^{(-0.042\ q_{x'}|z_1-z_2|)}$.

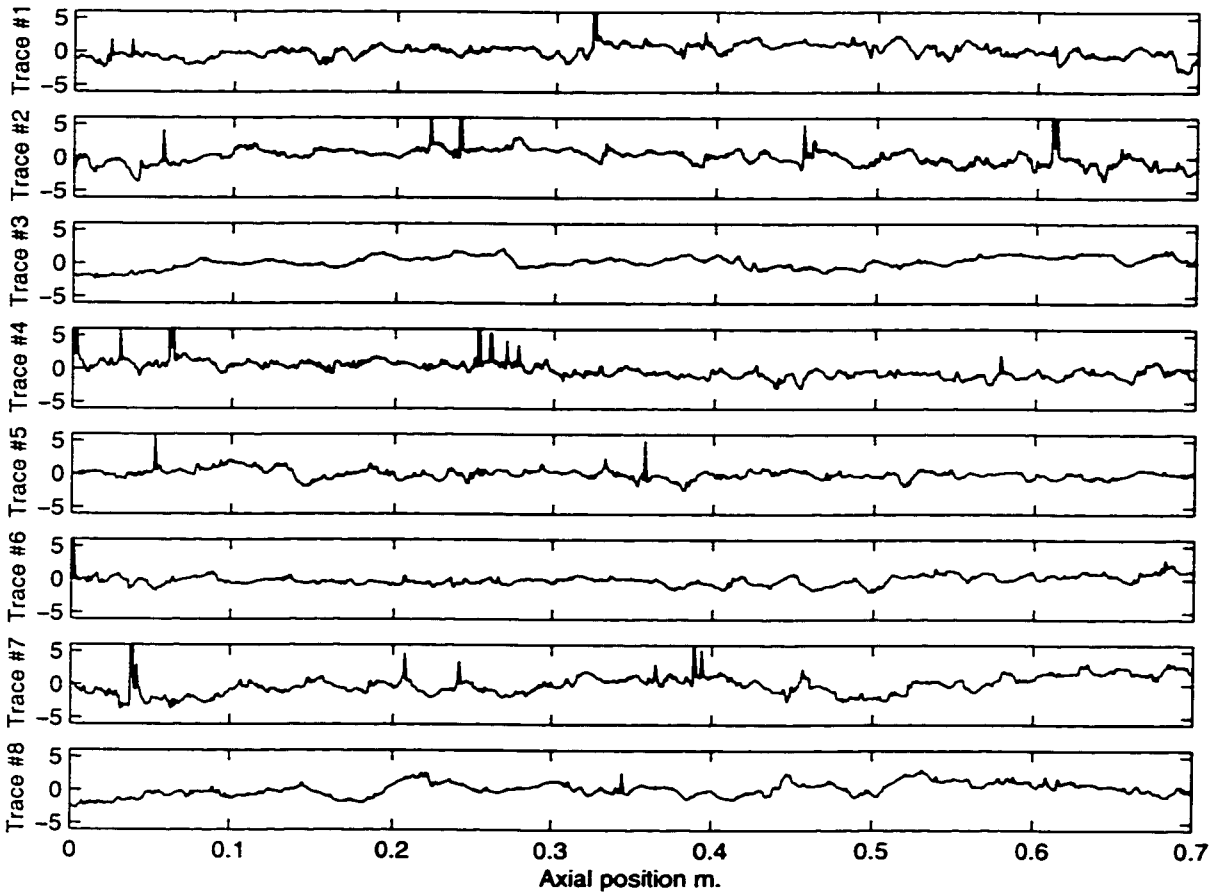

Figure 4.14: The eight statistically independent traces of the surface height profile of the rough conducting cylinder. Vertical height is in mm.

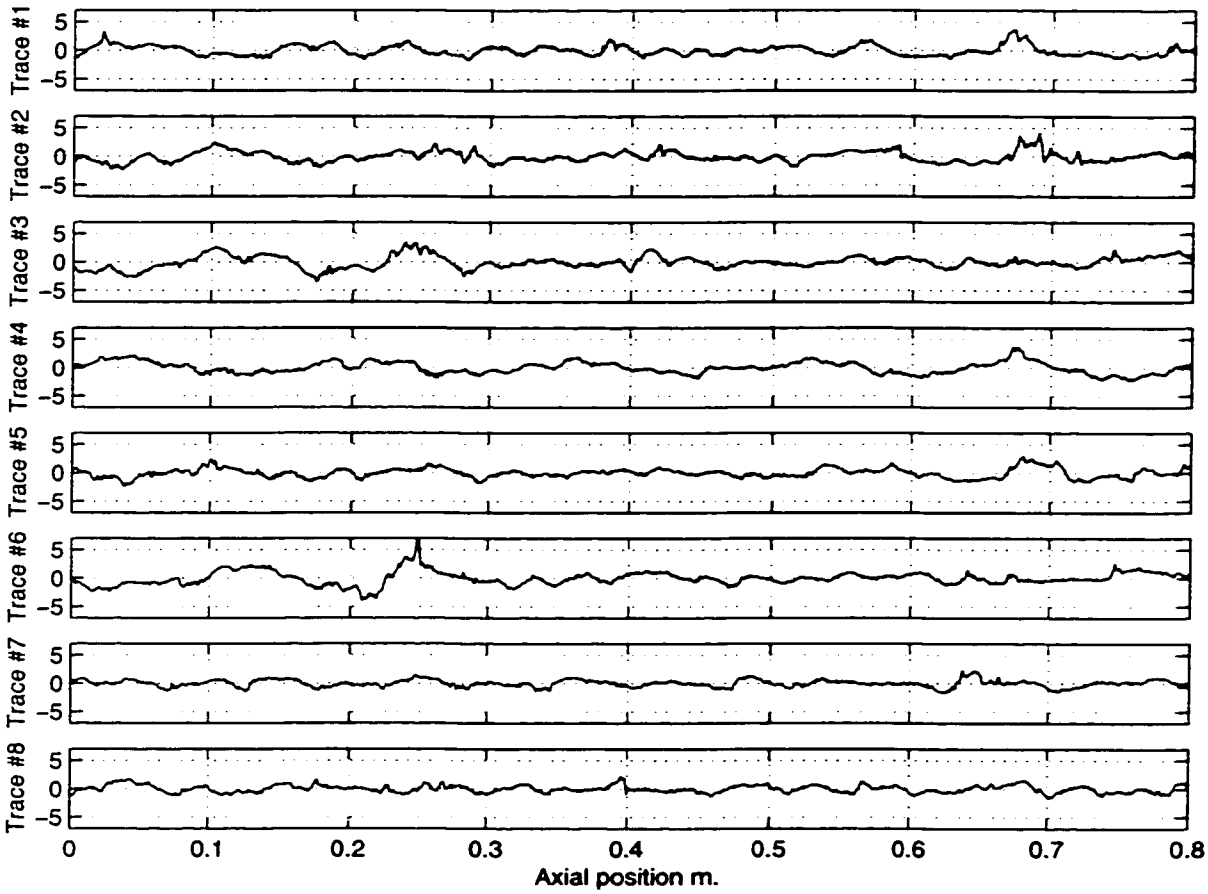

Figure 4.15: The eight statistically independent traces of the surface height profile of the section of the tree trunk section. Vertical height is in mm.

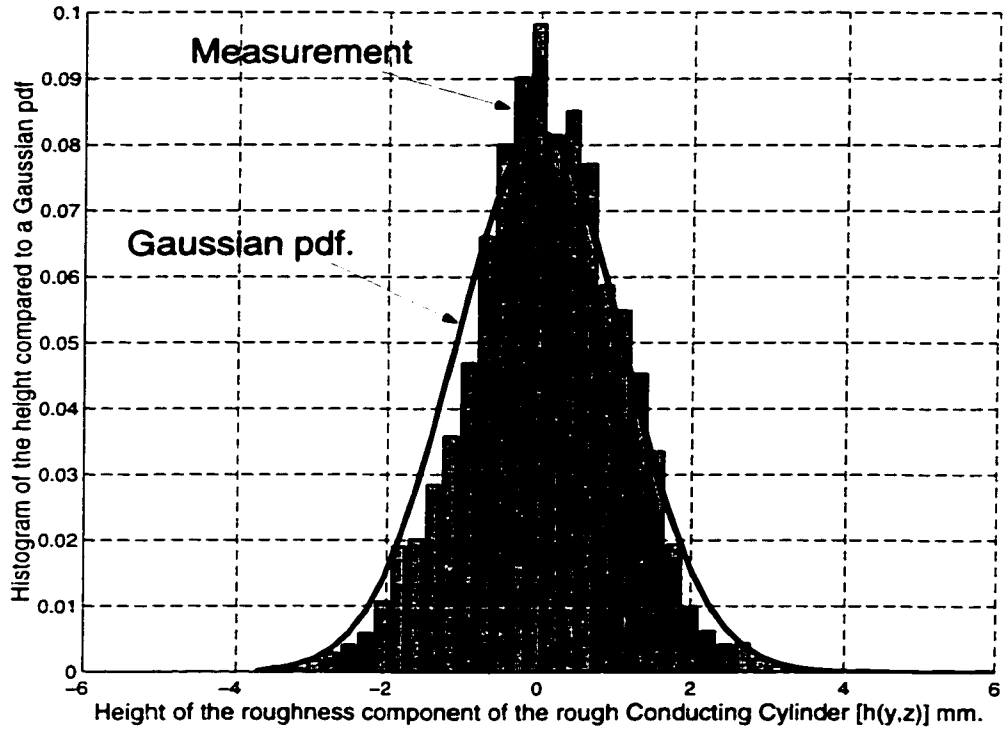

Figure 4.16: Histogram of the measured surface height profile of the rough conducting cylinder compared to a Gaussian pdf.

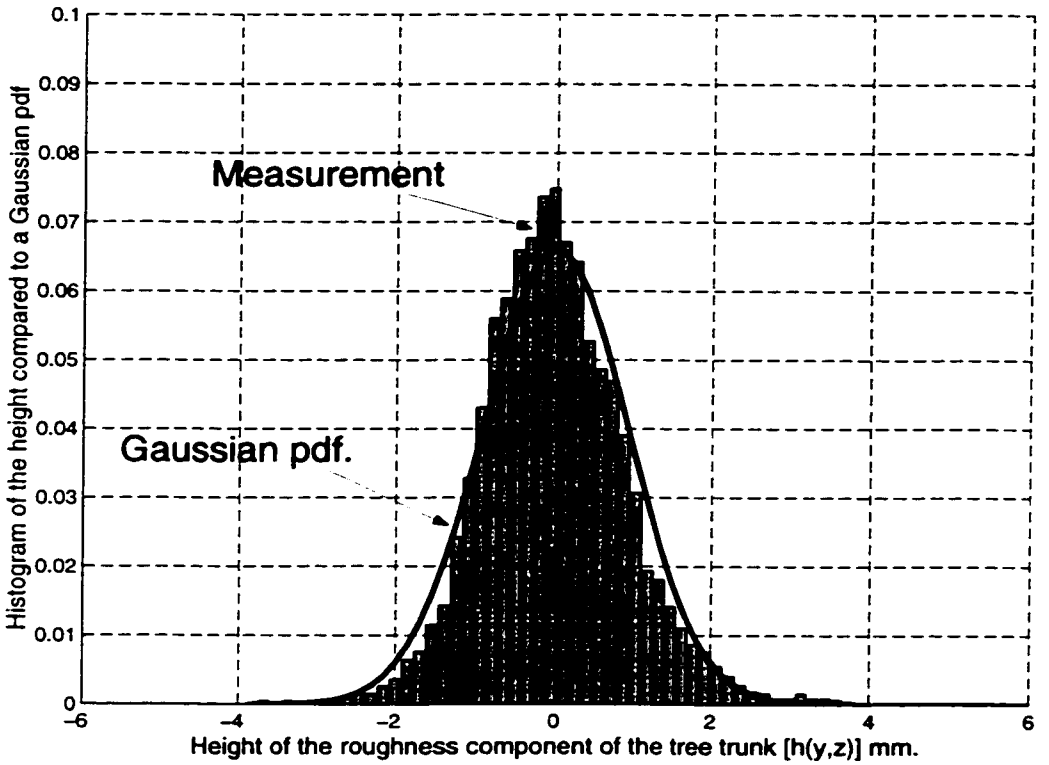

Figure 4.17: Histogram of the measured surface height profile of the tree trunk section compared to a Gaussian pdf.

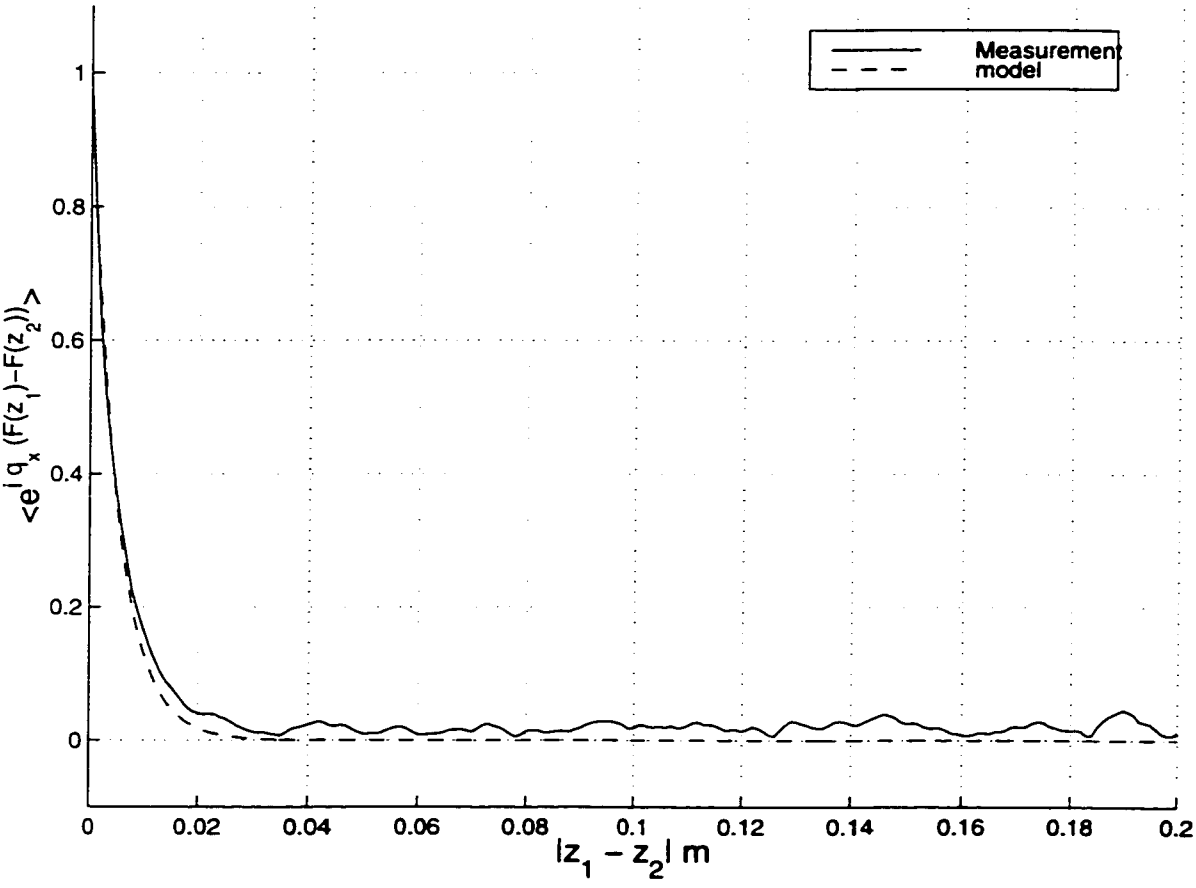

Figure 4.18: The measured ensemble average $< e^{iq_x(f(z_1)-f(z_2))} >$ for the rough conduction cylinder and the function that best fit it.

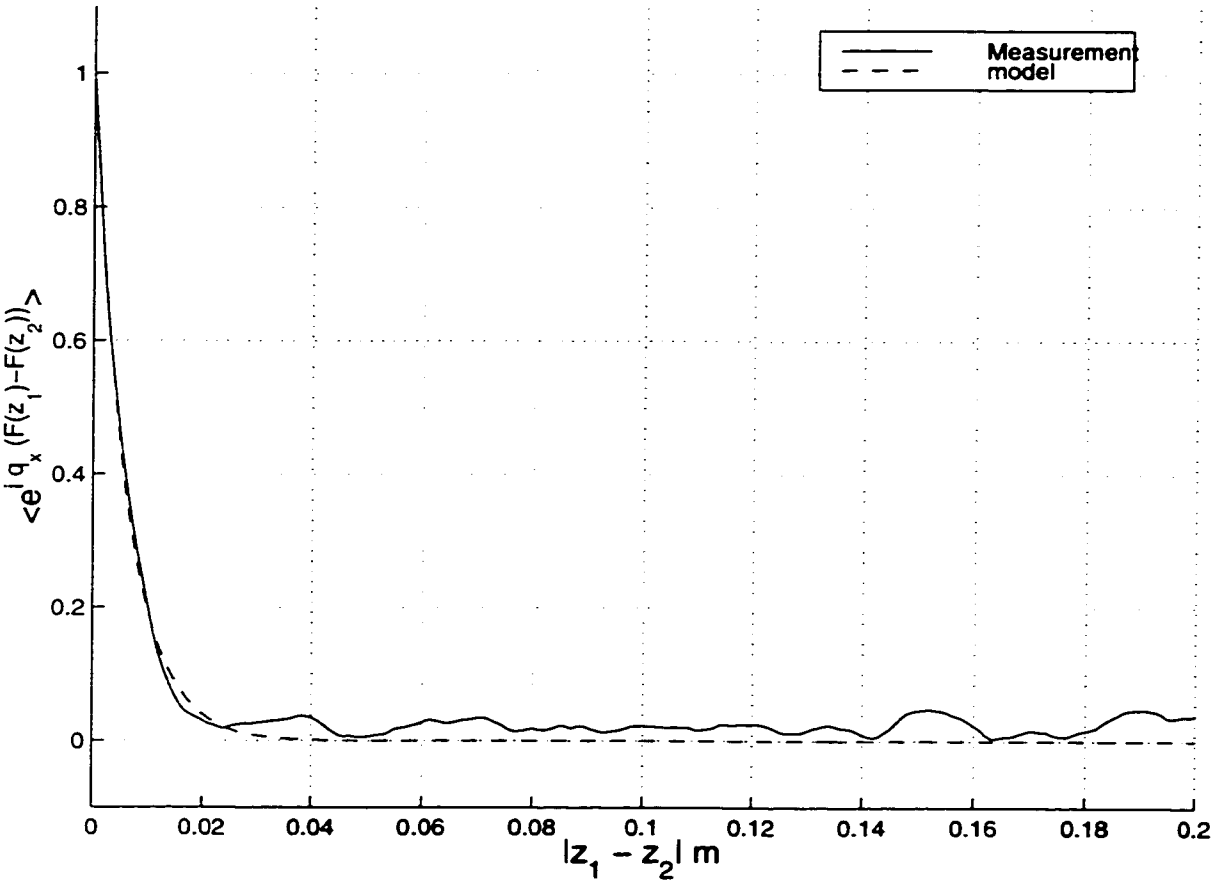

Figure 4.19: The measured ensemble average $< e^{iq_x(f(z_1)-f(z_2))} >$ for the section of the tree trunk and the function that best fit it.

4.7 Comparison Between the Theoretical Model Predictions and Measurements

Substituting the measured values of the standard deviation of the height profile of the conducting cylinder (the section of the trunk) into equation (3.21), the model predictions of the coherent component of the scattering by the rough cylinder (the section of the trunk) is obtained. Because of the high operating frequency, 95 GHz, the exponential term $e^{-\frac{\sigma^2}{2}q_{z'}^2}$ is of very small amplitude, hence, the peak amplitude of the theoretical response is close to the noise floor of the system ($\approx$ -70 dB). The small amplitude of the coherent component along with the high sensitivity of the measurement accuracy to axis displacement of the order of 1 mm, it was difficult to examine the accuracy of the coherent model, experimentally.

Substituting the measured correlated function, $< e^{iq_{z'}(f(z_1)-f(z_2))} >$, into the model of Section 3.2.3, the theoretical predictions of the incoherent backscattered responses of the rough cylinder and that of the tree trunk section are obtained. To compare the incoherent measurements to the theoretical model predictions, the effect of the radar antennas patterns must be incorporated into the theoretical model predictions. The one-dimensional radar equation approach of Section 4.4.1 can not be used for the incoherent case, as this approach adds the fields backscattered by all of the infinitesimal sections, of length dz', coherently. To apply similar concept on the incoherent case, the amplitude and phase variations of the incident field must be incorporated into the integral expression of $I(C_s)$, equation (3.16), before evaluating the incoherent

averaging, $< I(C_s)\ I^*(C_s) >$ in equation (3.22). Following this suggested procedure complicates the expression of equation (3.27) and prevents its reduction to an analytical closed form solution. Alternatives are either to evaluate equation (3.27) numerically (computationally highly demanding), or to come up with a new approach for the incoherent case.

The theoretical predictions, without accounting for the radar system effect, have very good agreement, pattern-wise, with the measurements. Hence an alternative approach is needed to correct for amplitude differences, between the model predictions and measurements, only. A descent alternative approach is to use one of the targets (the rough conducting cylinder for example) as a calibration target for the other one (the tree trunk in this case). Applying this approach results in very good agreements between measurements and theoretical predictions as shown in figures 4.20 and 4.21.

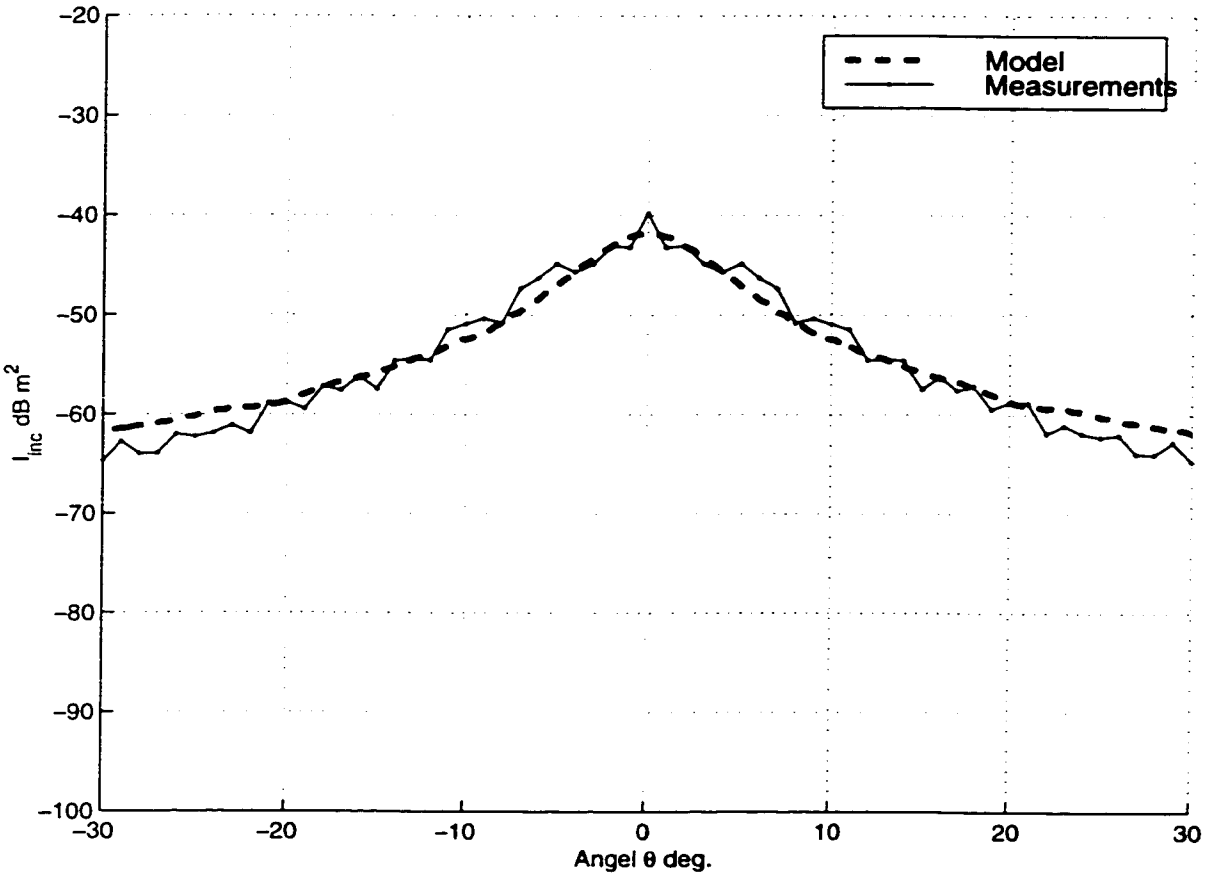

Figure 4.20: Comparison between the model predictions and measurements of the radar backscattered from the rough conducting cylinder.

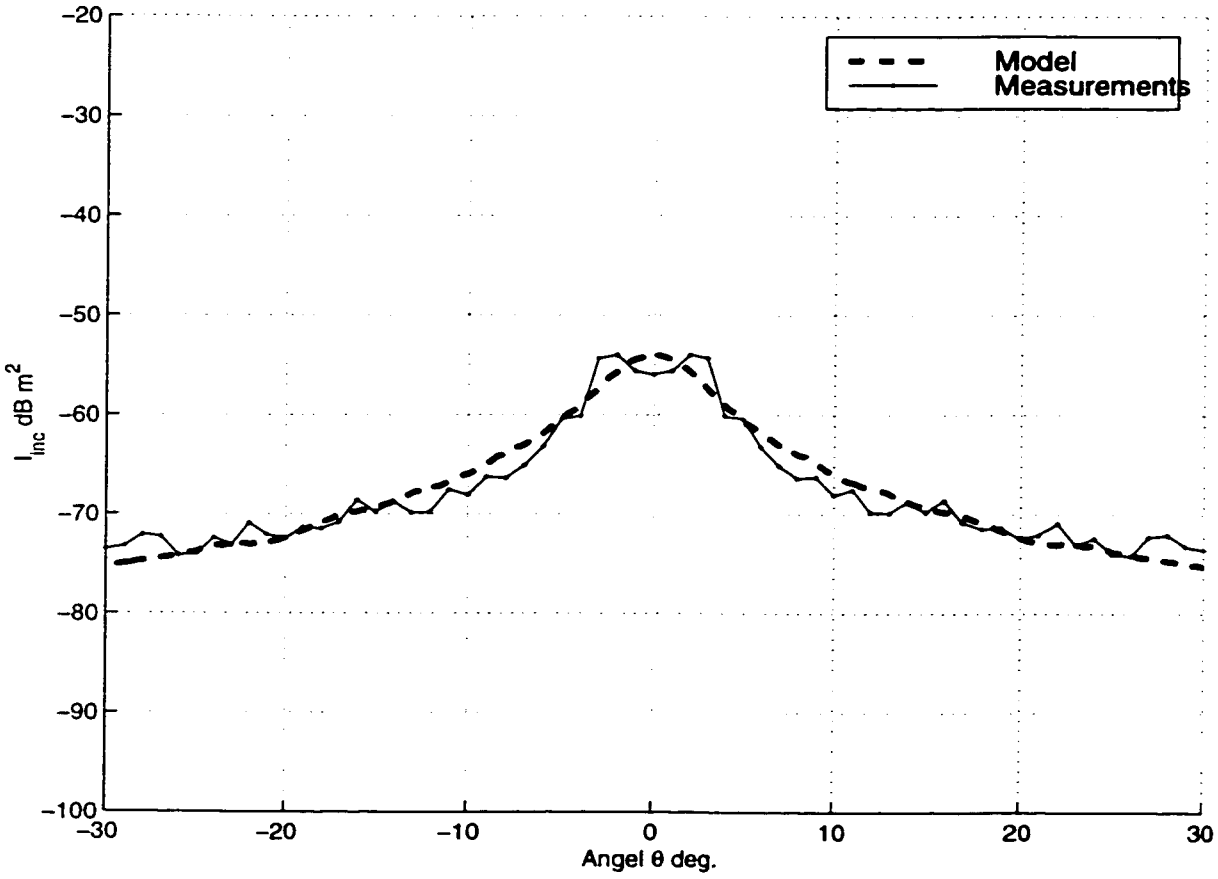

Figure 4.21: Comparison between the model predictions and measurements of the radar backscattered from the section of the tree trunk.

4.8 Conclusions

To experimentally verify the analytical models, a set of indoor measurements of the coherent and incoherent angular responses of a rough conducting cylinder and a section of a tree trunk were conducted. To examine these measurements versus the analytical models, the two main assumptions of these models were considered. These two main assumptions are: (a) the tree trunk is lossy to the level that it hides, from the radar point of view, the interior dielectric structure of the trunk, and (b) the radar is in the far field of the rough cylinder, which implies that, the models are independent of the radar system parameters. The first assumption was confirmed experimentally. Moreover, an approximate procedure were used to measure the dielectric constant of the wooden material of the tree trunk, which was found to be $2 + j0.7$ for samples with average water content of 30%. Then, to model the real measurement setup, different approaches to incorporate the radar system impulse response into the theoretical model predictions were examined and the best of them —up to our setup— was chosen and used. Also, a laser profiler system was used to measure the roughness parameters of both the rough conducting cylinder and the tree trunk section. All the measured parameters were, then, applied to the analytical model to evaluate its backscattered predictions. The evaluated incoherent model predictions were compared to the indoor measurements and very good agreements, between theory and measurements, for the two cases of the rough conducting cylinder and the tree trunk section were achieved.

CHAPTER 5

SCATTERING BY A TREE TRUNK ABOVE A GROUND PLANE

5.1 Introduction

Backscattering by a tree trunk above a ground plane is composed of four main scattering components which can be divided into three categories: (a) direct scattering by the tree trunk discussed in Chapters 3 and 4 and reported in [1, 5], (b) direct scattering by the ground plane which is the focus of other studies, such as [12], and (c) components of interaction between the tree trunk and the ground plane which is the focus of this chapter.

The interaction between the tree trunks and the ground plane includes, as mentioned in Section 3.1 and shown in Fig. 3.1, two main components. These are: (a) the wave reflected from the trunk to the ground, then back to the radar, and (b) the wave reflected from the ground to the trunk, then back to the radar. An exact model for

the backscattering by a tree trunk above a ground plane must take into consideration all of the power scattered from the illuminated area back towards the radar. Hence, an exact model for the interaction between the tree trunk and the ground plane, as illustrated in Fig. 5.1, must account for:

1. The electromagnetic wave scattered from the illuminated part of the trunk, $T1$, towards the ground area $A1$ then back to the radar, and

2. The electromagnetic wave scattered from the illuminated footprint on the ground, $A1$, towards the trunk part $T1$ then back to the radar.

Such an exact model would require a detailed ground truth information of the trunk-ground interface (grass parameters, surface roughness parameters, water-content profile and the geometry of the trunk-ground interface).

In an outdoor data acquisition campaign, described in details in Chapter 7, 50 different trunk-ground combinations were visited and their geometrics were observed. From this sample of outdoor natural configurations we found that: (a) usually there is a local hump of grass-covered surface at the trunk-ground interface, and (b) trunks, in general, have some sort of shape irregularities at the interface with the ground. In other words, we found the geometry of the trunk-ground interface too complex to be described mathematically.

The geometry description difficulty, along with the unavailability of a reliable model for the scattering by vegetation-covered surfaces at MMW frequencies (a model for bistatic scattering is needed), make it very difficult to accurately model the two

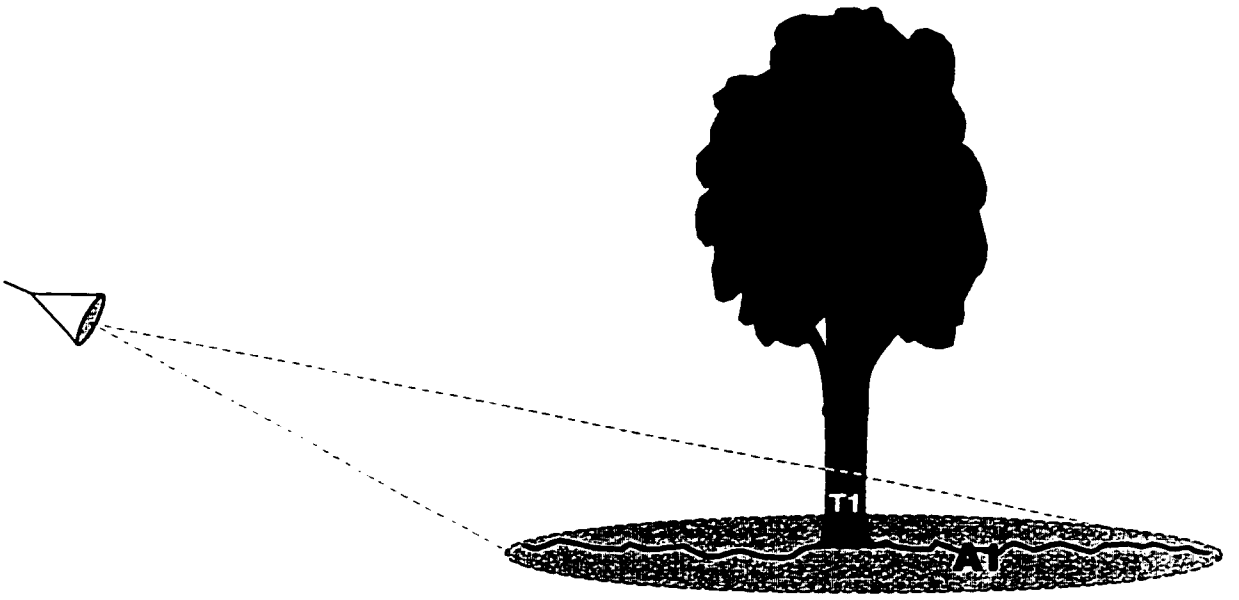

Figure 5.1: Illustration of the illuminated area of the trunk-ground scene.

components of interactions between the tree trunk and the ground plane analytically. Instead, and since a major goal of this study is to examine the possibility of occurrence of high RCS values from trunks, in what follows we will try to answer the following questions:

1. What are the possible scenarios of occurrence of high RCS values from a tree trunk above a ground plane (Section 5.2)?

2. What are the probabilities of these events (the occurrence of high RCS values based on each scenario) (Section 5.3)?

5.2 Possible Scenarios of Occurrence of High RCS Values

In this section we will try to explore bistatic scattering by tree trunk-ground configurations to study possible scenarios of occurrence of high RCS values. In other words, we will focus on the contributions of the interaction between the trunk and the ground plane as possible mechanisms that can lead to high RCS values in the backscattered direction. This analysis will be based on:

1. The analytical models, introduced in Chapter 3 (within their range of validity), for the bistatic scattering from rough, lossy, dielectric cylinders, or tree trunks.

2. The experimental measurements of the backscattering by the rough conducting cylinder and the section of the tree trunk described in Section 4.5.

Figure 5.2 shows the incoherent bistatic scattering pattern in the plane of incidence, defined by the direction of incidence and the axis of the cylinder, for three different values of the roughness parameter τ (the exponential coefficient of the characteristic function of the surface roughness). From the three plots we observe that:

1. The specular direction is indeed the direction of maximum incoherent average power.

2. The value of the maximum incoherent average power is a function of the roughness of the cylinder and it decreases with increasing roughness.

3. The difference between the level of the maximum incoherent average power and the levels at other directions decreases with the increase of roughness of the cylinder.

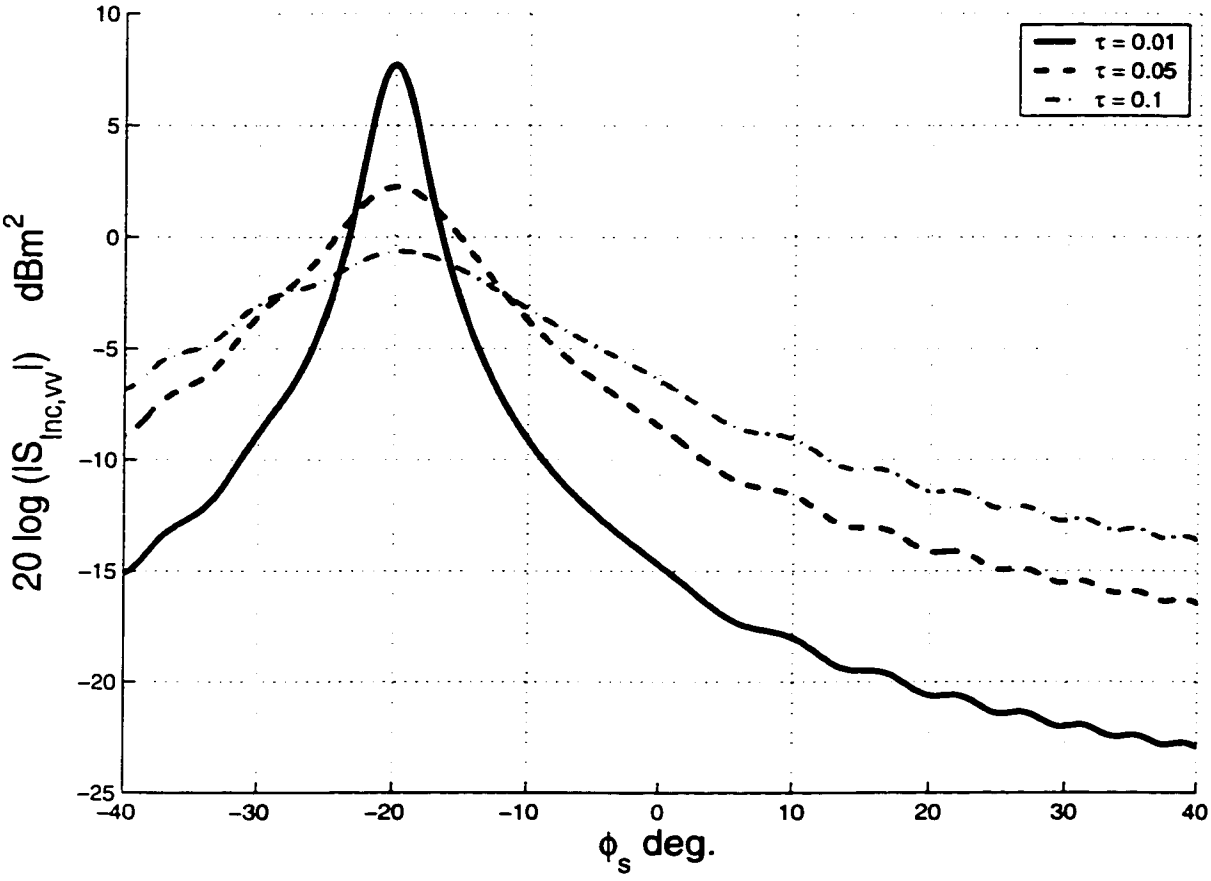

Figure 5.2: Variations of the incoherent bistatic $|S_{vv}|$ with ϕ_s for different values of the roughness parameter τ. The relevant angles are: $\theta_c = 90°$, $\phi_c = 80°$, $\theta_i = 90°$, $\phi_i = 180°$, and $\theta_s = 90°$, where θ_c and ϕ_c are the angles of the axis of the cylinder, θ_i and ϕ_i are the angles of the incident direction, and θ_s and ϕ_s are the angles of the scattering direction. All angles are with respect to the global coordinate system illustrated in Fig 3.2.

Figures 5.3 and 5.4 show the measurements of the incoherent mean and dynamic range of the backscattered $|S_{vv}|$ of the rough conducting cylinder and the section of the tree trunk, described in Section 4.5, as a function of the angle between the axis of the cylinder and the incident direction. From these two figures we observe that the dynamic ranges of the deviation of individual (statistically independent) measurements from the mean incoherent response (or from the model predictions which are in very good agreements with the measurements as shown in Section 4.7) are almost angle independent and are on the order of 20 dB.

Based on the above observations and associated conclusions, a high backscattered RCS value from a tree trunk above a ground plane is probable to occur according to one of the following scenarios:

1. The tree trunk is tilted such that the backscatter direction is along the specular direction. In other words, the tree trunk is tilted such that the incident direction is perpendicular to the axis of the tree trunk. This scenario implies a small tilt angle of the tree trunk at near grazing angles.

2. The high RCS value results from bistatic scattering by the trunk specularly towards the ground plane, then followed by specular reflection back to the radar. This scenario can occur at a wider range of incidence angles as opposed to the first scenario which is more probable to occur at near grazing incidence.

In the above scenarios we focused on the occurrence of high RCS values only in the specular direction (either in bistatic or backscattering configuration). This focus is based on the observations that the peak of the incoherent mean is in the specular direction and the dynamic range of the deviation of individual (statistically independent) measurements from the incoherent mean is almost angle independent. Therefore, if either of these two scenarios resulted in high RCS value, most probably this will be in the specular direction. However, our calculations of the probability of occurrence of high RCS values, presented in the next section, account for the occurrence of high RCS value in any direction.

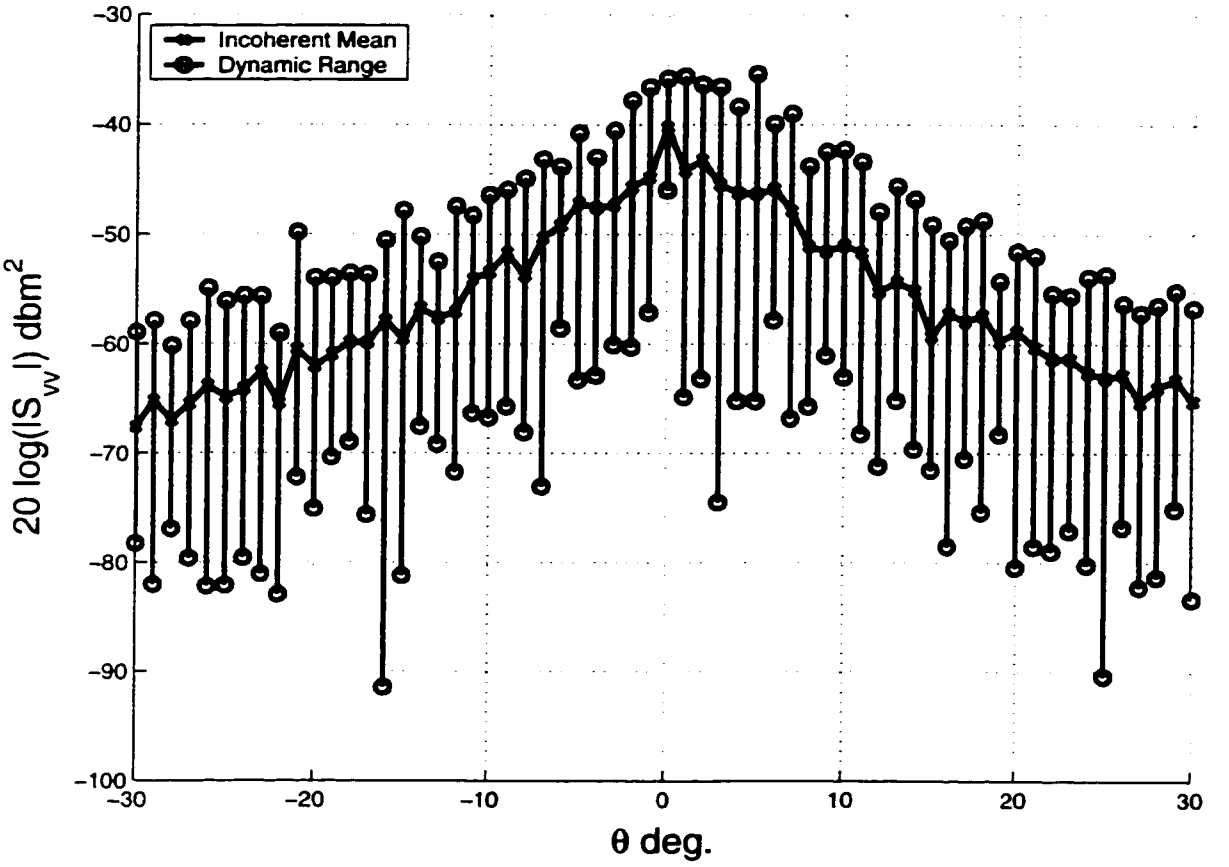

Figure 5.3: The incoherent mean response and dynamic ranges of the backscattered $|S_{vv}|$ of the rough conducting cylinder as functions of the angle between the axis of the cylinder and the incidence direction.

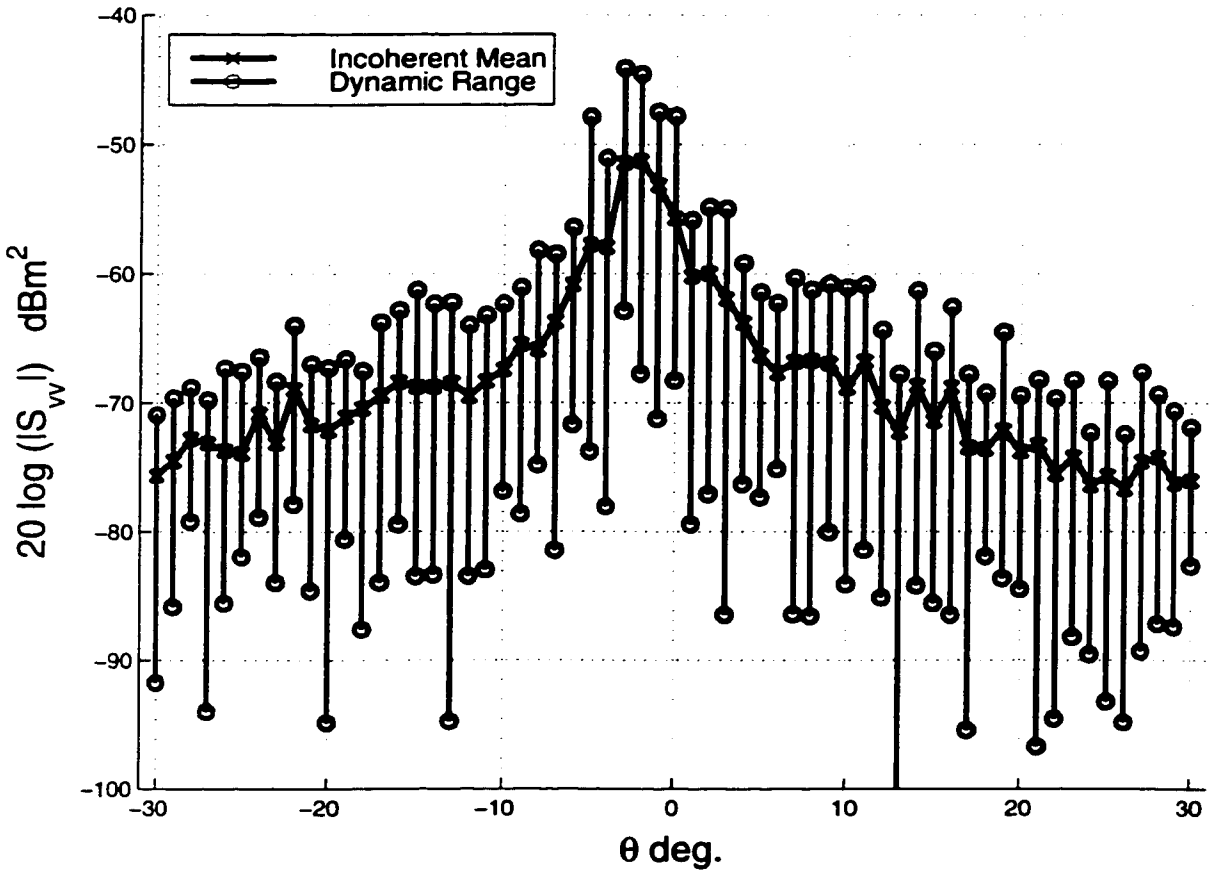

Figure 5.4: The incoherent mean response and dynamic ranges of the backscattered $|S_{vv}|$ of the tree trunk section as functions of the angle between the axis of the trunk and the incidence direction.

5.3 Probability of Occurrence of High RCS Values

Radar cross section is a quantity that is dependent on measurement configuration (radar antenna pattern, distance of the target from the radar, etc.). To define the term high RCS value we must choose the definition to be independent of the measurement configuration. Towards that, we shall use the scattering coefficient, which is a measurement-configurations independent quantity, as a reference and define high RCS value to be that corresponds to 0 dB scattering coefficient.

$$\text{Scattering Coefficient, } \sigma^{\circ} = \frac{RCS}{IA}, \tag{5.1}$$

where, IA is the illumination integral in m^2. Hence, high RCS value is that is greater that or equals to $(\sigma^{\circ} \cdot IA)$ dBm^2.

In the indoor measurements of Chapter 4 the cylinder and trunk were measured at 7 meters away from the radar system which has a beamwidth of 1.4°. This configuration results in an illumination integral $\approx$ .01 m^2 = -20 dBm^2. Therefore, the RCS value of the scattering by a trunk is considered to be high —under our indoor configuration— if its value is greater than or equal to -20 dBm^2. Also we will denote the incident angle as θ_i.

Examining the two possible scenarios of occurrence of high RCS values we observe that:

- According to the first scenario, a high RCS occurs if the backscatter signal is higher than or equal to -20 dBm^2.

- According to the second scenario, a high RCS occurs if the scattered signal is higher than or equals to $(-20 - \Gamma_g)$ dBm^2 where Γ_g is the power reflection coefficient of the ground plane at the angle θ_i. For simplicity, we will assume the reflection coefficient of the ground at θ_i to be 0.1 i.e. -10 dB. Hence, the second scenario results in a high RCS value if the scattered signal from the trunk is higher than or equal to -10 dBm^2.

To evaluate the probability of occurrence of high RCS value based on each scenario we need to know the incoherent mean value of the scattering by the trunk/cylinder and the pdf of the deviation of individual RCS values from it. To consider the probability of occurrence of high RCS value in any direction, not only the specular direction, we must calculate the probability of occurrence of RCS deviation from the incoherent mean with values greater than or equal to δ_o, where δ_o is the difference between the high RCS level (-20 dBm^2 for the first scenario or -10 dBm^2 for the second scenario) and the peak of the incoherent mean. Since the peak value of the incoherent mean is used in this calculation along with the cumulative density function of the RCS deviation from the incoherent mean, occurrence of high RCS value in any direction other than the specular on is implicitly included.

Therefore, the probability of occurrence of scattering from the trunk with RCS value greater than or equals to P_o (P_o equals -20 dBm^2 for the first scenario and equals -10 dBm^2 for the second scenario) depends on the pdf of the deviation of individual RCS values from the incoherent mean, and the magnitude of the peak (which is in

the specular direction) of the scattering by the trunk/cylinder. This peak depends on the roughness of the bark layer, the diameter of the trunk, and the dielectric constant of the bark layer. The RCS of the trunk (or rough cylinder) is a nonlinear function of the roughness parameters of the surface which, in turn, is a random variable. Due to this nonlinearity it is not possible to evaluate, analytically, the relationship between surface roughness and the pdf of the individual RCS deviation from the incoherent mean. A possible approach is to characterize this relation based on measurements. Hence, in what follows we will evaluate the pdf of the individual RCS deviation from the incoherent mean based on the available measurements, described in Section 4.5. Then we will use it to calculate the probability of occurrence of high RCS value based on each scenario.

A remark to mention here is that, since the scattering by smooth cylinders is deterministic and by rough cylinders is stochastic, the pdf of the deviation of individual RCS value from the incoherent mean is also a function of the roughness of the bark layer. Therefore, the results of this study will be limited to the cases of surface roughnesses at hand, however the approach is general.

To characterize the pdf of the individual RCS deviation from the incoherent mean we aggregate individual deviations of all the measurements at each angle into a single vector. This step resulted in a vector of 20×61 elements (the number of statistically independent samples at each angle $\times$ the number of angles). Then, we look for a pdf to fit the histogram of this vector. Doing this we implicitly ignore the dependence of

the pdf on angle as the measurements were performed over a relatively small range of angles, -30^{o} to 30^{o}. The results of this procedure are shown in figures 5.5 and 5.6 where the pdfs of the individual RCS deviation from the incoherent mean were fitted to a Gaussian pdf. For the case of the rough conducting cylinder this pdf can be expressed as:

$$pdf(\Delta S_{vv}) = \frac{1}{\sqrt{2\pi\sigma^2}}\, e^{-\frac{1}{2}\left(\frac{\Delta S_{vv}-\mu}{\sigma}\right)^2}, \qquad (5.2)$$

$$\mu = -1.48 \text{ dB}, \quad \sigma = 5.52 \text{ dB}$$

and for the case of tree trunk it can be expressed as:

$$pdf(\Delta S_{vv}) = \frac{1}{\sqrt{2\pi\sigma^2}}\, e^{-\frac{1}{2}\left(\frac{\Delta S_{vv}-\mu}{\sigma}\right)^2}, \qquad (5.3)$$

$$\mu = -1.51 \text{ dB}, \quad \sigma = 5.55 \text{ dB}$$

where

$$\Delta S_{vv} = 20\ log(S_{vv}) - 20\ log(mean(S_{vv})) \quad \text{dB} \qquad (5.4)$$

and is calculated at each angle, then aggregated in a single vector as described above.

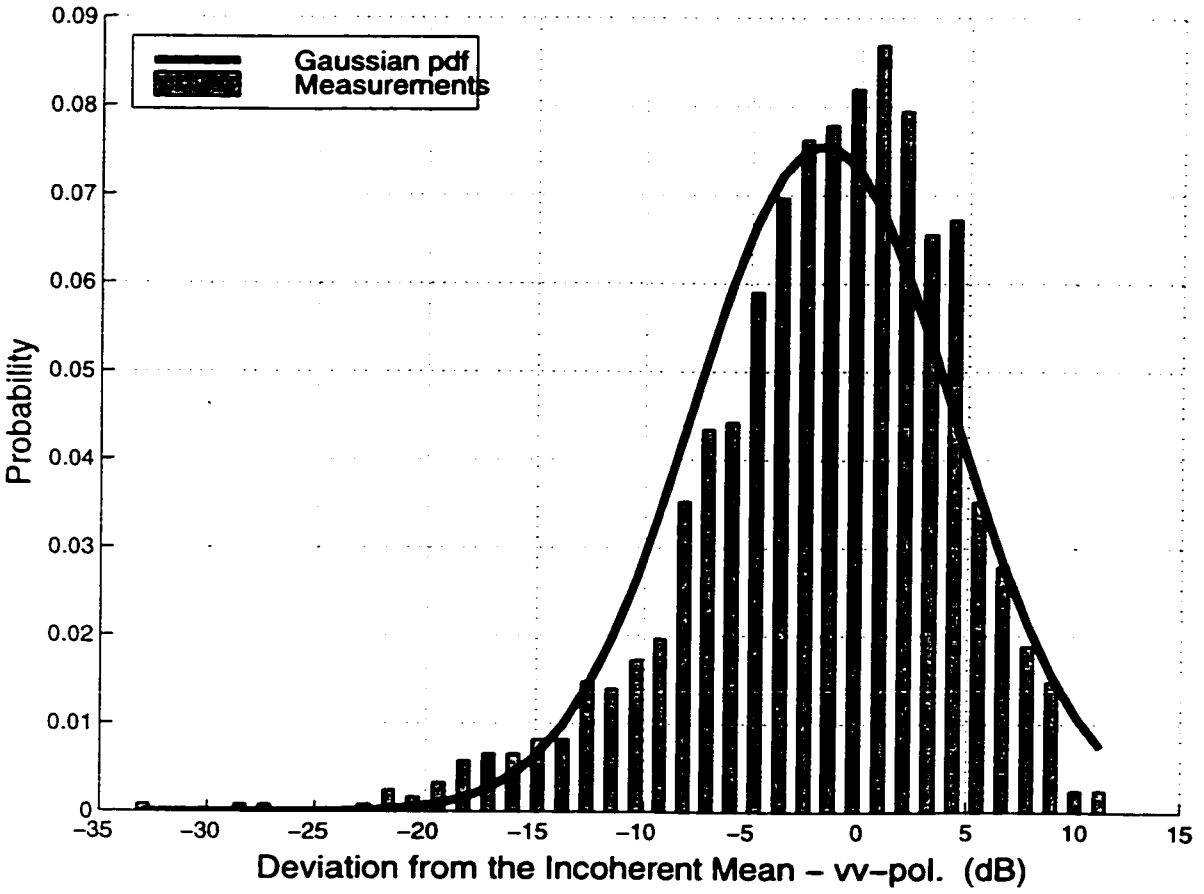

Figure 5.5: Histogram of the individual RCS deviation from the incoherent mean fitted to a Gaussian pdf (the case of the rough conducting cylinder).

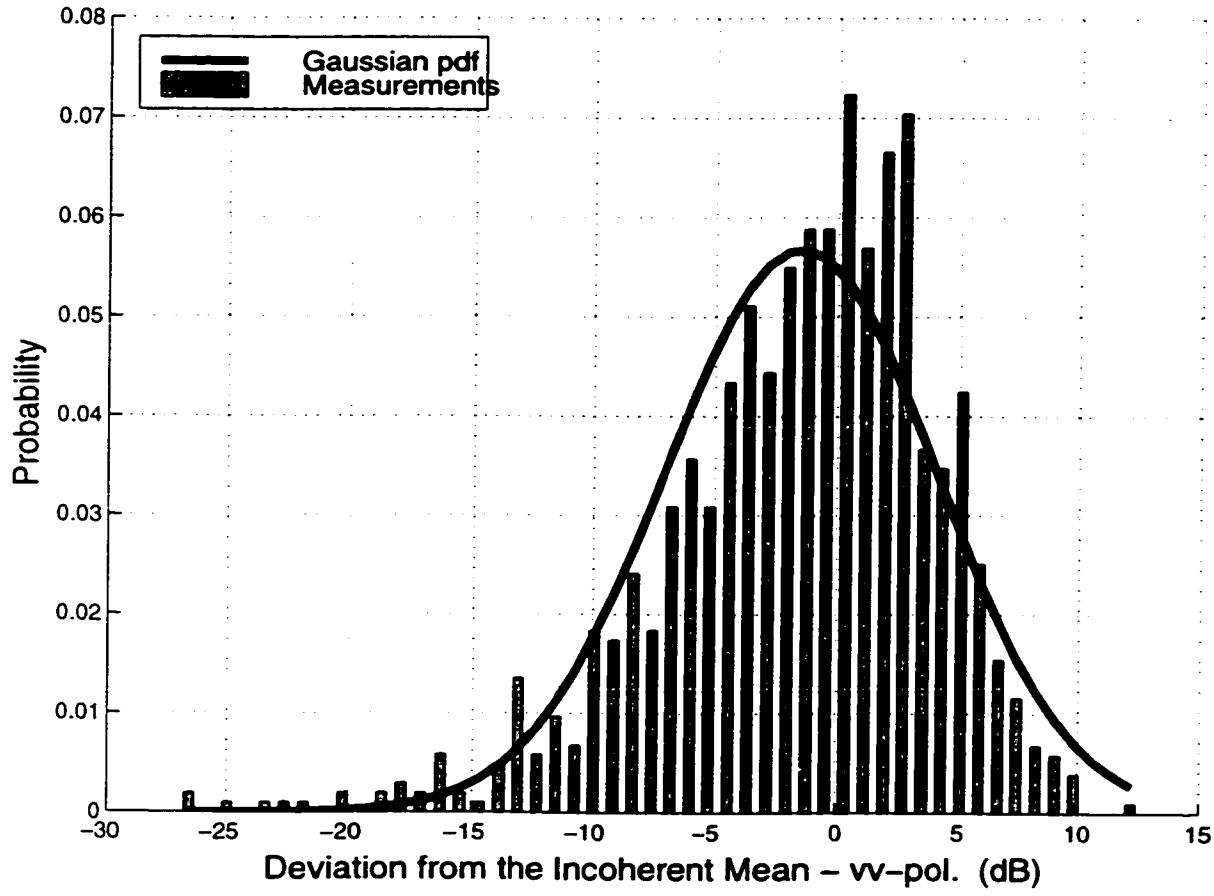

Figure 5.6: Histogram of the individual RCS deviation from the incoherent mean fitted to a Gaussian pdf (the case of the tree trunk section).

Since the histograms of the individual RCS deviation from the incoherent mean were fitted to Gaussian pdf's with the means and standard deviations calculated from the measurements, the probability of the ΔS_{vv} to be greater than or equals to δ_o is calculated as follows:

$$P(\Delta S_{vv} \geq \delta_o) = \int_{\delta_o}^{\infty} \frac{1}{\sqrt{2\pi\sigma^2}} e - \frac{1}{2}(\frac{\Delta S_{vv} - \mu}{\sigma})^2 d(\Delta S_{vv})$$

$$= 0.5 - erf(\frac{\delta_o - \mu}{\sigma}) \quad (\delta_o \geq \mu) \tag{5.5}$$

where $erf(x)$ is the error function of x. To examine the values of the probability of occurrence of each scenario, we used the model developed in Chapter 3 to evaluate the peak of the incoherent mean for cylinders (trunks) that have roughness function similar to the measured one but with different diameters (for details on the roughness parameters of the conducting cylinder and tree trunk, refer to Section 4.5). Figures 5.7 and 5.8 show the angular responses of the incoherent mean RCS for the rough conducting cylinders and for the tree trunks, respectively, for three different values of the diameter. Since for all the cases of conducting cylinder (tree trunk) we used the same roughness parameters as the measured case, we can use the pdf of equation (5.2) (equation (5.3)) to calculate the probabilities of occurrence of high RCS based on each scenario. Doing this we obtained the following results:

Cylinder's		Probability of High RCS	Probability of High RCS
Type	Diameter	Based on First Scenario	Based on Second Scenario
Rough	10.8 cm	9.65×10^{-6}	5.61×10^{-10}
Conducting	40.0 cm	9.9×10^{-4}	4.57×10^{-7}
Cylinder	80.0 cm	5.41×10^{-3}	6.39×10^{-6}
Tree	9.0 cm	5.42×10^{-11}	5.55×10^{-17}
Trunk	40.0 cm	6.72×10^{-8}	6.66×10^{-13}
	80.0 cm	1.13×10^{-6}	2.96×10^{-11}

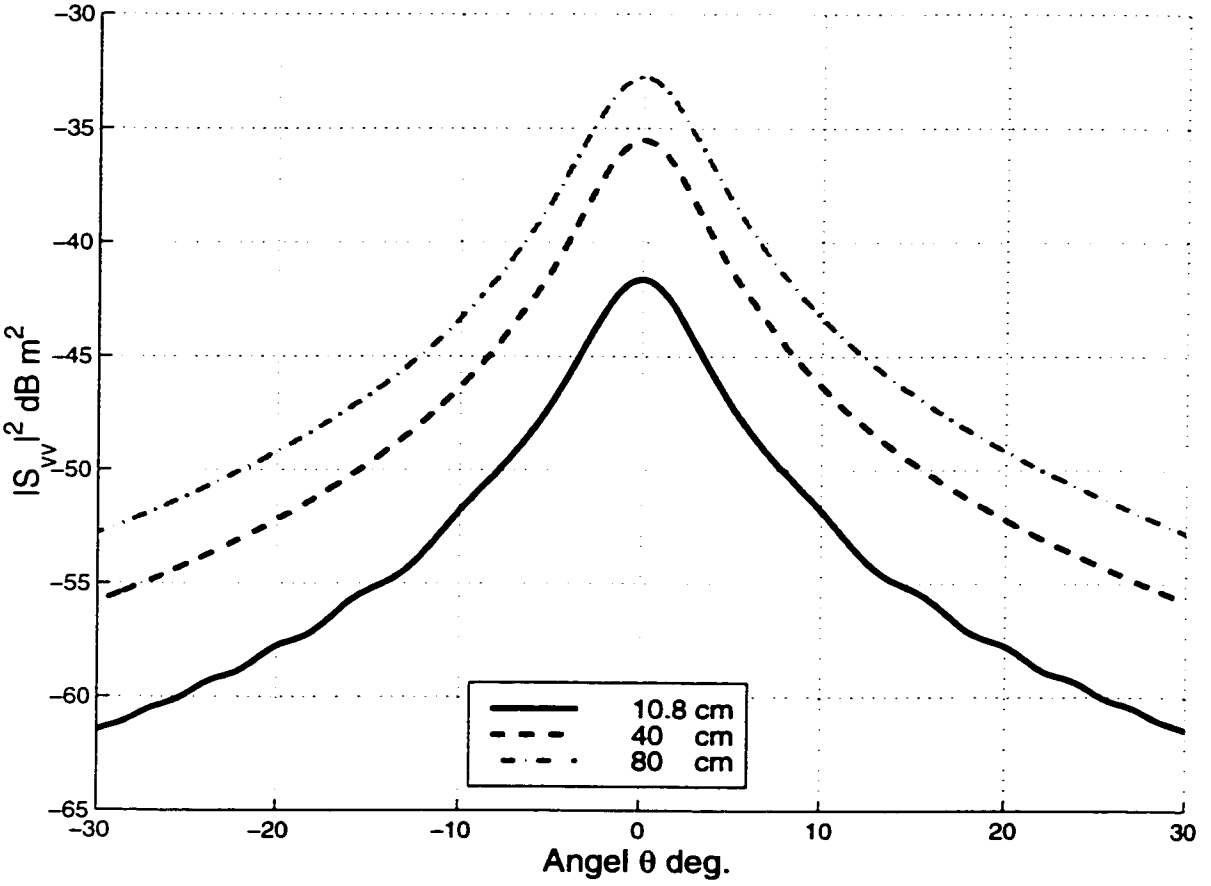

Figure 5.7: Dependence of the incoherent mean angular response on the diameter of the rough conducting cylinder. The angular response is shown for three different values of the cylinder diameter.

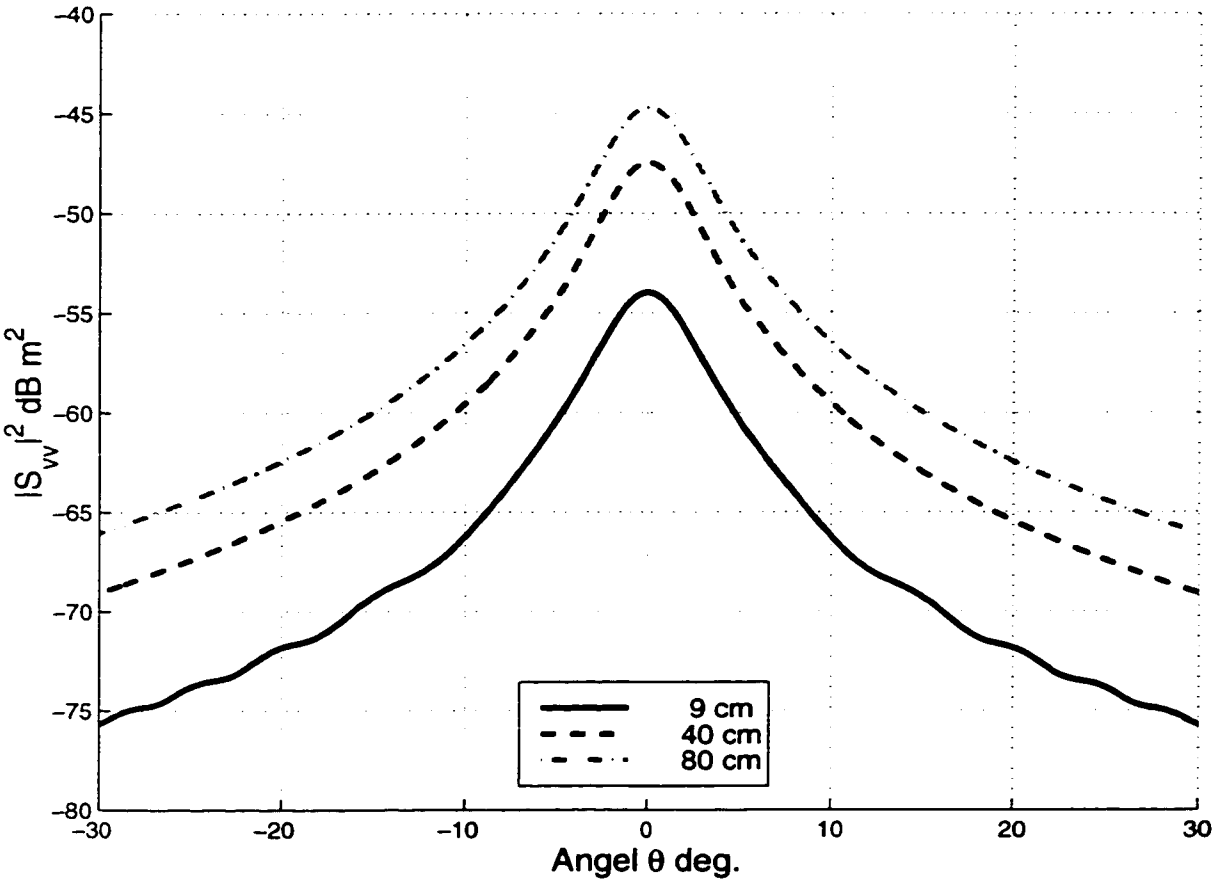

Figure 5.8: Dependence of the incoherent mean angular response on the diameter of the tree trunk. The angular response is shown for three different values of the trunk diameter.

5.4 Conclusions

Bistatic scattering from a tree trunk above a ground plane was studied with focus on the possible scenarios of occurrence of high RCS value from the trunk-ground combination. Two possible scenarios were identified and studied. One of them is due to the tilt angle of the trunk that makes it perpendicular to the incident direction, and the other one is due to the trunk bistatic component which bounce back to the radar after being scattered from the ground plane. The probability of occurrence of high RCS values from both scenarios depends on the pdf of the deviation of individual RCS values from the incoherent mean. The measurements of Section 4.5 that measured the scattering by a rough conducting cylinder and by a tree trunk were used to characterize this pdf. The incoherent model for scattering by a tree trunk, introduced in Chapter 3, was used to evaluate the incoherent angular response of the scattering from a tree trunk (rough cylinder) of different diameters but with the same roughness parameters as the measured one. The model prediction along with the pdf of the deviation of individual RCS from incoherent mean were used to evaluate the probabilities of occurrence of high RCS value based on both scenarios. The results showed that the first scenario is much more probable to occur and the probability of occurrence (in both cases) increases with the increase of the trunk (cylinder) diameter. This increase is expected to reach saturation when the size of the trunk (cylinder) fills the radar beam in the direction perpendicular to the axis of the cylinder. Even though, the shown results are limited to the measured cases, the methodology is general and can be applied to other cases.

CHAPTER 6

ANALYTICAL STUDY OF THE FCF FROM THE DETECTION POINT OF VIEW

6.1 Introduction

For a number of remote sensing applications, the ability to detect man-made targets in the presence of clutter is a desired feature. Examples of these applications are: automotive collision-avoidance systems and military target detection radars. The scattering problem of man-made targets in the presence of clutter is a very complex problem that involves a large number of parameters. The parameters involved in the scattering problem are the system parameters (incidence angle, system bandwidth, foot print, etc.), parameters associated with the man-made target (strength of the backscattering from the man-made target, frequency response, etc.), and clutter parameters (homogeneity of the clutter, physical parameters, water content, etc.). The high degree of complexity of the scattering problem along with the large number of parameters involved in it make the detection problem very convoluted. Many

approaches had been introduced in the past and applied to enhance the detection capabilities of remote sensing systems. Those approaches can be divided into two main categories:

I- Performing more radar measurements

An example of this approach involves the introduction of polarimetric measurements instead of power-only measurements. Another example involves the data fusion of multiple sensors output [51].

II- Exploiting more features from the available radar measurements

Examples of this approach are the E-pulse technique [11, 10], the use of information from both time and frequency domains, combined together, to make a detection decision [38], and the polarimetric feature analysis applied to automatic target recognetion [41].

In this study we will examine the application of the complex frequency correlation function (FCF), introduced in [34], in detection. That is we will adopt the second approach which depends on introducing new detection features as shown in [2, 3].

In this chapter, the definition of the FCF and its physical meaning will be introduced in Section 6.2. Then, in Section 6.3 we will investigate the characteristics of the FCF of the signal scattered from a single scatterer, two scatterers, and the general case of scattering by N scatterers. This will be done by positioning the one, two or N scatterers arbitrarily within a radar-illuminated cell, then examining their FCF analytically. Finally, in Section 6.4 a physical interpretation of the FCF and

its relationship to the time-domain signal will be introduced and used to gain more physical insight the characteristics of the FCF.

6.2 Definition of the FCF

The FCF (**F**requency **C**orrelation **F**unction) is the function generated by convolving the frequency response of a target, $X(f)$, with a conjugated, shifted version of the same response, $X^*(f+\gamma)$. Mathematically it is expressed as:

$$FCF_X(\gamma) = \int_{-\infty}^{\infty} X(f)\ X^*(f+\gamma)\ df \tag{6.1}$$

However, for many practical systems the bandwidth is limited and the frequency response is measured at discrete frequency steps, as opposed to a continuous frequency response. Hence, the discrete form representation of the FCF is:

$$FCF_X(m\ \Delta f) = \sum_{i=1}^{i=N_f-m} X(i\ \Delta f)\ X^*((i+m)\ \Delta f)\ \ \Delta f, \tag{6.2}$$

where, Δf is the frequency sampling resolution, $m\ \Delta f$ is the frequency shift, and $N_f\ \Delta f$ is the total system bandwidth. It is obvious that for $m = 0$, because of the phase conjugation, FCF takes its maximum value, then, it decreases in amplitude, due to frequency decorrelation, with the increase of the frequency shift (or equivalently, with the increase of m in the discrete form).

More physical insight in the characteristics of the FCF can be obtained from its time-domain expression, which is the Fourier transformation of its frequency-domain

expression (equation (6.1)) as follows:

$$\begin{aligned} FCF_X(t) &= \int_{-\infty}^{\infty} e^{i2\pi\gamma t} \left[\int_{-\infty}^{\infty} X(f)\ X^*(f+\gamma) df \right] d\gamma \\ &= \int_{-\infty}^{\infty} X(f) \left[\int_{-\infty}^{\infty} X^*(f+\gamma)\ e^{i2\pi\gamma t} d\gamma \right] df \end{aligned} \tag{6.3}$$

Let $f+\gamma = u, \quad \gamma = u - f, \quad d\gamma = du$, and substitute in the above equation, the time-domain expression of the FCF would be written as:

$$\begin{aligned} FCF_X(t) &= \int_{-\infty}^{\infty} X(f) \left[\int_{-\infty}^{\infty} X^*(u)\ e^{i2\pi u t}\ du \right] e^{-i2\pi f t}\ df \\ &= \int_{-\infty}^{\infty} X(f)\ e^{-i2\pi f t}\ df \int_{-\infty}^{\infty} X^*(u)\ e^{i2\pi u t}\ du \\ &= \left| \int_{-\infty}^{\infty} X(f)\ e^{-i2\pi f t}\ df \right|^2 \\ &= |X(-t)|^2 \end{aligned} \tag{6.4}$$

That is, the FCF is the frequency-spectral density of the absolute power of the inverse-time signal. Another important property of the FCF to mention here, which can be driven from its definition (equation (6.1)):

$$FCF_X(-\gamma) = FCF_X^*(\gamma), \tag{6.5}$$

which shows that the FCF is fully characterized by its positive half-domain, including the zero frequency-shift.

6.3 General Problem Formulation

Next, we shall develop a general formula for the FCF of the radar backscatter from a radar-illuminated cell which contains one, two, or more generally a set of N

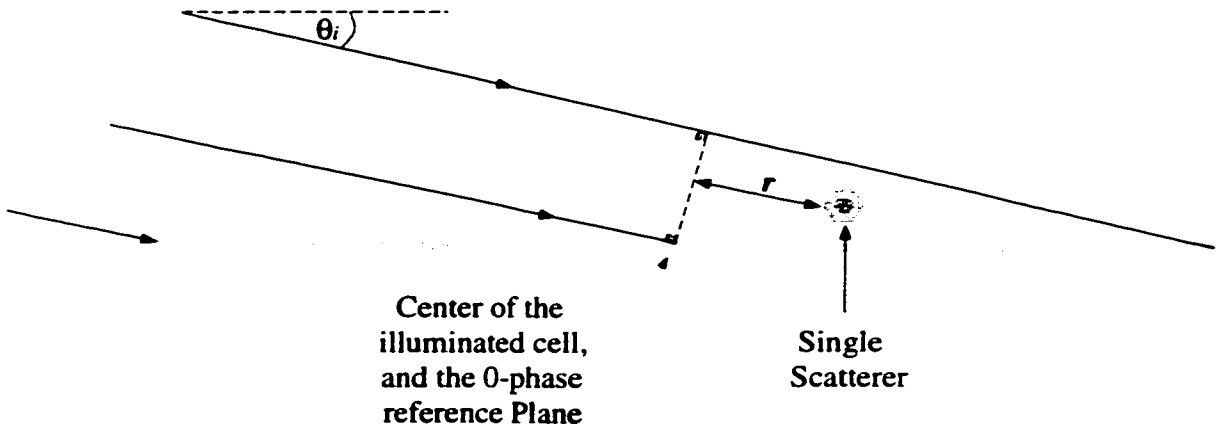

Figure 6.1: Illustration of the setup parameters for the case of a single scatterer.

single scatterers, which are arbitrarily positioned within the cell. For convenience, and without loss of generality, in what follows we will define our zero-phase reference plane to be intersecting with the center of the radar-illuminated cell.

For a single scatterer illuminated by an incident uniform plane wave E_i of polarization q ($q = v$ or h) the scattered p-polarized field ($p = v$ or h) by this target is given by:

$$E_s^p = \frac{e^{i\,2\frac{2\pi f}{c}r}}{r}\, S^{pq}\, E_i^q, \tag{6.6}$$

where, S^{pq} is the pq element of the scattering matrix S of this single scatterer, c is the phase velocity in free space, and the zero-phase reference plane is r meters, in the direction of propagation, away from the position of the target as shown in Fig. 6.1. Without loss of generality, the polarization notation will be dropped since what follows is independent of the polarization-combination, and the amplitude of

the incident field will be taken as unity. Therefore, the field scattered by the single scatterer can be expressed as:

$$E(f) = S \frac{e^{i2\frac{2\pi f}{c}r}}{r} = S^o \, e^{i2\frac{2\pi f}{c}r} \tag{6.7}$$

where $S^o = \frac{S}{r}$. Hence, the frequency correlation function (FCF) of a single scatterer, as a function of the frequency shift χ, is given by:

$$\begin{aligned} FCF(\chi) &= \int_{-\infty}^{\infty} S^o \, e^{i2\frac{2\pi f}{c}r} \, S^{o*} e^{-i2\frac{2\pi(f+\chi)}{c}r} \, df \\ &= \int_{-\infty}^{\infty} |S^o|^2 \, e^{-i2\frac{2\pi\chi}{c}r} \, df \end{aligned} \tag{6.8}$$

However, at MMW frequencies actual radar system has a limited bandwidth (BW), as opposed to infinite bandwidth, and that bandwidth (BW) is usually a small percentage of the operating frequency. Therefore, we can assume that the frequency response of a single scatterer is constant over the operating bandwidth. Hence, the above expression, for the case of positive χ, reduces to,

$$FCF(\chi) = \begin{cases} |S^o|^2 \, e^{-i2\frac{2\pi\chi}{c}r}(BW - \chi) & 0 \leq \chi \leq BW \\ 0 & \chi > BW, \end{cases} \tag{6.9}$$

and for negative χ, equation (6.5) can be used to evaluate the FCF.

For the case of two scatterers with scattered electric fields E_1 and E_2, the FCF of the total scattered E-field $(E_1(f) + E_2(f))$, which is equal to the coherent sum of the individual fields, is given by:

$$\begin{aligned} FCF(\chi) &= \int_{-\infty}^{\infty} \Big(E_1(f) + E_2(f)\Big) \Big(E_1(f+\chi) + E_2(f+\chi)\Big)^* \, df \\ &= \int_{-\infty}^{\infty} E_1(f) \, E_1(f+\chi)^* \, df \end{aligned}$$

$$+ \int_{-\infty}^{\infty} E_2(f)\, E_2(f+\chi)^*\, df$$
$$+ \int_{-\infty}^{\infty} E_1(f)\, E_2(f+\chi)^*\, df$$
$$+ \int_{-\infty}^{\infty} E_2(f)\, E_1(f+\chi)^*\, df$$
$$= FCF_{11} + FCF_{22} + FCF_{12} + FCF_{21}. \tag{6.10}$$

More generally, if the number of scatterers in the radar-illuminated cell is N, the resultant $FCF(\chi)$ can be expressed as:

$$FCF(\chi) = \sum_{k=1}^{N} \sum_{l=1}^{N} FCF_{kl}(\chi). \tag{6.11}$$

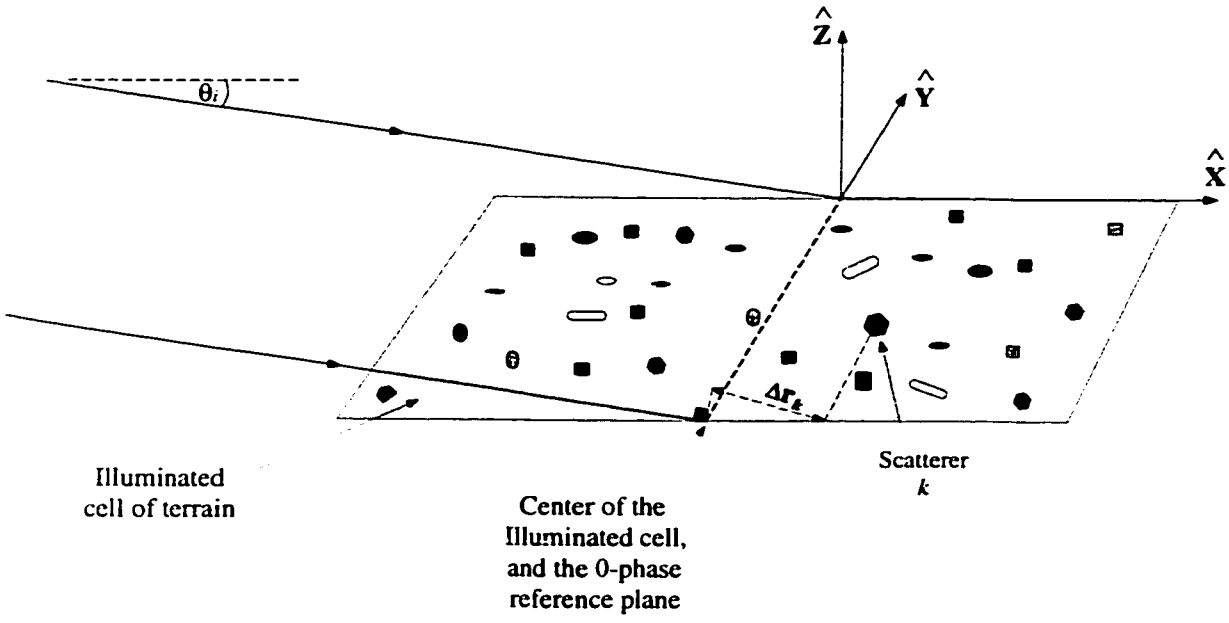

Figure 6.2: Illustration of the setup for the general case of backscattering by terrain.

Next, let us consider the case shown in Fig. 6.2 in which a radar system is used to measure the backscatter from a cell that contains a large number of scatterers at

a grazing angle θ_i. Taking the zero-phase reference plane to be intersecting with the center of the illuminated cell, which is r_o meters away from the radar system, we can express the distance of the scatterer number k (r_k) from the radar as follows:

$$r_k = r_o + x_k cos\theta_i - z_k sin\theta_i \tag{6.12}$$

In other words, Δr_k, measured with respect to r_o, is given by

$$\Delta r_k \;=\; r_k \;-\; r_o \;=\; x_k cos\theta_i \;-\; z_k sin\theta_i, \tag{6.13}$$

where x_k and z_k are the x- and z-coordinates of the position of scatterer number k, as shown in Fig. 6.2. The y-axis is chosen to be perpendicular to the plane of incidence which is defined as the plane containing the incident direction and the normal to the surface. Hence, the y-coordinate of a scatterer does not affect the phase shift due to propagation from/to the scatterer. Writing the field scattered from the scatterer number k in the following general form:

$$E_k(f) = \; S_k^o \; e^{i\; 2\frac{2\pi f}{c}\; \Delta r_k} \;=\; S_k^o \; e^{i\; 2\frac{2\pi f}{c}(x_k cos\theta_i - z_k sin\theta_i)}, \tag{6.14}$$

the expressions of $FCF_{kk}(\chi)$ and $FCF_{kl,k\neq l}(\chi)$, for positive χ are given by:

$$FCF_{kk}(\chi) = \begin{cases} |S_k^o|^2 e^{-i(\; 2\frac{2\pi\chi}{c}(x_k cos\theta_i - z_k sin\theta_i))}(BW - \chi) & 0 \;\leq\; \chi \;\leq\; BW \\ 0 & \chi \;>\; BW \end{cases}$$

$$FCF_{kl}(\chi) = \begin{cases} S_k^o (S_l^o)^* \; e^{-i(\; 2\frac{2\pi\chi}{c}(x_l cos\theta_i - z_l sin\theta_i))} \cdot \\ \quad \cdot e^{i(\; 2\frac{2\pi F_o}{c}[(x_k - x_l)cos\theta_i - (z_k - z_l)sin\theta_i])} \cdot \\ \quad \cdot \frac{e^{i\; 2\frac{2\pi}{c}(BW-\chi)[(x_k - x_l)cos\theta_i - (z_k - z_l)sin\theta_i] - 1}}{i\; 2\frac{2\pi}{c}[(x_k - x_l)cos\theta_i - (z_k - z_l)sin\theta_i]} & 0 \;\leq\; \chi \;\leq\; BW \\ 0 & \chi \;>\; BW. \end{cases} \tag{6.15}$$

where, F_o is the lower frequency-limit of the radar system bandwidth. I.e. the radar system is working from F_o to $F_o + BW$.

6.4 Physical Insight

Two notes worth mentioning here are that:

1. The frequency response associated with a target, $X(f)$, is composed of two components: (a) the system component which is a function of the setup parameters (incidence angle, radar beamwidth, etc.), and (b) the target component which is a function of the target parameters only (dimensions, constituents, orientation, etc.). For some applications, such as physical parameter retrieval, it is necessary to eliminate the system component from the FCF before using it as shown in [34]. For our case, the detection problem, we chose another approach. Our approach is to choose the system parameters to enhance our detection capabilities as will be explained in Chapter 8.

2. In this investigation the FCF will be examined from the target detection point of view. That is, because decisions in detection algorithms are usually made based on single-look measurements, the FCF also will be evaluated based on single-look measurements. This is contrary to physical parameter retrieval applications, such as those reported in [34], where the ensemble average of FCF, $< FCF >_{spatial}$ (averaged over the individual, statistically independent samples), is used.

To better understand the characteristics of the FCF, let us consider the general case of a radar-illuminated cell with N, where N is an arbitrary number, single scatterers randomly positioned in it. As explained in the previous section, equation(6.11), the FCF of the radar backscattered from such a case is the sum of all the FCF_{kk}'s and the FCF_{kl}'s terms where k and l takes any value between 1 and N. The expression of $FCF_{kl}(\chi)$ of equation(6.15) is a complicated non-linear function of x_k, z_k, S_k^o, x_l, z_l, and S_l^o. In case of clutter these parameters are random variables that change from one spot to the next for most cases. The total number of scatterers N in the illuminated cell is also a random variable. The complexity of equation(6.11), after substituting equation(6.15) into it, makes it almost impossible to further investigate the properties of the single-look FCF analytically.

Although it is difficult to characterize the behavior of the FCF analytically, the following properties of the FCF were observed (using equation (6.11) after the substitution of equation (6.15) into it):

I- The $FCF_{kk}(\chi)$ has its peak when $\chi = 0$ (due to phase conjugation) and its amplitude decreases with the increase of the frequency-shift χ due to the change of the relative phase angle of the backscatter from the target with frequency.

II- The zero-frequency shift is not necessarily the point at which $FCF_{kl}(\chi)$ is a maximum. This is because of the lack of phase conjugation at zero frequency-shift which, in turn, is a result of the dependence of the relative phase angle

on the positions of both scatterers, k and l, with respect to the zero reference plane.

III- based on the above observation, we expect the contribution of the cross-correlated components, FCF_{kl}, to the FCF to be much less than the contribution of the self-correlated components, FCF_{kk}.

IV- By ignoring the cross-correlated components, a less-complicated, but approximate, expression for the FCF of the total signal can be realized and used to gain more understanding of the behavior of the FCF, while the exact expression can be used in numerical simulations, as will be shown in Chapter 8, to guarantee accurate results. This simpler, but approximate, expression for the $FCF(\chi)$ is

$$FCF(\chi) \approx \sum_{k=1}^{N} FCF_{kk}(\chi). \tag{6.16}$$

6.5 Conclusions

To investigate the application of the FCF in the detection problem, its definition was introduced, and its physical meaning along with its relation to the time-domain signal were presented. In addition, a general expression for the FCF of the backscatter from a radar-illuminated cell of terrain that contains N single scatterers, where N is an arbitrary number, was developed. This general expression was then, based on a qualitative discussion, reduced to a simpler, but approximate, expression that gives more physical insight to the characteristics of the FCF. For consistency with the

structure of this thesis, this expression will be utilized, in Chapters 7 and 8, to gain more physical insight to the properties of the FCF, its relation to the number of scatterers in the illuminated cell, and its relation to the system parameters (system bandwidth, incidence angle, etc.). Also, the accuracy of this approximate expression will be examined in Chapter 8.

CHAPTER 7

EXPERIMENTAL STUDY OF THE FCF AND ITS APPLICATION TO THE DISCRIMINATION OF TREE TRUNKS FROM NEARBY TARGETS

7.1 Introduction

Of special interest to us is the detection of man-made targets near forest stands because of its significant importance for a number of remote sensing applications. Among those applications which are probable to work near forested areas are: low-altitude military helicopter radars, and automotive collision-avoidance systems. In forested areas, and at near grazing angles, tree trunks represent the first candidate class of targets probable to confuse —from radar standpoint— with man-made targets. The confusion is attributed to the expected high RCS of trunks which, in part, is due to its vertical physical extent, as well as to the bistatic nature of the scattering

process. As explained in Section 6.1, introducing new detection features can potentially enhance the ability of discriminating tree trunks from nearby targets, including man-made targets.

In this chapter we will investigate , through experimental study, the application of the FCF in discriminating tree trunks from nearby targets. In Section 7.3 we report on an outdoor measurement campaign that was designed and conducted to examine the use of FCF-based features in detection. In addition, we present some observations (from the detection standpoint) on this measurement campaign in Section 7.4. Based on the data analysis of the outdoor measurements, FCF bandwidth (FCFBW) defined in Section 7.2 is chosen as a detection feature and used to develop a detection algorithm. The details of this detection algorithm along with its performance evaluation are presented in Section 7.5.

From the FCF definition (equation (6.1)) we notice that the peak value of the FCF is proportional to the total power of the frequency response, hence, the FCF is proportional to the RCS. Since the RCS is a feature that causes MMW radar to confuse tree trunks and man-made targets (i.e. RCS is a source of confusion), it is useful to normalize the FCF with respect to its peak value (to eliminate its dependence on RCS) for the application at hand. Hence, throughout this chapter we shall use FCF to refer to the normalized FCF which is defined as $FCF/FCF(0)$.

7.2 Definition of the FCFBW

The definition of the FCFBW (**F**requency **C**orrelation **F**unction **B**and**W**idth), shown in Fig. 7.1, is the frequency shift β at which the FCF amplitude drops to $1/e$ of its value at zero-frequency shift. That is,

$$FCFBW = \beta : FCF(\beta) = \frac{FCF(0)}{e}. \tag{7.1}$$

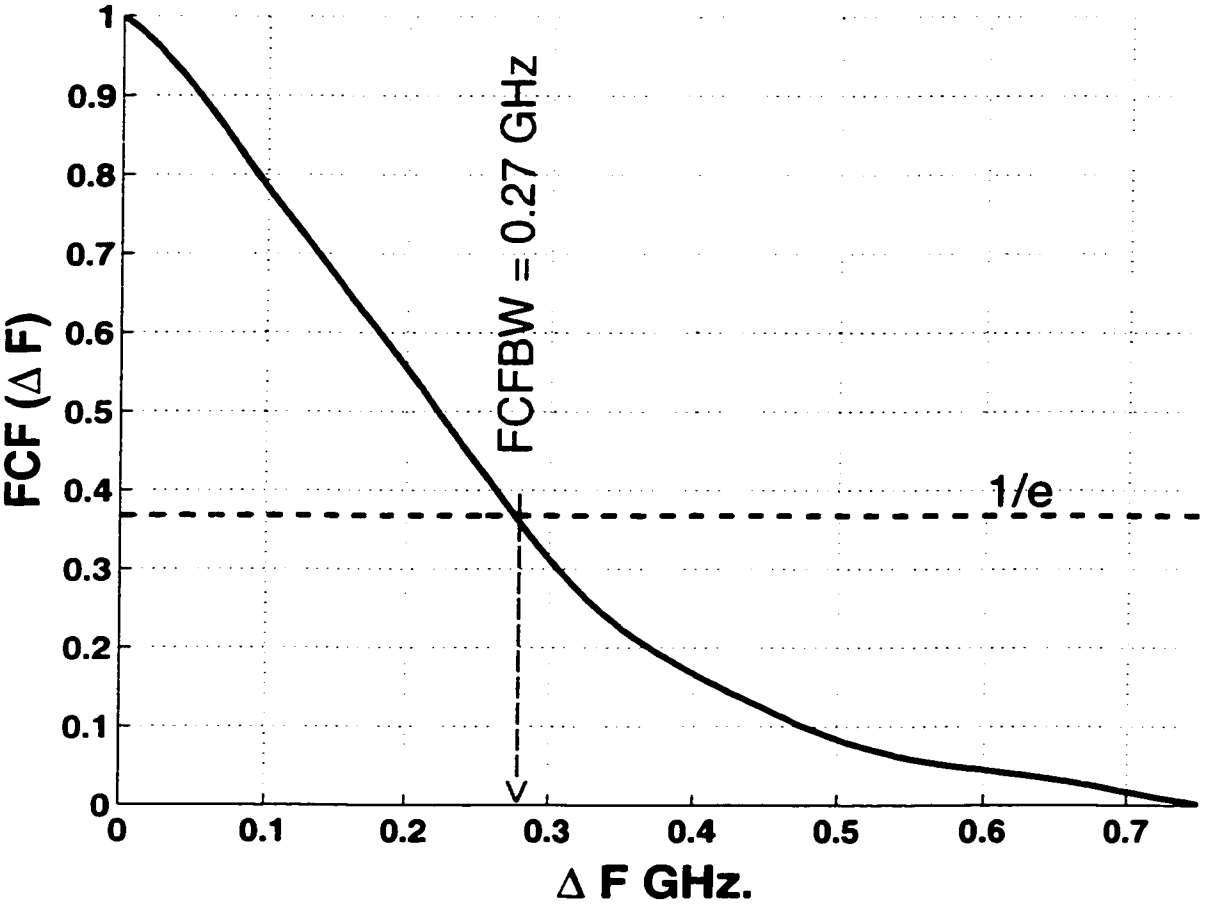

Figure 7.1: A typical behavior of the FCF with the illustration of the definition of the FCFBW.

7.3 Experimental Setup

To investigate the application of the FCF in target detection, an outdoor measurement campaign was designed and conducted at 35 and 95 GHz. Both radar systems were used to measure the polarimetric backscattering matrix S at 301 discrete frequency points spanning a bandwidth of 0.375 GHz. In this measurement campaign the two radar systems were used to vertically scan randomly selected trunk-ground scenes. Figure 7.2 shows some of the scenes which were scanned in this campaign. In these scans the backscattered responses of different sections of the trunk-ground combination (namely: the trunk, the trunk-ground corner, and the ground) were measured. The vertical scans were performed at 14 different look-angles with 1° separation. In each scan, the trunk section corresponds to look-angles from 8° to 1°, the ground corresponds to look-angles from $-1°$ to $-5°$, and the corner between the trunk and the ground corresponds to 0° look-angle, which we chose to be our reference angle. The reference zero-look-angle corresponds to a grazing-angle of 4.0° from horizontal.

In this campaign, the measurements were performed over 50 different trunk-ground combinations. The measured trunks varied in bark roughness, and were tilted with respect to the ground. Their tilt angles ranges from $-9°$ to $+2.6°$. In addition, the trunk circumferences were between 1.2 and 3.1 m.

The backscattered response of the tree canopy was obtained from earlier measure-

ments and merged with the measurements of this campaign to build a data set of the backscattered response of all the sections of the trunk-ground combination that are considered in this study, as shown in Fig. 7.3. For completeness, the backscattered responses of two different tanks in different positions standing in a field of a bare soil (man-made target with terrain in the background) were extracted from the SWOE data set collected by the army research laboratory (ARL) at 95 GHz described in Section 2.2. This data was used to evaluate the FCF of these tanks and to investigate the possibility of confusion between tree trunks and these tanks, and to examine the ability of FCF to resolve this confusion.

The 35 and 95 GHz radar systems used in this measurement campaign compose a fully polarimetric ultra-fast wideband millimeter-wave scatterometer system. The system is developed at the University of Michigan and consists of two RF-frontend units (one at 35 GHz and the other at 95 GHz) and an IF transceiver (transmit/receive) module. The scatterometer system operates in Real Aperture Radar (RAR) mode with an angular resolution of 2 and 1.4 degrees at 35 and 95 GHz respectively. In addition, the two scatterometers have 1 foot range resolution (500 MHz systems). The principle of operation of the ultra-fast scatterometer system can be summarized as follows: The transceiver module generates a C-band pulse chirped over 500 MHz. The chirped pulse is upconverted in the RF-frontend units to the desired MMW frequencies and transmitted as either vertically or horizontally polarized pulse. The backscattered response, intercepted by the receive antenna, is downconverted in the RF-frontend units to C-band and sent back to the IF transceiver module. Inside the

transceiver, the received signal is downconverted once again to baseband and detected directly using a Digitizing Oscilloscope. The data is then transfered to a personal computer where the time domain response and/or the frequency domain response of the target (or clutter) under test can be extracted.

An important feature of this system is the high speed with which it acquires the complete scattering matrix, thereby preserving phase coherence between polarizations. This later feature is very useful to accurately calculate the FCF which is performed based on the complex scattering matrix S.

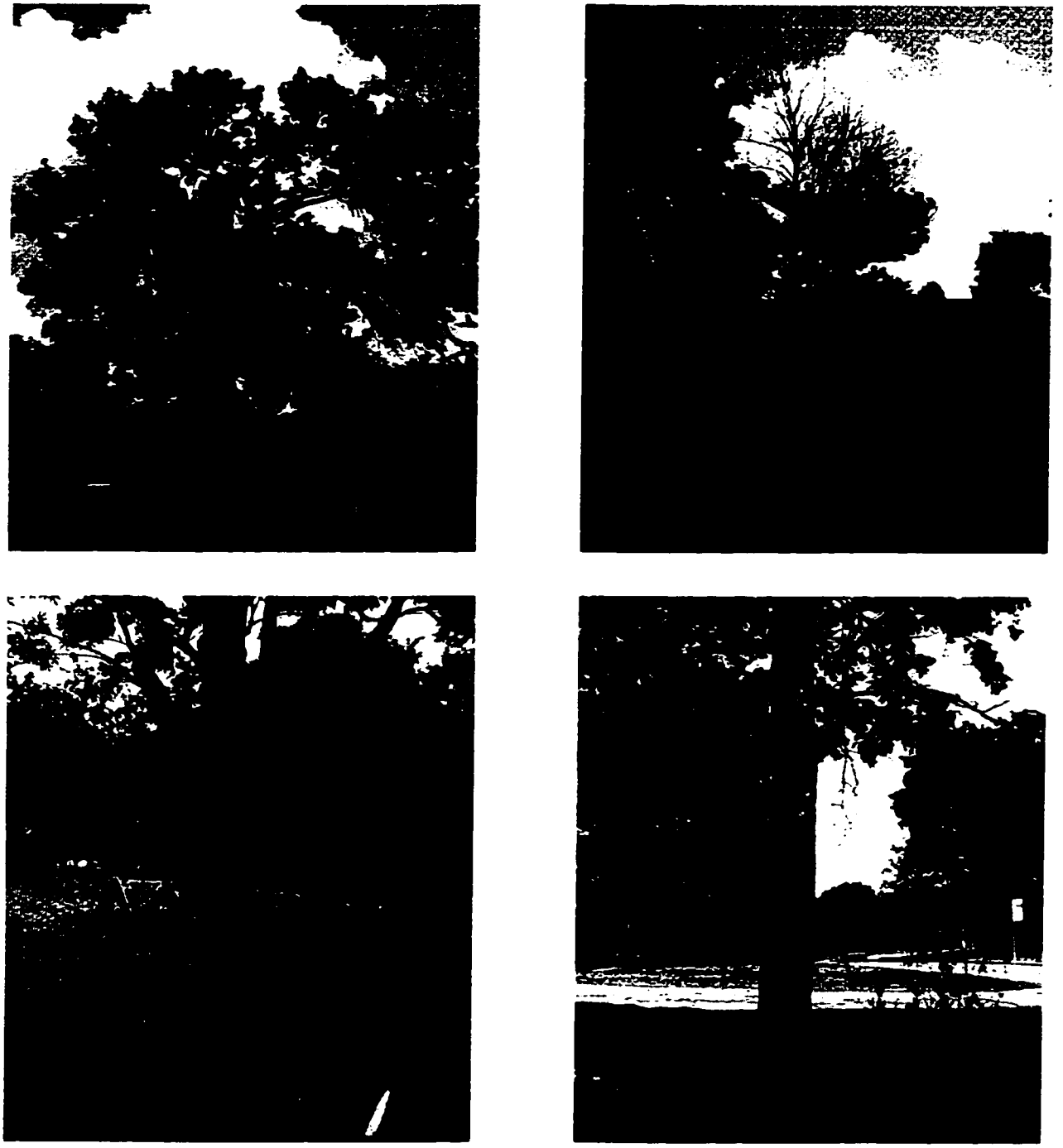

Figure 7.2: Examples of the scenes that were scanned in the measurement campaign.

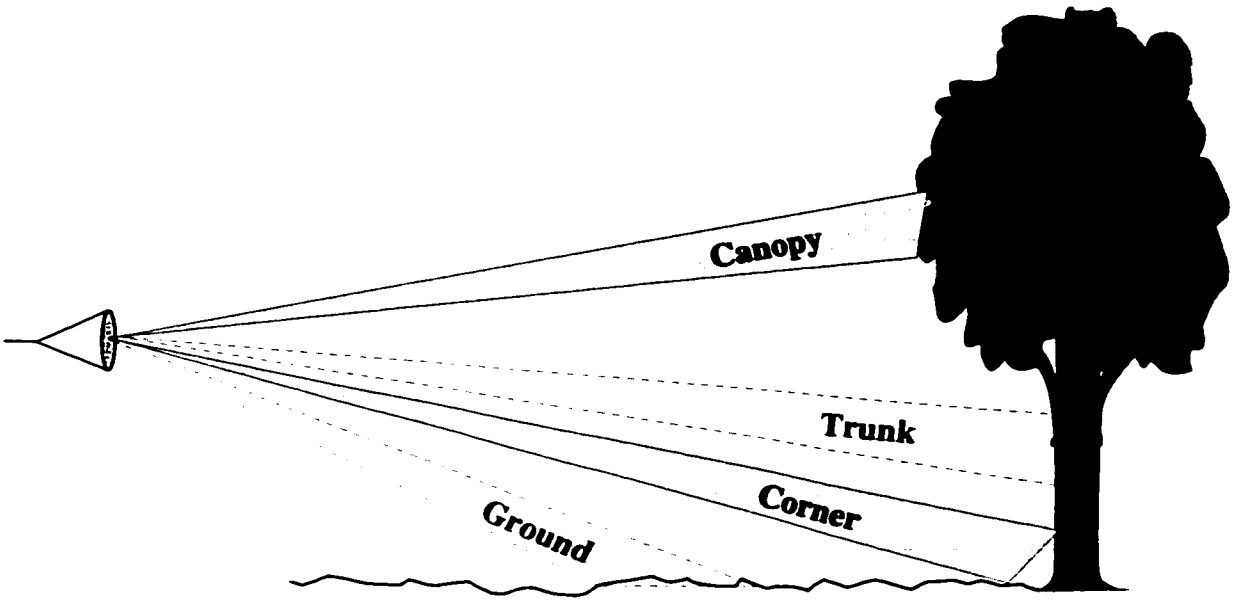

Figure 7.3: Illustration of the different sections of the trunk-ground combination considered in this study.

7.4 Observations on Trunk Measurements

Both 35 and 95 GHz data were processed and analyzed. The outcome of this analysis were similar for both frequencies. But, since the data of the man-made targets (tanks) is available only at 95 GHz, the comparison between man-made target and tree trunk will be based on the 95 GHz data alone.

The measured data indicates that the dynamic ranges of the co-polarized elements of the scattering matrix, $|S_{vv}|$ and $|S_{hh}|$, of the trunk section are overlapped with those of the trunk-ground corner and those of the ground, as shown in Fig. 7.4. Similarly (but based on the co-polarized scattering coefficient because the measurements were performed using two different radar systems), the dynamic ranges of the trunk measurements are overlapped with those of the man-made targets as shown in Fig. 7.5. These observations emphasize the need for a new feature (that is independent of RCS) to enhance the ability of discriminating tree trunks from nearby targets.

A point to mention here is that the backscatter from different sections of the trunk-ground combination were measured with a system that is different from the one that were used to measure the backscatter from tanks in a bare soil field. The backscatter from different sections of the trunk-ground combination were measured by the University of Michigan radar system described in Section 7.3 (0.5 GHz radar system bandwidth and an illuminated cell extending 12 m in range), while the backscatter from the tanks in the bare soil field were measured by the ARL system described in

Section 2.2 (0.64 GHz radar system bandwidth and an illuminated cell extending 15 m in range). In Chapter 8 we will show that the FCF behavior of a target depends on, among others, the along-range dimension of the illuminated cell and the radar system bandwidth. Therefore, comparing behaviors of measured FCFs of different targets based on measurements performed with different setups would result in inaccurate results. However, in the case at hand the limited differences among the main setup parameters —from FCF point of view— (along-range dimension of the illuminated cell and the radar system bandwidth) is expected to lead to fairly accurate results.

Looking for a new detection feature, the average frequency correlation function (averaged over spatially independent samples) was examined. Figure 7.6 depicts the average FCF of the corner, the ground, and the trunk sections at one angle each. From Fig. 7.6, we observe that the FCFBW of the tree trunk is larger than that of the trunk-ground corner and that of the ground. However being based on the average FCF instead of a single-look FCF as required for detection, this observation shows that the FCFBW is a candidate feature to be used in tree trunk discrimination from nearby targets in a natural scene.

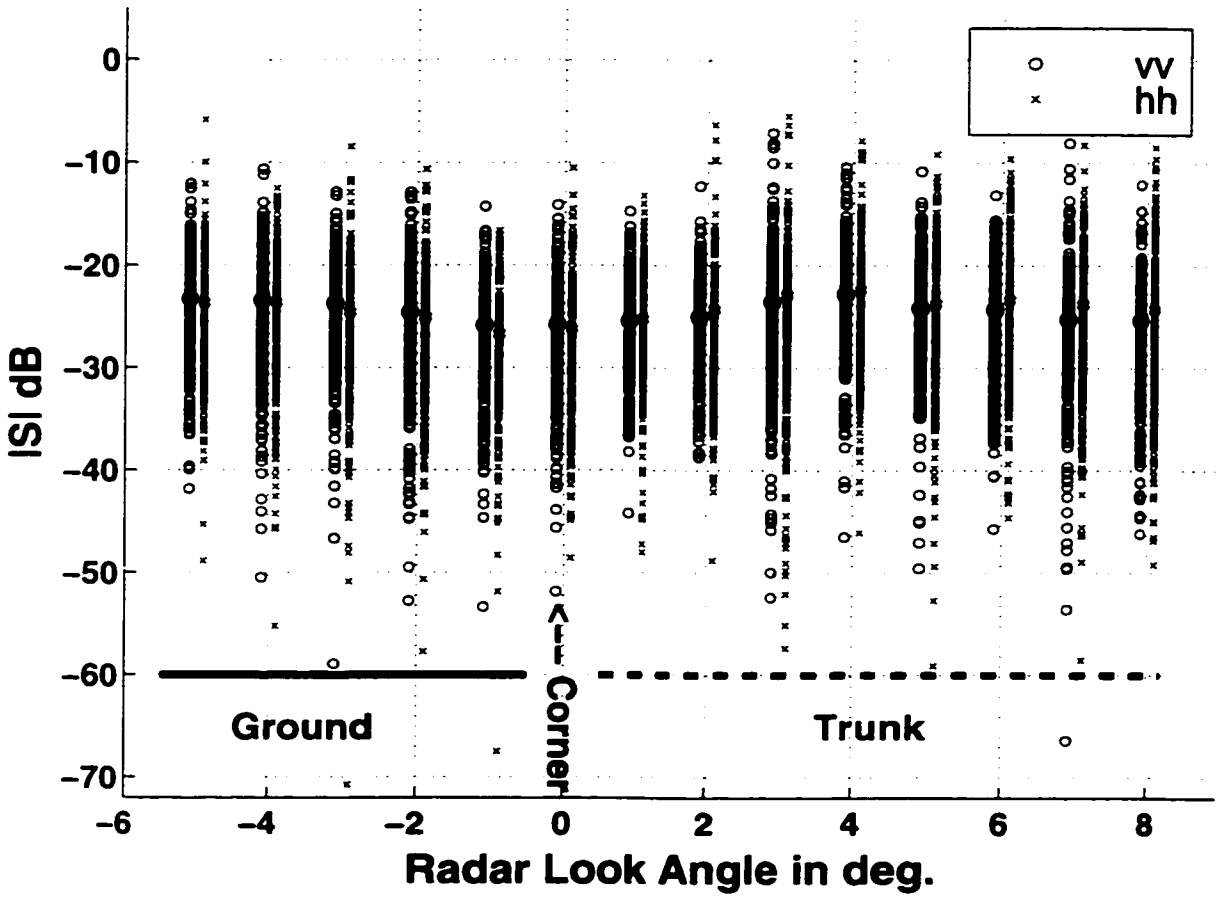

Figure 7.4: The dynamic range and mean values of $|S_{vv}|$ and $|S_{hh}|$ of different sections of the trunk-ground combinations at 35 GHz.

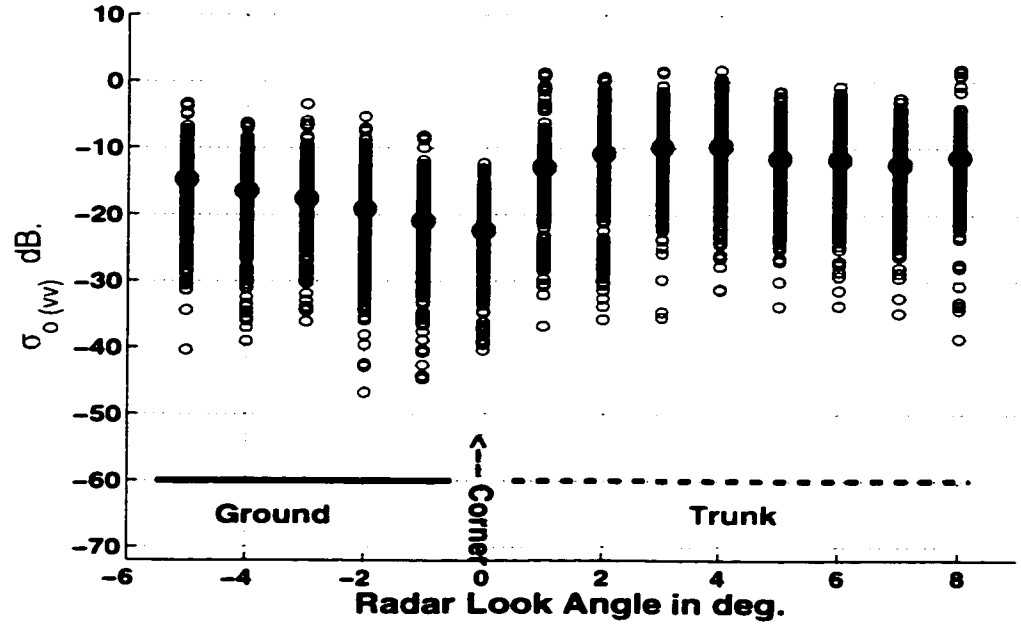

(a) Sections of trunk-ground combination

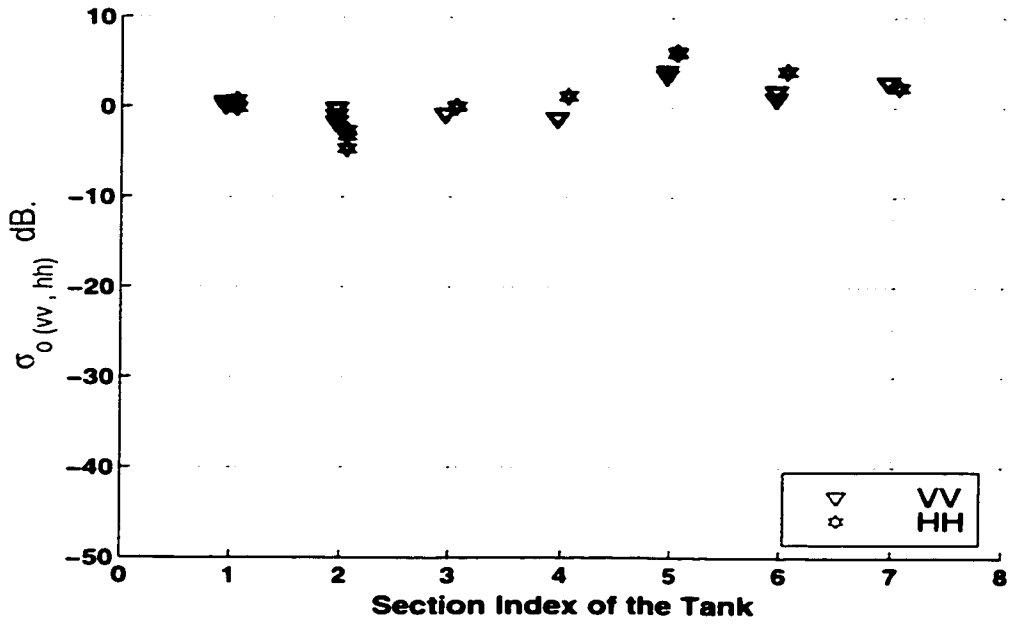

(b) Sections of man-made target (tank)

Figure 7.5: Comparison between the dynamic range of the scattering coefficient of tree trunks and surrounding environment, including man-made target at 95 GHz.

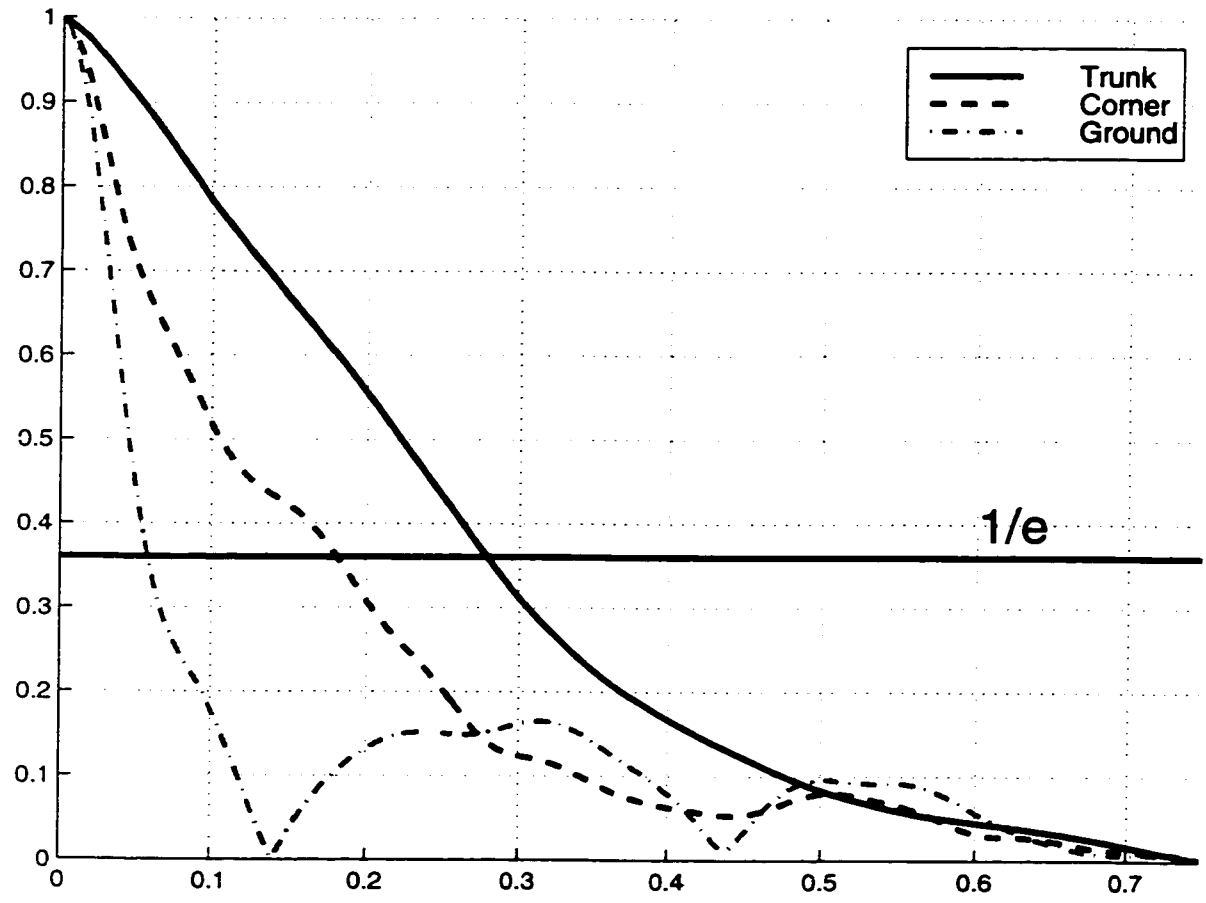

Figure 7.6: The average FCF of different sections of the trunk-ground combination.

7.5 Detection Feature and Algorithm

In many remote sensing applications, detection decisions are better to be based on a single measurement, as opposed to the mean measured response. In this section we shall examine the use of the FCFBW of individual measurements in detection. Towards that, the measured data of all the sections of the trunk-ground combination was used to calculate the FCFBW of individual measurements. Figure 7.7 shows the dynamic ranges and mean values of the FCFBW, based on S_{vv}, of all the sections of the trunk-ground combination at 95 GHz. From this figure we observe that, however the FCFBW values of individual measurements have wide dynamic ranges, for trunks they are centered around higher values than that of the other sections (trunk-ground corner, ground, and tree canopy). For completeness, the FCFBW of the individual man-made (tank) target measurements, shown in Fig. 7.8, were examined versus those of the sections of the trunk-ground setup at 95 GHz. Figures 7.7 and 7.8 demonstrate that the dynamic ranges of the FCFBW of these tanks are centered at values much smaller than those of the trunk cases. The above observation indicates the possibility of using the FCFBW in discriminating tree trunks from nearby targets including man-made targets.

An explanation for this behavior was thought. An ideal single scatterer, theoretically, is not expected to decorrelate with frequency at MMW frequencies except because of the limited radar system bandwidth. This is because its frequency response, amplitude-wise, is independent of frequency over the operating bandwidth which is a

small percentage of the center frequency. Also, its frequency response, phase-wise, is a linear function of frequency over the operating bandwidth. The slope of this linear function depends on the location of the scatterer with respect to the zero-phase reference plane. Therefore, the amplitude in-dependency of frequency, along with the phase linear dependency on frequency are believed to be the properties that control the value of the FCFBW. To examine the validity of this explanation, the frequency responses of the backscatter from the types of targets considered in this study were examined. Figure 7.9 shows examples of the frequency responses of a trunk, a tank, a tree canopy, and a ground at 95 GHz. From these plots we observe that the frequency response, amplitude-wise, of the trunk is the most independent of frequency and its phase is very close to be linear (when unwrapped) with frequency. Hence, this test supports our explanation which is; the tree trunk exhibit higher FCFBW than other nearby targets because its behavior is closer to that of a single scatterer than the other targets.

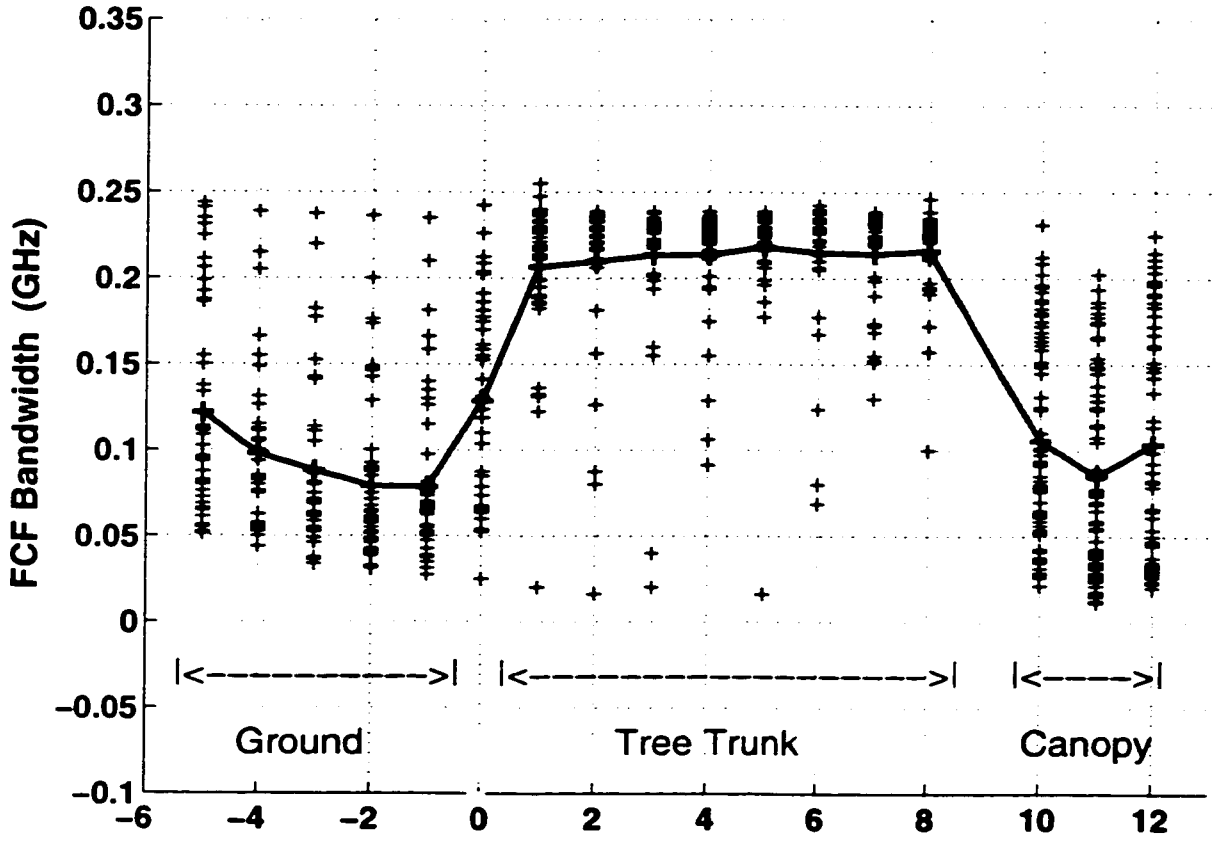

Figure 7.7: The dynamic range and mean values of the FCFBW, based on S_{vv}, of different sections of the trunk-ground combination at 95 GHz. Radar system bandwidth = 0.375 GHz.

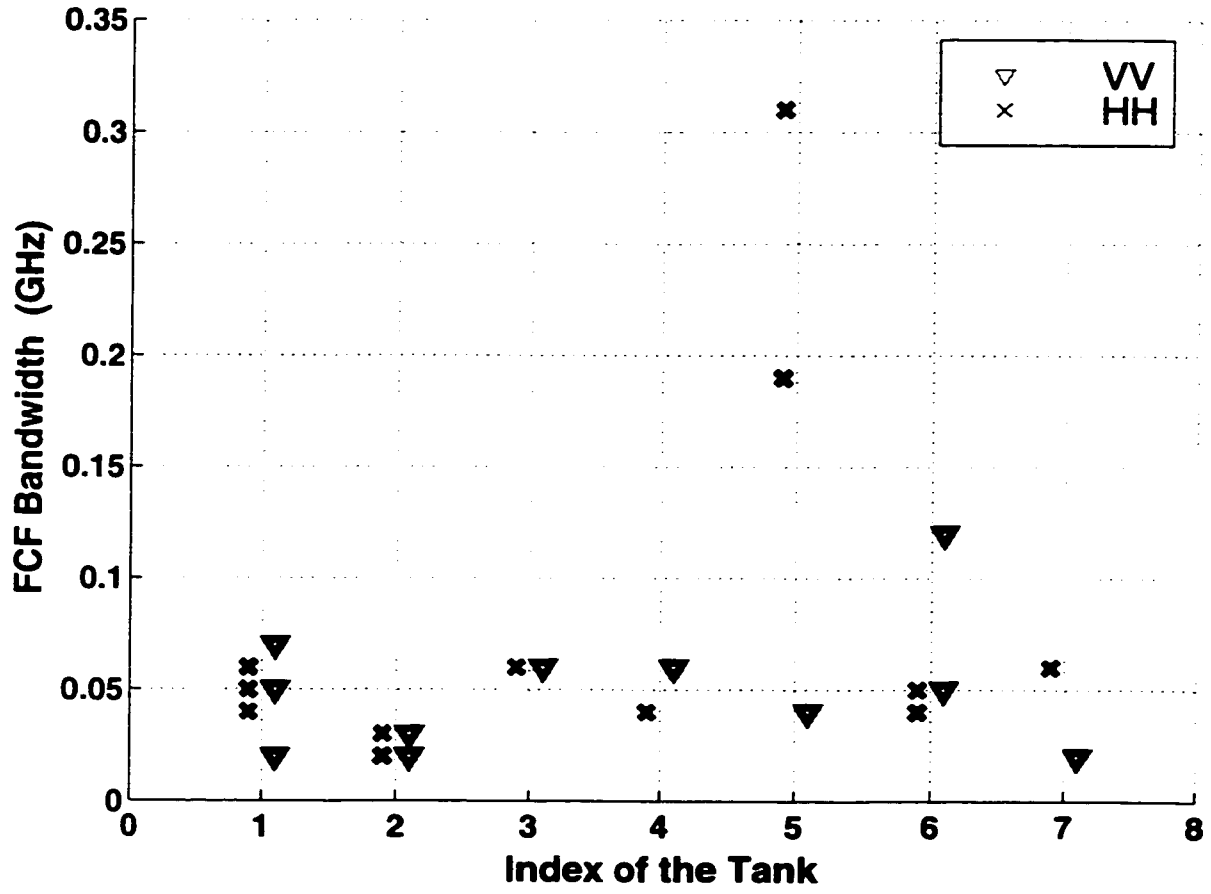

Figure 7.8: The FCFBW of individual man-made (tank) target measurements at 95 GHz.

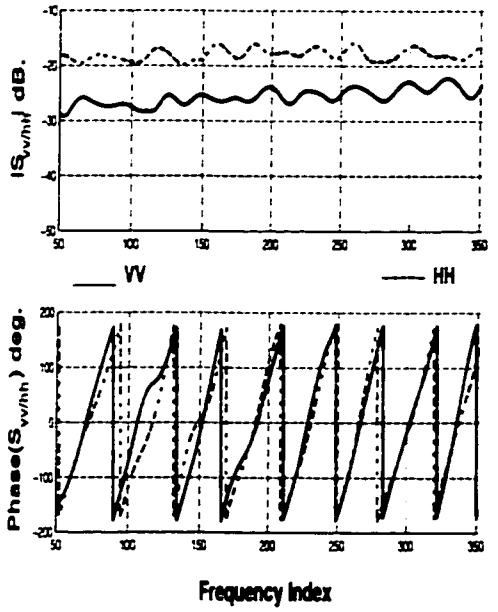

(a) Trunk

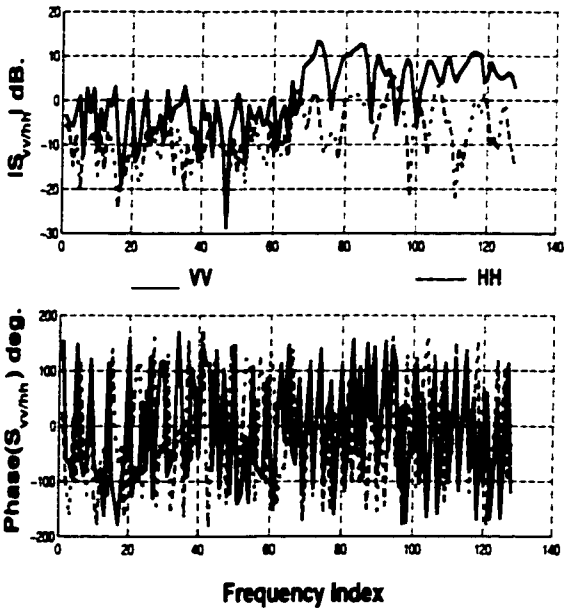

(b) Tank

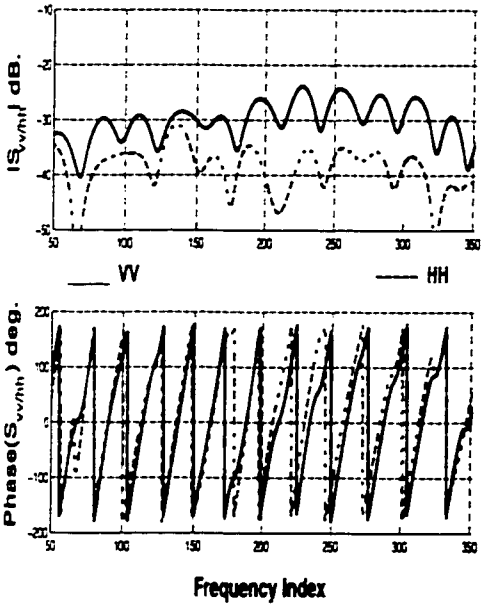

(c) Tree Canopy

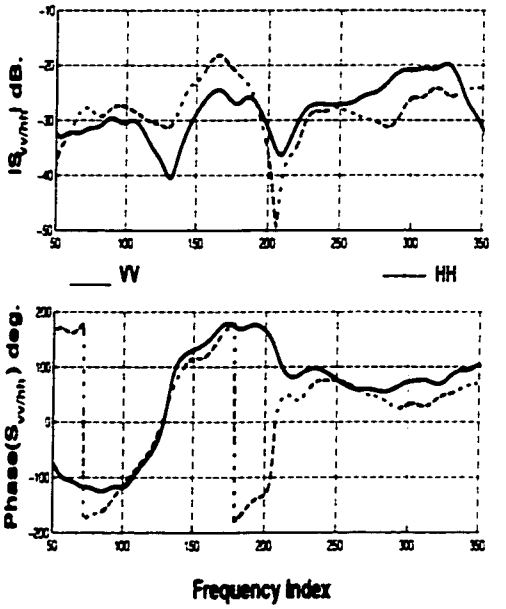

(d) Ground

Figure 7.9: Examples of the frequency responses of different targets considered in this study at 95 GHz.

As depicted in Fig. 7.10, an FCFBW threshold can be selected, based on any polarization-frequency combination (VV-polarization at 35 GHz for example), to separate most of the trunk measurements from those of the other targets including man-made targets. This observation suggests the simple detection algorithm shown in Fig. 7.11 to be applied. In this proposed algorithm, the FCFBW of each measurement is examined against FCFBW threshold. If, for both VV and HH-polarizations (i.e. based on S_{vv} and S_{hh}), the FCFBW of the measurements are greater than the FCFBW threshold, the algorithm will indicate a tree trunk.

This algorithm was applied to all the measurements and the percentage of measurements which the algorithm indicated as trunks (whether false or true) at each angle were calculated. The percentage of indicating a trunk using the FCFBW threshold are plotted in Fig. 7.12 as a function of the look-angle. The percent value represents the false alarm rate when the radar was looking at the ground, or at the tree canopy. But, it represents the detectability of trunks when the radar was looking at the trunk. This simple algorithm has greater than 89% detectability of trunks at different radar look angles at 35 GHz with a slightly lower performance at 95 GHz. In addition, its false alarm rate is less than 8% at 35 GHz and is a bit higher at 95 GHz. Applying this algorithm to the tank measurements, shown in Fig. 7.8, will not result in any case of indicating a tank as a tree trunk. In other words, this algorithm resolved all the confusions between the tanks and tree trunks for the measurements at hand.

A remark to mention here is that the 35 GHz radar is more stable —over frequency—

than the 95 GHz one. This higher stability is believed to be the reason for the superiority of the performance of this algorithm at 35 GHz when compared to its performance at 95 GHz.

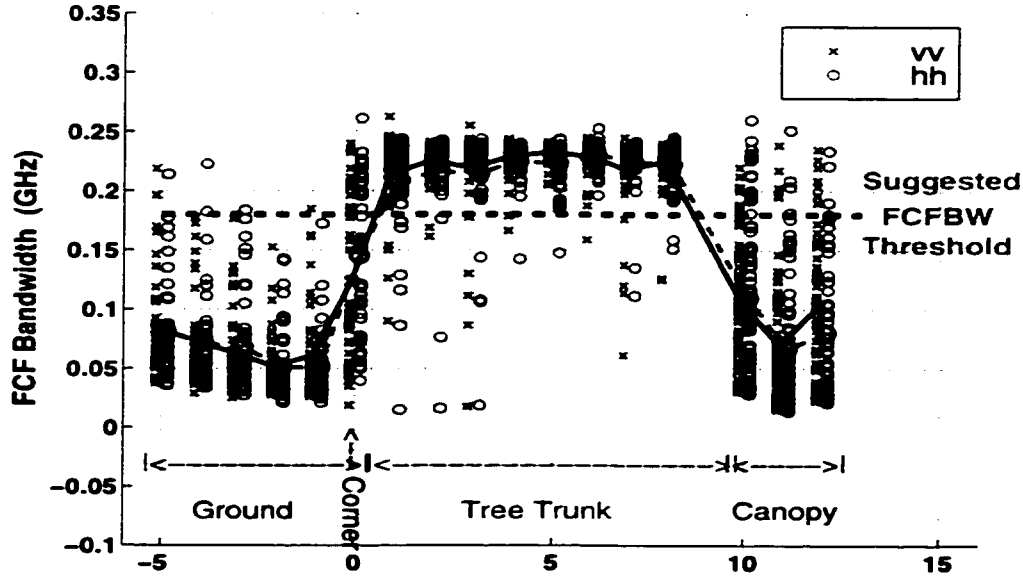

(a) 35 GHz

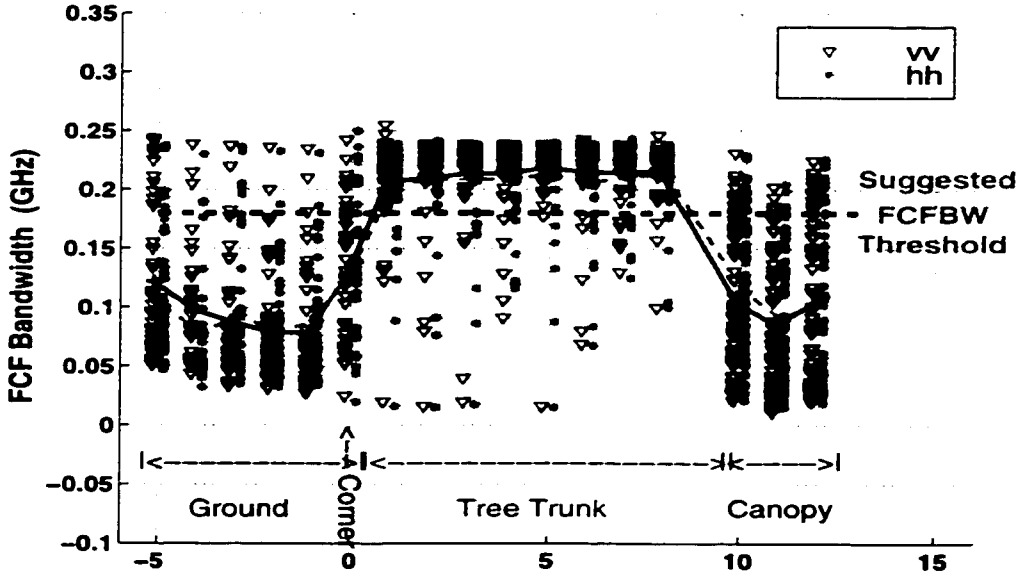

(b) 95 GHz

Figure 7.10: The dynamic range and mean values of the FCFBW, based on S_{vv}, and S_{hh} of different sections of the trunk-ground combination at both 35 GHz and 95 GHz. Radar system bandwidth = 0.375 GHz.

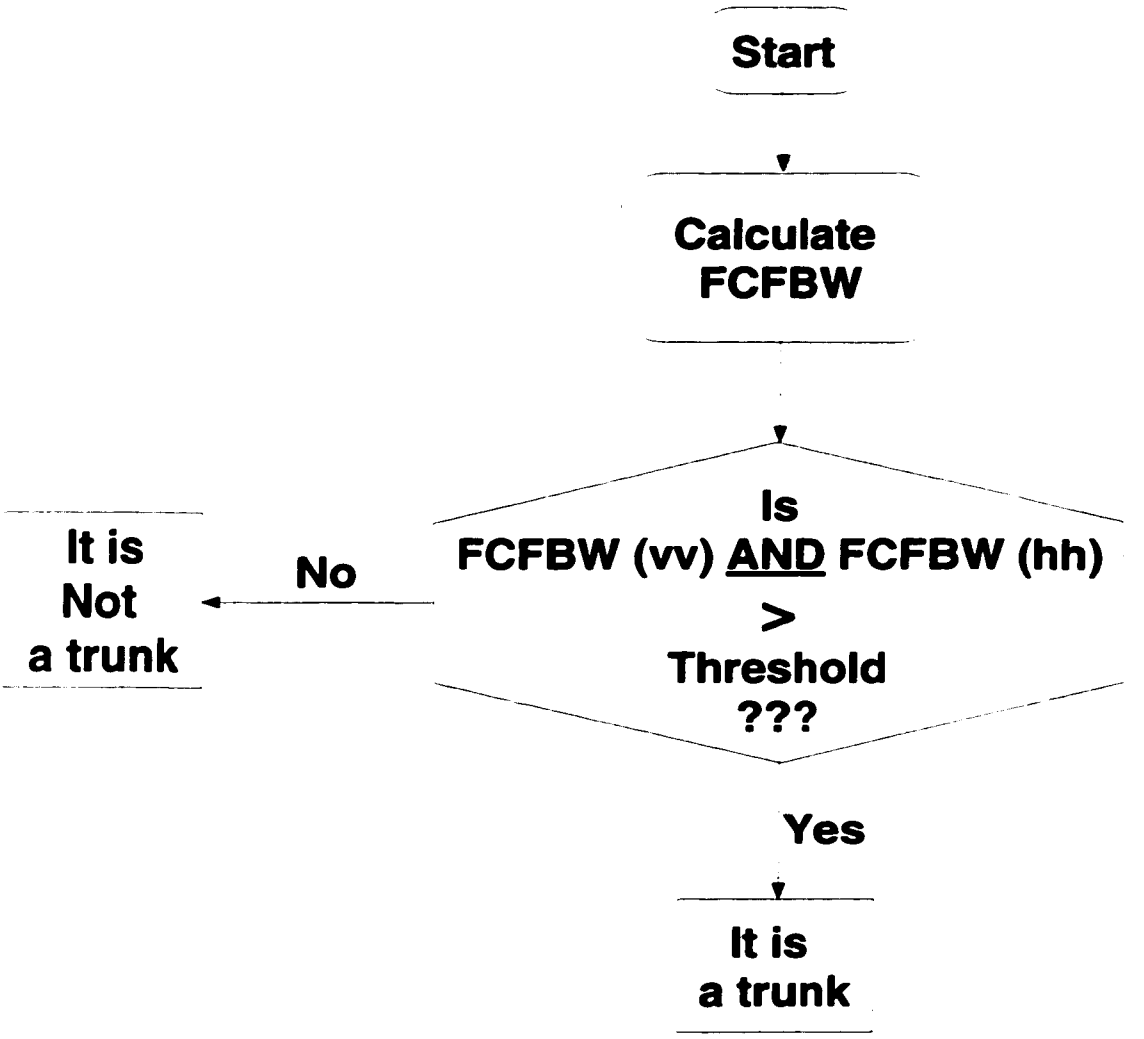

Figure 7.11: Flow chart of the proposed detection algorithm.

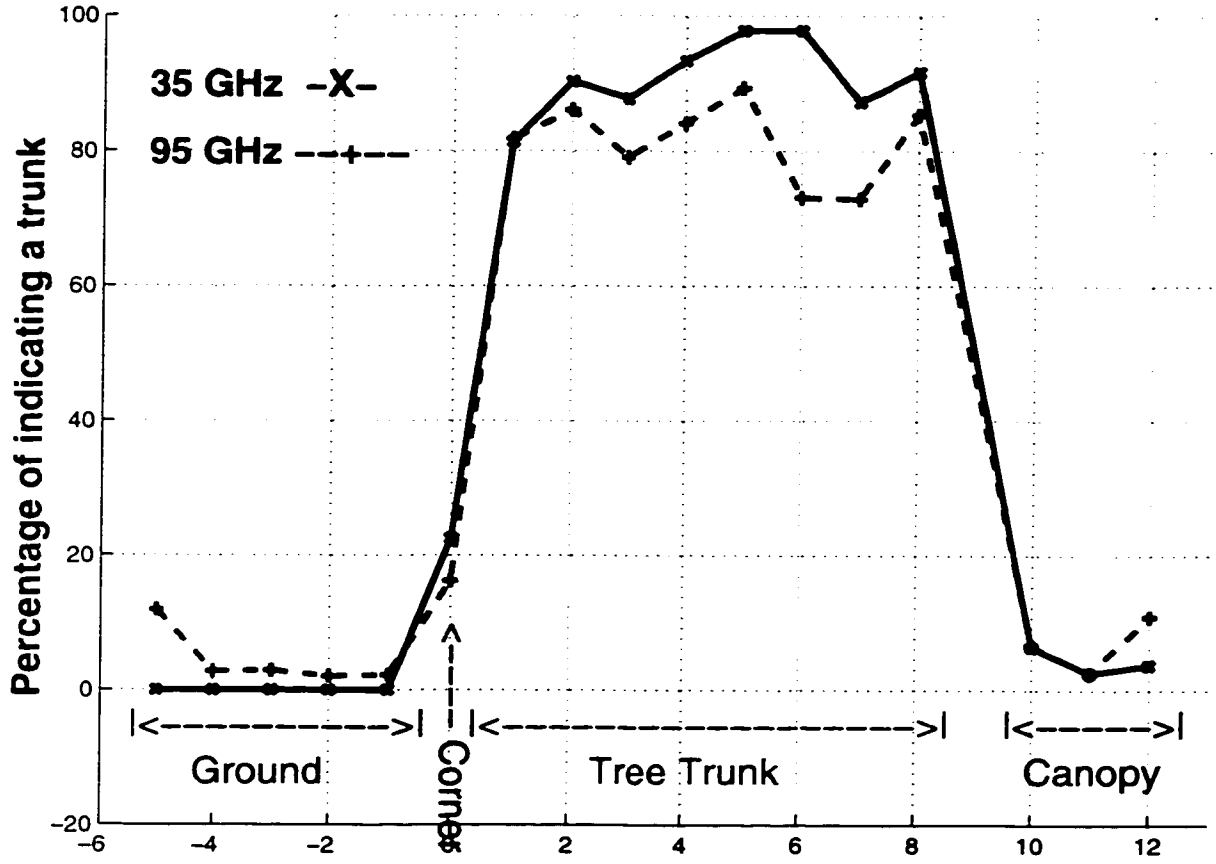

Figure 7.12: The performance of the proposed detection algorithm.

7.6 Conclusions

FCFBW is introduced as a new feature for target detection algorithms. The introduction of the FCFBW increases the input vector space of the detection problem, which in turn can potentially enhance the performance of target detection algorithms. An outdoor measurement campaign (at 35 GHz and 95 GHz) was designed and conducted to examine the usefulness of the FCFBW for discriminating tree trunk from nearby targets. Based on the acquired data, the FCFBW values of individual measurements of trunks were found to be centered around higher values than that of the other nearby targets (trunk-ground corner, ground, tree canopy, and tanks). This behavior was explained theoretically and verified by measurements. Moreover, based on this behavior, a simple detection algorithm was proposed, tested, and its performance was evaluated. This algorithm showed greater than 89% detectability of trunks at different radar look angles at 35 GHz with a slightly lower performance at 95 GHz. In addition, its false alarm rate is less than 8% at 35 GHz and is a bit higher at 95 GHz. Moreover, using this algorithm all the cases of confusion between man-made targets and tree trunks were resolved.

CHAPTER 8

NUMERICAL-SIMULATION STUDY OF THE FCF AND ITS APPLICATION IN TARGET DETECTION

8.1 Introduction

An exact expression for the FCF of the radar backscatter from N scatterers, where N is an arbitrary number, in a radar-illuminated cell was developed in Chapter 6. The high degree of nonlinearity and the random nature of this expression make a rigorous analytic study of the properties of the FCF a very difficult task. Instead, in this chapter we will study the characteristics of the FCF, its dependence on the system parameters (radar beamwidth, incidence angle, and system bandwidth), and its relation to the number of scatterers in the illuminated cell using numerical simulation. The numerical simulation, described in Section 8.2, will be used to analyze the problem of embedding a small number of scatterers in a radar-illuminated cell of terrain

and study their effects on the resultant FCF. In Section 8.3 we report on the use of the physical interpretation of the FCF and its relationship to the time-domain signal, introduced in Chapter 6, to gain more physical insight the characteristics of the FCF. The FCF characterization and its relation to the number of scatterers within the radar-illuminated cell along with the results of the numerical simulations will be used to develop an enhanced detection algorithm that is described in Section 8.4. Moreover, the numerical simulation will be used to generate a data set of the FCF of terrain and of terrain with one and more single scatterers embedded in it. This data set will be used to evaluate the performance of the developed detection algorithm. In addition, in Section 8.5 we will use the numerical simulation to study the relationship between the radar system bandwidth and both the characteristics of the FCF and the performance of the detection algorithm. The performance of the detection algorithm introduced in this chapter will be compared to the performance of the one presented in Chapter 7 and the effect of adding more detection features on the performance of the detection algorithm will be demonstrated in Section 8.6.

A point worth mentioning here is that, because the frequency response of tree trunk is the closest, compared to other nearby targets, to the behavior of a single scatterer (as shown in Chapter 6), the terms single scatterer and tree trunk will be interchangeably used throughout this chapter.

8.2 Numerical Simulation Procedure

As shown in chapter 2, the scattering from statistically homogeneous terrain follows the Rayleigh statistical model. Hence, we can simulate the FCF of the radar backscattered from a statistically homogeneous terrain as follows:
(a) simulate the total field backscattered from a statistically homogeneous terrain by coherently adding the scattering by a large number of scatterers with their scattering amplitudes following the Rayleigh statistics and are randomly positioned within the illuminated cell, then
(b) use the total backscattered field to calculate the FCF.

To reflect these properties into the simulation code, the illuminated cell is divided, as a mesh, into small pixels of dimensions $\Delta x \times \Delta y$ and the scatterers are positioned at the centers of these pixels. The amplitudes of the backscattered field from scatterers are presented in the simulation code as a sum of real and imaginary independent Gaussian random variables (to introduce random phase), and their $Z-$coordinates (heights) were assigned values based on a Gaussian random height profile generation with a predefined profile roughness standard deviation σ_{height}. The height profile is introduced to study the effect of the terrain roughness parameters on the properties of the FCF, while the complex backscattered amplitudes were introduced to provide random phases as substitution for the randomness in position within the illuminated cell.

The setup of the problem that we need to simulate is shown in Fig. 6.2, which

is reproduced in Fig 8.1 for convenience, where a radar system of bandwidth BW illuminates an area A of terrain at a grazing-angle θ_i. The radar beam is chosen, for convenience, to be of square cross section, $L \times L$ m. Hence, in one direction, chosen to be along the $X-$axis, the illuminated cell has a grazing-angle dependent dimension, $L/sin(\theta_i)$, while in the other direction, chosen to be along the $Y-$axis, its dimension remains constant, L, and independent of the grazing-angle θ_i.

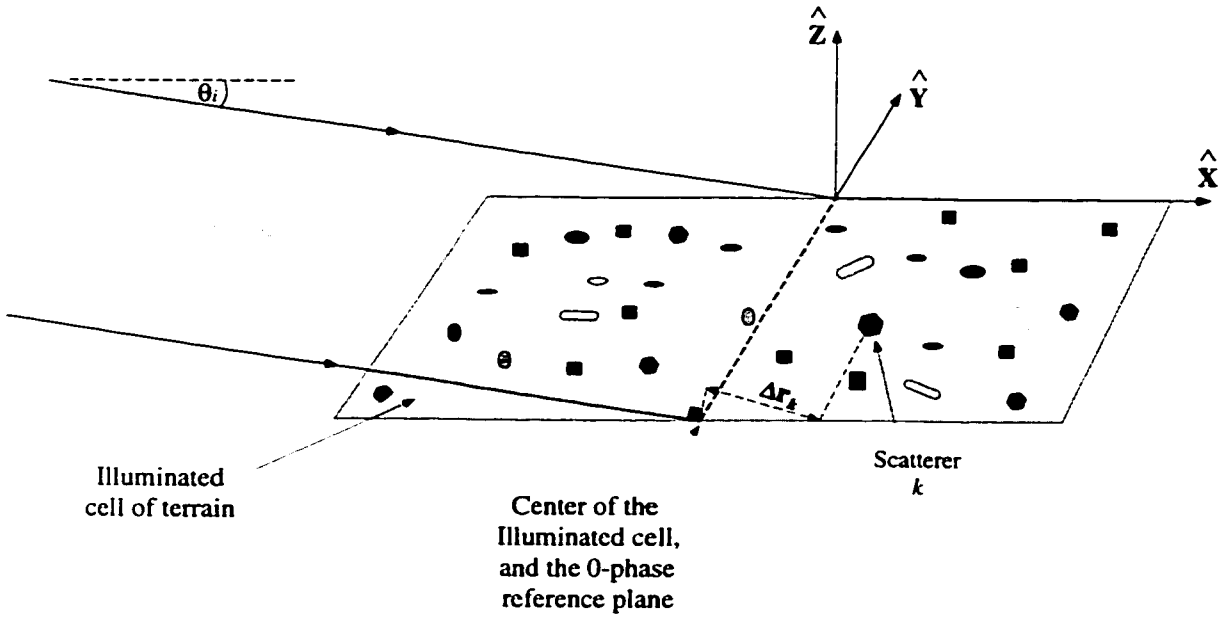

Figure 8.1: Illustration of the setup for the general case of backscattering by terrain.

8.2.1 Parameter Setup

Remote sensing detection of tree trunk(s) in an illuminated cell of terrain must be based on noticeable changes in some features of the signal backscattered from this cell due to the presence of this/these tree trunk(s). Moreover, the range of validity of a detection algorithm is defined such that it assures these detection features to exhibit as much changes as possible due to the presence of tree trunk(s). Hence, to investigate the usefulness of the FCF in detection, the setup parameters must be chosen to guarantee the maximum possible, but practical, differences between the FCF of terrain and that of a tree trunk.

It was shown in Chapter 6 that the FCF is the Fourier transform of the amplitude-squared time-domain reversed signal. This relationship suggests the choice of the setup parameters (the applicability range) that results in a wide (or spreaded) time-domain response from the terrain such that it is distinguishable from that of a single scatterer which is the closest to a delta function.

An important property of the FCF of the backscattered response of terrain that is worth mentioning here is that, the decrease of the grazing-angle θ_i, causes:

I- The decrease of FCF dependency on the parameters of the terrain (e.g. surface roughness), as shown in [34], and

II- The increase in spread in the time-domain backscattered response from the illuminated cell which in turn results in a narrower FCF.

On the other hand, increasing the radar grazing-angle, θ_i, causes the parameters of the terrain to come into the picture and affect the behavior of the FCF, and causes the time-domain backscattering response of the terrain to be narrower to the point that it becomes almost similar, in behavior, to that of a single scatterer at θ_i close to 90^o.

The dependence of the FCF on the incidence angle limits the range of usefulness (applicability) of the FCF in detecting one or more single scatterer(s) with a terrain in the background to the near grazing angles. In this configuration,

I- The dependence of the FCF on the parameters of the terrain is negligible, which makes the FCF-based features almost universal detection features with respect to the type of terrain, and

II- Better detectability is expected, since the behavior of the FCF of terrain is very distinguishable from that of a single scatterer. That is, at near-grazing angles the FCF of the terrain is much wider in the time domain, hence, much narrower than the FCF of a single scatterer .

Based on the above discussion, throughout this chapter the numerical simulations are performed at a grazing-angle θ_i of 10^o and the radar beam cross section is chosen to be 2×2 m to insure a wide, enough, time-domain response from the terrain. The system bandwidth is selected to be 2 GHz sampled over 801 discrete frequency points. However, the effect of the system bandwidth on the behavior of the FCF will

be studied in details later in this chapter.

To set the values of the terrain height profile parameters, their effects on the behavior of the FCF were studied. Five hundred realizations of the $FCF_{terrain}$ at 3 different values of standard deviation, σ_{height}, of the height profile (1, 5, and 10 mm) were generated using 2 GHz system bandwidth at 10^o grazing-angle. Comparisons among the behaviors of the FCF's in these three different cases showed σ_{height} to have an insignificant effect on the behavior of the FCF at this setup. This result can be attributed to the single look nature of this study and to the small look angle which makes the variations in σ_{height} of negligible effect on the spread of the backscattered signal in the time domain, hence, of negligible effect on the properties of FCF. Therefore, σ_{height} is chosen to be 1 mm throughout this study.

8.3 Physical Insight

The numerical simulations were used to generate the FCF of the backscatter from radar-illuminated cells of statistically homogeneous terrain and from cells that contain one or more single scatterer(s). These FCF's were then examined to characterize the dependence of the FCF on the type of scatterers (single versus terrain) existing in the illuminated cell.

The simulated FCF of the terrain, shown in Fig. 8.2, and those of one, two, three, and five single scatterers, shown in Fig. 8.3, exhibit the following differences:

1. $\mathrm{FCF}_{terrain}$ decorrelates much faster than FCF_{one}, and FCF_{two}. In other words, the FCFBW of terrain is much smaller than the FCFBW of one, and two single scatterers.

2. The average slope of the tail of the $|FCF_{terrain}|$ is less negative than that of $|FCF_{one}|$, $|FCF_{two}|$, $|FCF_{three}|$, and $|FCF_{five}|$.

3. The variation of the tail of the $|FCF|$ around the line of average slope is zero in the case of a single scatterer, and in the case of terrain the variation is smaller than the cases of two or more scatterers.

However the above results are for one or more single scatterers positioned arbitrarily in a radar-illuminated cell in the absence of the background-terrain, they depict some difference in behavior to be considered in detection. The more realistic situations (which must be considered for detection) are those of one or more single scatterers being arbitrarily positioned in an illuminated cell in the presence of the background terrain.

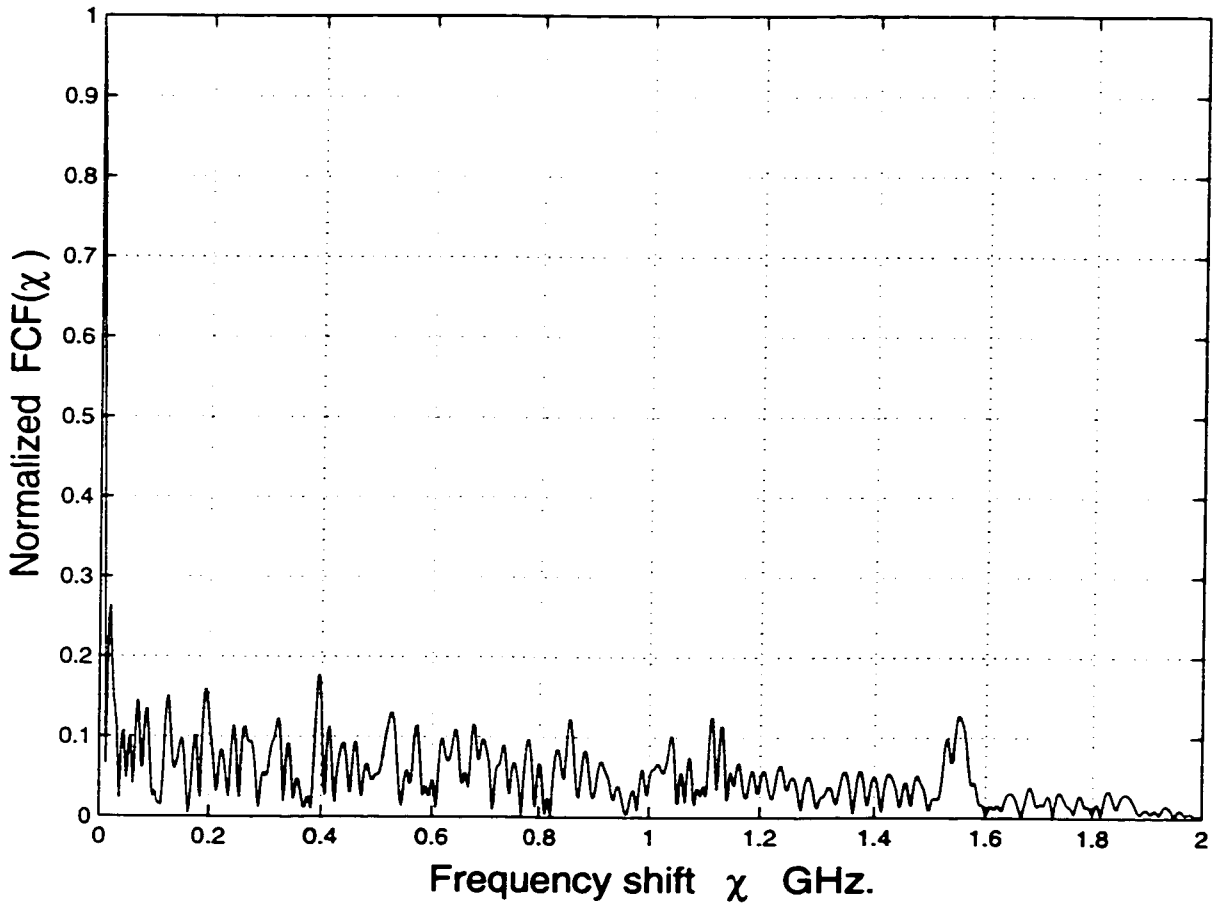

Figure 8.2: Example of the normalized $|\mathrm{FCF}(\chi)|$ of a statistically homogeneous terrain.

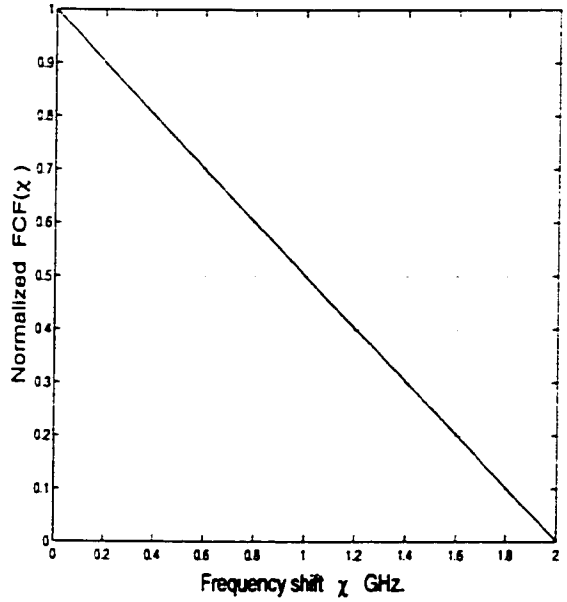

(a) One scatterer

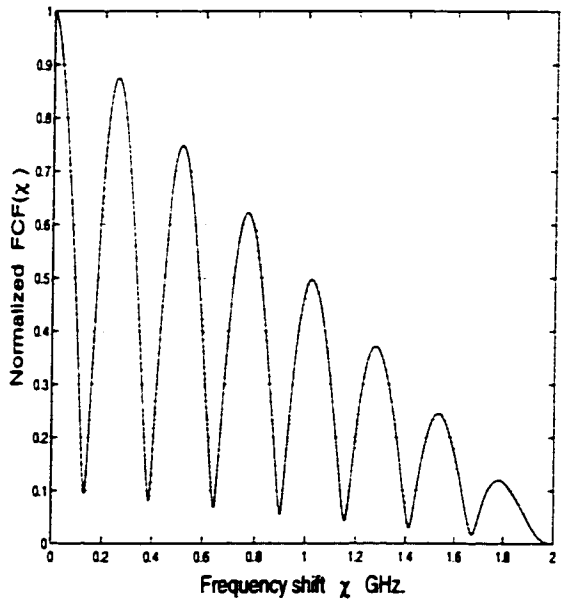

(b) Two scatterers

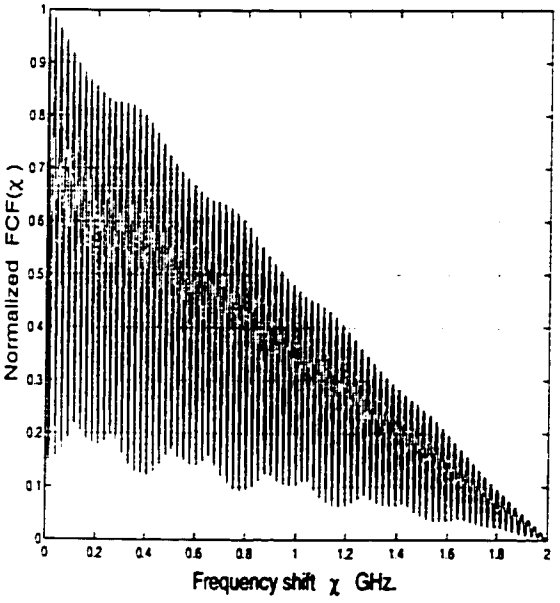

(c) Three scatterers

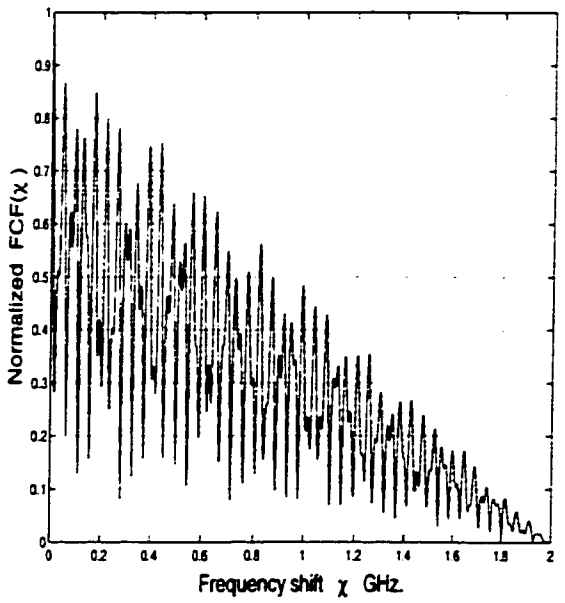

(d) Five scatterers

Figure 8.3: Examples of $|\mathrm{FCF}(\chi)|$ variation as a function of frequency shift χ for different numbers of identical scatterers randomly positioned in a radar-illuminated cell.

8.3.1 Verification of Concept

Before analyzing the results of simulating the more realistic cases of one or more single scatterers embedded in an illuminated cell of terrain, we can deploy equation(6.16) to get more physical insight the behavior of the FCF. Equation(6.16),

$$FCF(\chi) \approx \sum_{k=1}^{N} FCF_{kk}(\chi),$$

states that the FCF of the backscatter from a radar-illuminated cell is, approximately, the coherent sum of the FCF of all the scatterers existing in this cell. Considering all the scatterers composing the terrain —all together— as scatterer number #1 and the group of single scatterers as scatterer number #2, enables us to predict the resultant FCF by deploying the approximate expression of equation(6.16). However, we need to examine its accuracy first.

To evaluate the accuracy of this approximate expression, we used the simulation code to generate the FCF for many cases of terrain with one or more single scatterer(s) embedded in it, based on both (the exact and the approximate) expressions, then compared their results.

Figure 8.4 shows the exact and the approximate variations of the $|FCF(\chi)|$ of terrain with one, two, and three single scatterers embedded in the illuminated cell. The plots of Fig. 8.4 show the high degree of accuracy of the approximate expression of FCF, equation(6.16), compared to the exact expression, equation(6.11). Hence, it can be used to predict the effects of embedding one or more single scatterer(s) in a

radar-illuminated cell of terrain on the behavior of FCF_{total}.

Another test for the accuracy of the approximate expression, equation (6.16), is to examine the amplitude of the neglected cross-correlated components. Figure 8.5 shows the amplitudes of the four components of the FCF(χ) (which are: FCF_{11}, FCF_{12}, FCF_{21}, and FCF_{22}) for three different cases of a cell of terrain with one, two, and three single scatterers embedded in it. The figure demonstrates that the amplitudes of the FCF_{12}, and FCF_{21} are negligible to the sum of FCF_{11}, and FCF_{22} (as expected from equation(6.15)) with the exception near the end of the tail of the $|FCF|$ where the four components are of small amplitude. Hence, plots of Fig. 8.5 represents another verification for the accuracy of the approximate expression of equation (6.16).

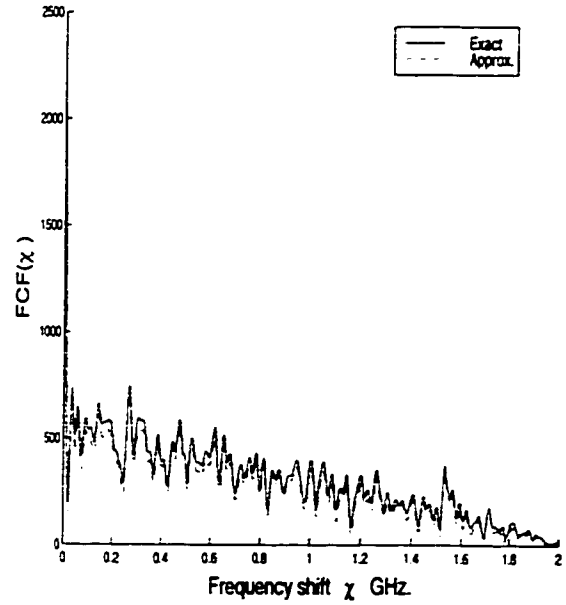

(a) One single scatterer

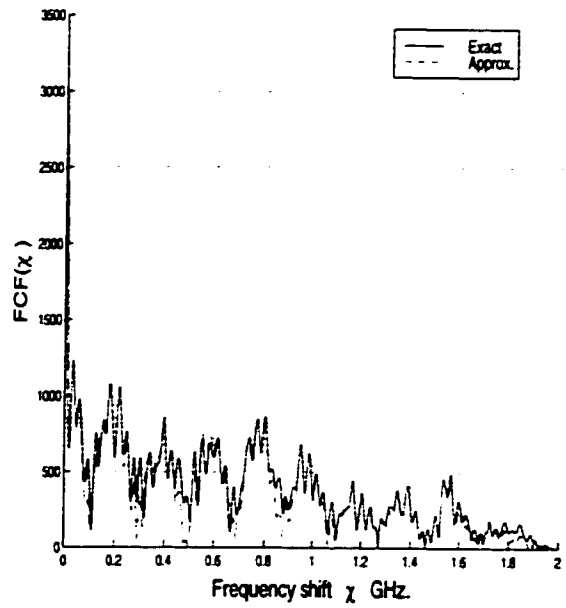

(b) Two single scatterers

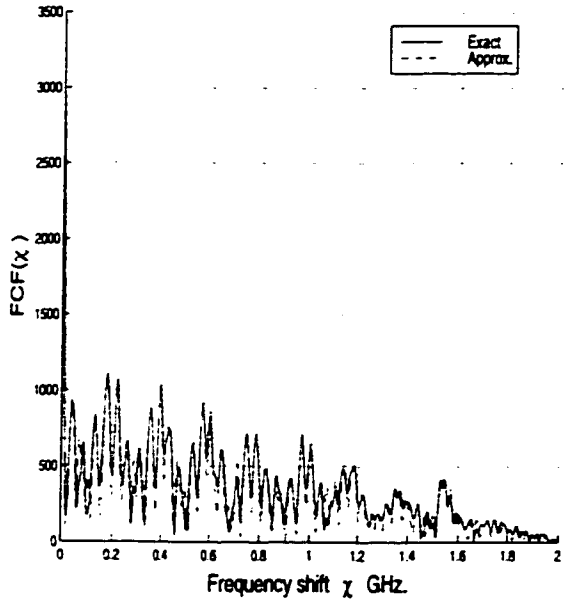

(c) Three single scatterers

Figure 8.4: Comparison between the exact and approximate FCF(χ) of a terrain (random surface) with one or more single scatterers embedded in it.

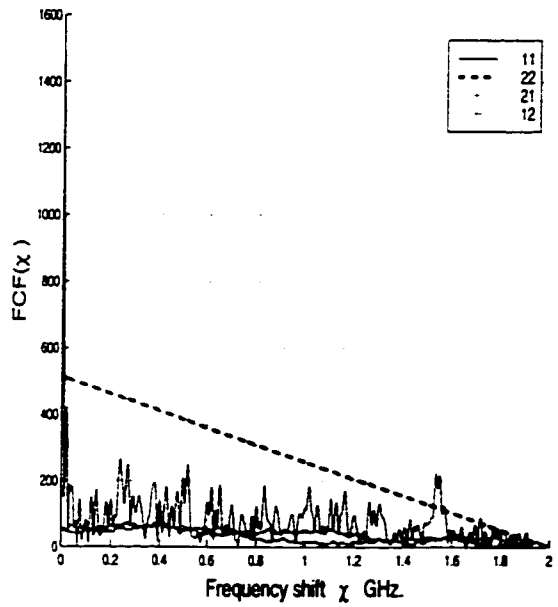

(a) One single scatterer

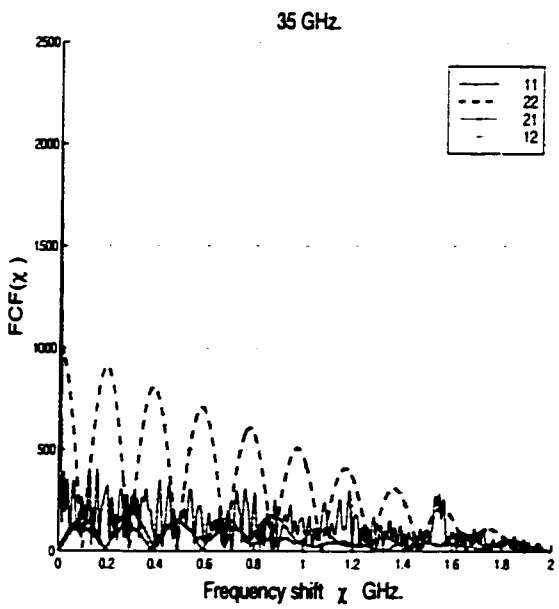

(b) Two single scatterers

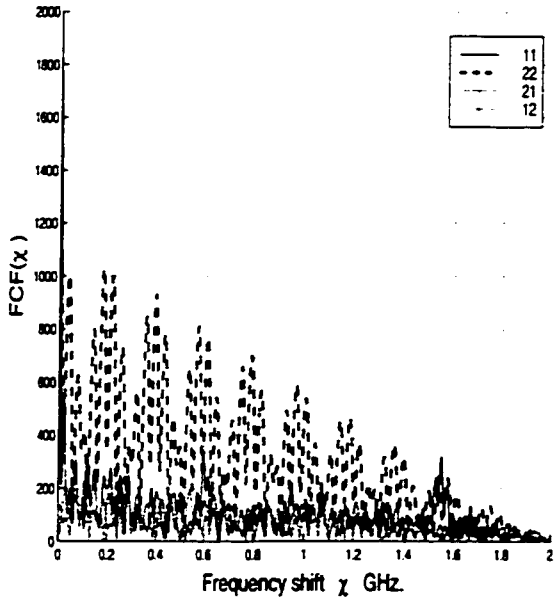

(c) Three single scatterers

Figure 8.5: The four components of the FCF(χ) of a terrain (random surface) with one or more single scatterers embedded in it.

8.3.2 Qualitative Analysis

To visualize the effects of embedding a single scatterer in an illuminated cell of homogeneous terrain on the resultant FCF, the simulation code was used to evaluate the FCF for terrain with a single scatterer embedded in it for different values of the **T**arget to Clutter **R**atio (TCR). The TCR is defined as the ratio of the backscattered power from the single scatterer to the average backscattered power from the terrain. Mathematically it is expressed as:

$$\textbf{Target to Clutter Ratio} \;=\; TCR \;=\; \frac{(SS_{Amp})^2}{N * \bar{P}}, \tag{8.1}$$

where, SS_{Amp} is the amplitude of the radar backscattered from the single scatterer which exist in one pixel of the illuminated cell, N is the number of pixels of the illuminated cell, and $\bar{P}$ is the average backscattered power from a pixel of the terrain.

Figure 8.6 shows the amplitude-variations of the FCF(χ) of a cell of terrain with a single scatterer (for four different TCRs of the single scatterer) embedded in it. It is observed, from Fig. 8.6, that based on the TCR of the single scatterer, the FCF_{total} will be either closer to the shape of the $\text{FCF}_{terrain}$ (as in Fig. 8.6-a), closer to the FCF_{one} (as in Fig. 8.6-c,d), or in between (as Fig. 8.6-b). Also, from Fig. 8.6 along with Fig. 8.4, it is observed that the effects —from radar standpoint— of embedding one or more single scatterers in an illuminated cell of terrain is more noticeable at the tail of the $|FCF|$. This is attributed to the small amplitude at the tail of the $|FCF_{terrain}|$ (Fig. 8.2) which allows the behavior of the FCF of a single scatterer(s) to dominate, even if it has a small TCR. This is as opposed to the range of small

frequency-shift where the $|FCF_{terrain}|$ has a large amplitude. Hence, using the FCF-based features near the tail of the $|FCF|$ to detect single scatterers in an illuminated cell of terrain is more promising than using them in the vicinity of the zero-frequency shift.

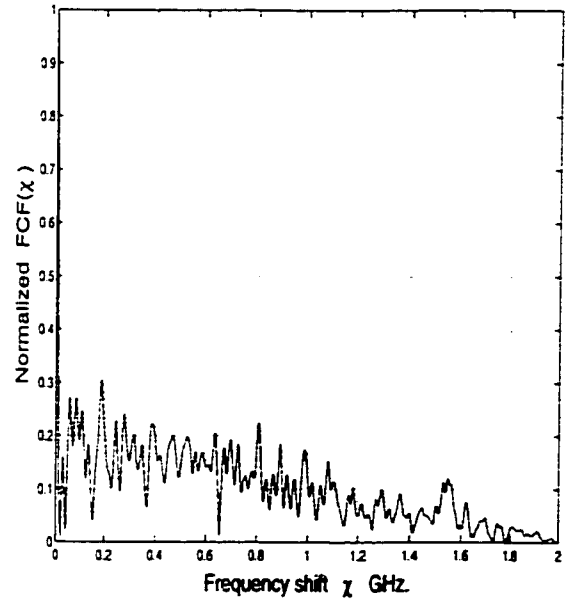

(a) TCR = 0.35

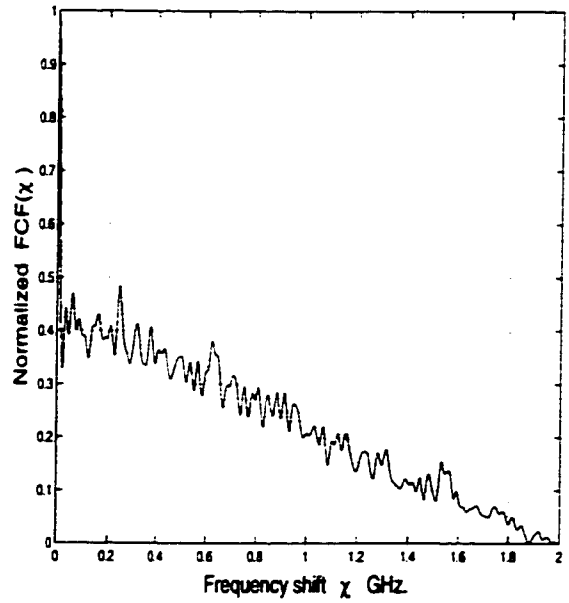

(b) TCR = 1.27

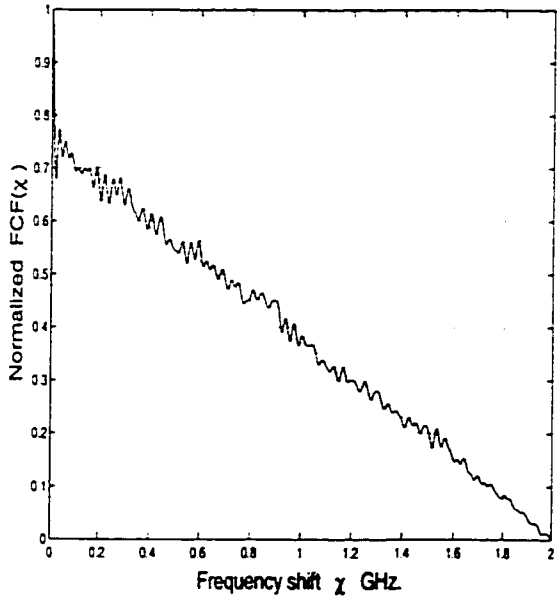

(c) TCR = 6.14

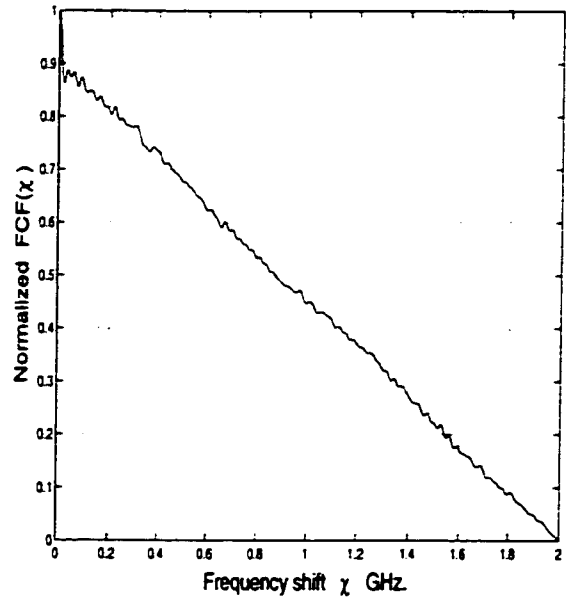

(d) TCR = 19

Figure 8.6: The amplitude of the FCF(χ) of terrain with single scatterer embedded in it for four different TCR.

8.4 Detection Features and Algorithm

Since, the behavior of the FCF of terrain differs from those of one, two, or more single scatterers, as shown in figures 8.2 and 8.3, embedding one or more single scatterers in an illuminated cell of terrain would (based on the relative amplitudes of the two FCF's) cause noticeable differences in the behavior of FCF_{total} from that of $\mathrm{FCF}_{terrain}$. These possible changes in the behavior of FCF_{total} are the keys to detect the presence of single scatterers in the illuminated cell. Therefore, the candidate detection features are: **F**requency Correlation **F**unction **B**and**W**idth (FCFBW), the average slope of the tail of the $|FCF|$, the squared error of the amplitude of the tail with respect to the line of average slope, and the ratio of the last two features. These features are defined as follows:

FCFBW: is, as defined in Section 7.2, the frequency shift β at which the FCF amplitude drops to $1/e$ of its value at zero frequency-shift. That is,

$$FCFBW = \beta \; : \qquad FCF(\beta) = \frac{FCF(0)}{e}. \tag{8.2}$$

Average Slope: is the average slope of the middle section of $|FCF|$. In the simulations at hand, this corresponds to frequency steps 76-726 out of the total 801 frequency steps,

Squared Error: is the average of the difference-squared between the $|FCF|$ and the line of average slope at the middle section of $|FCF|$ corresponds to frequency steps 76-726, and

Ratio: is the ratio of the average slope to the squared error.

A note worth mentioning here is that, for convenience, we chose the average slope and the squared error to be calculated with respect to the number of frequency steps instead of the frequency shift.

To examine the usefulness of these features in detection, a data set of FCFs of the backscattered response of statistically homogeneous terrain with no single scatterer embedded and with one, two, and more single scatterers embedded were generated. For each case (of certain number of single scatterer embedded), the FCFs were generated at 20 different values of TCR of single scatterers. In addition, for the case of terrain with no single scatterer embedded, 1000 statistically independent realizations were generated, while for each case of a specific number of embedded single scatterers with specific TCR, 50 different realizations were generated.

Figures 8.7-8.10 show examples (no single scatterer, one single scatterer, two single scatterers, and five single scatterers embedded) of the variations of the four FCF-based detection features of concern with the TCR of the embedded single scatterers as well as their variabilities (due to randomness of the scatterers positions and randomness of the terrain in the background) at each specific case (specific number of embedded single scatterers with specific TCR). Based on figures 8.7-8.10, the following observations were made:

1. FCFBW in the case of terrain with one, two, and five single scatterers embedded (at TCRs of single scatterers greater than 0.5, 0.4, and 0.35 respectively) are, in

most of the cases, greater than the FCFBW of terrain with no single scatterer embedded . This behavior makes the FCFBW a candidate detection feature for the presence of single scatterer(s) of large TCRs.

2. The average slope of $|FCF_{terrain}|$ is mostly greater than -1×10^{-4}, while it is, mostly, less than -1×10^{-4} in the cases of terrain with one, two, and five single scatterers embedded with TCRs greater than or equal to 0.12. This behavior makes the average slope a candidate detection feature to detect the presence of single scatterer(s) embedded in a terrain at, almost, all range of TCR.

3. The squared error in case of terrain with no single scatterers embedded is less than 1.6×10^{-3}, while it is less than 2×10^{-3} in case of terrain with one single scatterer embedded and it decreases with the increase of TCR. In contrast, for terrain with two or five single scatterers embedded, the squared error is greater (in most of the cases of TCRs ≥ 0.25) than 2×10^{-3} and it increases with the increase of the TCR. This behavior makes the squared error a candidate detection feature to discriminate one single scatterers from two or more single scatterers embedded.

4. The ratio in case of terrain with one single scatterer embedded is smaller, in most of the cases, than -0.12, while it is greater than -0.12 in most of the other cases. This behavior makes this ratio a candidate detection feature to discriminate the cases of terrain with one single scatterer embedded from the others.

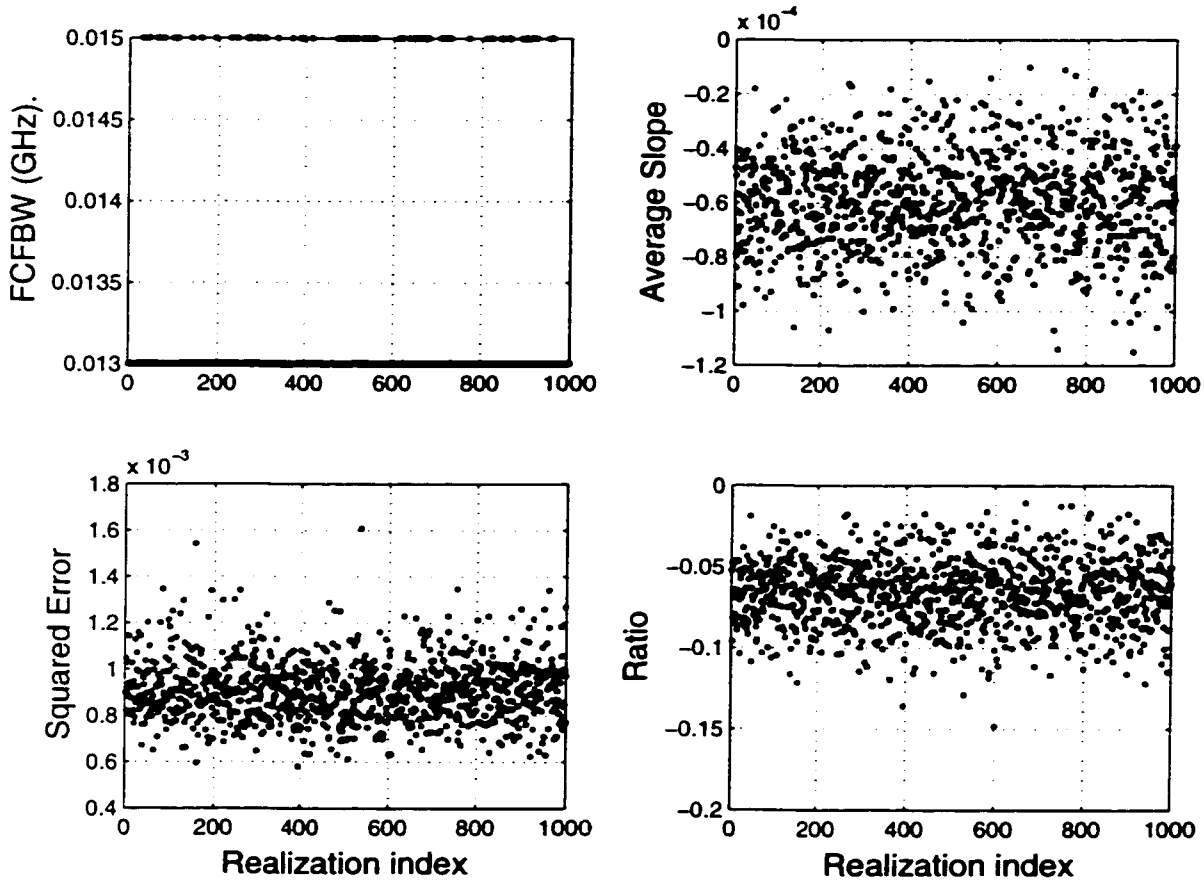

Figure 8.7: Variations of the four detection features for the case of terrain with no single scatterer embedded, with 2.0 GHz system bandwidth.

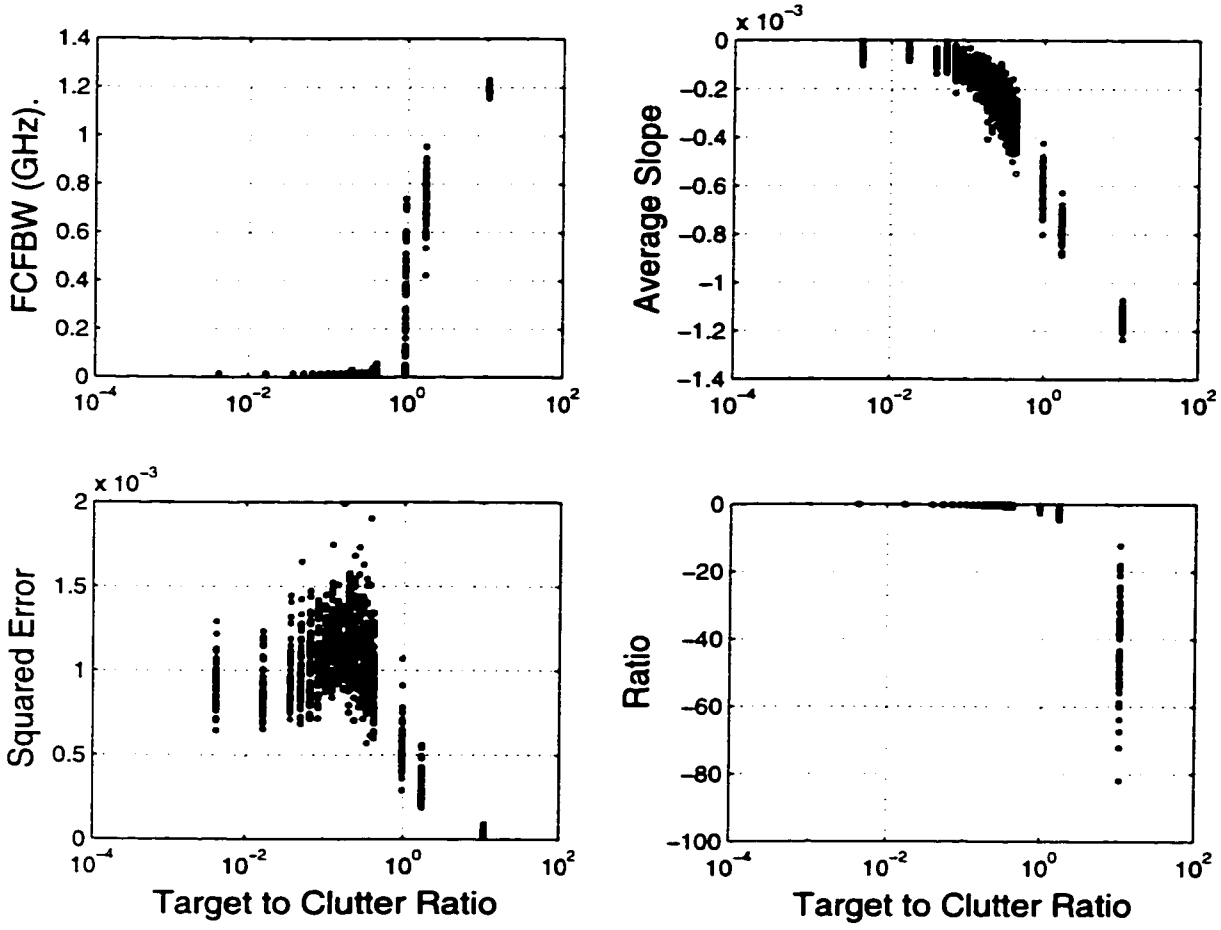

Figure 8.8: Variations of the four detection features as functions of the single scatterer TCR for the case of terrain with one single scatterer embedded, with 2.0 GHz system bandwidth.

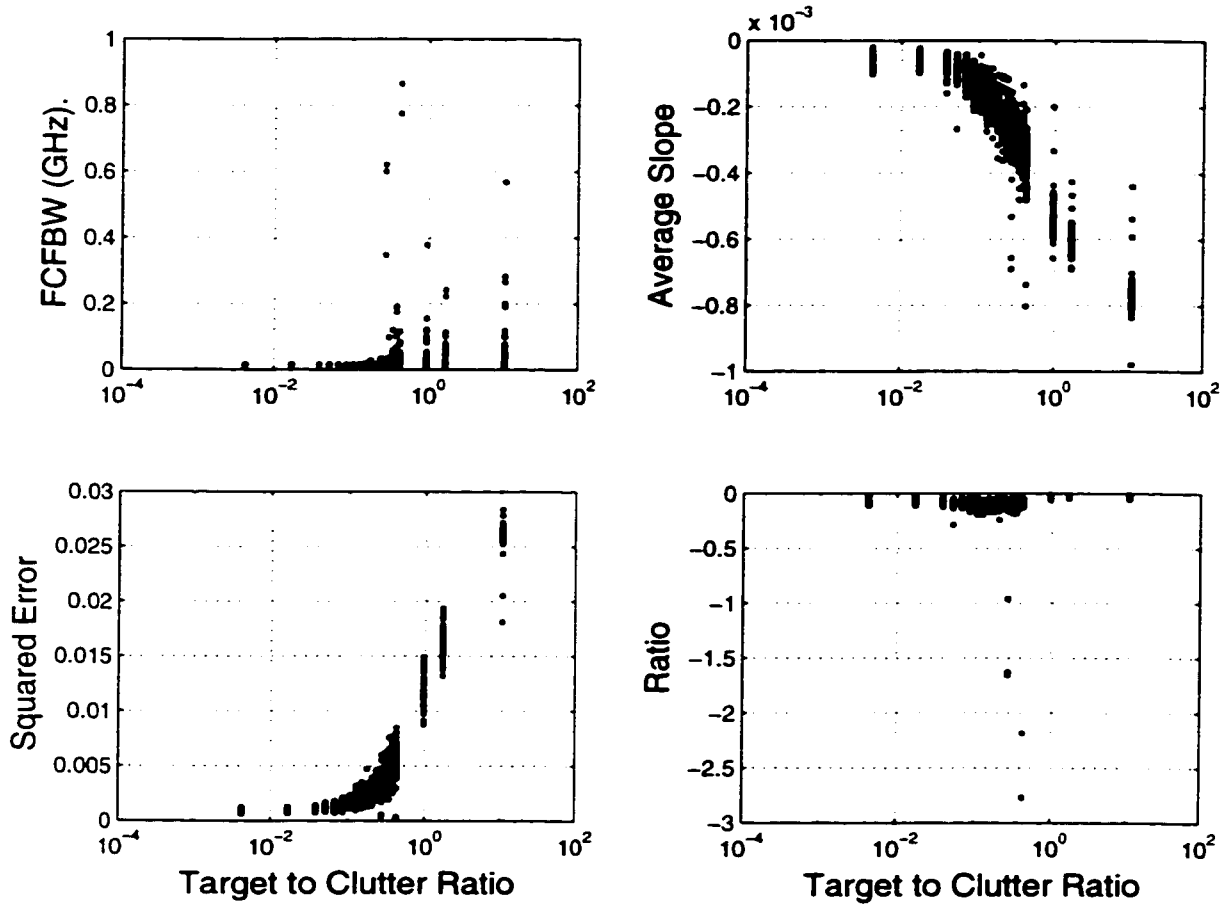

Figure 8.9: Variations of the four detection features as functions of the single scatterer TCR for the case of terrain with two single scatterers embedded, with 2.0 GHz system bandwidth.

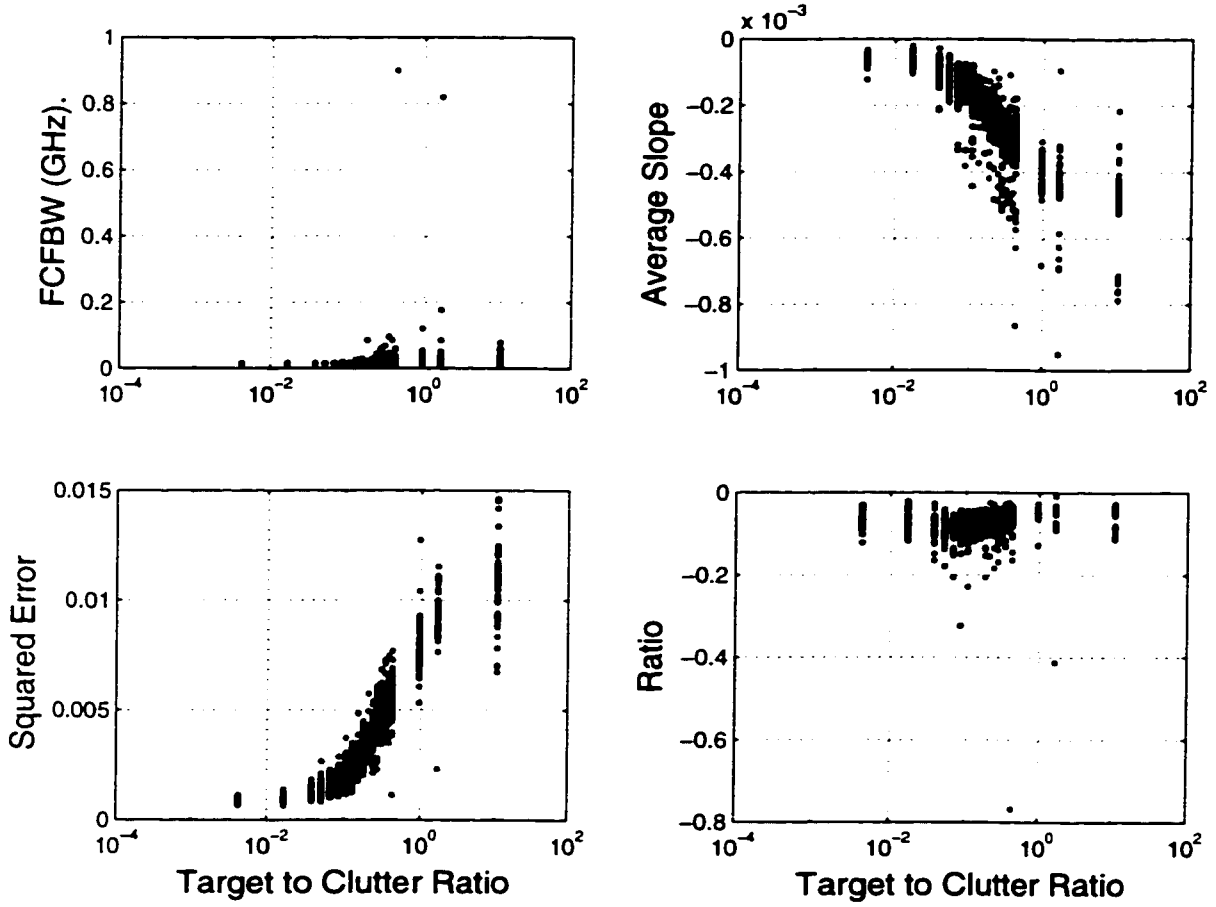

Figure 8.10: Variations of the four detection features as functions of the single scatterer TCR for the case of terrain with five single scatterers embedded, with 2.0 GHz system bandwidth.

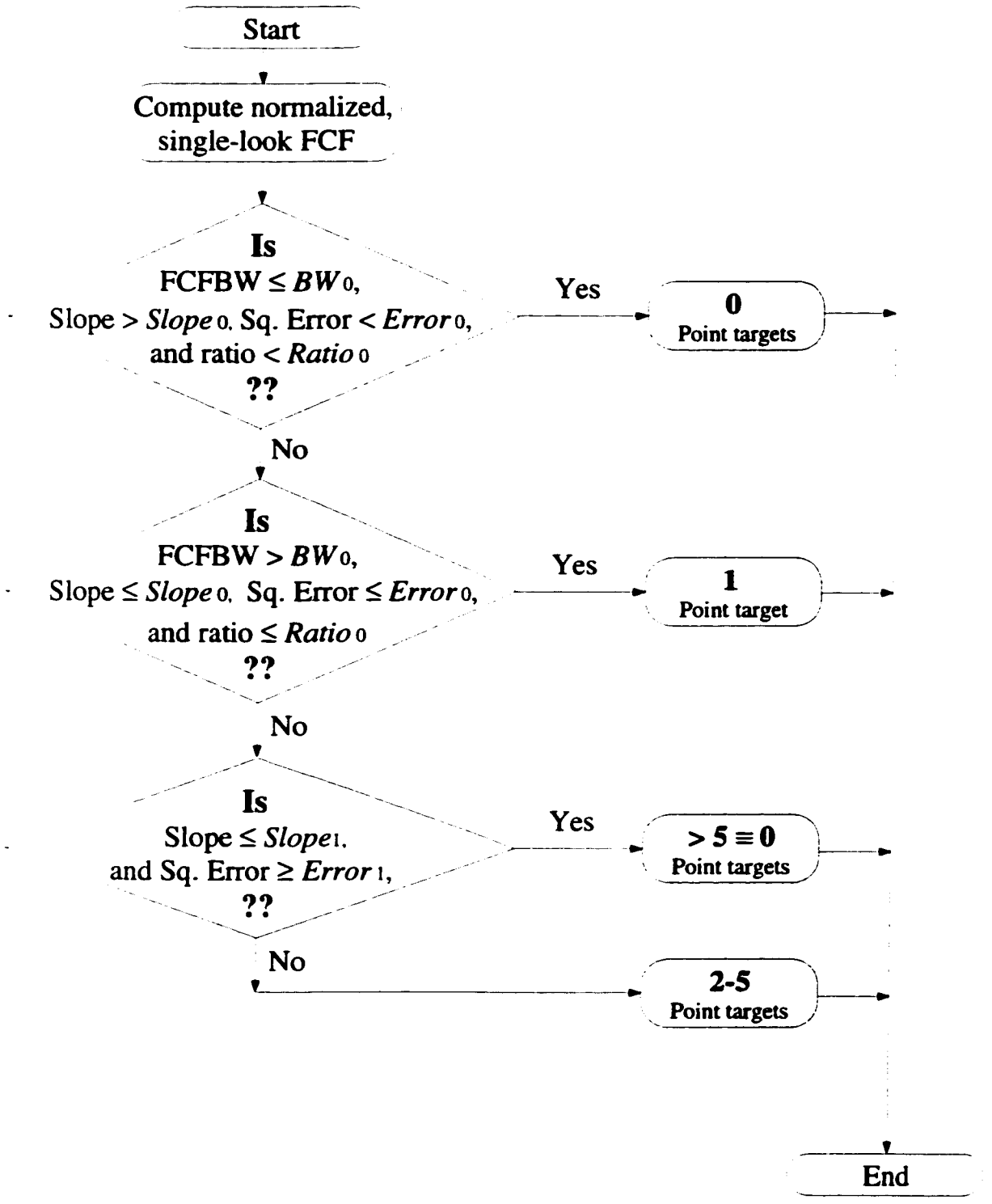

Figure 8.11: Flow chart of the enhanced detection algorithm. Parameters of the algorithm are in italic font.

Using the FCFBW, the average slope, the squared error, and the ratio, an enhanced detection algorithm, shown in Fig. 8.11, is designed with the following properties:

1. The detection algorithm is designed to make one of three possible decisions which are: 0 (no single scatterer embedded), 1 (one single scatterer embedded), 2-5 (a number of single scatterers embedded and this number is between two and five).

2. The case of more then 5 single scatterers embedded in the illuminated cell is considered as a case of no single scatterer embedded.

The performance of the developed detection algorithm was evaluated by applying it to the data set generated by the numerical simulation. Based on the variations of the four FCF-based detection features (some cases are shown in figures 8.7-8.10), the parameters of the detection algorithm were set to the following values:

- $BW_o = 0.015$ GHz,
- $Slope_0 = 0.95 \times 10^{-4}$, $Slope_1 = 6.0 \times 10^{-4}$,
- $Err_0 = 0.0015$, $Err_1 = 0.01$, and
- $Ratio_0$ = -0.12.

The decision, either 0, 1, or 2-5, resulted from applying the detection algorithm to each case, of specific number of single scatterers with specific TCR, of the data set is

recorded, then the percentage of indicating each of the three possible decisions were calculated and plotted. These plots of the performance of the detection algorithm, shown in figures 8.12-8.14, show the following:

- For the case of no single scatterer embedded, Fig. 8.12-a, the detection algorithm results in 0% false alarm rate. In other words, the detection algorithm made a correct decision in all the cases of terrain with no single scatterer.

- For the case of one single scatterer embedded, Fig. 8.12-b, the detection algorithm shows the ability to detect a single scatterer in all the cases of TCR $\geq$ 0.4. The ability of detecting a single scatterer decreases with the decrease of the TCR to the level of reaching almost 0% for single scatterers with TCR $\leq$ 0.05. In case of failure to detect the presence of a single scatterer, the detection algorithm, wrongly, indicates no single scatterer embedded.

- For the cases of two, three, four, and five single scatterers embedded (shown in figures 8.12-c, 8.12-d, 8.13-a, and 8.13-b respectively), the detection algorithm shows its ability to indicate the correct decision for large values of TCR.

- For the cases of more than five single scatterers embedded, 8.13-c, 8.13-d, and 8.14, the detection algorithm indicates 0 (as desired) in most of the cases except for the cases of 6, and 7 single scatterers with high values of TCR, which represents a smooth transition from the cases of 5 single scatterers.

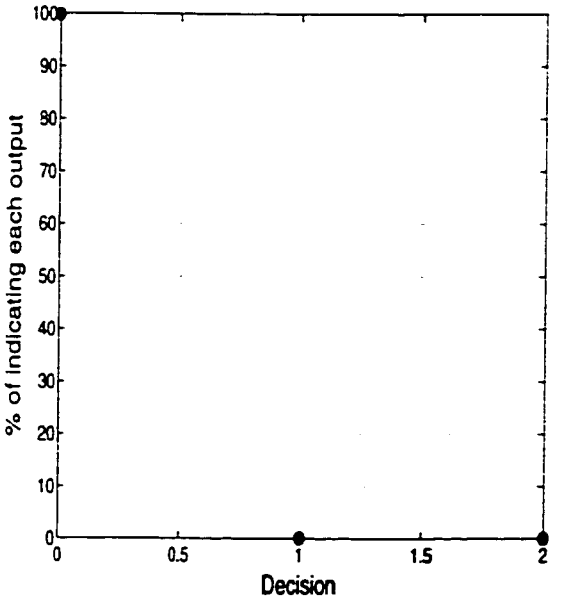

(a) 0 single scatterers

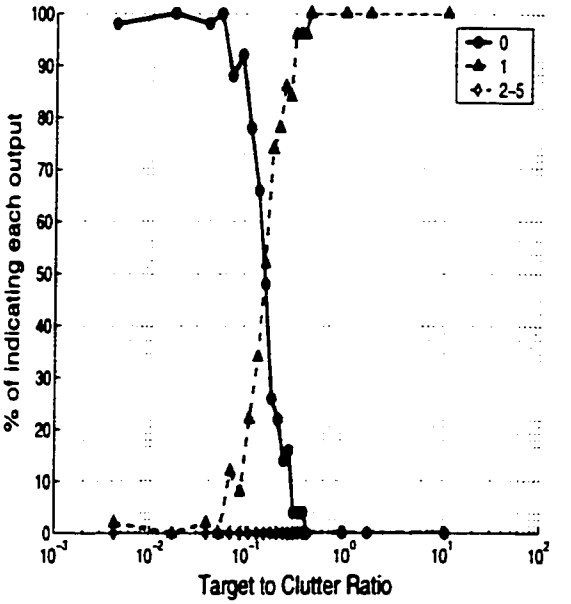

(b) 1 single scatterer

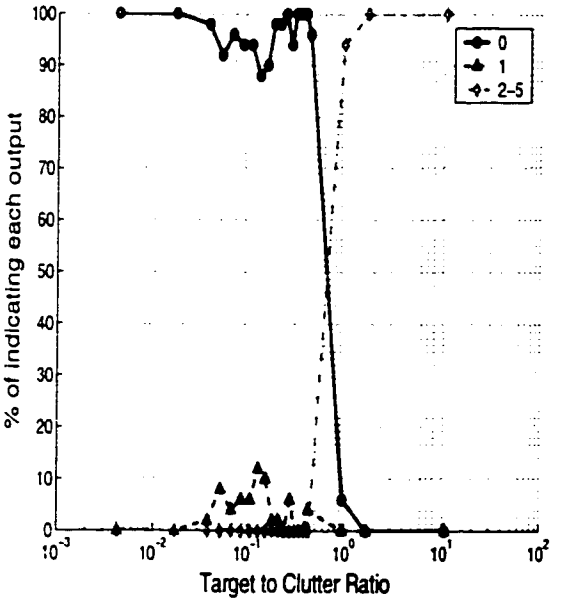

(c) 2 single scatterers

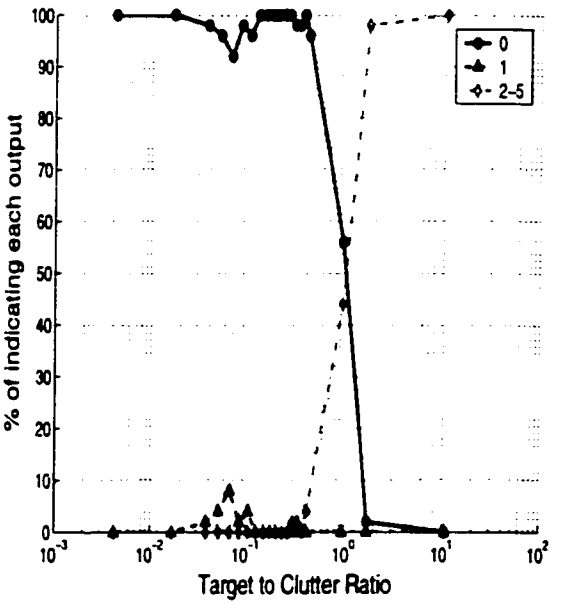

(d) 3 single scatterers

Figure 8.12: Performance of the detection algorithms for the cases of terrain with 0,1,2, and 3 single scatterers embedded in it with 2.0 GHz system bandwidth.

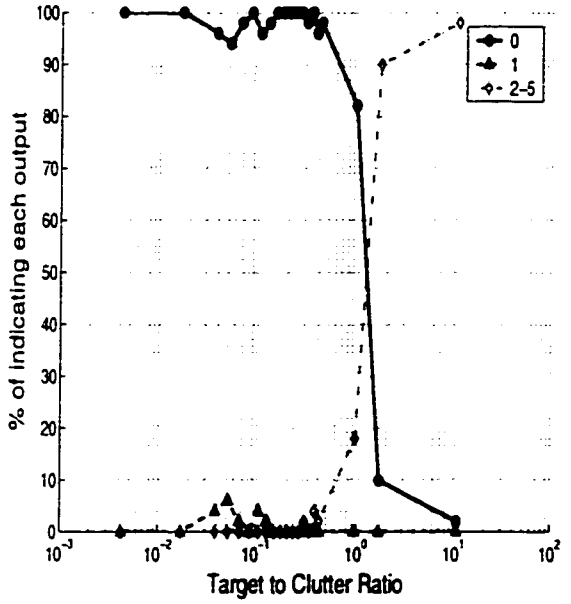

(a) 4 single scatterers

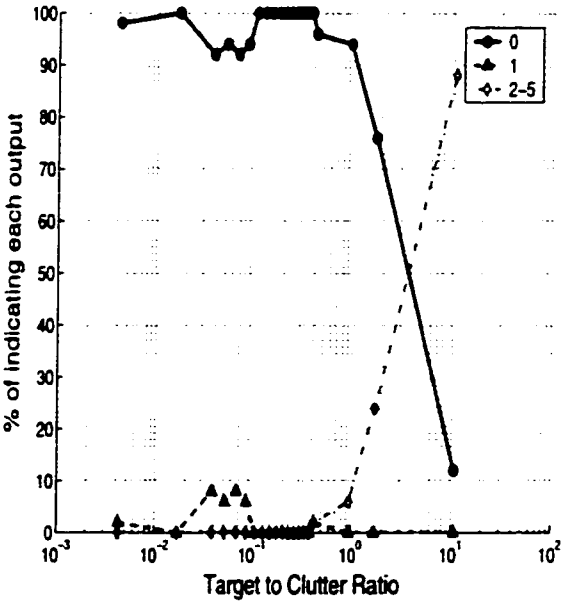

(b) 5 single scatterers

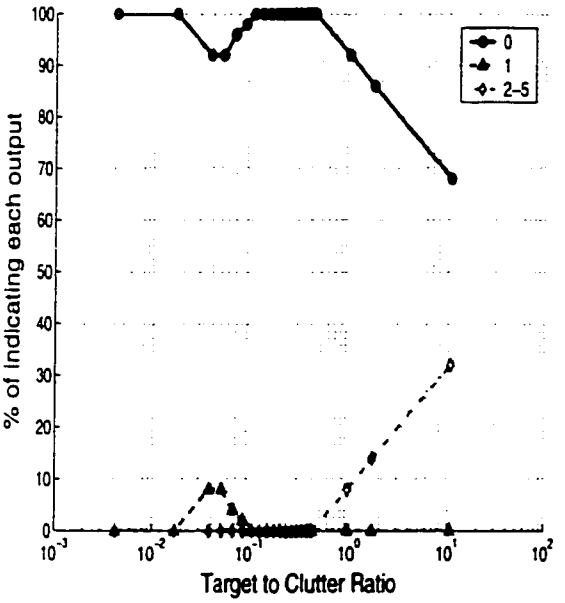

(c) 6 single scatterers

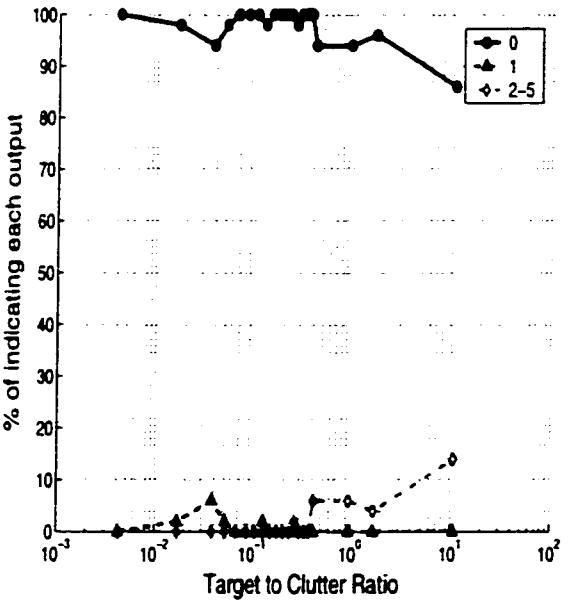

(d) 7 single scatterers

Figure 8.13: Performance of the detection algorithms for the cases of terrain with 4,5,6, and 7 single scatterers embedded in it with 2.0 GHz system bandwidth.

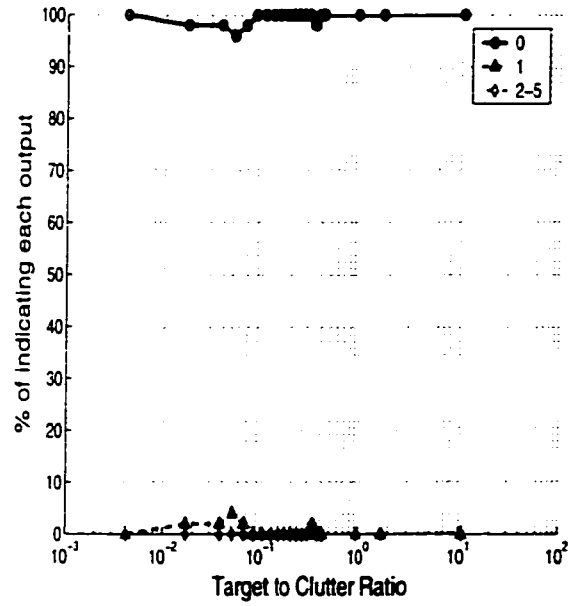

(a) 8 single scatterers

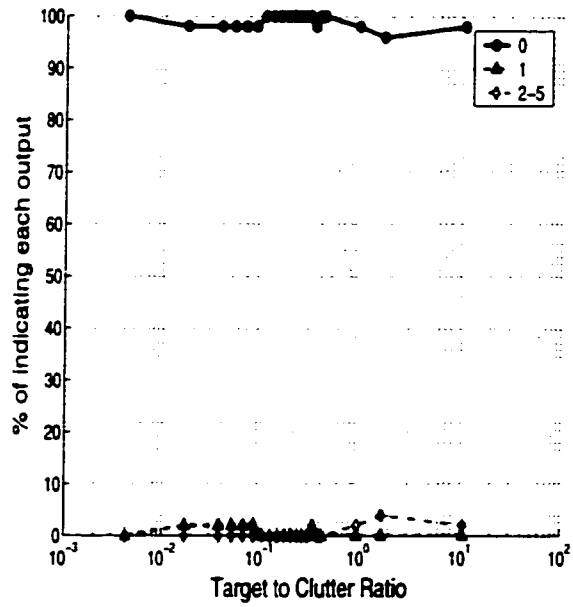

(b) 10 single scatterers

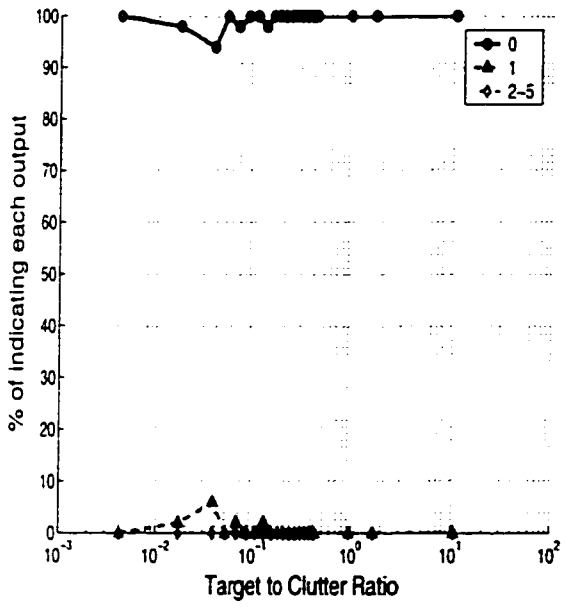

(c) 30 single scatterers

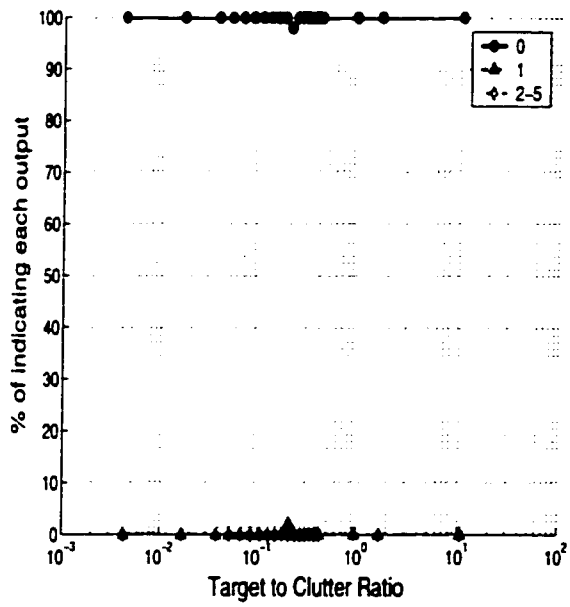

(d) 100 single scatterers

Figure 8.14: Performance of the detection algorithms for the cases of terrain with 8,10,30, and 100 single scatterers embedded in it with 2.0 GHz system bandwidth.

Important Comment

A practical situation that is important to consider here is that, for many remote sensing applications the radar system will be working at near grazing angles at a large distance (1 or 2 km) from the the illuminated cell. Such a situation will result in a large illuminated area, even for a narrow beam radar system. This large area will result in a a small target to clutter ratio (TCR) for any single scatterer that might exist in the cell. This small TCR, as explained earlier in this chapter, will reduce the probability of detecting single scatterers. To overcome this deficiency, the radar system bandwidth can be used in range gating and dividing the radar illuminated cell into sub-cells of smaller areas as shown in Fig. 8.15. Then, apply the FCF-based detection algorithm to each of these sub-cells individually.

The smaller the area of these sub-cells the higher the TCR, but also, the closer the behavior of $FCF_{sub-cell}$ to that of a single scatterer. Consequently, this close behavior of $FCF_{sub-cell}$ to that of a single scatterer will oppose the effect of the increase in TCR. Therefore, the size of the sub-cells need to be optimized to result in the highest possible detectability. In other words, the number of range bins that should be aggregated to make a sub-cell must be selected so as to result in the highest possible detectability of single scatterers.

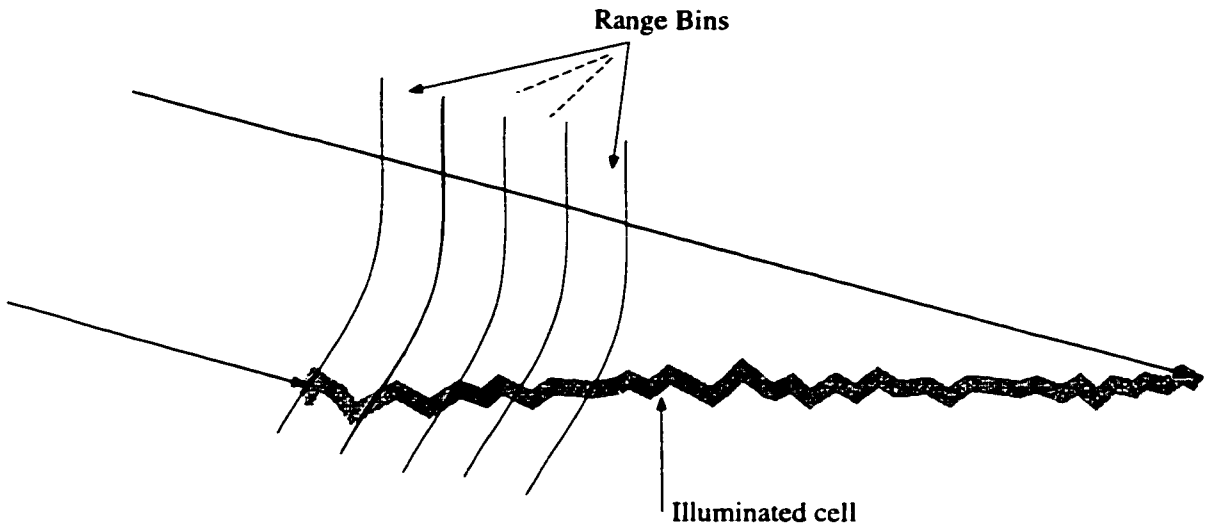

Figure 8.15: Illustration of a practical situation.

8.5 Studying the Effects of the System Bandwidth on the Behavior of FCF and the Performance of the Detection Algorithm

In the previous sections, the characteristics of the FCF of the signal backscattered from terrain with and without single scatterer(s) embedded were studied. In addition, the effects of the system and setup parameters on the behavior of the FCF were discussed except for the effects of the radar system bandwidth. In this section we will investigate the relationship between the radar system bandwidth and the behavior of the FCF. Then, we will examine the dependence of the performance of the detection algorithm on the radar system bandwidth.

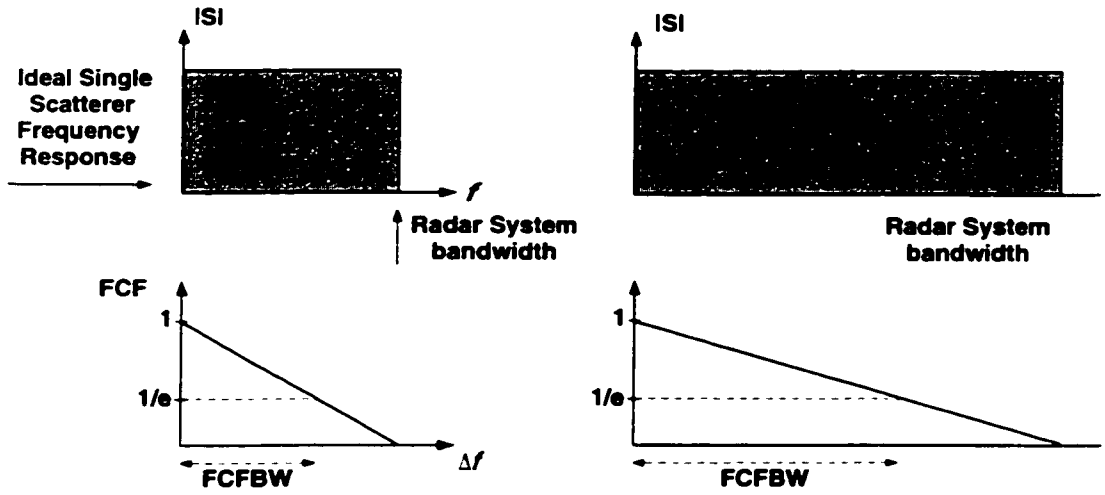

Figure 8.16: The (theoretical) effect of the radar system bandwidth on FCF and FCFBW of an ideal single scatterer.

Theoretically, a single scatterer has a response at MMW frequencies that is frequency-independent, amplitude-wise, and linearly dependent on frequency, phase-wise, over the bandwidth of the radar system. Therefore, for a single scatterer, increasing the radar system bandwidth will cause the FCFBW to increase, as shown in Fig. 8.16. This relation can be precisely explained by equation (6.9) which states that the FCFBW of a single scatterer is linearly proportional to the radar system bandwidth. For terrain, $\mathrm{FCF}_{terrain}$ is approximately the coherent sum of the FCF of a large number of single scatterers. The radar system bandwidth will affect the individual FCF of these large number of scatterers in a way similar to the case of a single scatterers. But, on the other hand, the frequency decorrelation of the FCF_{total} due to the coherent sum is much faster than the linear dependency of the $\mathrm{FCF}_{single\ scatterer}$ on the system bandwidth. Therefore, the effect of the coherent sum dominates and causes the FCFBW of a large set of scatterer (homogeneous terrain) to be independent of the radar system bandwidth.

To rigorously study the effects of the radar system bandwidth on the behavior of FCF, the numerical simulation code was used to evaluate the FCF of homogeneous terrain at three different radar system bandwidths 0.5, 1.0, and 2.0 GHz. Figure 8.17 shows examples of the $|FCF_{terrain}|$ in these three different cases. From Fig. 8.17 (note the difference in the horizontal axis scale) we notice that the FCFBW does not change with the change of the radar system bandwidth (as long as the system bandwidth doesnot become very small).

On the other hand, we notice that the average slope of the $FCF_{terrain}$, slightly, decreases (becomes more steeper) with the decrease of the radar system bandwidth. While this is the case for the homogeneous terrain, the slope of the FCF of a single scatterer remains the same —despite the value of the radar system bandwidth— if the number of frequency steps doesnot change. That is, with the change of the radar system bandwidth, the FCF of one single scatterer (in absence of the terrain) remains a line with a slope $= -1.25 \times 10^{-3}$ and a squared error $= 0$.

For cases of two or more single scatterers (in the absence of the background too), the FCF is expected to decorrelate slower (on the average) with the decrease of the radar system bandwidth, unless the number of single scatterers becomes very large where the resultant FCF becomes similar to the case of homogeneous terrain.

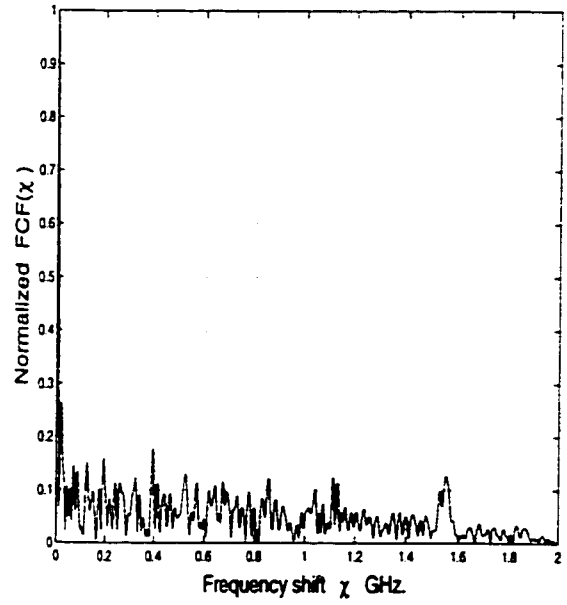

(a) System BW = 2 GHz

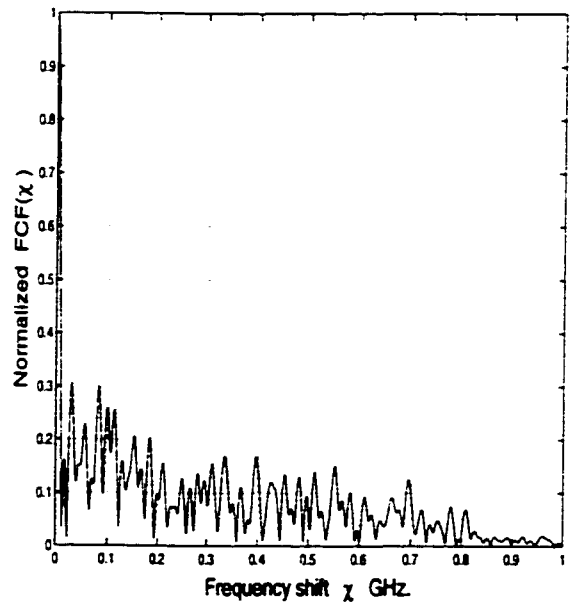

(b) System BW = 1 GHz

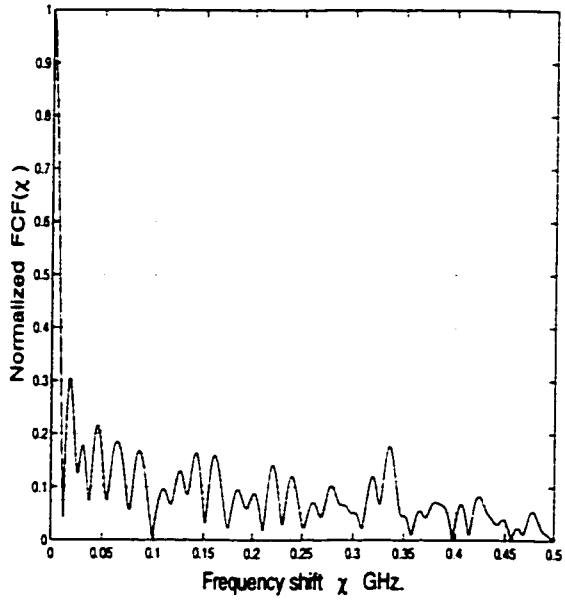

(c) System BW = 0.5 GHz

Figure 8.17: Variations of the $|\mathrm{FCF}_{terrain}(\chi)|$ as a function of the frequency shift χ for different values of the radar system bandwidth.

Keeping the above effects of the radar system bandwidth in mind, the detectability of one or/and more single scatterer(s), based on the four FCF features, is expected to become lower with the decrease of the radar system bandwidth. To examine this expectation further, the numerical simulations were used to study the same previous cases of terrain and of terrain with one and more single scatterers (of variable TCR) embedded in it at 0.5 GHz radar system bandwidth. These simulations showed that the average slope of $|FCF_{terrain}|$ is more steeper than the previous case of 2.0 GHz system bandwidth, and the squared error is larger than the previous case of 2.0 GHz system bandwidth. These results verify our expectation and clearly will lead to a lower capability of detecting single embedded scatterer(s). Comparisons between the cases of 1, 2, and 5 single scatterers embedded in a homogeneous terrain with 0.5 GHz system bandwidth and their corresponding cases of 2.0 GHz radar system bandwidth, demonstrated the following differences :

I- The FCFBW is capable of distinguishing the cases of single scatterers with large TCR from cases of homogeneous terrain. But, for the same level of discrimination —based on FCFBW only— TCR should be larger than their corresponding cases of 2.0 GHz radar system bandwidth.

II- The dynamic range of the FCFBW is almost 25% of that of the case of 2.0 GHz radar system bandwidth, which is similar to the ratio of reduction of the system bandwidth.

III- The average slopes of FCF are of wider dynamic ranges for all cases when compared to their corresponding cases of 2.0 GHz radar system bandwidth.

IV- There is an overlap between the dynamic ranges of the average slope in the cases of one, two, and five single scatterers on one side and that of the homogeneous terrain on the other side. In the case of 0.5 GHz radar system bandwidth, this overlap exists for TCRs larger than their corresponding cases of 2.0 GHz radar system bandwidth.

The applicability of this observed behavior, from the numerical simulations, to the measurements, reported in Chapter 7, was examined. This examination was done by calculating the FCFBW of all the measurements of the sections of the trunk-ground combination using the data of 0.25 GHz only and compare it to the previous results of Chapter 7 which was based on data of 0.375 GHz. The result is illustrated in Fig. 8.18. Comparison between Fig. 7.10 and Fig. 8.18 shows the increase of overlap between the dynamic range of the FCFBW corresponding to trunks with those of the other sections. It is clear that the reduction of the radar system bandwidth results in poorer performance of the FCF-based detection algorithm. This conclusion is examined further by applying the detection algorithm to the data set of FCF's with 0.5 GHz radar system bandwidth. These results of the performance of the detection algorithm, based on the 0.5 GHz radar system bandwidth data set, are shown in figures 8.19—8.21, which when compared to figures 8.12—8.14, show the lower performance of the detection algorithm associated with the decrease of the radar system bandwidth.

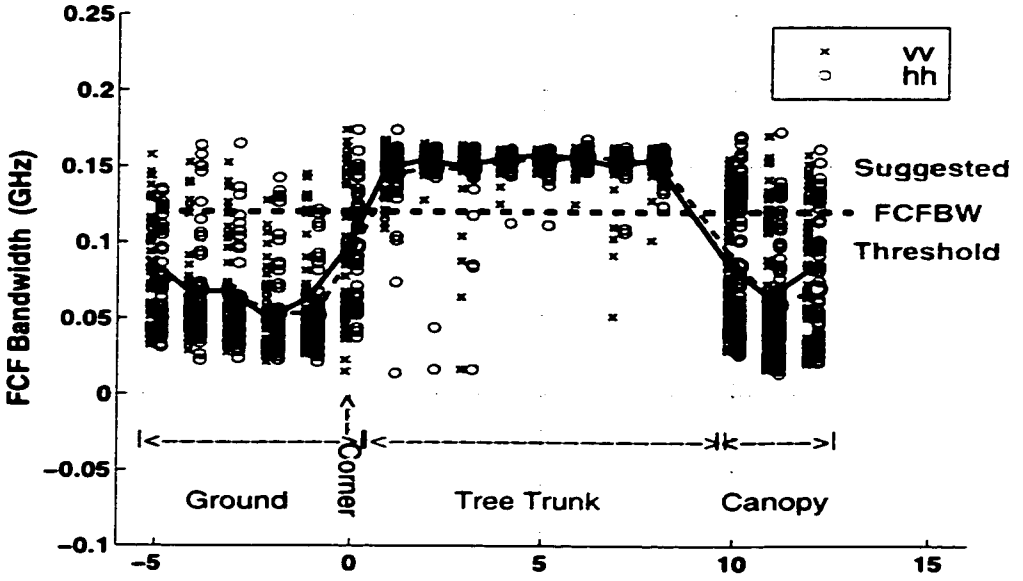

(a) 35 GHz

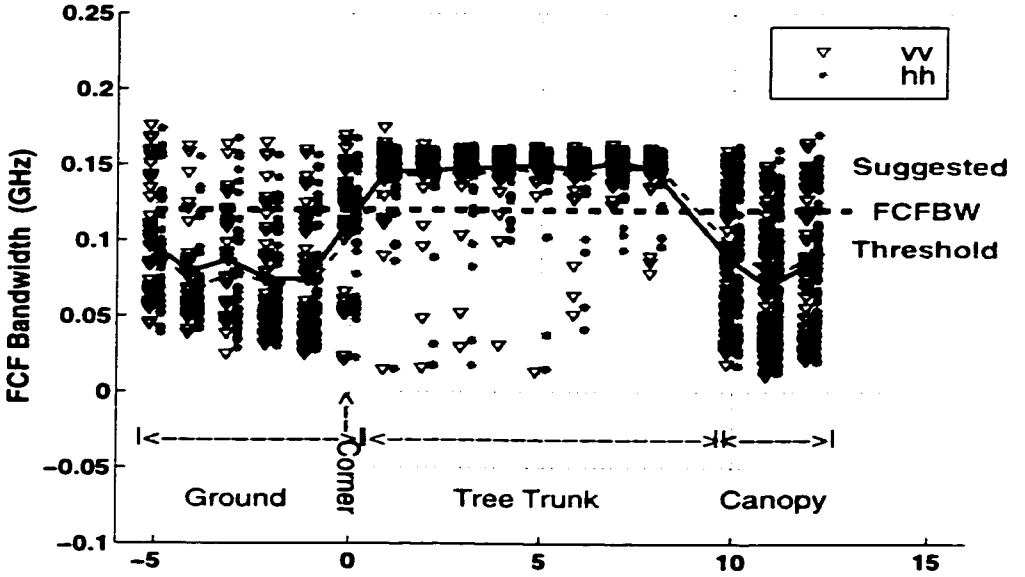

(b) 95 GHz

Figure 8.18: The dynamic range and mean values of the FCFBW, based on S_{vv} and S_{hh}, of different sections of the trunk-ground combination at both 35 GHz and 95 GHz. Radar system bandwidth = 0.25 GHz.

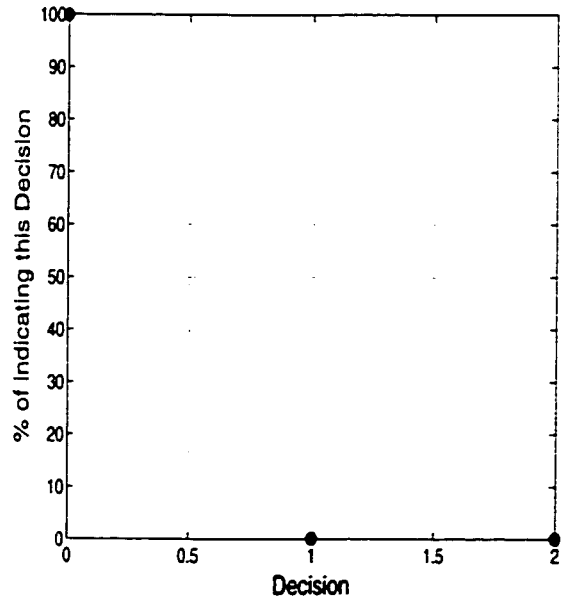

(a) 0 single scatterers

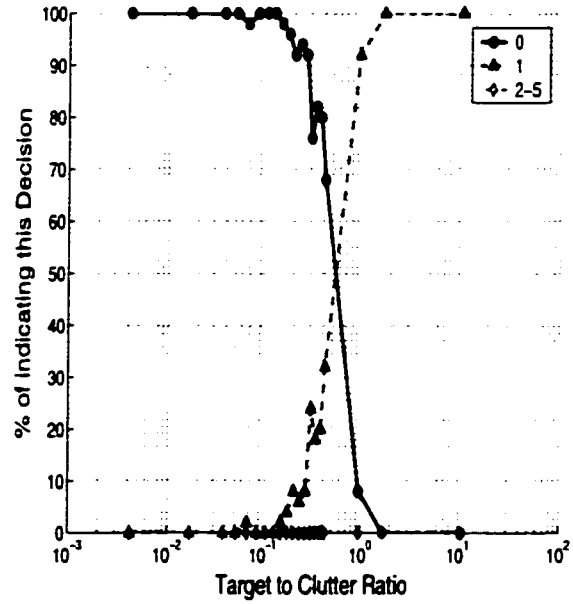

(b) 1 single scatterer

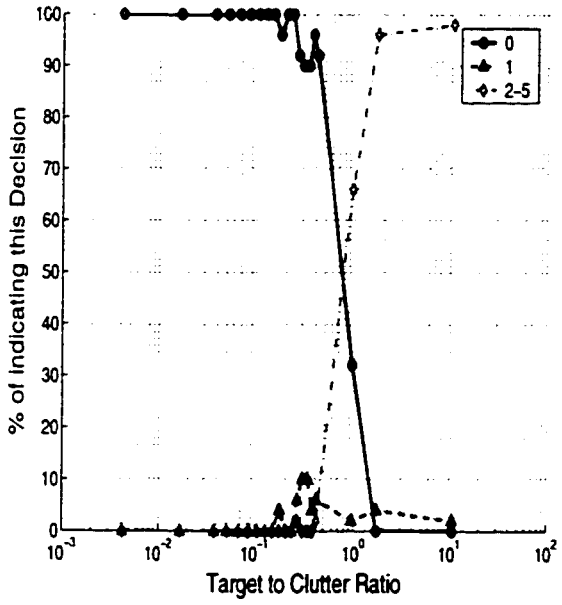

(c) 2 single scatterers

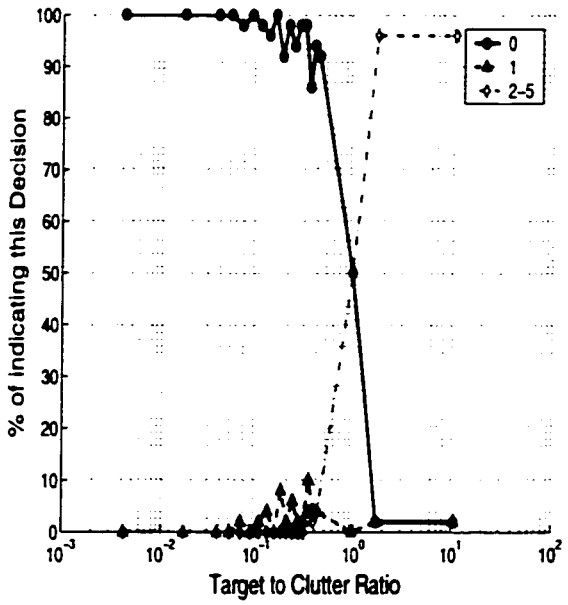

(d) 3 single scatterers

Figure 8.19: Performance of the detection algorithms for the cases of terrain with 0,1,2, and 3 single scatterers embedded in it with 0.5 GHz system bandwidth.

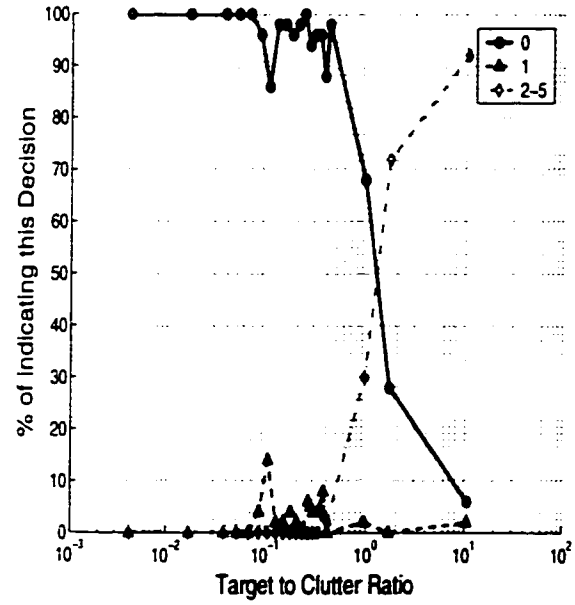

(a) 4 single scatterers

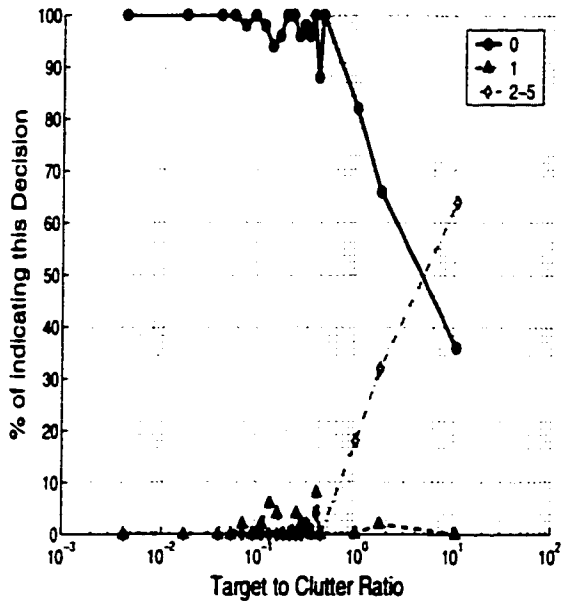

(b) 5 single scatterers

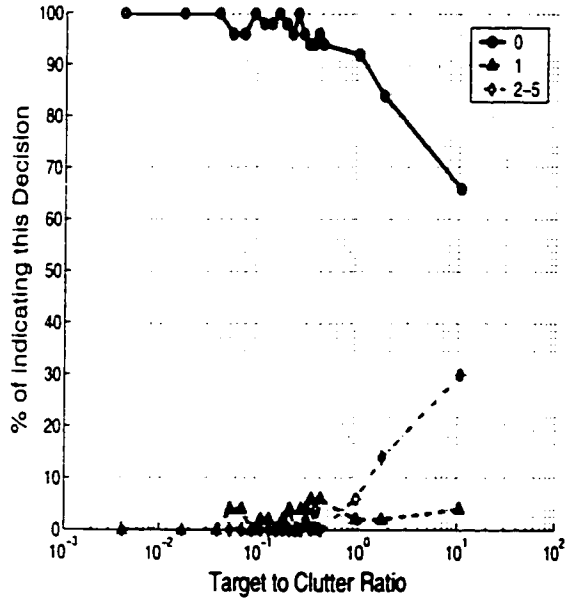

(c) 6 single scatterers

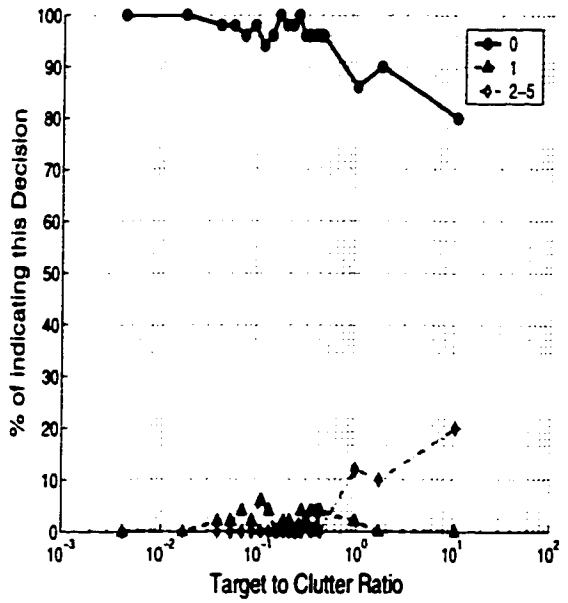

(d) 7 single scatterers

Figure 8.20: Performance of the detection algorithms for the cases of terrain with 4,5,6, and 7 single scatterers embedded in it with 0.5 GHz system bandwidth.

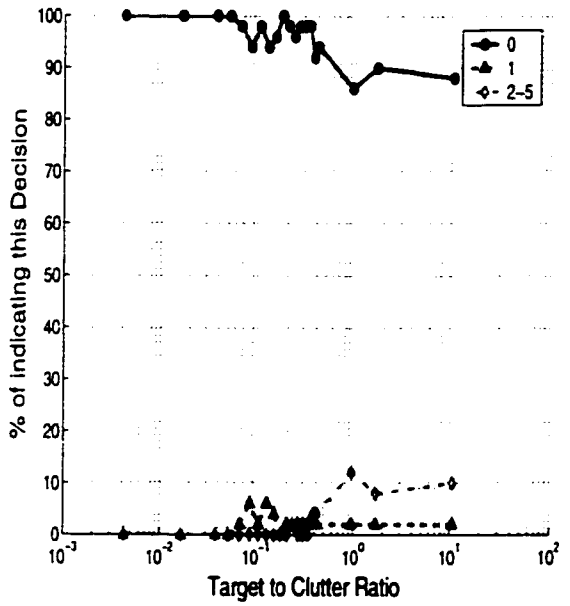

(a) 8 single scatterers

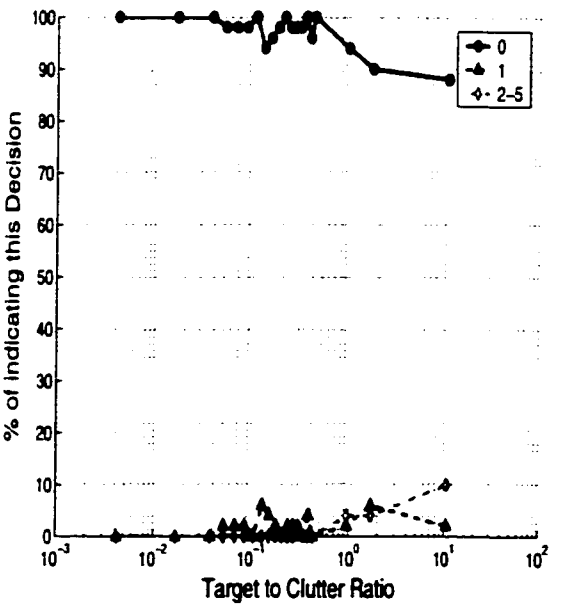

(b) 10 single scatterers

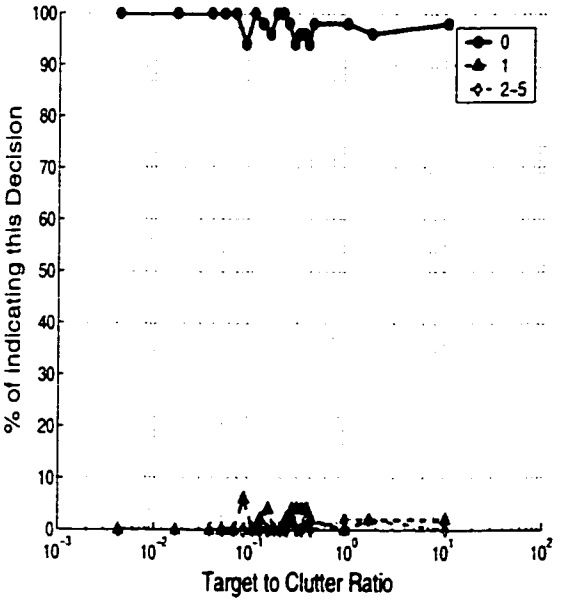

(c) 30 single scatterers

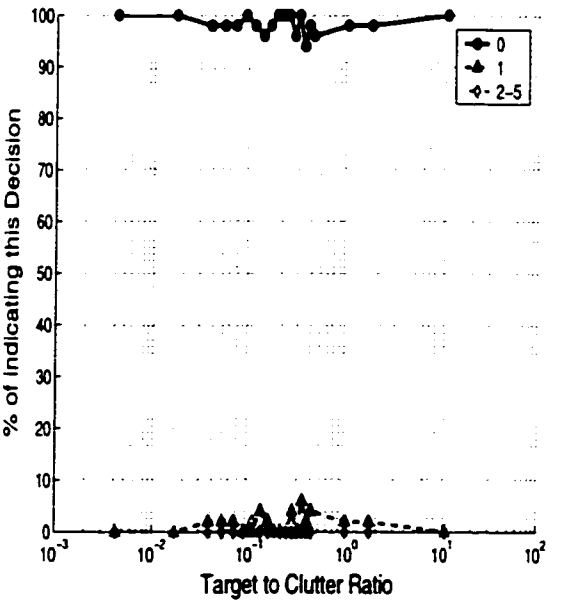

(d) 100 single scatterers

Figure 8.21: Performance of the detection algorithms for the cases of terrain with 8,10,30, and 100 single scatterers embedded in it with 0.5 GHz system bandwidth.

8.6 The Application of the Detection Algorithm to the Measured Data

The enhanced detection algorithm of Section 8.4 was applied to the measured data of Chapter 7, and its results were compared to the results of the simple detection algorithm of Chapter 7. The simple algorithm of Chapter 7 uses one detection feature (FCFBW) while the enhanced detection algorithm uses four detection features (FCFBW, Average Slope, Squared error, and Ratio). Figure 8.22 shows the comparison between the results of the two detection algorithms, which show that the enhanced detection algorithm has a slightly better detection ability. Also, the comparison shows that the maximum detectability improvement corresponds to the corner of the trunk-ground setup. The corner of the trunk-ground setup is a practical example of a cell of terrain (ground) with one single scatterer embedded (the lower part of the trunk). Hence, the addition of more detection features enhanced the capability of the FCF-based detection algorithm to detect the tree trunk and discriminate it from the surrounding environment.

A point to mention here is that, the performance improvement is small ($\approx 8\%$) and this is attributed to the limited bandwidth of the system used in measurement ($BW = 0.375$ GHz).

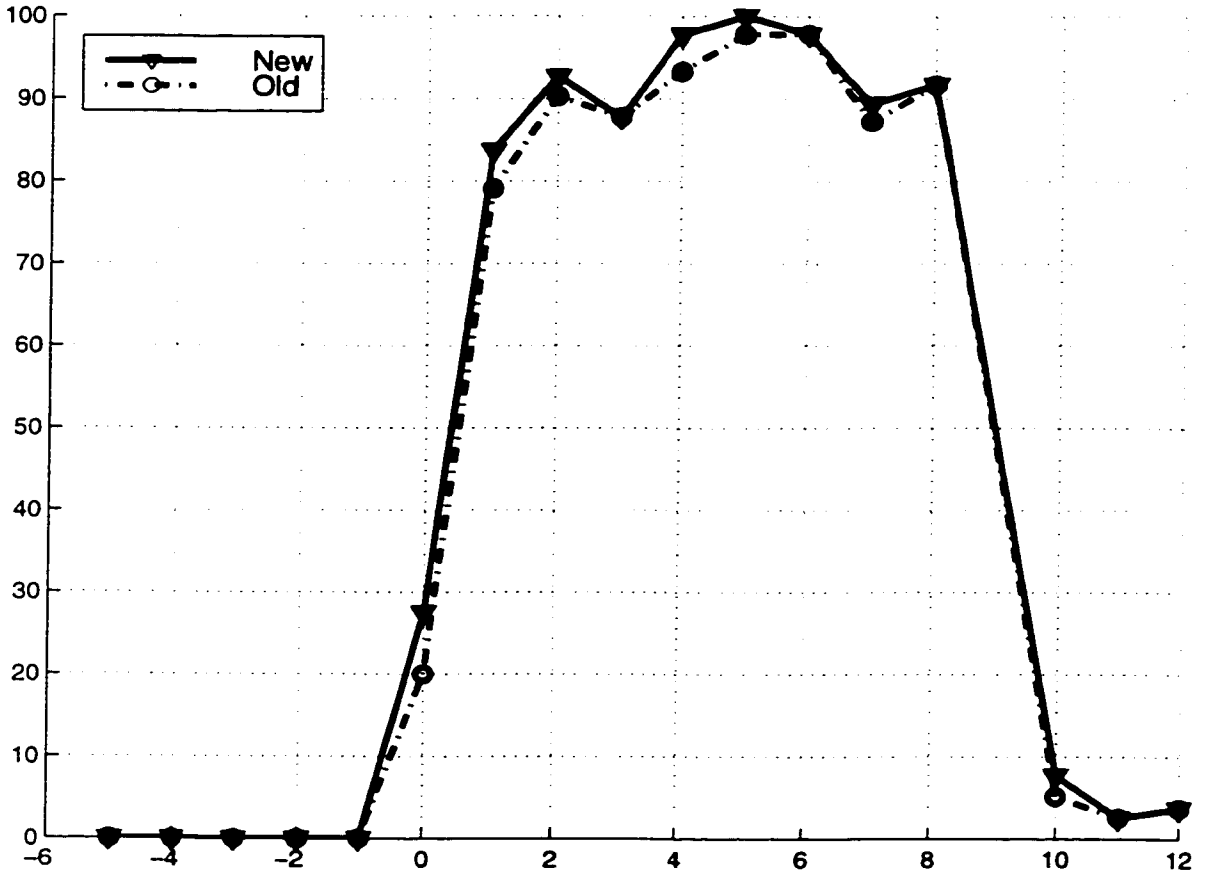

Figure 8.22: Comparison between the results of the simple and the enhanced detection algorithms.

8.7 Conclusions

A numerical simulation procedure is developed to simulate the FCF of the backscattering by a radar-illuminated cell of terrain without and with a few single scatterers embedded in it. The numerical simulation was used along with the analytical derivation of Chapter 6 to physically interpret the behavior of the FCF and its relation to the type of scatterers (single scatterer versus terrain) in the radar illuminated cell. Also, the numerical simulation was used to generate a data set of FCF of the backscattering by terrain with and without single scatterers embedded in it. The analysis of this data set along with the analytical analysis and measurement observations, reported in Chapters 6 and 7 [4], led to the development of an enhanced detection algorithm that is based on four FCF-based features. The detection algorithm was tested and its high ability of discriminating tree trunks from nearby targets, including man-made targets, was shown. In addition, we showed that the performance of the detection algorithm improves with the increase of the radar system bandwidth.

CHAPTER 9

CONCLUSIONS AND FUTURE WORK

In this thesis we studied and analyzed the MMW scattering by natural terrain at near grazing angles, in general, and focused, in particular, on the MMW scattering by tree trunks. The characterization of the MMW scattering by terrain and tree trunks were studied due to their necessity in the design of optimal MMW sensors that are capable of detecting man-made targets with terrain in the background.

9.1 Conclusions

The statistical analysis of the MMW backscattering by various types of natural terrain at near grazing angles showed that the Rayleigh fading model is applicable for characterizing the statistical behavior of the radar backscatter from homogeneous distributed targets, such as terrain surfaces, so long as the illuminated cell is large enough to contain many scatterers, and, additionally, no single (or few) scatterer(s) dominate over all others. In addition, this study showed that, the radar backscatter

from heterogeneous terrain obeys conditional Rayleigh distribution. In other words, knowing the pdf of the local mean scattering levels of heterogeneous terrain $p(\sigma_i^o)$ can be used along with the Rayleigh model to derive its statistical properties. Further study of this latter point led to the application of the Bayes formula to derive the pdf of the scattering from heterogeneous terrain as follows, [42]:

$$p(\sigma_A) = \int_0^\infty p_i(\sigma_A \mid \sigma_i^o)\, p(\sigma_i^o)\, d\sigma_i^o,$$

or in the discrete format

$$p(\sigma_A) = \sum_{all\ local\ fields} p_i(\sigma_A \mid \sigma_i^o)\, P(\sigma_i^o). \tag{9.1}$$

Based on geometric optics approximation, general solutions for both the coherent and incoherent components of the scattering by rough, lossy, dielectric cylinder were developed. These general coherent and incoherent solutions are in the forms of two and four folded integrals, respectively. For the common case of a rough cylinder having a Gaussian distributed roughness, we reduced the coherent solution to a closed-form expression. Also, for the common case of a cylinder having a surface roughness with exponential characteristic function, we reduced the solution to a closed-form expression. The models for both the coherent and the incoherent components are valid for the backscattering and a wide range of bistatic configurations.

These analytical models were verified experimentally by performing a set of indoor measurements of the coherent and incoherent angular responses of a rough conduct-

ing cylinder and a section of a tree trunk. In addition, an approximate procedure was used to measure the dielectric constant of the wooden material of the tree trunk, which was found to be $2 + j0.7$ for samples with average water content of 30%, and a laser profiler system was used to measure the roughness parameters of both the rough conducting cylinder and the tree trunk section. All the measured parameters were, then, applied to the analytical model to evaluate its backscattered predictions. The evaluated incoherent model predictions were compared to the indoor measurements and very good agreements, between theory and measurements, for the two cases of the rough conducting cylinder and the tree trunk section were achieved.

Two possible scenarios for occurrence of high RCS value from trunk-ground setup were considered and studied. One of them is based on a direct scattering from the tree trunk, and the other one is based on bistatic scattering from the trunk-ground setup. A method to calculate the probability of occurrence of high RCS value based on both scenarios was introduced. The results of this method showed that the first scenario is much more probable to occur and the probability of occurrence, in both cases, increases with the increase of the trunk (cylinder) diameter. This increase is expected to reach saturation when the size of the trunk (cylinder) fills the radar beam in the direction perpendicular to the axis of the cylinder.

To enhance the ability of detection algorithms to detect man-made targets with terrain in the background, the application of the FCF in the detection problem and its physical meaning along with its relation to the time-domain signal were studied

analytically, where a general expression for the FCF of the backscattering by a radar-illuminated cell that contains an arbitrary number of scatterers was developed.

In addition, the application of FCF to the detection problem was studied experimentally, where an outdoor measurement campaign (at 35 GHz and 95 GHz) was designed and conducted for this purpose. Based on the acquired data, the FCFBW values of individual measurements of trunks were found to be centered around higher values than that of the other nearby targets (trunk-ground corner, ground, tree canopy, and tanks). This behavior was explained theoretically and verified by measurements. Based on this behavior, a simple detection algorithm was proposed, tested, and its performance was evaluated. This algorithm showed greater than 89% detectability of trunks at different radar look angles at 35 GHz with a slightly lower performance at 95 GHz. In addition, its false alarm rate is less than 8% at 35 GHz and is a bit higher at 95 GHz. The algorithm's ability to discriminate tree trunks from other nearby targets, including man-made targets, was also demonstrated.

Further study of the properties of the FCF, its relation to the number of scatterers in the illuminated cell, and its relation to the radar system parameters (system bandwidth, incidence angle, etc.) were also performed based on a numerical simulation procedure. In addition, the numerical simulation was used to generate a data set of the FCF of the backscattering by terrain with and without single scatterers embedded in it. The analysis of this data set along with the analytical analysis and the experimental observations led to the development of an enhanced detection algo-

rithm that is based on four FCF features. This detection algorithm was tested and its high ability of discriminating tree trunks from nearby targets was demonstrated. In addition, we showed that the performance of the detection algorithm improves with the increase of the radar system bandwidth.

9.2 Future Work

In Chapter 3 we developed closed-form solutions for the coherent and incoherent components of the scattering by rough lossy dielectric cylinder for some common cases of roughness functions. Developing closed-form solution for general cases and/or other common cases of roughness function is a natural extension of this work.

In Chapter 4 we performed an extensive experimental verification of the incoherent component of the scattered field from a rough lossy dielectric cylinder in the backscatter direction. Since the developed model is valid for the backscatter configuration as well as for a wide range of bistatic configurations, performing experimental verification of this model under bistatic configuration is the next step to complete this work.

In our study and analysis of the FCF and its application to the detection problem, Chapters 6–8, we considered only the FCF amplitude of the co-polarized radar backscatter. A possible extension of this work is to search for useful information or detection features based on the complex co-polarized and/or cross-polarized radar

backscatter.

BIBLIOGRAPHY

BIBLIOGRAPHY

[1] A. E. El-Rouby, F. T. Ulaby, A. Y. Nashashibi, "Modeling the Backscattering Response of Tree Trunks at MMW Frequencies", IEEE AP-S international Symposium, July 11-16, 1999, Orlando, Florida, USA

[2] A. E. El-Rouby, A. Nashashibi, and F. T. Ulaby, "A Novel MMW Radar Detection Feature and its Dpplication to the Discrimination of Tree Trunks from Nearby Targets," in Proceedings, Fourth Annual FedLab Symposium on Advanced Sensors, University of Maryland, 21–23 March 2000.

[3] A. E. El-Rouby, A. Nashashibi, and F. T. Ulaby, "A New MMW Radar Detection Feature and its Application to the Discrimination of Tree Trunks from Nearby Targets", IEEE International Geoscience and Remote Sensing Symposium, IGARSS 00, July 24-28, 2000, Honolulu, HI, USA.

[4] A. E. El-Rouby, A. Y. Nashashibi, and F. T. Ulaby,"Study of the Frequency Correlation Function and its Application to Radar Target Detection", To be submitted to one of the IEEE Transactions July, 2000.

[5] A. E. El-Rouby, F. T. Ulaby, and A. Nashashibi," MMW Scattering by Rough Lossy Dielectric Cylinders and its Application to Tree Trunks", To be submitted to one of the IEEE Transactions July, 2000.

[6] A. Y. Nashashibi, K. Sarabandi, and F. T. Ulaby, "A Calibration Technique for Polaremetric Coherent-on-Receive Radar System" IEEE Trans. on Antenna and Prop, Vol-43, No. 4, April 1995.

[7] A. Y. Nashashibi, F. T. Ulaby, and K. Sarabandi, "Measurement and modeling the millimeter-wave backscatter response of soil surfaces," *IEEE Trans. Geosci. Remote Sensing,* vol. 34, no. 2, pp. 561-572, March 1996.

[8] C. Eftimiu, "Electromagnetic Scattering By Rough Conducting Circular Cylinders ,"Radio Science, Vol. 23, No. 5, p 760-768, Septemper 1988.

[9] E. Jakeman, "On the statistics of K-distributed noise," *J. Phys. A; Math. Gen.,* vol. 13, pp. 31-48, 1980.

[10] E. J. Rothwell, D. P. Nyquist, Kun-Mu Chen, and B. Drachman, "Radar Target Discrimination Using the Extinction-Pulse Technique" IEEE Trans. on Antenna and Prop, Vol-33, No. 9, September 1985.

[11] E. J. Rothwell, Kun-Mu Chen, and D. P. Nyquist, "Extraction of the Natural Frequencies of a Radar Target from a Measured Response Using E-Puls Techniques" IEEE Trans. on Antenna and Prop, Vol-35, No. 6, June 1987.

[12] E. S. Li, Millimeter-Wave Polarimetric Radar System as an Advanced Vehicle Control and Warning Sensor, Ph.D. Thesis, The University of Michigan,1998.

[13] F. T. Ulaby, R. K. Moore, and A. K. Fung, *Microwave Remote Sensing*, vol. II, Chapter 12, Artech House Publishing Cp., Norwood, Mass, 1982.

[14] F. T. Ulaby, C. T. Allen, and A. K. Fung, "Method for Retrieving the True Backscattering Coefficient from Measurements with Real Antenna," IEEE Trans. Geosci. and Remote Sensing, Vol. GE-21, No. 3, p. 308, July 1983.

[15] F. T. Ulaby, R. K. Moore, and A. K. Fung, *Microwave Remote Sensing*, vol. III, Appendix E, Artech House Publishing Co., Norwood, Mass, 1986.

[16] F. T. Ulaby and M. C. Dobson, *Handbook of Radar scattering Statistics for Terrain,* Artech House Publishing Co., Norwood, Mass, 1989.

[17] F. T. Ulaby, C. Elachi, Radar Polarimetry for Geoscience and Applications, Chapter 4, Norwood, MA: Artech house, 1990.

[18] F. T. Ulaby, M. W. Whitt, and K. Sarabandi, "AVNA-based polarimetric scatterometers," *IEEE AP magazine,* vol. 32, 1990.

[19] F. T. Ulaby and C. Elachi, *Radar polarimetry for geoscience applications,* Artech House, Dedham MA, 1990.

[20] F. T. Ulaby, T. F. Haddock, R. T. Austin, and Y. Kuga, "Millimeter-wave radar scattering from snow: II. Comparison of theory with experimental observation," Radio Science, vol. 26, No. 2, pp. 343-351, 1991.

[21] F. T. Ulaby, R. McIntosh, and W. Flood (eds.), "Handbook of millimter-wave polarimetric radar response of terrain," University of Michigan Radiation Laboratory Report, Ann Arbor, MI, March 1995.

[22] F. T. Ulaby, P. Siqueira, A. Nashashibi, and K. Sarabandi, "Semi-empirical model for radar backscatter from snow at 35 and 94 GHz," *IEEE Trans. Geosci. Remote Sensing,* vol. 34, No. 5, pp. 1059-1065, Sept 1996.

[23] F. T. Ulaby, A. Nashashibi, A. El-Rouby, E. S. Li, R. De Roo, K. Sarabandi, R. J. Wellman, and H. B. Wallace, "95-GHz Scattering by Terrain at Near Grazing Incidence," IEEE Trans. On Antenna and Propagation, pp. 3-13, Jan, 1998

[24] F. T. Ulaby, A. El-Rouby, R. De Roo, A. Nashashibi, K. Sarabandi, R. J. Wellman, H. B. Wallace, and J. Silvious"MMW Radar Clutter Statistics at Near Grazing Incidence," Second Annual FedLab Symposium on Advanced Sensors", Feb 2-6, 1998, University of Maryland, pp 103–108.

[25] F. T. Ulaby, A. Y. Nashashibi, R. D. Deroo, P. Frantzis, and A. E. El-Rouby. "Preliminary Handbook of Near-Grazing Millimeter-Wave Polarimetric Radar Response of Terrain", University of Michigan, Ann Arbor, MI, Radiation Laboratory, December 1998.

[26] G. T. Ruck, D. E. Barrick, W. D. Stuart, and C. K. Krichbaum, Radar Cross Section Handbook, Volume 1, New York: Plenum Press, 1970.

[27] H. S. Cabayan, and R. C. Murphy, "Scattering of Electromagnetic Waves by Rough Perfectly Conducting Circular Cylinders," IEEE Trans. On Antenna and Propagation, pp. 893-895, November, 1973.

[28] I. S. Gradshteyn, I. M. Ryzhik, Table of Integrals, Series, and Products, pages 480, 495, Academic Press Inc., 1980.

[29] J. B. Mead, P.S. Chang, S.P. Lohmeier, P.M. Langlois, and R.E. McIntosh, "Polarimetric observations and theory of millimeter wave backscatter from snowcover," *IEEE Trans. on Antennas and Propagat.*, vol. 41, No. 1, pp. 38-46, Jan. 1993.

[30] J. B. Mead, A.L. Pazmany, P.S. Chang, and R.E. McIntosh, "Comparisons of coherent and noncoherent polarimetric radar measurement techniques at 95 GHz," *Radio Science,* vol. 31, No. 2, pp. 325-333, March-April 1996.

[31] J. K. Jao, "Amplitude distribution of composite terrain radar clutter and the K-distribution" *IEEE Trans. Antennas Propagat.*, vol. AP-32, pp. 1049-1062, October 1984.

[32] J. M. López-Sánchez. *et. al.*, " An Electromagnetic Scattering Model for Multiple Tree Trunk Above a Tilted Rough Ground Plane," IEEE Trans. Geosci. and Remote Sensing, Vol. 37, No. 2, pp. 659-667, March 1999.

[33] K. Sarabandi, Electromagnetic Scattering From Vegetation Canopies, Ph.D. Thesis, The University of Michigan,1989.

[34] K. Sarabandi, and A. Nashashibi, "Analysis and Applications of Backscattering Frequency Correlation Function," IEEE Trans. On Geoscience and Remote Sensing, pp. 1895-1906, July, 1999.

[35] M. A. Karam and A. K. Fung, "Electromagnetic Scattering from a layer of Finite-length, randomly oriented dielectric circular cylinder over a rough interface with application to vegetation," Int. J. Remote Sensing, Vol. 9, no. 6, pp. 1109-1134, 1988.

[36] M. I. Skolnik, Introduction to Radar Systems, New York : McGraw-Hill, 1980.

[37] M. W. Whitt and F. T. Ulaby, "Radar Response of Periodic Vegetation Canopy" Int. J. Remote Sensing, 1994, Vol. 15, No. 9, pp 1813-1848.

[38] O. Li, E. J. Rothwell, Kun-Mu Chen, and D. P. Nyquist, "Radar Target Discrimination Schemes Using Time-Domain and Frequency-Domain Methods for Reduced Data Storage" IEEE Trans. on Antenna and Prop, Vol-45, No. 6, June 1997.

[39] P. S. Chang, J. B. Mead, E. J. Knapp, G. A. Sadowy, R. E. Davis, and R. E. McIntosh, "Polarimetric backscatter from fresh and metamorphic snow-cover at millimeter wavelengths," *IEEE Trans. on Antennas and Propagat.*, vol. 44, No. 1, pp. 58-73. Jan. 1996.

[40] R. Wellman, G. Goldman, J. Silvious, and D. Hutchins, "Analyses of millimeter wave radar low-angle ground-clutter measurements for European-like and desert environments," Army Research Laboratory Technical Report ARL-TR-1102, Adelphi, Md., July 1996.

[41] R. De Roo, F. T. Ulaby, A. E. El-Rouby, "Polarimetric Feature Analysis As Applied to Automatic Target Recognition", Second Annual FedLab Symposium on Advanced Sensors", Feb 2-6, 1998, University of Maryland, pp 147–151.

[42] R. De Roo, F. T. Ulaby, A. El-Rouby, and A. Nashashibi, "MMW Radar Scattering Statistics of Terrain at Near Grazing Incidence," IEEE Trans. On Aerospace and Electronic Systems, pp. 1010-1018, July, 1999.

[43] R. De roo, F. T. Ulaby, A. El-Rouby, A. Nashashibi, " MMW Radar Scattering Statistics of Terrain at Near Grazing Incidence," IEEE AP-S international Symposium, July 11-16, 1999, Orlando, Florida, USA

[44] R. D. De Roo, F. T. Ulaby, A. E. El-Rouby, A. Y. Nashashibi, and G. S. Samples, "SPRI: Simulator of polarimetric radar images," in Proceedings, Low Grazing Angle Clutter: Its Characterization, Measurement and Application, Laurel, MD, 25–27 April 2000, NATO Sensors and Electronic Technology Panel (SET).

[45] R. D. De Roo, F. T. Ulaby, G. S. Samples, J. Munn, J. Costanza, A. Y. Nashashibi, A. E. El-Rouby, and L. E. Pierce, "MMW Polarimetric Data Base of Terrain Reflectivity and an Associated Image Simulator", IEEE

International Geoscience and Remote Sensing Symposium, IGARSS 00, July 24-28, 2000, Honolulu, HI, USA.

[46] S. H. Yueh, J.A. Kong, J.K. Jao, R.T. Shin, and L.M. Novak, "K-distribution and polarimetric terrain radar clutter," *J. of Electromagnetic Waves and Applications,* vol. 3, No. 8, pp. 747-768, 1989.

[47] S. O. Rice, "Mathematical Analysis of Random Noise," in Selected Papers on Noise and Stochastic Processes, N. Wax, Ed. New York: Dover, 1954.

[48] T. Chiu and K. Sarabandi, "Electromagnetig Scattering Interaction Between a Dielectric Cylinder and a slightly Rough Surface," IEEE Trans. On Antenna and Propagation, pp. 902-913, May, 1999.

[49] Y. Lin, K. Sarabandi, "Electromagnetic Scattering Model for a Tree Trunk Above a Tilted Ground Plane," IEEE Trans. Geosci. and Remote Sensing, Vol. 33, No. 4, p. 1063, July 1995.

[50] Y. Dong, and J. A. Richards, "Studies of the Cylinder-Ground Double Bounce Scattering Mechanism in Forest Backscatter Model," IEEE Trans. Geosci. and Remote Sensing, Vol. 33, No. 1, pp. 229-231, Jan. 1995.

[51] Y. Kouskoulas; L. Pierce; F. T.Ulaby, M. C. Dobson, "Classification of short vegetation using multifrequency SAR," International Geoscience and Remote Sensing Symposium (IGARSS), v 2 1999. p 735-737

[52] Y. Kuga, F.T. Ulaby, T.F. Haddock, and R.D. DeRoo, "Millimeter-wave radar scattering from snow: 1. Radiative transfer model," *Radio Sci.,* vol. 26, No. 2, pp. 329-341, 1991.

[53] Y. Oh, K. Sarabandi, and F.T. Ulaby, "An empirical model and an inversion technique for radar scattering from bare soil surfaces," *IEEE Trans. Geosci. Remote Sensing,* vol. GE-30, pp. 370-381, March 1992.

[54] Personal Communications with Researchers at the Army Research Laboratory (ARL).